Viscoelastic Modeling of Calving Processes at Antarctic Ice Shelves

vom Fachbereich Maschinenbau und Verfahrenstechnik
der Technischen Universität Kaiserslautern
zur Verleihung des akademischen Grades
Doktor-Ingenieur (Dr.-Ing.)
genehmigte Dissertation

von
Dipl.-Math. techn. Julia Christmann
aus Neustadt an der Weinstraße

Hauptreferent:	Prof. Dr.-Ing. Ralf Müller
Korreferenten:	Prof. Dr. Angelika Humbert
	Prof. Dr.-Ing. Dietmar Gross
Vorsitzender:	JP Dr. Felix Walker
Dekan:	Prof. Dr.-Ing. Jörg Seewig

Tag der Einreichung:	21.04.2017
Tag der mündlichen Prüfung:	02.06.2017

Kaiserslautern, 2017

D 386

Herausgeber

Lehrstuhl für Technische Mechanik
Technische Universität Kaiserslautern
Gottlieb-Daimler-Straße
Postfach 3049
67653 Kaiserslautern

Ich danke der „Prof. Dr. Hans Georg und Liselotte Hahn Stiftung“ für die finanzielle Unterstützung bei der Drucklegung.

Druck

Technische Universität Kaiserslautern
Hauptabteilung 5/ Bau-Technik-Energie
Abteilung 5.6 Foto-Repro-Druck

ISBN 978-3-942695-14-5

Vorwort

Die vorliegende Arbeit entstand während meiner Tätigkeit als wissenschaftliche Mitarbeiterin am Lehrstuhl für technische Mechanik der Technischen Universität Kaiserslautern.

An erster Stelle bedanken möchte ich mich bei meinem Doktorvater Prof. Dr.-Ing. Ralf Müller und meiner Doktormutter Prof. Dr. Angelika Humbert für die hervorragende Betreuung und Unterstützung meiner Arbeit. Außerdem danke ich Herrn Prof. Dr.-Ing. Gross für das Interesse an meiner Arbeit und für die Übernahme eines der Korreferate sowie Herrn JP Dr. Felix Walker für die Übernahme des Vorsitzes.

Mein besonderer Dank gilt meinen ehemaligen und aktuellen Kolleginnen und Kollegen für die angenehme Atmosphäre sowohl während der Arbeitszeit als auch bei den zahlreichen außeruniversitären Aktivitäten. Durch die Zeit am Lehrstuhl sind viele Freundschaften entstanden, welche auch die kommende Zeit überdauern werden. Ich konnte mich immer auf die stete Hilfbereitschaft und ein offenes Ohr verlassen. Zusätzlich will ich auch meinen Kollegen in Bremerhaven am AWI danken für die Unterstützung mit COMSOL und die hilfreichen Diskussionen über mein Thema.

Zu guter Letzt bedanken möchte ich mich bei meiner Familie, meinen Freunden und insbesondere meinem Freund für die immerwährende Unterstützung, den uneingeschränkten Glauben an meine Arbeit und die nicht endende Geduld während der gesamten Zeit der Promotion.

Danke!

Kaiserslautern, Juni 2017 Julia Christmann

Kurzfassung

Gletscher, Eiskappen, Eisschilde, und Schelfeise bedecken heute etwa 10 % der Oberfläche der Erde. Mit etwa 70 % des gesamten Süßwasservorrats liegt die größte Eismasse auf dem antarktischen Kontinent und formt den gegründeten Antarktischen Eisschild. Der Erdanziehung folgend fließt das viskose Eis zur Küste und speist die Schelfeise, welche die schwimmenden Erweiterungen des Eisschildes bilden. Verschiedene Komponenten des Klimasystems der Erde treffen an den Rändern dieser Schelfeise aufeinander (die Atmosphäre, das Eis und der Ozean). Am Wichtigsten dabei ist, dass die Schelfeise durch ihre Rückhaltekraft den Eispanzer der Antarktis stärken und das Eis daran hindern, ungebremst in den Ozean zu fließen. Im Gleichgewichtszustand verlieren die Schelfeise hauptsächlich durch basales Schmelzen und das Kalben von Eisbergen an Masse. Diese abgetrennten Stücke des Schelfeises können driftend große Entfernungen zurücklegen. Ihr Schmelzwasser bildet einen bedeutenden Beitrag in der Süßwasserbilanz des Ozeans und beeinflusst die Modifikation der Wassermassen in hohen Breiten und somit die globale Ozeanzirkulation. Das Aufstellen eines auf physikalischen Prinzipien basierenden Kalbungsgesetzes ist deshalb dringend erforderlich, um die Auswirkungen des Klimawandels auf die Eisschilde und ihre Wechselwirkungen mit den Ozeanen zu analysieren.
Bisher existieren allerdings nur phänomenologische Ansätze, um das Kalben in Eisschildmodellen abzubilden. Zum Teil ist das bedingt durch die Vielfalt an Kalbungsszenarien, welche sich an gegründeten oder an schwimmenden Eiskörpern orientieren, für unterschiedlich temperiertes Eis oder für Eiskanten an Süß- wie auch Salzwasser. Zusätzlich ist die Aufgabenstellung einer physikalischen Kalbungsbeschreibung kompliziert, das Kalbungsgesetz muss nicht nur sinnvoll und praxisnah sein, sondern auch numerisch effizient. Daher ist es die Zielsetzung dieser Dissertation, ein geeignetes Materialmodell zu etablieren, anhand welchem mögliche Kalbungskriterien diskutiert werden können. Von besonderem Interesse ist hier die Entwicklung von Ansätzen, die in numerischen Eischildmodellen mit einer realistischen Topografie genutzt werden können, um gegenwärtige und zukünftige Entwicklungen des antarktischen Eisschildes zu beschreiben.

Der Prozess des Kalbens besteht einerseits aus dem Abbruchvorgang und der sich ergebenden Lastveränderung beschrieben durch eine elastische Materialantwort auf kurzer Zeitskala. Andererseits sind es die viskosen Eigenschaften, welche den Eisfluß zwischen zwei Kalbungsereignissen über einen längeren Zeitraum beschreiben. Deshalb wird ein viskoelatisches Materialmodell aufgestellt, um das Kalben von Eisbergen an antarktischen Schelfeisen zu untersuchen.

In dieser Arbeit werden alle numerischen Berechnungen mit Hilfe der Finiten Element Software COMSOL durchgeführt. Die Diskretisierung beruht dabei auf Prismen oder Dreiecken. In dieser Arbeit werden vier verschiedene Materialgesetze betrachtet. Das Erste verbindet die Spannungen mit den Dehnungen durch eine zeitunabhängige Beziehung eines linear elastischen Materials. Als zweites folgt das viskose Modell, in dem die Spannungen mit den Dehnraten verknüpft werden. Als letztes werden aus diesen zwei grundlegenden Materialbeschreibungen die viskoelastischen Modelle eines Festkörpers (Kelvin-Voigt-Modell) oder einer Flüssigkeit (Maxwell-Modell) zusammengesetzt. Die Verschiebungen sind dabei die Knotenfreiheitsgrade der Elemente und die Spannungen und Dehnungen können daraus bestimmt werden. Um allerdings das Maxwell-Modell vollständig beschreiben zu können, sind noch zusätzliche interne Variablen notwendig.
Das Kalben als eine Art von Materialversagen muss aus bruchmechanischen Konzepten wie etwa kritischen Spannungs- oder Dehnungszuständen aufgebaut werden. Aus den Berechnungen wird klar, dass für das Beispiel einer vertikalen Eisfront die größten Zugspannungen und Dehnungen an der Oberfläche auftreten. Dies ist durch den Wasserdruck an der Eisfront zu begründen, welcher eine exzentrisch angreifende Kraft und somit ein Biegemoment bedingt. Durch diese Randstörung wird das Kalben ohne vorher existierende Risse verursacht. Kalben dieser Art wird in der Arbeit als kleinskaliges Kalben bezeichnet. Die Ergebnisse eines zentral gelegenen Querschnitts einer dreidimensionalen Geometrie können auch mit einem zweidimensionalen Untersuchungsgebiet berechnet werden, wenn die seitlichen Ränder keinen Einfluss mehr auf den Querschnitt haben (der nötige Abstand ist abhängig von der Eisdicke). Durch die Annahme dieses ebenen Verzerrungszustandes kann die Berechnungszeit stark reduziert werden. Wenn die Länge der Geometrie größer als $20\times$ die Dicke ist, dann sind die Ergebnisse darüber hinaus auch längenunabhängig. Weitere Sensitivitätsstudien untersuchen den Einfluß von Variationen der Geometrie und der Materialkennwerte auf die Ergebnisse. Zusätzlich zu diesen Untersuchungen wird auch noch die Abfolge von Kalbungsereignissen mit MATLAB untersucht.
Die Kennwerte eines isotropen Materials bestehen aus zwei elastischen Konstanten (Elastizitätsmodul und Querdehnungkontraktion) und der Viskosität, welche von dem Verformungszustand des Eises abhängen. In dieser Arbeit wird die Viskosität über weite Teile als konstant angenommen, wobei auch der Unterschied zu der nichtlinearen Beschreibung anhand des Fließgesetzes von Glen analysiert wird. Für die viskosen Stoffgesetze werden die Annahmen von kleinen Verformungen nach einer gewissen Simulationszeit verletzt und die verwendete Linearisierung der kinematischen Beziehungen wird ungenau. Die Ergebnisse führen zu einer Missachtung von wichtigen physikalischen Prinzipien, beispielsweise dem Schwimmgleichgewicht. Um unpräzise Spannungsantworten zu vermeiden, wird das Maxwell-Modell auf große Verformungen erweitert. Die daraus resultierenden nichtlinearen Materialmodelle im dreidimensionalen Raum benötigen eine feinere Diskretisierung und somit auch höhere Berechnungszeiten als bisher.

Die Vergleiche der hier berechneten numerischen Ergebnisse mit den analytischen eines eindimensionalen Balkens belegen die Eignung des linearen elastischen und des viskosen Materialmodells, beim letzteren allerdings nur für kurze Simulationszeiten. Mit einem Balken ist es jedoch unmöglich, den atmosphärisch beeinflussten Bereich an der Eisfront abzubilden. Dieser Bereich ist jedoch laut der zweidimensionalen Rechnung von extremer Wichtigkeit, um den Spannungszustand an der Eisoberfläche (kritisch fürs Kalben) genau zu bestimmen. Beim viskosen Balken kann auch die horizontale Streckung nicht abgebildet werden und die resultierenden Zustände auf langer Zeitskala sind ungenau. Numerische Berechnungen sind somit nötig, um die Gründe des kleinskaligen Kalbens nahe der Eisfront beschreiben zu können. Unter gleichen Voraussetzungen konnte zusätzlich gezeigt werden, dass die viskosen zweidimensionalen Ergebnisse mit denen eines laminaren Models, welches in COMSOL vordefiniert ist um Fließen zu modellieren, übereinstimmen.
Die genaue Untersuchung der Spannungszustände weist ihre Abhängigkeit von der Eisdicke an der Eisfront aber auch von der Höhe des Freibords, also des wasserfreien Bereichs, nach, welches sich aus dem Verhältnis von Eis- zu Ozeandichte ergibt. Für alle Parameterstudien liegt die Position der maximalen Zugspannung in einem Abstand von einer halben bis ganzen Eisdicke von der Eisfront entfernt. Die Zeit zwischen zwei aufeinanderfolgenden Kalbungsereignissen ist von der charakteristischen Zeit des Modells abhängig und somit nur von Materialkennwerten und unabhängig von der Geometrie. Dabei ist direkt nach einem Kalbungsereignis die Eisfront erst vertikal, bevor sie sich mit der Zeit durch Schmelzprozesse verändert. Diese Veränderungen werden anhand des linear elastischen Materialmodells diskutiert, um ihren Einfluss auf die Ergebnisse abzuschätzen. Einerseits führt das Schmelzen der unteren Ecke der Eisfront zu erhöhten Zugspannungen. Anderseits entstehen diese durch Schmelzprozesse in Bereichen, die bisher von Druckspannungen dominiert waren. So verlagert sich die kritische Spannung von der Ober- an die Unterseite, wenn ein "Unterwasserbauch" gebildet wird, der mindestens die Breite der halben Eisdicke hat. Das lässt den Schluss zu, dass die Spannungszustände im Wesentlichen von der Geometrie abhängig sind. Darüber hinaus wurde gezeigt, dass die Ergebnisse mit konstanter und gemessener Eisdicke gut übereinstimmen. Aus diesem Grund reicht es völlig aus, mit einer konstanten, aber geeignet gewählten Dicke zu modellieren und die Folgerungen auf reale Schelfeise zu übertragen.
Ein weiterer Fokus dieser Arbeit liegt auf den verschiedenen Kalbungskriterien. Das kritische Spannungskriterium ist für ein Kelvin-Voigt-Modell zweckmäßig, wobei der Grenzfall durch das linear elastische Materialverhalten vorbestimmt ist. Aufgrund der Abhängigkeit der Spannungszustände von der Mächtigkeit ist dieses Kriterium leider nur auf einen sehr kleinen Bereich anwendbar. Sinnvolle und stabile Kalbungsraten werden mit einem Selbstähnlichkeitskriterium erzeugt, welches zum Abbruch führt, wenn ein ehemals kritischer Zustand, zum Beispiel der Stationärwert, wieder eintritt. Während mit dem Kelvin-Voigt Material kein viskoses Langzeitverhalten von Eis modelliert werden kann, erfüllt das Maxwell-Modell die erforderlichen Merkmale: Elastisches Verhalten auf kurzer Zeitskala, viskoses auf

einer langen. Die damit erzeugten Ergebnisse für Schelfeise, welche durch den Wasserdruck belastet sind, zeigen für dieses Materialmodell einen anfänglichen Spannungsanstieg mit nachfolgendem Rückgang der Spannungen für ungeänderte Belastungszustände. In diesem Fall ist das Spannungskriterium nur während des Anstiegs (abhängig von der Viskosität) sinnvoll. Als weitere Möglichkeit kann ein Dehnungskriterium verwendet werden. Da die Dehnungszustände von der Verformungsgeschichte des Schelfeises abhängen, führt diese Kriterium allerdings zu einem Anwachsen der Dehnungen über die Zeit und somit zu einer Beschleunigung der aufeinander folgenden Kalbungsereignisse.
Es stellte sich heraus, dass sich bei einem viskoelastischen Ansatz mit der Annahme von kleinen Verformungen die Oberfläche mit größer werdenden Verzerrungen immer weiter absenkt, während die Unterseite auf einer unveränderten Position bleibt. Um den Einfluss diese Aspekts auf das Kalben zu untersuchen, werden verschiedene Modelle, welche für große Dehnungen gültig sind, aufgestellt. Nachdem die beiden Modellansätze für die anfänglich kleinen Verformungen übereinstimmen, werden mit der Zeit die Spannungszustände bei dem Modell für die großen Deformationen größer als mit dem linearen Materialmodell. Der allgemeine Einblick in kritische Kalbungssituationen ist von dem Modell für große Deformationen unabhängig und ein linearisiertes Materialmodell reicht zur Beschreibung einzelner Kalbungsereignisse aus. Wenn viele aufeinander folgende Vorkommnisse mit allen physikalischen Gegebenheiten (z. B. Schwimmgleichgewicht) genau abgebildet werden sollen, wird ein Modell basierend auf großen Dehnungen mit variablen Rändern benötigt.

Abstract

At the present day glaciers, ice caps, ice sheets, and ice shelves add up to approximately 10 % of the surface of planet Earth. Containing around 70 % of the world's freshwater, the largest mass of ice covers the Antarctic continent and forms the grounded Antarctic Ice Sheet. The gravity-driven flow of ice to the coast supplies mass to the ice shelves, which are the floating extensions of the Antarctic Ice Sheet. Fundamental components of Earth's climate system interact at the margins of these ice shelves (the atmosphere, the ice, and the ocean). By their buttressing force the ice shelves reinforce the ice shield of Antarctica and reduce the velocity of the glaciers that channel the flow of ice from the continental ice sheet toward the ocean. Even in a steady state, ice shelves lose mass by basal melting and calving of icebergs. These separated pieces of ice can drift over large distances. Their meltwater contributes to the freshwater budget of the ocean, which in turn affects the water mass modification in high latitudes and the large-scale ocean circulation. In order to obtain a meaningful representation of ice sheets and ice sheet–ocean interaction in scenarios considering climate change, a calving law based on physical processes is therefore absolutely essential.
So far only phenomenological approaches are used in the ice sheet models trying to predict the future evolution of the ice. This is partly due to the diversity of calving mechanisms relevant for either grounded or floating ice bodies, for different temperatures of ice or with ice margins at fresh- or tidewater. Furthermore, the task to determine a physics-based description of calving is complex, a calving law has not only to be useful and practical but also robust and efficient. In consequence, the aim of this thesis is to establish a suitable material model and to discuss possible calving criteria. These are relevant components for the use in numerical ice sheet models with a realistic topography in order to assess the present and future evolution of the Antarctic Ice Sheet.

The calving process consists on the one hand of the short-term elastic ice response due to the break-off event and the consequent reaction to the modified traction conditions. On the other hand the viscous properties are significant to describe the long-term behavior of ice between successive calving events. Hence, a viscoelastic material model is established to analyze the process of iceberg calving at Antarctic ice shelves.
All numerical computations in this work are performed with the finite element software COMSOL. The discretization applied consists of prism or triangular elements. Four different types of material behavior are considered during this work. The first one addresses the rate-independent relation between stresses and strains of a linear

elastic material. Secondly, a linear viscous model proportionally links stresses to strain rates. Finally, the combination of these basic approaches results either in the Kelvin-Voigt model depicting a viscoelastic solid or in the Maxwell model defining a viscoelastic fluid. The nodal unknowns of the finite elements are the displacements and all stresses and strains are computed out of these quantities. Only in the case of the Maxwell model, the displacement vector is insufficiently defined and internal variables are needed additionally.
Calving as a type of material failure has to be based on fracture mechanical concepts such as critical stress or strain states. For the vertical ice front mainly examined in this work the numerical evaluation shows that the largest tensile stress and strain values occur directly at the upper surface in the flow direction. This can be attributed to the bending moment of the eccentric water pressure at the ice front. Caused by this boundary disturbance the process of ice breaking off without pre-existing cracks is denoted as small-scale calving. The results in the central cross section of a three-dimensional domain can be mimicked with a two-dimensional geometry if the lateral boundaries are sufficiently far away (the necessary distance depends on the ice thickness). With the assumption of plane strain conditions the computational time is reduced. In case the length exceeds 20× the thickness the results are not only width- but also length-independent. Concerning the variability of geometries and material values, several parameter studies help to obtain an understanding of their influence on the results. These investigations and those that consider a sequence of calving events are accomplished by the numerical computing environment MATLAB.
The material parameters of isotropic ice consist of two elastic material constants (Young's modulus, Poisson's ratio) and the viscosity, which depends on the deformation state of ice. Although the viscosity is mostly assumed to be constant during this work, differences to the nonlinear formulation derived by the use of Glen's flow law are also studied. For the fluid models the assumption of small strains is violated after a certain simulation time and thus the linearization of the kinematic relation applied so far is invalid. The results lead to the disregard of important physical principles, for instance, the disregard of the buoyancy equilibrium. To prevent inaccurate stress responses the Maxwell model is extended to finite deformation models. These nonlinear material models are implemented in a three-dimensional geometry and need a fine discretization and thus high computational times.

Comparisons of the numerical results from this study to the analytical solution for a one-dimensional beam prove the applicability of the linear elastic and the viscous material model, for the latter only with the restriction to short simulation times. However, it is impossible to model the traction-free atmospheric part at the front within the limits of the beam approach. The investigations of the two-dimensional continuum reveal that this part is essential to obtain the crucial stress states at the upper ice surface accurately (critical for calving). The viscous beam fails to determine the horizontal extension due to the viscous flow of ice and after some time the consequent evolving stress and strain states get inaccurate. In consequence, a

numerical computation is necessary to describe the causes for small-scale calving in the vicinity of the ice front. Beside that, the viscous results of the two-dimensional continuum for longer simulation times agree under consistent conditions to the one of the laminar flow model already given in COMSOL.
The analysis of the stress states reveals their dependency on the thickness at the ice front as well as on its traction-free part influenced by the density ratio of ice and sea water. For all parameter studies the position of the maximum stress in the numerical simulation occurs within a distance between half the thickness to the full thickness away from the ice front. The time between two consecutive calving events depends on the characteristic time of the model and thus only on the material and not on geometric parameters. Directly after a calving event the ice front is vertical, but the impact of melting modifies this boundary with time. This variation is discussed for the linear elastic model to get an idea of its effect on the results. On the one hand, the sole melting of the lower edge of the vertical ice front leads to increased tensile stresses. On the other hand, tensile stresses arise for appropriate melting in the part below the water surface so far dominated by compression. Hence, the critical stress value shifts to the bottom for an underwater "belly" of almost half the ice thickness. Finally, the stress states depend highly on the actual geometry. However, the results including a measured geometry are in good agreement with those using a constant thickness. Therefore it is sufficient to consider the ice shelf geometry with constant thickness during this work and transfer the results to real ice shelf scenarios.
Another focus of this work is put on the search for a calving law to appropriately model the calving situation at Antarctic ice shelves. The critical stress criterion is applicable for the Kelvin-Voigt material as this model results in the stationary case of the linear elastic model. In consequence of the thickness dependency of the stresses, this criterion with a constant critical stress value is only valid for a small range of ice thicknesses at the front. A self-similarity criterion in which calving occurs when the stationary state is almost reached is more robust and leads to sensible calving rates. While a Kelvin-Voigt solid is inapplicable to describe the long-term viscous behavior of ice, the Maxwell model fulfills the requested ice characteristics: short-term elastic and long-term viscous behavior. For ice shelves loaded by sea-water pressure at the front the results of this material model indicate a stress increase followed by a stress decrease with time for unchanged traction conditions. The stress criterion makes sense only during the viscosity-dependent period of increasing stresses. Another possibility is to use the strain criterion for calving. Based on the dependency of the deformation on the ice shelf history, the strain states grow in time and this criterion yields an incomprehensible speed-up between consecutive calving events.
For a viscoelastic approach assuming small deformations, the bottom boundary remains at the same position while the upper surface of the ice shelf lowers with time. In order to analyze the influence of this issue on calving, different models valid for large deformations are established. After an initial accordance, the stress states of the finite deformation models achieve larger results with time than the one for the small deformations. However, the general insight in critical calving situations

is unaffected and a linearized material model is sufficient to model the calving behavior of a few successive calving events. The numerical computation of continuous small-scale calving that satisfies all physical conditions (like buoyant equilibrium) over a long time has to be extended to a material model valid for finite deformations.

Contents

1 Introduction

1.1 Framework and Motivation

Although Earth is often referred as the Blue Planet, large parts of the surface are presently covered by ice. Next to a high amount of relatively small mountain glaciers, two huge bodies of grounded ice are found on top of the continents Greenland and Antarctica. The Greenland Ice Sheet holds roughly 3 million cubic kilometers of ice (Bamber et al., 2013), indeed this is small compared to the almost 26 million cubic kilometers of ice stored in the Antarctic Ice Sheet (Fretwell et al., 2013). A total melt of the grounded ice from the Greenland and the Antarctic Ice Sheet is equivalent to about 7 m and 60 m sea-level rise, respectively. The future evolution of these ice sheets is therefore not only of scientific interest but also immediately relevant to human society. The dominant source in the mass balance of any of the two ice sheets is the mass gained from accumulating snowfall. Over millions of years an ice body with a thickness of up to 4 000 m has formed over the Antarctic continent. The pressure of this large body of ice together with the surface tilt force causes a viscous flow of ice to the periphery of the Antarctic continent.
When the ice reaches the coast, it either calves directly into the ocean (this is the normal case for Greenland, but unusual for Antarctica) or becomes afloat and feeds one of the ice shelves that surround almost 60 % of Antarctica's coastline today. While few floating ice tongues exist along the coast of Greenland, the vast majority of the ice shelves are located in Antarctica. Wesche et al. (2013) detected in total 183 ice shelves with areas between 20 km^2 and 490 000 km^2 (Ross Ice Shelf), while all ice shelves smaller than 20 km^2 were neglected and involve roughly 0.16 % of the total ice shelf area. The thickness of Antarctic ice shelves ranges from less than 100 m to more than 1 000 m, see Giggs and Bamber (2011), and is color coded with white to blue in Fig. 1.1. The dark blue area in this figure represents the Southern Ocean that surrounds the Antarctic continent. It is covered by sea ice with a seasonal extent up to the size of the continent in the austral winter. The thickness of the grounded Antarctic Ice Sheet (Fig. 1.1, brown to yellow colors) reaches a maximum of more than 4000 m. Nevertheless around 2 % of the area remain free of ice (green areas in Fig. 1.1), they consist of mountain tops, rock outcrops and the Antarctic Dry Valleys, which actually represent the most extreme deserts on Earth.
A hierarchy of numerical models considering both the local energy balances (thermodynamics) and the flow of ice (dynamics) has been developed to investigate sensitivities of the ice sheets to climate change and try to predict future developments. Famous examples of dynamic-thermodynamic ice sheet models are the Ice

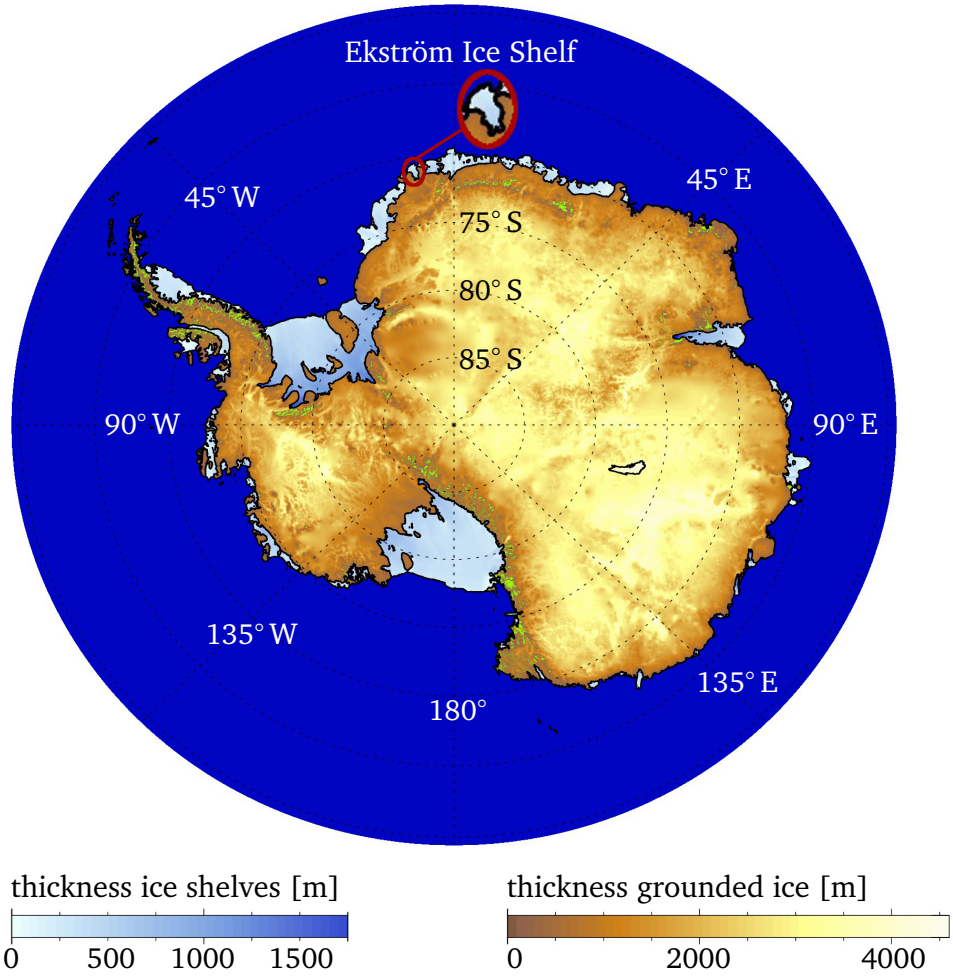

Figure 1.1: A map of Antarctica including the thicknesses of ice shelves (white to blue) and grounded ice (brown to pale yellow) created from the RTopo-2 data set (Schaffer et al., 2016). The green areas are free of ice and the Southern Ocean is depicted in dark blue. The closed black line on the East Antarctic continent indicates the location of the sub-glacial Lake Vostok.

Sheet System Model (ISSM; Larour et al., 2012, Habbal et al., 2017), the Parallel Ice Sheet Model (PISM; Bueler et al., 2007), the SImulation COde for POLythermal Ice Sheets (SICOPOLIS; Greve et al., 2011), and Elmer/Ice (Seddik et al., 2012). In the Sea-level Response to Ice Sheet Evolution (SeaRISE) project, several ice sheet models have been used to investigate the upper bound of ice sheet contributions to sea-level change in the next 100 – 200 years. The assessment was based on a suite of idealized perturbations to ice sheet boundary conditions. Some of these were (intentionally) outside the range of climate change that can be expected even for a worst case scenario. Detailed information on the complete set of numerical experiments together with validations and results are given in Bindschadler et al. (2013), Nowicki et al. (2013a), and Nowicki et al. (2013b). A more scenario-oriented approach was followed by the EU project: Estimating the future contribution of continental

ice to sea-level rise (Ice2sea). With high-resolution forcing from atmosphere and ocean models, the ice sheet simulations of Cornford et al. (2015) helped to improve projections of the contribution of ice to future sea-level rise. Both projects clearly show that the best prediction of the future evolution of ice sheets is obtained if all natural processes are described as accurately as possible.
One of the elements that is only crudely represented in the models discussed so far is the process of calving, i.e. the mass loss at the edge of any body of ice. Calving occurs at margins of grounded ice as well as at floating ice bodies. Based on observations, Benn et al. (2007) characterized different calving mechanisms according to their causes. Ice shelves are supported by the gravity-driven flow of ice from the ice sheet towards the ocean. They can be characterized as ice tongues that become afloat at a zone that is (slightly misleadingly) called the grounding line. In Antarctica, large icebergs calve from ice shelves as a natural, intermittent process. Their drift and also their melting is modeled quite reliably by now (e.g. Rackow et al., 2017). The calving, however, is still not well understood. Even recent estimates of the total contribution of calving to the mass loss at Antarctic ice shelves range from one third (Liu et al., 2015) to one half (Depoorter et al., 2013).
Given that icebergs calve from ice shelves that by definition are already afloat, this calving process does not lead directly to variations in global sea level. However, the grounded ice in the ice sheet is stabilized by the back pressure (buttressing) of a floating ice shelf (Dupont and Alley, 2005). After the collapse of Larsen Ice Shelf in 1995, several glaciers were found to accelerate rapidly (De Angelis and Skvarca, 2003). Also the acceleration of mass loss from the Antarctic Ice Sheet since the 1990s (Rignot et al., 2011) has been attributed to the thinning of ice shelves and a reduced buttressing particularly in the Amundsen/Bellingshausen Sea sector (Pritchard et al., 2012). Given the short timescales on which Larsen A and B ice shelves collapsed, break-up and calving may well become the dominant processes in determining the fate of Antarctic ice shelves in a warming climate. A useful assessment of the present and future mass balance of the Antarctic Ice Sheet thus requires a robust description of calving. From observations of the current situation an adequate representation of the governing processes can be derived. The location of calving lines (ice shelf fronts) suggested by such a calving law, however, needs to respond to varying boundary conditions (like a warming climate) in an appropriate way. This can only be achieved if the parametrization is replaced by or at least augmented and supported by physics-based calving laws.

1.2 Calving and Material Laws

The key objective within this work is the development of reliable calving criteria that are required to obtain physics-based calving rates. Although the calving mechanisms are diverse and the physics behind these processes are complex, a comprehensive, generalized description of the governing processes is necessary. Local effects shall be neglected in the model of the calving behavior until these details become important

for the general problem. In the current generation of ice sheet models, phenomenological or even heuristic approaches prevail so far, while a few ice sheet models still omit calving laws for their prognostic computations completely. In some of the models highly simplified methods are applied in which the calving fronts are either fixed (e.g. ISSM) or heuristically cut off as soon as the ice thickness is smaller than a certain value, for example 200 m (Amundson and Truffer, 2010). However, satellite imagery of the past illustrates fluctuations at the ice fronts. It is likely that ongoing climate changes will increase rather than decrease the variability over the next decades and centuries. In addition, several ice shelves have thicknesses below 200 m near the ice front. The Ekström Ice Shelf in East Antarctica (see Fig. 1.1) belongs to this category with an ice front thickness of around 100 m – much thinner than most of the thickness-based calving criteria would suggest. Another strategy to determine calving laws considers the horizontal strain rate as a possible criterion obtained by observations (PISM-PIK). A simple first-order relation describes the connection of calving to the spreading rate based on the two principal directions of the horizontal flow at ice shelves. For this dynamic calving law, certain assumptions have to be fulfilled (not valid for all ice shelves) and extensions to include the vertical shear were offered in order to describe a wider range of calving situations, see Levermann et al. (2012). Clearly the calving laws currently included in ice sheet models are better than the simple disregard of this important process, but all are based on empirical considerations only and suffer from a lack of physical background.
To obtain a physics-based calving law, an appropriate material description is required. Ice has different material behaviors according to the considered timescale and hence the phenomena of interest. On the one hand calving happens elastically on a rather short timescale in which cracks arise or propagate or cease in the detachment of an iceberg. On the other hand, the evolution of the ice shelf between two subsequent calving events has to be described on a long timescale by the viscous flow of ice. In consequence, a viscoelastic material model is imperative to discover the complex calving behavior of ice shelves. Other examples where viscoelasticity is essential are the phase shift between the load due to tidal forces and its evoked reaction, the bending near the grounding line or the development of sub-glacial melt channels.

Advanced numerical techniques are needed to model the processes inside an ice shelf. Especially the finite element method (FEM) is well approved in the glaciological context due to the complex geometry of ice sheet margins. In the FEM, the continuous domain is subdivided into finite-sized elements and thus discretized with a fixed number of elements and nodes. In general, the unknown velocities in ice sheets are computed at this discrete number of nodes by an incompressible laminar flow model using the pressure as an additional nodal unknown. This technique is not extendable to viscoelasticity in any straightforward way. From the view of material modeling, the viscous flow can also be described by the one-dimensional (1d) rheological model of a viscous damper. In the two-dimensional (2d) or three-dimensional (3d) extension, this method provides the same results for the limiting

case of an incompressible material as the laminar flow model. A relevant advantage of this approach is that the rheological relations of dampers and springs are widely used to represent all kinds of viscoelastic materials (Flügge, 1975). In contrast to the laminar flow model, the system of differential equations is solved in this work for the unknown displacements instead of the velocities by the use of the commercial software COMSOL. Additional parameter studies and the sequence of several calving events are implemented in MATLAB. The relevant stress and strain states for calving are determined by the computed unknowns inside the ice shelf. Analytical solutions obtained for a beam with a length much larger than its (constant) thickness contribute to a better understanding of the numerical results. Nevertheless, the numerical computation is essential and not replaceable as the crucial traction-free part at the ice front caused by the non-smooth water pressure distribution at the ice front cannot be captured in an analytical ansatz, see Christmann et al. (2016a).

1.3 Objectives and Overview

One core topic of this thesis is the development of a viscoelastic material model to compute the deformation and stress state inside the ice shelf due to internal and external forces. This mathematical representation of the ice behavior is used to discuss different calving criteria and determine critical stress and strain states that lead to the failure of the material. All viscoelastic models in this work are a compound of elastic and viscous components, which are responsible either for the short-term or long-term behavior of the material. On the one hand the linear elastic approach is rate-independent and the instantaneous reaction yields a stress state proportional to the strain response. On the other hand the stress is proportional to the strain rate and the deformation is time-dependent in the linear viscous material. Strain and strain rate are maximal in the flow direction of the ice shelf. As a consequence the considered ice shelf slightly thins out in the downstream direction towards the ice front.
In general, a sufficiently long ice shelf is in buoyant equilibrium apart from the area near the ice front. At this specific location the depth-dependent water pressure and the traction-free atmospheric part trigger a bending moment. The calving from homogeneous, crevasse-free surface structures happens as a result of this boundary disturbance and the aim is to investigate the stress in these situations. The Ekström Ice Shelf (cf. Fig. 1.2) reveals such a crevasse-free shape near the calving front. At this ice shelf thickness measurements with a ground-penetrating radar have been obtained along flow lines including a region close to the ice front (see the blue and the red lines). Additionally surface flow velocities were available from the Antarctic summer 2011/2012, which are required to determine calving rates. In this thesis, the results of the measured geometries are studied in comparison to those achieved by a constant thickness. Numerical simulations show that the boundary traction affects the ice front by bending it downwards. Consequently the critical quantities will occur at the upper surface for a vertical calving front. The analysis in this work

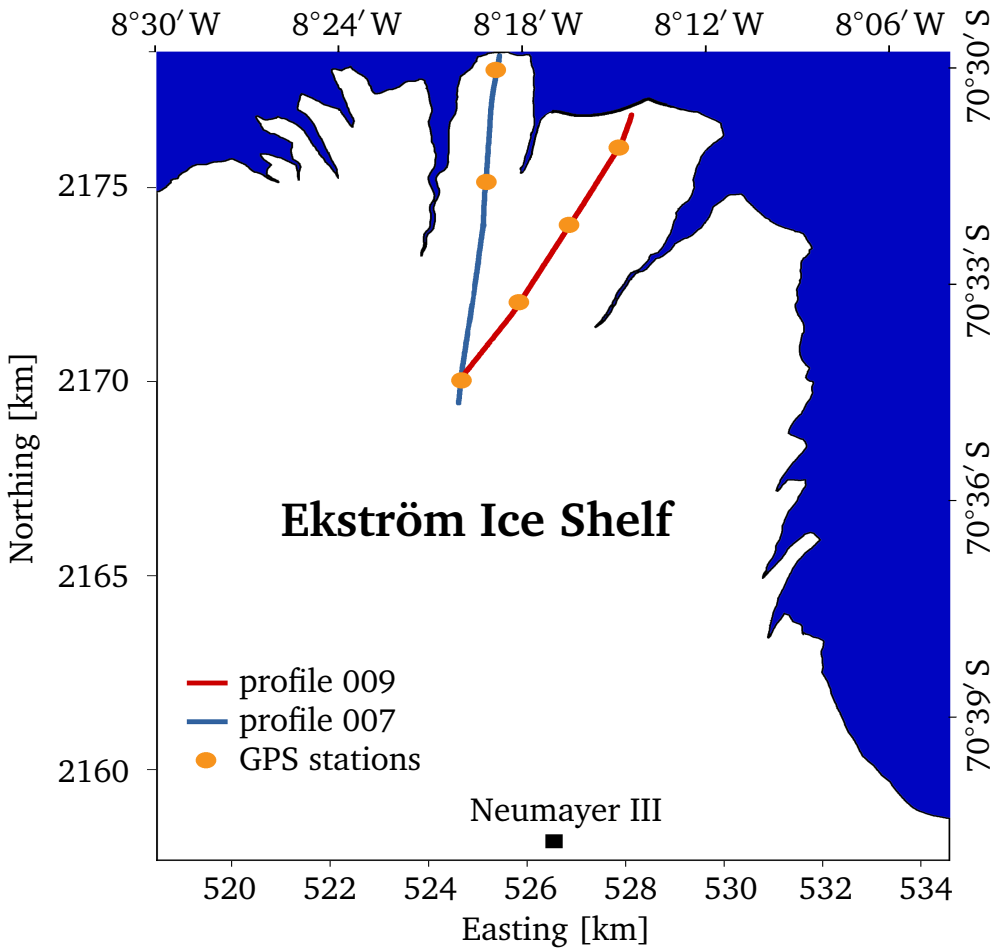

Figure 1.2: Inlet of the Ekström Ice Shelf with two selected radar profiles along flow lines of the ice shelf at which thickness measurements and surface velocities from the GPS stations are available. The German research station Neumayer III is located at this ice shelf with the recognizable shape of separated fingers.

indicates that the geometry in the vicinity of the ice front plays an important role for the calving behavior based on the boundary disturbance of the sea water pressure. In situations, where the ice front is not vertical anymore and modified by melting, the bending moment can change the direction under certain conditions. Then the bottom of the ice shelf experiences the larger load by an upward directed moment, while the surface is stabilized. However, if the load at the ice front is critical an iceberg detaches although no surface or basal crack has arisen previously. Therefore it is assumed that the bending moment of the sea water pressure is sufficient for calving once the crack is initiated near the ice front and crack propagation is not considered any further. For details of crack propagation in ice shelves see Plate (2015) and the literature cited in there.

Observations of calving are sparse and often only large calving events based on existing discontinuities like crevasses or rifts have been monitored for Antarctic ice shelves. However, Larour et al. (2004a) discussed calving events near Hemmen Ice Rise on the Filchner-Ronne Ice Shelf in Antarctica. Some of these events are

explainable solely by the boundary disturbance at the ice front. Nevertheless, no time series of calving events caused by bending are available until now. Based on improved satellite imagery with up to 3 m resolution, calving events of smaller-size icebergs are more and more detectable. A continuous satellite-supported monitoring of these events will strengthen the understanding of calving processes. The calving based on the boundary disturbance rather leads to small sized icebergs of 100 m^2 to a few km^2. This process is investigated and denoted as small-scale calving during this work. To understand the physical effects controlling this basic type of calving is the main issue of this work. As all ice shelves terminate in the ocean, small-scale calving occurs at small as well as large ice shelves. At ice shelves with lots of crevasses, other factors will superpose this basic process. Therefore, the ice sheet models have to include the continuous calving rates, which contributes beside basal melting to the typical conservation of mass at an ice shelf.
Another difficulty arises from calving as a repetitive process of many successive events. For the linear material models, the kinematic relation between displacements and strains is valid in a linearized form due to the assumption of small strains. The simplification is no longer appropriate if the strains inside the ice shelf increase progressively, which happens for a chronological analysis of calving. In addition, the large extent of Antarctic ice shelves in flow direction up to several hundreds of kilometers can lead to finite elongations. Hence, a further aspect shown in this work is that a finite deformation setting is necessary to model the viscoelastic calving behavior of ice shelves over several decades. A comparison of these results to the one of the linear model yields the limits to describe the calving behavior at ice shelves within a small deformation model.

1.4 Outline

This thesis is structured into eight chapters. The basic equations of continuum mechanics that are relevant to describe the deformations and stresses in an ice shelf are concisely summarized in the next chapter. The theory comprises kinematics, balance equations and material equations for small and finite deformation.

Different mechanisms of calving are explained in Chapter 3 with a special focus on small-scale calving. The modeling domain is defined together with suitable boundary and necessary initial conditions. As the last point the finite-element implementation provides the means to solve numerically the system of differential equations which model the behavior of an ice shelf.

In order to assess the consequences of a viscoelastic material description on calving, some insights into the separate impact of a purely elastic or a purely viscous material model are required. Chapter 4 demonstrates the elastic stress states that are time-independent and crucial for continuous calving in the 3d and 2d settings. The latter is sufficient to discuss calving with the use of linear material laws as the lateral effects of the side boundaries are negligibly small for the typical geometries

of ice shelves. At the 2d cross section assuming plane strain conditions parameter studies of the geometry and the material show the rate-independent responses of a linear elastic material. In addition, the stress results are confirmed by the analytical solutions of a 1d beam. Including the thickness of the Ekström Ice Shelf in the numerical model allows for a comparison of the results from the simplified geometry to the more complex real situation. Finally, the influence of a geometry modification due to melting at the ice front leads to a shift of the position of the critical calving quantity. In this case the location of maximal tensile stress value shifts from the top to the bottom boundary.

Chapter 5 clarifies the consequences of a purely viscous material. The comparison of results attained with the continuum model to the viscous beam is presented and the limits of this 1d approach are discussed. To confirm the correctness of the material ansatz taken in this work, its stress outcome is shown to correlate well with the results of the already given laminar flow models.

Prior to the examination of two different viscoelastic materials, possible calving criteria are outlined in Chapter 6. The applicability of these criteria and the corresponding results are first shown for the Kelvin-Voigt solid. The impracticality to model the viscous long-term behavior of ice leads to the cessation of this viscoelastic model, although the achievement of a stationary elastic state makes sense for the definition of a calving criterion. A special focus of this chapter is on the Maxwell material model that represents the elastic response on short timescales and the viscous flow on long timescales equivalent to the observable reaction at an ice shelf. The evolution of stress and strain states gives an identification on the position of calving and the time between two adjacent calving events. With the Maxwell model all different types of calving criteria are investigated, namely the stress and strain criterion as well as the self-similarity criterion. To this end the linear viscosity is replaced by a rate-dependent viscosity based on Glen's flow law and consequences of this nonlinear material parameter are discussed.

Chapter 7 deals with the finite viscoelasticity of a Maxwell material. The buoyant equilibrium is valid at all times in contrast to the results of the linear material laws so far. Indeed, the deformation from a specific moment in time violates the assumption of small strains, i.e. the requirement to linearize the kinematic relation. Thus a nonlinear material model becomes absolutely essential. The computation time is more extensive due to the finer resolution of the discretization in order to deal with this material law and the required 3d formulation. The maximum stress and strain states which are crucial for calving laws occur at the upper surface and are studied for this concept of finite deformations. The accordance of both models, the finite one and the one assuming only small deformations, are depicted at the beginning of the simulation when small strains are obtained. At the end, the responses of different approaches for finite deformation models are analyzed and their results coincide for the processes at ice shelves.

The last chapter provides a conclusion and an outlook to future works.

2 Continuum Mechanics

This chapter provides the basic equations and theoretical background needed for the computation of stress and deformation states in the vicinity of ice shelf fronts. The structure of this chapter is inspired by books on continuum mechanics, such as Haupt (2000), Altenbach (2012) or Holzapfel (2001), which provide a more detailed presentation of this theory.

2.1 Kinematics

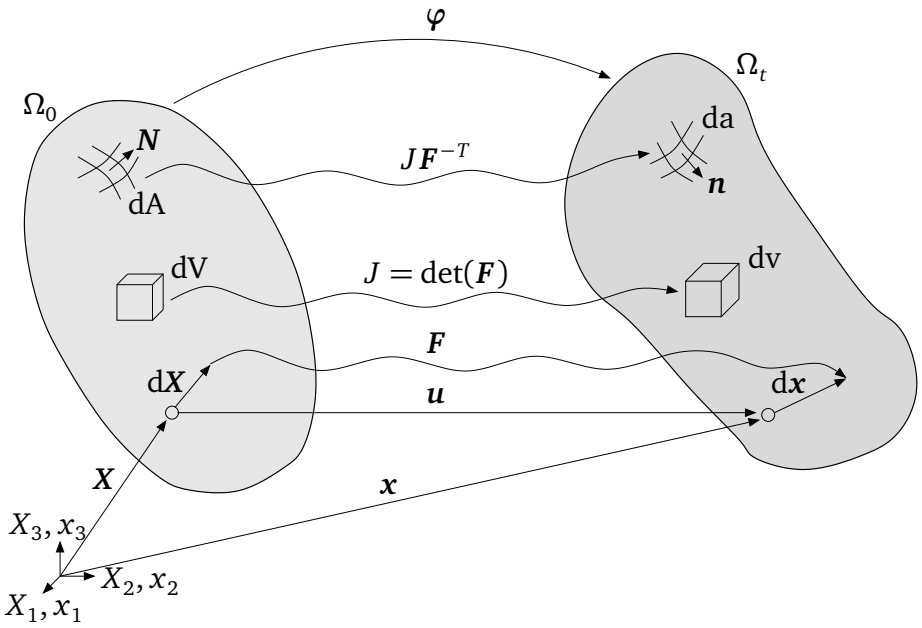

Figure 2.1: Reference and current configuration.

In continuum mechanics a body consists of material points, which experiences a deformation due to internal and external loading. All positions $\boldsymbol{X}$ of material points in an undeformed domain specify the *reference configuration* Ω_0, see Fig. 2.1. Depending on the time t, a unique deformation $\boldsymbol{\varphi}$ maps the positions of material points to positions $\boldsymbol{x}$ of spatial points in the *current configuration* Ω_t

$$\boldsymbol{x} = \boldsymbol{\varphi}(\boldsymbol{X}, t). \tag{2.1}$$

The *displacement field* $\boldsymbol{u}$ relates the particle position $\boldsymbol{X}$ in the reference configuration to its position $\boldsymbol{x}$ in the current configuration (Fig. 2.1) and hence, the displacement

is determined by

$$\boldsymbol{u} = \boldsymbol{x} - \boldsymbol{X}. \tag{2.2}$$

Furthermore, it is common to distinguish between different representations. On the one hand, $\boldsymbol{u}(\boldsymbol{X}, t) = \boldsymbol{x}(\boldsymbol{X}, t) - \boldsymbol{X}$ specifies the displacement at time t in terms of the position $\boldsymbol{X}$ in the reference configuration, which is called the *Lagrangian* or *material description*. On the other hand, the *Eulerian* or *spatial description* expresses the current position $\boldsymbol{x}$ as a result from its referential position, and the displacement and is thus given by $\boldsymbol{u}(\boldsymbol{x}, t) = \boldsymbol{x} - \boldsymbol{X}(\boldsymbol{x}, t)$. This distinction is also applicable to other quantities. For example, the spatial description of the *velocity field* for current positions $\boldsymbol{x}$ of material points is determined by

$$\boldsymbol{v}(\boldsymbol{x}, t) = \frac{\partial \boldsymbol{x}}{\partial t} = \dot{\boldsymbol{x}}, \tag{2.3}$$

where the dot designates the first derivative with respect to t.

2.1.1 Deformation Gradient

The *deformation gradient* $\boldsymbol{F}$ characterizes the material gradient of motion

$$\boldsymbol{F}(\boldsymbol{X}, t) = \frac{\partial \boldsymbol{x}}{\partial \boldsymbol{X}}. \tag{2.4}$$

The combination of eq. (2.4) and eq. (2.2) leads to the link between the deformation gradient $\boldsymbol{F}$ and the displacement vector $\boldsymbol{u}$

$$\boldsymbol{F} = \frac{\partial \boldsymbol{x}}{\partial \boldsymbol{X}} = \frac{\partial \boldsymbol{u}}{\partial \boldsymbol{X}} + \frac{\partial \boldsymbol{X}}{\partial \boldsymbol{X}} = \boldsymbol{H} + \mathbf{1}, \tag{2.5}$$

with the *displacement gradient* $\boldsymbol{H}$ and the *second order identity tensor* $\mathbf{1}$. The components of $\mathbf{1}$ are given by the Kronecker delta symbol δ_{ij} defined by $\delta_{ij} = 1$ for $i = j$ and $\delta_{ij} = 0$ for $i \neq j$.
The transformation of material line elements $\mathrm{d}\boldsymbol{X}$ in the reference configuration to line elements $\mathrm{d}\boldsymbol{x}$ in the current configuration is indicated in Fig. 2.1 and obtained by the deformation gradient

$$\mathrm{d}\boldsymbol{x} = \boldsymbol{F}\,\mathrm{d}\boldsymbol{X}. \tag{2.6}$$

In order to relate the volume change of infinitesimal volume elements dV defined in the reference configuration to those volume elements dv defined in the current configuration, see Fig. 2.1, the *Jacobian determinant* $J(\boldsymbol{X}, t)$ is introduced

$$\mathrm{dv} = \det(\boldsymbol{F})\,\mathrm{dV} = \det\left(\frac{\partial \boldsymbol{\varphi}(\boldsymbol{X}, t)}{\partial \boldsymbol{X}}\right)\,\mathrm{dV} = J\,\mathrm{dV}. \tag{2.7}$$

As a consequence of the assumed invertibility of the mapping $\boldsymbol{\varphi}$, it is necessary that the determinant $\det(\boldsymbol{F}) \neq 0$, and therefore the inverse motion $\boldsymbol{F}^{-1}(\boldsymbol{x}, t)$ exists. The

orientation of the mapping is preserved by the requirement $J > 0$ on the basis that volume elements cannot be negative. In the special case of incompressibility, the volume is constant in time and the volume ratio J is equal to 1.
The last mapping to be considered is the change of infinitesimal surface elements, also shown in Fig. 2.1. *Nanson's formula*

$$\boldsymbol{n}\,\mathrm{da} = J\boldsymbol{F}^{-T}\boldsymbol{N}\,\mathrm{dA} \tag{2.8}$$

provides the relationship between infinitesimal areas $\boldsymbol{n}\,\mathrm{da}$ and $\boldsymbol{N}\,\mathrm{dA}$ in the current and reference configuration, respectively. In this equation, the inverse of the transposed deformation gradient or identically the transposed of the inverse deformation gradient is denoted by $\boldsymbol{F}^{-T} = (\boldsymbol{F}^T)^{-1} = (\boldsymbol{F}^{-1})^T$.

2.1.2 Strain Tensors

The deformation gradient $\boldsymbol{F}$ is unsuitable for measuring strains of a deformed body, as it also includes rigid body motions. These rigid body motions preserve the distance between two points of a continuum and therefore induce no strains. One possibility to compute strain tensors is the unique multiplicative *polar decomposition* of $\boldsymbol{F}$. The deformation gradient consists of a pure rotation tensor $\boldsymbol{R}$ in combination with right and left pure stretch tensors $\boldsymbol{U}$ and $\boldsymbol{V}$, respectively:

$$\boldsymbol{F} = \boldsymbol{R}\boldsymbol{U} = \boldsymbol{V}\boldsymbol{R}. \tag{2.9}$$

Hence, $\boldsymbol{F}$ is split up into a proper orthogonal part $\boldsymbol{R}$ ($\boldsymbol{R}\boldsymbol{R}^T = \mathbf{1}, \det(\boldsymbol{R}) = 1$) and a symmetric and positive definite part $\boldsymbol{U}$ or $\boldsymbol{V}$ $\left(\boldsymbol{U} = \boldsymbol{U}^T, \boldsymbol{w}\cdot(\boldsymbol{U}\boldsymbol{w}) > 0, \boldsymbol{V} = \boldsymbol{V}^T, \boldsymbol{w}\cdot(\boldsymbol{V}\boldsymbol{w}) > 0\right.$ with $\left.\boldsymbol{w} \neq \mathbf{0}\right)$.
In the following, the most common definitions of strain tensors are briefly described. Those related to the reference configuration are expressed by capital letters, those associated with the current configuration by small letters. Detailed derivations are given in continuum mechanic textbooks, such as Holzapfel (2001).
The *Green-Lagrange strain tensor* is defined as

$$\boldsymbol{E} = \frac{1}{2}(\boldsymbol{C} - \mathbf{1}), \tag{2.10}$$

where the *right Cauchy-Green tensor* $\boldsymbol{C}$ only includes the right stretch tensor $\boldsymbol{U}$

$$\boldsymbol{C} = \boldsymbol{F}^T\boldsymbol{F} = \boldsymbol{U}^T\boldsymbol{U} = \boldsymbol{U}^2. \tag{2.11}$$

The change of the squared length of line elements in reference and current configuration vividly demonstrates the interpretation of the Green-Lagrange strain tensor

$$\mathrm{d}\boldsymbol{x}\cdot\mathrm{d}\boldsymbol{x} - \mathrm{d}\boldsymbol{X}\cdot\mathrm{d}\boldsymbol{X} = (\boldsymbol{F}\,\mathrm{d}\boldsymbol{X})\cdot(\boldsymbol{F}\,\mathrm{d}\boldsymbol{X}) - \mathrm{d}\boldsymbol{X}\cdot\mathrm{d}\boldsymbol{X} = 2\,\mathrm{d}\boldsymbol{X}\cdot(\boldsymbol{E}\,\mathrm{d}\boldsymbol{X}) \tag{2.12}$$

with the mapping of the squared length $\mathrm{d}\boldsymbol{x} \cdot \mathrm{d}\boldsymbol{x} = \mathrm{d}\boldsymbol{X} \cdot (\boldsymbol{C}\,\mathrm{d}\boldsymbol{X})$. Furthermore, the Green-Lagrange strain measure is zero for rigid body motion, where $\boldsymbol{C} = \mathbf{1}$. An alternative formulation of the Green-Lagrange strain tensor is found by inserting eq. (2.5) into eq. (2.10)

$$\boldsymbol{E} = \frac{1}{2}\left(\boldsymbol{H} + \boldsymbol{H}^T + \boldsymbol{H}^T\boldsymbol{H}\right). \tag{2.13}$$

In this formulation, the strain tensor $\boldsymbol{E}$ is only related to the displacement gradient $\boldsymbol{H}$. On the basis of analogous considerations, another material strain tensor, the so-called *Piola strain tensor*, is defined as

$$\boldsymbol{A} = \frac{1}{2}\left(\boldsymbol{C}^{-1} - \mathbf{1}\right) \tag{2.14}$$

with $\boldsymbol{C}^{-1} = \boldsymbol{F}^{-1}\boldsymbol{F}^{-T}$.
In the current configuration, one possibility of a spatial strain measure is given by the *Euler-Almansi strain tensor*

$$\boldsymbol{e} = \frac{1}{2}\left(\mathbf{1} - \boldsymbol{b}^{-1}\right) \tag{2.15}$$

with the *left Cauchy-Green tensor*

$$\boldsymbol{b} = \boldsymbol{F}\boldsymbol{F}^T = \boldsymbol{V}\boldsymbol{V}^T = \boldsymbol{V}^2. \tag{2.16}$$

A second possible spatial strain measure is the *Finger strain tensor*

$$\boldsymbol{a} = \frac{1}{2}(\mathbf{1} - \boldsymbol{b}). \tag{2.17}$$

Certain types of material laws also need the rate of the strain tensor. As an example, the *material time derivative* of the Green-Lagrange strain tensor $\dot{\boldsymbol{E}}$ is given by

$$\dot{\boldsymbol{E}} = \frac{1}{2}\left(\dot{\boldsymbol{F}}^T\boldsymbol{F} + \boldsymbol{F}^T\dot{\boldsymbol{F}}\right) \tag{2.18}$$

with the *material velocity gradient*

$$\dot{\boldsymbol{F}} = \frac{\partial}{\partial t}\left(\frac{\partial \boldsymbol{x}}{\partial \boldsymbol{X}}\right) = \frac{\partial}{\partial \boldsymbol{X}}\left(\frac{\partial \boldsymbol{x}}{\partial t}\right) = \frac{\partial \boldsymbol{v}}{\partial \boldsymbol{X}} = \mathrm{Grad}\,\boldsymbol{v}. \tag{2.19}$$

Conventionally, $\mathrm{Grad}\,(\cdot)$ is used for the derivative with respect to the position $\boldsymbol{X}$ in the reference configuration.
The *spatial velocity gradient* $\boldsymbol{l}$ is defined by

$$\boldsymbol{l} = \frac{\partial \boldsymbol{v}}{\partial \boldsymbol{x}} = \mathrm{grad}\,\boldsymbol{v}, \tag{2.20}$$

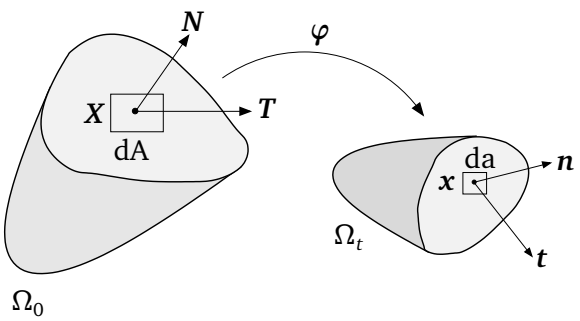

Figure 2.2: Traction and normal vectors, which operate on infinitesimal surface elements in the reference (Ω_0) or current (Ω_t) configuration.

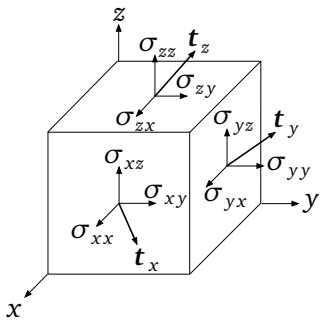

Figure 2.3: Positive components of the traction vector decomposed in Cartesian coordinates.

where grad$(\cdot)$ denotes the derivative with respect to $\boldsymbol{x}$ in the current configuration. The chain rule provides the useful relation

$$\boldsymbol{l} = \operatorname{grad} \boldsymbol{v} = \frac{\partial \boldsymbol{v}}{\partial \boldsymbol{x}} = \frac{\partial \boldsymbol{v}}{\partial \boldsymbol{X}} \frac{\partial \boldsymbol{X}}{\partial \boldsymbol{x}} = \dot{\boldsymbol{F}} \boldsymbol{F}^{-1}. \tag{2.21}$$

2.2 Stress Tensors

In the reference as well as in the current configuration the continuum is cut into two parts by a plane surface, see Fig. 2.2. For every surface element on the sectional plane, the stress resultant force $\mathrm{d}\boldsymbol{f}$ in the current configuration can be expressed as

$$\mathrm{d}\boldsymbol{f} = \boldsymbol{t}\,\mathrm{da} = \boldsymbol{T}\,\mathrm{dA} \tag{2.22}$$

with the *Cauchy (or surface) traction vector* $\boldsymbol{t}$ or the *first Piola-Kirchhoff (or nominal) traction vector* $\boldsymbol{T}$. *Cauchy's stress theorem*, an important axiom in continuum mechanics, postulates the unique existence of the *Cauchy stress tensor* $\boldsymbol{\sigma}$ and the *first Piola-Kirchhoff stress tensor* $\boldsymbol{P}$. This theorem states that

$$\boldsymbol{t} = \boldsymbol{\sigma}\boldsymbol{n} \qquad \text{and} \tag{2.23}$$

$$\boldsymbol{T} = \boldsymbol{P}\boldsymbol{N} \tag{2.24}$$

with the normal vector $\boldsymbol{n}$ in the current configuration and the normal vector $\boldsymbol{N}$ in the reference configuration. The Cauchy stress tensor denotes a symmetric spatial tensor, while the first Piola-Kirchhoff stress tensor is, in general, not symmetric. These tensor properties will be verified in Section 2.3.3. The components of the Cauchy stress tensor in Cartesian coordinates are illustrated in Fig. 2.3.
The relation between the Cauchy stress tensor $\boldsymbol{\sigma}$ and the first Piola-Kirchhoff stress tensor $\boldsymbol{P}$ is given by

$$\boldsymbol{P} = J\boldsymbol{\sigma}\boldsymbol{F}^{-T} \qquad \text{or} \qquad \boldsymbol{\sigma} = \frac{1}{J}\boldsymbol{P}\boldsymbol{F}^{T} \tag{2.25}$$

based on Nanson's formula with

$$\mathrm{d}\boldsymbol{f} = \boldsymbol{\sigma}\boldsymbol{n}\,\mathrm{da} = J\boldsymbol{\sigma}\boldsymbol{F}^{-T}\boldsymbol{N}\,\mathrm{dA} = \boldsymbol{P}\boldsymbol{N}\,\mathrm{dA}. \tag{2.26}$$

2.3 Balance Equations

A deformed material volume $B_t \subset \Omega_t$ in the current configuration originates from a material volume $B_0 \subset \Omega_0$ in the reference configuration by applying external and internal forces. Balance equations are differential equations, which specify temporal changes of field quantities. These axiomatic laws are summarized in the following, especially the fundamental principles of the conservation of mass and the momentum balance.

2.3.1 Gauß and Reynolds Transport Theorem

The *Gauß theorem*, also known as divergence theorem, reveals that the integral of the outward flux of a vector field $\boldsymbol{a}$ through the surface ∂B_t is equal to the integral of the divergence over a control volume B_t assuming appropriate differentiability

$$\int_{B_t} (\operatorname{div}\boldsymbol{a})\,\mathrm{dv} = \int_{\partial B_t} (\boldsymbol{a}\cdot\boldsymbol{n})\,\mathrm{da}. \tag{2.27}$$

The divergence in the current configuration of a vector field $\boldsymbol{a}$ is defined by

$$\operatorname{div}\boldsymbol{a} = \frac{\partial a_i}{\partial x_i} \tag{2.28}$$

using the Einstein summation convention for repeated indices. The temporal change of any physical quantity φ integrated over a material volume B_t consists of a local and a convective part

$$\frac{\mathrm{d}}{\mathrm{d}t}\int_{B_t} \varphi\,\mathrm{dv} = \underbrace{\int_{B_t} \frac{\partial\varphi}{\partial t}\,\mathrm{dv}}_{\text{local part}} + \underbrace{\int_{\partial B_t} (\varphi\boldsymbol{v}\cdot\boldsymbol{n})\,\mathrm{da}}_{\text{convective part}}. \tag{2.29}$$

This relation is known as *Reynolds transport theorem*. To derive this equation, the temporal change of the quantity φ is transformed to the reference configuration. For the time-independent control volume the interchange of differentiation and integration is possible if the field quantities are assumed to be sufficiently smooth. By applying the product rule and the fact that the material time derivative of the Jacobian determinant is $\dot{J} = J\operatorname{div}\boldsymbol{v}$, the temporal change can be rewritten in the current

configuration as

$$\frac{\mathrm{d}}{\mathrm{d}t}\int\limits_{B_t}\varphi(\boldsymbol{x},t)\,\mathrm{dv}=\int\limits_{B_t}\left(\frac{\mathrm{d}\varphi}{\mathrm{d}t}+\varphi\operatorname{div}\boldsymbol{v}\right)\mathrm{dv}. \tag{2.30}$$

Due to the chain rule, the material time derivative is related to the local time derivative by

$$\frac{\mathrm{d}\varphi}{\mathrm{d}t}=\frac{\partial\varphi}{\partial t}+(\operatorname{grad}\varphi)\cdot\boldsymbol{v}. \tag{2.31}$$

Additionally, applying the product rule for the divergence and the Gauß theorem leads to Reynolds transport theorem eq. (2.29).

2.3.2 Balance of Mass

The *total mass* m of a given material body is temporally constant

$$\frac{\mathrm{d}}{\mathrm{d}t}m=\frac{\mathrm{d}}{\mathrm{d}t}\int\limits_{B_t}\rho\,\mathrm{dv}=0 \tag{2.32}$$

with the *mass density* ρ. With Reynolds transport theorem this leads to

$$\frac{\mathrm{d}}{\mathrm{d}t}\int\limits_{B_t}\rho\,\mathrm{dv}=\int\limits_{B_t}\left(\frac{\partial\rho}{\partial t}+\operatorname{div}(\rho\boldsymbol{v})\right)\mathrm{dv}=0. \tag{2.33}$$

This relation must be valid for arbitrary volumes B_t and therefore the integrand must be zero. The continuity equation reads

$$\frac{\partial\rho}{\partial t}+\operatorname{div}(\rho\boldsymbol{v})=\frac{\mathrm{d}\rho}{\mathrm{d}t}+\rho\operatorname{div}\boldsymbol{v}=0 \tag{2.34}$$

which is the *local mass balance equation*. The mass balance for the special case of incompressible materials $\left(\rho=\text{const},\,\mathrm{d}\rho/\,\mathrm{d}t=0\right)$ simplifies to

$$\operatorname{div}\boldsymbol{v}=0. \tag{2.35}$$

2.3.3 Balance of Linear and Angular Momentum

Newton's Second Law states that the sum of all external forces $\boldsymbol{f}$ (e.g., gravity) and surface tractions $\boldsymbol{t}$ is equal to the temporal change of the *linear momentum* $\boldsymbol{P}$

$$\frac{\mathrm{d}\boldsymbol{P}}{\mathrm{d}t}=\frac{\mathrm{d}}{\mathrm{d}t}\int\limits_{B_t}\rho\boldsymbol{v}\,\mathrm{dv}=\int\limits_{\partial B_t}\boldsymbol{t}\,\mathrm{da}+\int\limits_{B_t}\boldsymbol{f}\,\mathrm{dv} \tag{2.36}$$

with the *momentum density* $\rho \boldsymbol{v}$. The Cauchy theorem (2.23) expresses the traction dependent on the Cauchy stress tensor. Additionally, the application of Reynolds transport theorem and Gauß theorem determines the following global relation

$$\int_{B_t} \left(\frac{\partial(\rho \boldsymbol{v})}{\partial t} + \operatorname{div}(\rho \boldsymbol{v} \otimes \boldsymbol{v}) - \operatorname{div} \boldsymbol{\sigma} - \boldsymbol{f} \right) \mathrm{dv} = 0. \tag{2.37}$$

The outer product $\boldsymbol{v} \otimes \boldsymbol{v}$ symbolizes the dyadic multiplication $\boldsymbol{v}\boldsymbol{v}^T$ of two first order tensors. The local form reads

$$\frac{\partial(\rho \boldsymbol{v})}{\partial t} + \operatorname{div}(\rho \boldsymbol{v} \otimes \boldsymbol{v}) = \operatorname{div} \boldsymbol{\sigma} + \boldsymbol{f} \tag{2.38}$$

with

$$\frac{\partial(\rho \boldsymbol{v})}{\partial t} + \operatorname{div}(\rho \boldsymbol{v} \otimes \boldsymbol{v}) = \rho \frac{\partial \boldsymbol{v}}{\partial t} + \boldsymbol{v} \frac{\partial \rho}{\partial t} + \boldsymbol{v} \operatorname{div}(\rho \boldsymbol{v}) + (\operatorname{grad} \boldsymbol{v}) \cdot \rho \boldsymbol{v} \tag{2.39}$$

$$= \rho \underbrace{\left(\frac{\partial \boldsymbol{v}}{\partial t} + (\operatorname{grad} \boldsymbol{v}) \cdot \boldsymbol{v} \right)}_{\text{material time derivative of } \boldsymbol{v}} + \boldsymbol{v} \underbrace{\left(\frac{\partial \rho}{\partial t} + \operatorname{div}(\rho \boldsymbol{v}) \right)}_{=0 \text{ (mass balance)}}. \tag{2.40}$$

The local momentum balance in the current configuration results in

$$\rho \frac{\mathrm{d}\boldsymbol{v}}{\mathrm{d}t} = \operatorname{div} \boldsymbol{\sigma} + \boldsymbol{f}. \tag{2.41}$$

The change of the linear momentum in the reference configuration

$$\frac{\mathrm{d}\boldsymbol{P}}{\mathrm{d}t} = \frac{\mathrm{d}}{\mathrm{d}t} \int_{B_0} \rho \boldsymbol{v} J \, \mathrm{dV} = \int_{\partial B_0} \boldsymbol{\sigma} J \boldsymbol{F}^{-T} \boldsymbol{N} \, \mathrm{dA} + \int_{B_0} \boldsymbol{f} J \, \mathrm{dV} \tag{2.42}$$

simplifies to

$$\frac{\mathrm{d}}{\mathrm{d}t} \int_{B_0} \rho_0 \boldsymbol{v} \, \mathrm{dV} = \int_{\partial B_0} \boldsymbol{P} \boldsymbol{N} \, \mathrm{dA} + \int_{B_0} \boldsymbol{f}_0 \, \mathrm{dV}. \tag{2.43}$$

with the mass density $\rho_0 = \rho J$ defined per volume of the reference configuration and the external force vector $\boldsymbol{f}_0 = \boldsymbol{f} J$ in the reference configuration. Hence, the local momentum balance in the reference configuration yields under the assumption of $\mathrm{d}\rho_0 / \mathrm{d}t = 0$

$$\rho_0 \frac{\mathrm{d}\boldsymbol{v}}{\mathrm{d}t} = \operatorname{Div} \boldsymbol{P} + \boldsymbol{f}_0. \tag{2.44}$$

The divergence of the first Piola-Kirchhoff stress tensor in the reference configuration is denoted by $\operatorname{Div} \boldsymbol{P} = \partial P_{iJ} / \partial X_J$.
The angular momentum $\boldsymbol{L}$ of a mass point is the cross product of its position vector

with the linear momentum

$$\boldsymbol{L} = \boldsymbol{x} \times \boldsymbol{P}. \tag{2.45}$$

The local form of the temporal change of angular momentum $\mathrm{d}\boldsymbol{L}/\mathrm{d}t$ in the current configuration results in the symmetry of the Cauchy stress tensor

$$\boldsymbol{\sigma} = \boldsymbol{\sigma}^T. \tag{2.46}$$

This equation is derived with the help of Reynolds transport theorem, Gauß theorem, the mass balance, and the balance of linear momentum. However, the first Piola-Kirchhoff stress tensor is generally not symmetric as

$$\boldsymbol{P} = J\boldsymbol{\sigma}\boldsymbol{F}^{-T} \neq J\boldsymbol{F}^{-1}\boldsymbol{\sigma}^T = \boldsymbol{P}^T, \tag{2.47}$$

but

$$\boldsymbol{\sigma} = \frac{1}{J}\boldsymbol{P}\boldsymbol{F}^T = \frac{1}{J}\boldsymbol{F}\boldsymbol{P}^T = \boldsymbol{\sigma}^T \qquad \Rightarrow \boldsymbol{P}\boldsymbol{F}^T = \boldsymbol{F}\boldsymbol{P}^T. \tag{2.48}$$

In order to obtain a symmetric stress tensor in the reference configuration, the *second Piola-Kirchhoff stress tensor* $\boldsymbol{S}$ is introduced

$$\boldsymbol{S} = \boldsymbol{F}^{-1}\boldsymbol{P} \tag{2.49}$$

and with eq. (2.48)

$$\boldsymbol{F}\boldsymbol{S}\boldsymbol{F}^T = \boldsymbol{F}\boldsymbol{S}^T\boldsymbol{F}^T \qquad \Rightarrow \boldsymbol{S} = \boldsymbol{S}^T. \tag{2.50}$$

Thus, the local momentum balance results in

$$\rho_0 \frac{\mathrm{d}\boldsymbol{v}}{\mathrm{d}t} = \mathrm{Div}(\boldsymbol{F}\boldsymbol{S}) + \boldsymbol{f}_0. \tag{2.51}$$

In this investigation only the static case of the local momentum balance is relevant as the acceleration and Coriolis terms are neglected in all ice models and hence, also in the following models of ice shelves. The local momentum balance simplifies to

$$\boldsymbol{0} = \mathrm{Div}(\boldsymbol{F}\boldsymbol{S}) + \boldsymbol{f}_0 \tag{2.52}$$

in the reference configuration and

$$\boldsymbol{0} = \mathrm{div}\,\boldsymbol{\sigma} + \boldsymbol{f} \tag{2.53}$$

in the current configuration.

2.4 Linear Theory

In the case of small deformations, which means that the components of the displacement gradient satisfy

$$\left|H_{ij}\right| = \left|\frac{\partial u_i}{\partial X_j}\right| \ll 1 \qquad \forall i,j, \tag{2.54}$$

the distinction between different configurations disappears. Hence, the strain tensors in the reference and current configuration are identical. In a small strain model, the second-order terms of $\boldsymbol{H}$ are disregarded, see for example eq. (2.13). Hence, the *linearized strain tensor* becomes

$$\boldsymbol{\varepsilon} = \frac{1}{2}\left(\boldsymbol{H} + \boldsymbol{H}^T\right) = \frac{1}{2}\left(\frac{\partial \boldsymbol{u}}{\partial \boldsymbol{x}} + \left(\frac{\partial \boldsymbol{u}}{\partial \boldsymbol{x}}\right)^T\right) \tag{2.55}$$

as it is no longer necessary to distinguish between material and spatial derivatives

$$\frac{\partial}{\partial \boldsymbol{x}}(\cdot) \approx \frac{\partial}{\partial \boldsymbol{X}}(\cdot). \tag{2.56}$$

For viscous or viscoelastic materials, the strain rate tensors are also important. If analogous assumptions of small deformation rates are valid, the relation $\dot{\boldsymbol{\varepsilon}} \approx \dot{\boldsymbol{E}} \approx \dot{\boldsymbol{e}}$ is fulfilled.
In addition, the Cauchy stress tensor $\boldsymbol{\sigma}$ and the first Piola-Kirchhoff stress tensor $\boldsymbol{P}$ coincide assuming small deformations. This is comprehensible with the relation $\boldsymbol{P} = J\boldsymbol{\sigma}\boldsymbol{F}^{-T}$, since the inverse of the deformation gradient $\boldsymbol{F}$ is approximated by $\boldsymbol{F}^{-1} = \mathbf{1} - \boldsymbol{H} \approx \mathbf{1}$ and the Jacobian determinant $J = \det \boldsymbol{F} \approx 1$, see Haupt (2000). Consequently, the static local momentum balance in the reference and current configuration results in

$$\operatorname{div} \boldsymbol{\sigma} + \boldsymbol{f} = \mathbf{0}. \tag{2.57}$$

2.5 Linear Material Laws

So far, the equations are valid for all materials and thus a suitable material law has to complete the system of differential equations. These *constitutive equations* are determined by the individual material properties, which entail that different materials react differently to identical external conditions. The material laws are mathematical models that express the characteristic features of the material behavior in an idealized way. Hence, constitutive equations are either mathematically generalized (axiomatic) relations or based on experimental data (empirical).
First of all, the constitutive equations are given assuming small deformations. The elasticity model, presented first, describes a rate-independent material behavior. Afterwards, viscous or viscoelastic material models are introduced for rate-dependent behaviors. To include also a nonlinear material behavior, a viscosity according to

Glen's flow law is discussed in the next section. Finally, the viscoelastic Maxwell material model, which describes the motion of ice best, is extended to finite deformations in Section 2.7.

2.5.1 Linear Elasticity

Hooke's law defines the linear stress-strain relation

$$\sigma = f(\varepsilon) = E\varepsilon \tag{2.58}$$

Figure 2.4: Hooke's model.

in a 1d model with *Young's modulus* E as the constant of proportionality. In order to illustrate this linear elastic material behavior in a rheological model, a spring with a constant E is chosen, see Fig. 2.4. The generalization to a 3d tensor representation reads

$$\boldsymbol{\sigma} = \mathbb{C}\boldsymbol{\varepsilon} \tag{2.59}$$

with the forth-order tensor $\mathbb{C}$, the so-called *stiffness* or *elasticity tensor*. Based on the symmetry of the stress and strain tensors, the elasticity tensor has 36 independent constants. The existence of the strain energy reduces the components of the elasticity tensor to 21 independent constants. The additional assumption of an isotropic material, which has the same material properties in all directions, results in simply two independent constants. These material parameters are called *Lamé constants* λ and μ and the material law becomes

$$\boldsymbol{\sigma} = \lambda \mathrm{tr}(\boldsymbol{\varepsilon})\mathbf{1} + 2\mu\boldsymbol{\varepsilon}. \tag{2.60}$$

with the trace $\mathrm{tr}(\cdot)$. The constants λ and μ are related to Young's modulus E and *Poisson's ratio* ν in the following way

$$\lambda = \frac{\nu E}{(1+\nu)(1-2\nu)}, \qquad \mu = \frac{E}{2(1+\nu)}. \tag{2.61}$$

With the help of measurements, Young's modulus and Poisson's ratio can be roughly determined for ice.
In the case of small strains, the relative change in volume $\Delta V/V$ is equal to the trace of the strain tensor $\boldsymbol{\varepsilon}$. In order to utilize this feature, it is useful to split the infinitesimal strain tensor into a volumetric (isotropic) part and a traceless deviator $\boldsymbol{\varepsilon}^D$

$$\boldsymbol{\varepsilon} = \frac{1}{3}\mathrm{tr}(\boldsymbol{\varepsilon})\mathbf{1} + \boldsymbol{\varepsilon}^D. \tag{2.62}$$

An alternative formulation of the material eq. (2.60) results in

$$\boldsymbol{\sigma} = \left(\lambda + \frac{2}{3}\mu\right)\mathrm{tr}(\boldsymbol{\varepsilon})\mathbf{1} + 2\mu\boldsymbol{\varepsilon}^D. \tag{2.63}$$

The *bulk modulus* $K = \left(\lambda + \frac{2}{3}\mu\right)$ describes the resistance of the material to hydrostatic compression. An analogous additive decomposition to the one of the strain tensor is therefore also possible for the stress tensor

$$\boldsymbol{\sigma} = \frac{1}{3}\mathrm{tr}(\boldsymbol{\sigma})\mathbf{1} + \boldsymbol{\sigma}^D = K\mathrm{tr}(\boldsymbol{\varepsilon})\mathbf{1} + \boldsymbol{\sigma}^D \quad \text{with } \boldsymbol{\sigma}^D = 2\mu\boldsymbol{\varepsilon}^D. \tag{2.64}$$

Hence, the stress tensor is divided into a volume-changing (hydrostatic) part and a volume-preserving deviatoric (anisotropic) part.

2.5.2 Linear Viscosity

In the second material model, the stress is linearly dependent on the strain rate $\dot{\varepsilon}$ in a 1d model and is given by

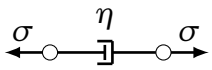

Figure 2.5: Viscous model.

$$\sigma = f(\dot{\varepsilon}) = \eta\dot{\varepsilon}. \tag{2.65}$$

The *viscosity* η is the proportionality constant, similar to Young's modulus E in the elastic material model. The behavior of the viscous material is represented by a damper in the rheological model, see Fig. 2.5. This linear viscous material is often called *Newtonian fluid*. In order to generalize the material equation for a 3d case, an analogous approach to the one of the linear elastic solid suggests the following relation

$$\boldsymbol{\sigma} = K\mathrm{tr}(\boldsymbol{\varepsilon})\mathbf{1} + \boldsymbol{\sigma}^D = K\mathrm{tr}(\boldsymbol{\varepsilon})\mathbf{1} + 2\eta\dot{\boldsymbol{\varepsilon}}^D. \tag{2.66}$$

This material equation contains the fundamental assumption that the volume-changing part of the stress tensor is purely elastic, cf. Altenbach (2012). The hypothesis is based on the common assumption for compressible materials that changes of the volume are reversible. Thus, the viscosity of the material is only characterized by the stress deviator. Greve and Blatter (2009) stated that a linear viscous material is described by

$$\boldsymbol{\sigma} = -p(\rho,T)\mathbf{1} + \xi\mathrm{tr}(\dot{\boldsymbol{\varepsilon}})\mathbf{1} + 2\eta\dot{\boldsymbol{\varepsilon}} = -p(\rho,T)\mathbf{1} + \left(\xi + \frac{2}{3}\eta\right)\mathrm{tr}(\dot{\boldsymbol{\varepsilon}})\mathbf{1} + 2\eta\dot{\boldsymbol{\varepsilon}}^D. \tag{2.67}$$

In this equation the *thermodynamic pressure* p is dependent on the density ρ and the *temperature* T. The *coefficients of viscosity* ξ and η are also included. The *total pressure* $p_{\mathrm{tot}} = p(\rho,T) - \left(\xi + \frac{2}{3}\eta\right)\mathrm{tr}(\dot{\boldsymbol{\varepsilon}})$ in the constitutive equation of a linear viscous fluid

$$\boldsymbol{\sigma} = -p_{\mathrm{tot}}\mathbf{1} + \boldsymbol{\sigma}^D \tag{2.68}$$

is approximated in eq. (2.66) using an elastic isometric stress as suggested in Darby (1976). Hence, the material law (2.67) is also similar to Hooke's law with the exception of the pressure term and the strain rate tensor $\dot{\boldsymbol{\varepsilon}}$, which is used instead of the strain tensor $\boldsymbol{\varepsilon}$.

For the special case of an incompressible Newtonian fluid, the trace of the strain rate tensor is zero ($\mathrm{tr}(\dot{\boldsymbol{\varepsilon}}) = \mathrm{div}\,\boldsymbol{v} = 0$) based on the mass balance eq. (2.35). Therefore, the material eq. (2.66) simplifies to

$$\boldsymbol{\sigma} = 2\eta\dot{\boldsymbol{\varepsilon}}, \tag{2.69}$$

as $\dot{\boldsymbol{\varepsilon}}^D = \dot{\boldsymbol{\varepsilon}}$ and $\mathrm{tr}(\boldsymbol{\varepsilon}) = 0$ for appropriate initial conditions.

2.5.3 Linear Viscoelasticity

The rheological model of a 1d viscoelastic material model consists of a combination of elastic springs and viscous dampers, which are arranged in parallel or in series, see Flügge (1975). In the following, the two fundamental combinations of one spring and one damper in parallel, the so-called Kelvin-Voigt model, as well as one spring and one damper in series, the so-called Maxwell model, are introduced. Based on these two models, more complex viscoelastic material models can be established.

Kelvin-Voigt Model

The 1d rheological representation of the *Kelvin-Voigt model* is shown in Fig. 2.6. The material behavior is described by only two parameters, namely Young's modulus E and the viscosity η.

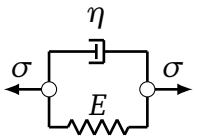

Figure 2.6: Kelvin-Voigt model.

The differential equation of the Kelvin-Voigt model is the result of the mechanical condition of equilibrium

$$\sigma = \sum_{i=1}^{2} \sigma_i = \sigma_\mathrm{e} + \sigma_\mathrm{v}. \tag{2.70}$$

Considering Fig. 2.6, it is deduced that the strains in spring and damper have to be the same $\varepsilon = \varepsilon_\mathrm{e} = \varepsilon_\mathrm{v}$. This approach results in the differential equation for the Kelvin-Voigt model

$$\sigma = E\varepsilon + \eta\dot{\varepsilon} \tag{2.71}$$

using additionally eqs. (2.58) and (2.65). The model represents a viscoelastic solid, where the short-term behavior is viscous and the long-term behavior is elastic. This feature is illustrated in Fig. 2.7, which depicts the creep function of a Kelvin-Voigt model with a constant applied stress σ_0 at time $t = 0$. The maximum strain σ_0/E is based on the strain response of a linear elastic material. The tangent of the creep function in the origin is equal to the maximum strain for $t = \tau$, the so-called *retardation time*. This is the characteristic time of the Kelvin-Voigt model that is determined by the material parameters $\tau = \eta/E$. At this point in time ($t = \tau$), nearly 2/3 of the maximum strain is reached.
An analogous procedure is possible to obtain the 3d formulation. However, the

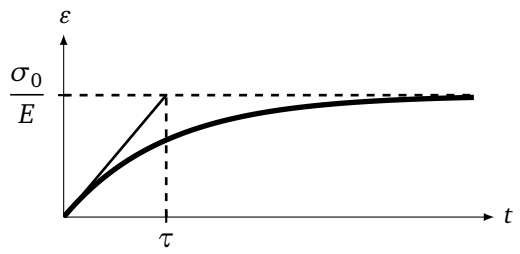

Figure 2.7: Creep function of the Kelvin-Voigt model.

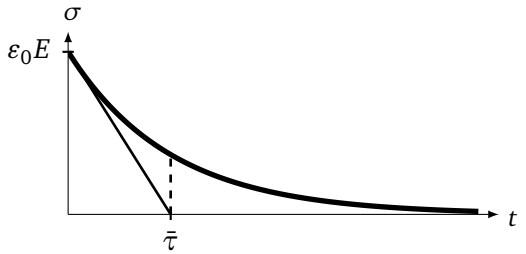

Figure 2.8: Relaxation function of the Maxwell model.

material law is only applied to the stress deviator, comparable to the purely elastic and purely viscous case. The deviatoric stress tensor is calculated by

$$\boldsymbol{\sigma}^D = 2\mu\boldsymbol{\varepsilon}^D + 2\eta\dot{\boldsymbol{\varepsilon}}^D \tag{2.72}$$

using $\boldsymbol{\sigma}^D = \boldsymbol{\sigma}^D_{\mathrm{e}} + \boldsymbol{\sigma}^D_{\mathrm{v}}$ and $\boldsymbol{\varepsilon}^D = \boldsymbol{\varepsilon}^D_{\mathrm{e}} = \boldsymbol{\varepsilon}^D_{\mathrm{v}}$. A linear viscous fluid, see eqs. (2.66) and (2.68), can also be categorized as a special case of a Kelvin-Voigt model as the stresses are added up in a similar way. The characteristic time of a 3d Kelvin-Voigt model is given by $\tau = \eta/\mu$.

Maxwell Model

In contrast to the parallel structure, the *Maxwell material model* describes a viscoelastic material, where one spring and one damper are arranged in series, see the 1d rheological model in Fig. 2.9.

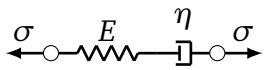

Figure 2.9: Maxwell model.

Based on the geometric condition of compatibility for the case of elements ordered in series, the strain results in

$$\varepsilon = \sum_{i=1}^{2} \varepsilon_i = \varepsilon_{\mathrm{e}} + \varepsilon_{\mathrm{v}}. \tag{2.73}$$

The differential equation of a Maxwell material is derived by the use of the assumption $\sigma = \sigma_{\mathrm{e}} = \sigma_{\mathrm{v}}$ additionally to the constitutive equations of an elastic and a viscous material. Hence, the differential equation is given by

$$\sigma + \frac{\eta}{E}\dot{\sigma} = \eta\dot{\varepsilon}. \tag{2.74}$$

To solve this equation, either the viscous strain rate or the elastic strain is needed. One possibility is that mechanical state variables are introduced, which are mathematically constructed and characterize structural properties of the material. This procedure is explained in the following.
In the context of viscoelastic materials, it is possible to describe constitutive models for inelastic materials based on the concept of internal variables. Internal variables

specify aspects of the internal structure of materials, which are correlated to dissipative effects. The evolution of internal variables captures indirectly the history of the deformation. In contrast to external variables, which are measurable quantities and directly observable, such as the deformation gradient $\boldsymbol{F}$, the internal variables are hidden to an external observer.
An example for an internal variable is the viscous strain in a Maxwell model. This state variable is computable by the following evolution equation

$$\mu\left(\varepsilon - \varepsilon_{\mathrm{v}}\right) = \eta\dot{\varepsilon}_{\mathrm{v}}, \tag{2.75}$$

which is derived from the stress equilibrium $\sigma_{\mathrm{e}} = \sigma_{\mathrm{v}}$. Based on this technique, the viscous strain is used as an additional unknown. In conclusion, it is equivalent to solve eq. (2.75) and $\sigma = \eta\dot{\varepsilon}_{\mathrm{v}}$ instead of the differential eq. (2.74). In accordance to the Kelvin-Voigt model, the characteristic time $\bar{\tau} = \eta/E$ specifies in the Maxwell model the point in time at which nearly 2/3 of the stress is reduced, see Fig. 2.8. This characteristic time is called *relaxation time*.
The generalized 3d constitutive equation of the Maxwell material is given by

$$\boldsymbol{\sigma}^D + \frac{\eta}{\mu}\dot{\boldsymbol{\sigma}}^D = 2\eta\dot{\boldsymbol{\varepsilon}}_{\mathrm{v}}^D. \tag{2.76}$$

To solve this equation with the concept of internal variables, the evolution equation for the viscous strain

$$\mu\left(\boldsymbol{\varepsilon}^D - \boldsymbol{\varepsilon}_{\mathrm{v}}^D\right) = \eta\dot{\boldsymbol{\varepsilon}}_{\mathrm{v}}^D \tag{2.77}$$

is required. This equation is valid on the one hand due to the additive decomposition of the strain tensor into an elastic and viscous strain tensor. On the other hand, the deviatoric stress tensors of both elements are equal ($\boldsymbol{\sigma}_{\mathrm{e}}^D = \boldsymbol{\sigma}_{\mathrm{v}}^D$). To complete the constitutive eq. (2.66), the deviatoric stress tensor is computed by $\boldsymbol{\sigma}^D = 2\eta\dot{\boldsymbol{\varepsilon}}_{\mathrm{v}}^D$. Hence, the following equation provides the complete stress-strain relation

$$\boldsymbol{\sigma} = K\mathrm{tr}\left(\boldsymbol{\varepsilon}\right)\mathbf{1} + 2\eta\dot{\boldsymbol{\varepsilon}}_{\mathrm{v}}^D \tag{2.78}$$

for a Maxwell material. Also in the 3d case, it is equivalent to solve eqs. (2.77) and (2.78) instead of eq. (2.76).
Another possibility to derive the stress-strain relation is to assume that the stress tensor is a function of the rate-independent strain tensor, i.e. $\boldsymbol{\sigma} = f\left(\boldsymbol{\varepsilon}_{\mathrm{e}}\right)$. If Hooke's law for an isotropic material is valid for the elastic strain tensor

$$\boldsymbol{\sigma} = \lambda\mathrm{tr}\left(\boldsymbol{\varepsilon}_{\mathrm{e}}\right)\mathbf{1} + 2\mu\boldsymbol{\varepsilon}_{\mathrm{e}} = K\mathrm{tr}\left(\boldsymbol{\varepsilon}_{\mathrm{e}}\right)\mathbf{1} + 2\mu\boldsymbol{\varepsilon}_{\mathrm{e}}^D, \tag{2.79}$$

eq. (2.78) will be derived on the one hand by $\boldsymbol{\sigma}^D = 2\eta\dot{\boldsymbol{\varepsilon}}_{\mathrm{v}}^D = 2\mu\boldsymbol{\varepsilon}_{\mathrm{e}}^D$. On the other hand, the assumption of an incompressible viscous deformation $\mathrm{tr}\left(\dot{\boldsymbol{\varepsilon}}_{\mathrm{v}}^{\mathrm{D}}\right) = 0$, which means that $\dot{\boldsymbol{\varepsilon}}_{\mathrm{v}}^D = \dot{\boldsymbol{\varepsilon}}_{\mathrm{v}}$, simplifies to $\boldsymbol{\varepsilon}_{\mathrm{v}}^D = \boldsymbol{\varepsilon}_{\mathrm{v}}$, if suitable initial conditions are used. This assumption yields a vanishing trace of the viscous strain tensor $\mathrm{tr}\left(\boldsymbol{\varepsilon}_{\mathrm{v}}\right) = 0$, and eq. (2.79) results in eq. (2.78). Hence, the volumetric part of the stress tensor is

purely elastic and the viscous part of the deformation results only from the deviatoric stress tensor.
So far, all material descriptions are only linear. In order to get a better description of strain and viscosity, the material models are extended by a nonlinear shear viscosity according to Glen's flow law, see the next section. Hence, the viscosity is dependent on the current strain state. However, this nonlinearity is only contained in the viscous material parameter η. Another possibility to include large deformations also in the material model is the nonlinear finite viscoelasticity, see Section 2.7.

2.6 Glen's Flow Law

Ice in ice shelves and glaciers consist of *polycrystalline ice*, which is composed of large numbers of *grains* (single ice crystals). The microscopic behavior of a single ice crystal is anisotropic, but the random compound of grains in an ice shelf makes the macroscopic behavior isotropic. Polycrystalline ice reacts to an applied shear stress with an initial instantaneous elastic deformation succeeded by viscous creep. The detailed derivation of the nonlinear viscous flow law is given in Greve and Blatter (2009) and summarized in the following.
The viscous deformation of polycrystalline ice is essentially characterized by the constant shear rate. In a 1d model this rate is correlated to the shear stress by a nonlinear flow law dependent on the shear viscosity η. The viscous relation is based a on large number of laboratory tests. The 3d generalization of the nonlinear flow law results in

$$\dot{\boldsymbol{\varepsilon}}^D = \frac{1}{2\eta(T,p,\sigma_\mathrm{e})}\boldsymbol{\sigma}^D \tag{2.80}$$

with the *effective stress* $\sigma_\mathrm{e} = \sqrt{\frac{1}{2}\mathrm{tr}(\boldsymbol{\sigma}^D)^2}$, the second scalar invariant of the stress deviator $\boldsymbol{\sigma}^D$. In *Nye's generalization of Glen's flow law*, the viscosity is given by

$$\eta(T,p,\sigma_\mathrm{e}) = \frac{1}{2A(T,p)\sigma_\mathrm{e}^{n-1}}. \tag{2.81}$$

The rate factor $A(T,p)$ is determined by the Arrhenius law. The stress exponent $n = 3$ is mostly used, as discussed for example in Cuffey and Paterson (2010). According to the relations given in Greve and Blatter (2009), the flow law of polycrystalline ice can be rewritten as

$$\boldsymbol{\sigma}^D = 2\eta(T,p,d_\mathrm{e})\dot{\boldsymbol{\varepsilon}}^D \tag{2.82}$$

with $d_\mathrm{e} = \sqrt{\frac{1}{2}\mathrm{tr}\left(\dot{\boldsymbol{\varepsilon}}^\mathrm{D}\right)^2}$ denoting the *effective strain rate*. The nonlinear shear viscosity η results in

$$\eta(T,p,d_\mathrm{e}) = \frac{1}{2}A(T,p)^{-\frac{1}{n}} d_\mathrm{e}^{-\frac{n-1}{n}}. \tag{2.83}$$

The flow laws eq. (2.80) and eq. (2.82) are comparable to the material equation of a Newtonian fluid, except for the nonlinear viscosity. Hence, the linear viscous or

viscoelastic material models are expandable to a nonlinear material law by including the viscosity according to Glen's flow law. This viscosity, see eq. (2.81) or (2.83), is in general nonlinear, since it depends on the deformation based on the effective stress or the effective strain rate. In the next section, the equations for viscoelasticity in the case of large deformations are established. In that model, the nonlinearity is directly included in the evolution equations.

2.7 Finite Viscoelasticity

In order to model the viscous creep of ice under pressure for long time periods, the assumption of small deformation has to be discarded. To evaluate the time range in which a linearized model yields sufficient results, a finite viscoelastic Maxwell model is proposed. Hence, the applicability of a linear Maxwell model for calving is analyzed by a comparison with results from a model with finite deformations.
Different ways are possible to derive evolution equations for viscoelastic materials at large strains. The presented approach uses the multiplicative decomposition of the deformation gradient into rate-independent (elastic) and rate-dependent (viscous) parts. However, this method is in contrast to the decoupled representation of the Helmholtz free-energy function that uses the multiplicative decomposition of the deformation gradient into dilational and volume-preserving parts, see Simo (1987) and Holzapfel (2001).
Before the constitutive equations are derived, some necessary notions and basic relations are clarified. For detailed explanations, the reader is referred to textbooks on nonlinear continuum mechanics like Simo and Hughes (1998), Haupt (2000) or Holzapfel (2001).

2.7.1 Objectivity

An *observer* measures the relative positions of points in a Euclidean space and furthermore time intervals. The stress and strain state in a continuum as well as any other physical quantity is invariant relative to a change of observer. Hence, different observers have to detect the same relative distance between two points and the same elapsed time of two events $(\boldsymbol{x}_0, t_0)$ and $(\boldsymbol{x}, t)$. The *Euclidean transformation*

$$\boldsymbol{x}^+ - \boldsymbol{x}_0^+ = \boldsymbol{Q}(t)(\boldsymbol{x} - \boldsymbol{x}_0), \qquad t^+ - t_0^+ = t - t_0 \tag{2.84}$$

with a proper orthogonal tensor $\boldsymbol{Q}(t)$ $\left(\boldsymbol{Q}^{-1}(t) = \boldsymbol{Q}^T(t), \det \boldsymbol{Q} = 1\right)$ preserves the distance and time interval of these events $(\boldsymbol{x}_0, t_0)$ and $(\boldsymbol{x}, t)$ during the mapping to the events $(\boldsymbol{x}_0^+, t_0^+)$ and $(\boldsymbol{x}^+, t^+)$. A scalar α, a vector $\boldsymbol{a}$, and a second-order tensor $\boldsymbol{A}$ will be objective spatial values if the following relations are fulfilled

$$\alpha^+(\boldsymbol{x}^+, t^+) = \alpha(\boldsymbol{x}, t) \tag{2.85}$$

$$\boldsymbol{a}^+(\boldsymbol{x}^+, t^+) = \boldsymbol{Q}(t)\boldsymbol{a}(\boldsymbol{x}, t) \tag{2.86}$$

$$\boldsymbol{A}^+(\boldsymbol{x}^+, t^+) = \boldsymbol{Q}(t)\boldsymbol{A}(\boldsymbol{x}, t)\boldsymbol{Q}^T(t). \tag{2.87}$$

Generally, a physical quantity will be independent of an observer, if this quantity is objective. For example, the Cauchy stress tensors $\boldsymbol{\sigma}$ and the Jacobian determinant J are objective. The first Piola-Kirchhoff stress tensor $\boldsymbol{P}$ and the deformation gradient $\boldsymbol{F}$ are objective in terms of a vector field transformation. In a similar way, the second Piola-Kirchhoff stress tensor $\boldsymbol{S}$, the Green-Lagrange strain tensor $\boldsymbol{E}$, and the right Cauchy-Green tensor $\boldsymbol{C}$ transform like a scalar and hence are objective too. On the other hand, the velocity $\boldsymbol{v}$ or the spatial velocity gradient $\boldsymbol{l}$ are in general not objective. The consequence is that constitutive equations, which have to be objective, cannot be formulated using non-objective quantities.

2.7.2 Objective Time Derivatives of Objective Tensors

Objective time derivatives are necessary to determine objective constitutive equations in the rate form, see Oldroyd (1950). The time derivatives of an objective vector $\boldsymbol{a}$ and an objective second-order tensor $\boldsymbol{A}$ are given by

$$\dot{\boldsymbol{a}}^{+} = \dot{\boldsymbol{Q}}\boldsymbol{a} + \boldsymbol{Q}\dot{\boldsymbol{a}} \tag{2.88}$$

$$\dot{\boldsymbol{A}}^{+} = \dot{\boldsymbol{Q}}\boldsymbol{A}\boldsymbol{Q}^{T} + \boldsymbol{Q}\dot{\boldsymbol{A}}\boldsymbol{Q}^{T} + \boldsymbol{Q}\boldsymbol{A}\dot{\boldsymbol{Q}}^{T} \tag{2.89}$$

based on the product rule. Obviously, neither $\dot{\boldsymbol{a}}$ nor $\dot{\boldsymbol{A}}$ is in general an objective quantity unless $\boldsymbol{Q}$ is constant, i.e. the rate of rotation is zero. Hence, the material derivative does not preserve the objectivity. Thus, modified material time derivatives, so-called *objective rates*, are needed that satisfy the objectivity requirements. A summary of objective tensors and objective rates in continuum mechanics were given in Korobeynikov (2008) on the basis of Ogden (1997).
Many objective time derivatives are deducible from *Lie time derivatives*, as those time derivatives of objective spatial tensors yield objective quantities. To understand the concept of Lie time derivatives, a more in-depth understanding of the transformation of quantities between different configurations is essential.

Transformation Between Different Configurations

Push-forward operations transform quantities based on the reference to the current configuration. The inverse operation, a so-called *pull-back operation*, converts a quantity based on the current to the reference configuration.
Tensors are classified based on the corresponding basis vectors as co- or contravariant. On the one hand, the Green-Lagrange strain tensor $\boldsymbol{E}$, the right Cauchy-Green tensor $\boldsymbol{C}$, the Euler-Almansi strain tensor $\boldsymbol{e}$ and the inverse of the left Cauchy-Green tensor $\boldsymbol{b}^{-1}$ are covariant tensors. On the other hand, the Piola strain tensor $\boldsymbol{A}$, the inverse of the right Cauchy-Green tensor $\boldsymbol{C}^{-1}$, the Finger strain tensor $\boldsymbol{a}$, the left Cauchy-Green tensor $\boldsymbol{b}$ as well as all introduced stress tensors are contravariant tensors. According to these distinctions, the transformation rules between configurations are different. For further descriptions of co- and contravariant tensors see Marsden and Hughes (1994).

The push-forward and pull-back operations of an arbitrary covariant second order tensor $(\cdot)$ are given by

$$\varphi(\cdot) = \boldsymbol{F}^{-T}(\cdot)\boldsymbol{F}^{-1}, \qquad \varphi^{-1} = \boldsymbol{F}^{T}(\cdot)\boldsymbol{F}. \tag{2.90}$$

For example, the Euler-Almansi strain tensor $\boldsymbol{e}$ is derived with $\boldsymbol{e} = \boldsymbol{F}^{-T}\boldsymbol{E}\boldsymbol{F}^{-1}$ and the Green-Lagrange strain tensor $\boldsymbol{E}$ vice versa with $\boldsymbol{E} = \boldsymbol{F}^{T}\boldsymbol{e}\boldsymbol{F}$.
On the other side, an arbitrary contravariant second order tensor $(\cdot)$ is transformed corresponding to

$$\varphi(\cdot) = \boldsymbol{F}(\cdot)\boldsymbol{F}^{T}, \qquad \varphi^{-1} = \boldsymbol{F}^{-1}(\cdot)\boldsymbol{F}^{-T}. \tag{2.91}$$

An example for this case is the *Kirchhoff stress tensor* $\boldsymbol{\tau} = J\boldsymbol{\sigma} = \boldsymbol{F}\boldsymbol{S}\boldsymbol{F}^{T}$ (also called weighted Cauchy stress tensor) and the other way round the second Piola-Kirchhoff stress tensor $\boldsymbol{S} = \boldsymbol{F}^{-1}J\boldsymbol{\sigma}\boldsymbol{F}^{-T}$.

Lie Time Derivatives

The reason for the consideration of the Lie time derivative is that it preserves the objectivity of an objective tensor. Hence, this derivative is an essential component in the formulation of constitutive rate equations when considering finite deformations. In order to compute the Lie time derivative $\mathcal{L}_v(\boldsymbol{f})$, the following three steps are required to evaluate the change of a function $\boldsymbol{f}$ in the current configuration relative to a vector field $\boldsymbol{v}$

- convert $\boldsymbol{f}$ to the reference configuration using the pull-back operation,
- compute the material time derivative with respect to the fixed reference configuration,
- use the push-forward operation to the current configuration.

This results in different Lie time derivatives for covariant and contravariant strain tensors. For example, using the covariant Euler-Almansi strain tensor $\boldsymbol{e}$, the Lie time derivative of this tensor is given by

$$\mathcal{L}_v(\boldsymbol{e}) = \boldsymbol{F}^{-T}\left(\frac{\mathrm{d}(\boldsymbol{F}^{T}\boldsymbol{e}\boldsymbol{F})}{\mathrm{d}t}\right)\boldsymbol{F}^{-1} = \boldsymbol{F}^{-T}\left(\boldsymbol{F}^{T}\boldsymbol{e}\boldsymbol{F}\right)^{\cdot}\boldsymbol{F}^{-1} \tag{2.92}$$

$$= \boldsymbol{F}^{-T}\dot{\boldsymbol{F}}^{T}\boldsymbol{e} + \dot{\boldsymbol{e}} + \boldsymbol{e}\dot{\boldsymbol{F}}\boldsymbol{F}^{-1} = \dot{\boldsymbol{e}} + \boldsymbol{l}^{T}\boldsymbol{e} + \boldsymbol{e}\boldsymbol{l} \tag{2.93}$$

with the spatial velocity gradient $\boldsymbol{l} = \dot{\boldsymbol{F}}\boldsymbol{F}^{-1}$. The generalization of this derivative to an arbitrary objective tensor $\boldsymbol{A}$

$$\overset{\triangle}{\boldsymbol{A}} = \dot{\boldsymbol{A}} + \boldsymbol{l}^{T}\boldsymbol{A} + \boldsymbol{A}\boldsymbol{l} \tag{2.94}$$

is denoted as *covariant (lower) Oldroyd rate*. This objective rate is not uniquely defined as several strain tensor definitions exist in the current configuration. The Lie time derivative of the contravariant Finger strain tensor $\boldsymbol{a}$ results in

$$\mathcal{L}_v(\boldsymbol{a}) = \boldsymbol{F}\left(\boldsymbol{F}^{-1}\boldsymbol{a}\boldsymbol{F}^{-T}\right)^{\cdot}\boldsymbol{F}^{T} = \boldsymbol{F}\dot{\boldsymbol{F}}^{-1}\boldsymbol{a} + \dot{\boldsymbol{a}} + \boldsymbol{a}\dot{\boldsymbol{F}}^{-T}\boldsymbol{F}. \tag{2.95}$$

Based on the often used relation

$$\boldsymbol{F}\boldsymbol{F}^{-1} = \boldsymbol{1} \quad \Rightarrow \quad \dot{\boldsymbol{F}}\boldsymbol{F}^{-1} + \boldsymbol{F}\dot{\boldsymbol{F}}^{-1} = \boldsymbol{0}, \tag{2.96}$$

eq. (2.95) becomes $\mathscr{L}_v(\boldsymbol{a}) = \dot{\boldsymbol{a}} - \boldsymbol{l}\boldsymbol{a} - \boldsymbol{a}\boldsymbol{l}^T$. Hence, the *contravariant (upper) Oldroyd rate* of an arbitrary objective tensor $\boldsymbol{A}$ yields

$$\overset{\triangledown}{\boldsymbol{A}} = \dot{\boldsymbol{A}} - \boldsymbol{l}\boldsymbol{A} - \boldsymbol{A}\boldsymbol{l}^T, \tag{2.97}$$

which is also an objective rate.
These two objective rates are used to formulate the constitutive equations of a finite viscoelastic Maxwell model. Nevertheless, more objective rates involving the Lie time derivative are possible, for example the Jaumann-Zaremba rate often used in plasticity or the Green-Naghdi rate. A comparison of these two objective rates was done by Xiao et al. (2005). However, there are also other possible objective rates like the Truesdell rate, which are not developed using the Lie time derivative. For more details see Holzapfel (2001).

2.7.3 Constitutive Equations

In the following, the approach of a Maxwell material with small deformations is generalized to the case for finite viscoelasticity. The concept is developed in detail in Haupt (2000), and this section summarizes the most important material equations necessary to set up the computational model. For finite deformations, the formulation of constitutive models and evolution equations for internal variables are applied to *intermediate configurations* that characterize the motion of a body. Thus, an intermediate configuration Ω_v is introduced with the constitutive assumption of a multiplicative decomposition of the deformation gradient $\boldsymbol{F}$

$$\boldsymbol{F} = \boldsymbol{F}_\mathrm{e}\boldsymbol{F}_\mathrm{v}, \tag{2.98}$$

see Fig. 2.10 for illustration. This decomposition is only conceptual and is not based on experimental facts. However, this approach implies directly the additive decomposition of the strain tensor $\boldsymbol{\Gamma}$ based on the intermediate configuration

$$\boldsymbol{\Gamma} = \boldsymbol{F}_\mathrm{v}^{-T}\boldsymbol{E}\boldsymbol{F}_\mathrm{v}^{-1} = \frac{1}{2}\boldsymbol{F}_\mathrm{v}^{-T}(\boldsymbol{F}^T\boldsymbol{F} - \boldsymbol{1})\boldsymbol{F}_\mathrm{v}^{-1} = \frac{1}{2}\left(\boldsymbol{F}_\mathrm{e}^T\boldsymbol{F}_\mathrm{e} - \boldsymbol{F}_\mathrm{v}^{-T}\boldsymbol{F}_\mathrm{v}^{-1}\right) = \boldsymbol{\Gamma}_\mathrm{e} + \boldsymbol{\Gamma}_\mathrm{v} \tag{2.99}$$

in analogy to the situation where small deformations are assumed. In this equation, the elastic and viscous strain tensors are given by $\boldsymbol{\Gamma}_\mathrm{e} = 1/2\left(\boldsymbol{F}_\mathrm{e}^T\boldsymbol{F}_\mathrm{e} - \boldsymbol{1}\right)$ and $\boldsymbol{\Gamma}_\mathrm{v} = 1/2\left(\boldsymbol{1} - \boldsymbol{F}_\mathrm{v}^{-T}\boldsymbol{F}_\mathrm{v}^{-1}\right)$, respectively. The expression $\boldsymbol{F}_\mathrm{v}^{-T}(\cdot)\boldsymbol{F}_\mathrm{v}^{-1}$ is the push-forward operation for the Green-Lagrange strain tensor in the reference to the intermediate configuration. It should be noted that the additive decomposition of the strain tensor into a purely elastic and a purely viscous part is neither in the reference nor in the current configuration possible. For instance, the Green-Lagrange strain

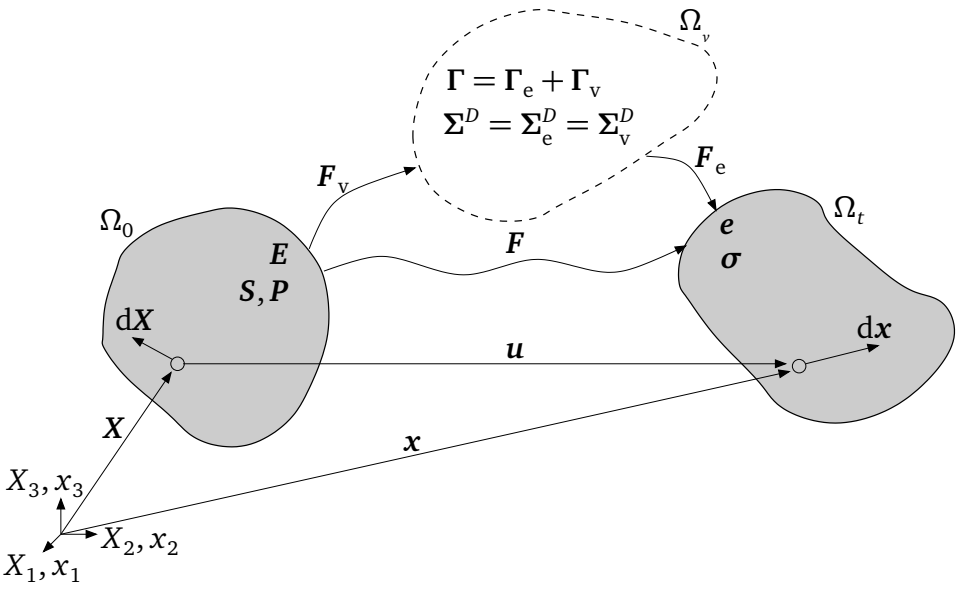

Figure 2.10: Reference Ω_0, intermediate Ω_v and current configuration Ω_t.

tensor $\boldsymbol{E}$ is split into

$$\boldsymbol{E} = \frac{1}{2}\left(\boldsymbol{F}^T\boldsymbol{F} - \boldsymbol{F}_\mathrm{e}^T\boldsymbol{F}_\mathrm{e} + \boldsymbol{F}_\mathrm{e}^T\boldsymbol{F}_\mathrm{e} - \mathbf{1}\right) = \underbrace{\frac{1}{2}\left(\boldsymbol{F}_\mathrm{e}^T\boldsymbol{F}_\mathrm{e} - \mathbf{1}\right)}_{=\boldsymbol{E}_\mathrm{e}} + \underbrace{\frac{1}{2}\boldsymbol{F}^T\left(\mathbf{1} - \boldsymbol{F}_\mathrm{v}^{-T}\boldsymbol{F}_\mathrm{v}^{-1}\right)\boldsymbol{F}}_{=\boldsymbol{E}_\mathrm{ve}}. \quad (2.100)$$

However, the second part $\boldsymbol{E}_\mathrm{ve}$ depends not only on the viscous part of the deformation gradient but also on the elastic part $\boldsymbol{F}_\mathrm{e}$ within $\boldsymbol{F}$. Hence, the additive decomposition of the strain tensor is the motivation for the use of a different configuration as this decomposition is only realizable in the intermediate configuration.
In order to establish the material equations, the stress in the intermediate configuration is assumed to be dependent on the rate-independent part of the deformation gradient

$$\boldsymbol{\Sigma} = f(\boldsymbol{F}_\mathbf{e}). \quad (2.101)$$

The generalization of Hooke's law (H) defines a possible stress-strain relation

$$\boldsymbol{\Sigma}_\mathrm{H} = \mathbb{C}\boldsymbol{\Gamma}_\mathrm{e} \quad (2.102)$$

assuming a linear elastic material law for the elastic strain tensor. This ansatz simplifies to

$$\boldsymbol{\Sigma}_\mathrm{SVK} = \lambda \mathrm{tr}\left(\boldsymbol{\Gamma}_\mathrm{e}\right)\mathbf{1} + 2\mu\boldsymbol{\Gamma}_\mathrm{e} \quad (2.103)$$

for an isotropic material. This phenomenological description of observed elastic material behavior belongs to the class of hyperelastic material models and is called *Saint Venant-Kirchhoff material* (SVK). This formulation is also derivable by the choice of a certain density function of the strain energy.
The assumption that viscous deformations are incompressible results in a vanishing

trace of the viscous strain rate tensor as discussed in detail in the case of small deformations. In particular, the trace of the viscous strain tensor $\mathrm{tr}\left(\boldsymbol{\Gamma}_\mathrm{v}\right) = 0$ for suitable initial conditions, which will be discussed later on. Hence, eq. (2.103) is expressed differently based on the additive decomposition of the strain tensor

$$\boldsymbol{\Sigma}_{\mathrm{e}_1} = \boldsymbol{\Sigma}_\mathrm{SVK} = \lambda \mathrm{tr}\left(\boldsymbol{\Gamma}_\mathrm{e}\right)\mathbf{1} + 2\mu\left[\boldsymbol{\Gamma}_\mathrm{e} + \frac{1}{3}\mathrm{tr}\left(\boldsymbol{\Gamma}_\mathrm{e}\right)\mathbf{1} - \frac{1}{3}\mathrm{tr}\left(\boldsymbol{\Gamma}_\mathrm{e}\right)\mathbf{1}\right] \tag{2.104}$$

$$= \underbrace{\left(\lambda + \frac{2}{3}\mu\right)\mathrm{tr}\left(\boldsymbol{\Gamma}\right)\mathbf{1}}_{=\boldsymbol{\Sigma}^\mathrm{vol}_\mathrm{SVK}} + \underbrace{2\mu\left[\boldsymbol{\Gamma}_\mathrm{e} - \frac{1}{3}\mathrm{tr}\left(\boldsymbol{\Gamma}_\mathrm{e}\right)\mathbf{1}\right]}_{=\boldsymbol{\Sigma}^D_\mathrm{SVK}}. \tag{2.105}$$

This equation is separable to a volumetric (spherical) and deviatoric part according to $\boldsymbol{\Sigma} = 1/3\mathrm{tr}(\boldsymbol{\Sigma})\mathbf{1} + \boldsymbol{\Sigma}^D$. Equation (2.105) corresponds to the generalization of small to finite deformations, see eq. (2.78) with $2\eta\dot{\boldsymbol{\varepsilon}}^D_\mathrm{v} = 2\mu\boldsymbol{\varepsilon}^D_\mathrm{e}$, as the stress-strain relation is the same. In general, the relative change in volume $\Delta V/V$ corresponds only for small strains to the trace of the strain tensor. In the case of finite deformation, the relative change in volume also includes higher order terms. To express the volumetric part of the stress tensor by the trace of the strain tensor is only consistent for the special case of the Saint Venant-Kirchhoff material. Hence, this approach is obviously limited to problems with large deformations but moderate (small) strains. Exceptional difficulties appear additionally for large compressive strains, see Wriggers (2008).

To overcome these problems, another possible stress-strain relation is introduced. The material equation of the *neo-Hookean material* (NH) is also derived from a density function of the strain energy. A possible constitutive assumption for the stress relation is given by

$$\boldsymbol{\Sigma}_{\mathrm{e}_2} = \boldsymbol{\Sigma}_\mathrm{NH} = \underbrace{\frac{\left(\lambda + \frac{2}{3}\mu\right)}{2}\left(J^2 - 1\right)\boldsymbol{C}^{-1}_\mathrm{e}}_{=\boldsymbol{\Sigma}^\mathrm{vol}_\mathrm{NH}} + \underbrace{\mu J^{-\frac{2}{3}}\left(\mathbf{1} - \frac{1}{3}\mathrm{tr}\left(\boldsymbol{C}_\mathrm{e}\right)\boldsymbol{C}^{-1}_\mathrm{e}\right)}_{=\boldsymbol{\Sigma}^D_\mathrm{NH}} \tag{2.106}$$

with the elastic right Cauchy-Green tensor $\boldsymbol{C}_\mathrm{e} = \boldsymbol{F}^T_\mathrm{e}\boldsymbol{F}_\mathrm{e}$. It is nontrivial to show that a decomposition of the right Cauchy-Green tensor in an elastic and a viscous part is possible. Thus the elastic and the analog viscous right Cauchy-Green tensor are derived by further assumptions. The neo-Hookean material is often only characterized by the deviatoric part. The expression for the volumetric part can differ. However, Wriggers (2008) established a material equation divided in volumetric and deviatoric part in this way. The results of these two different estimations of the elastic material eqs. (2.105) and (2.106) are compared later.

However, the evolution equation for the internal variable is still missing. To transform the viscous flow relation to finite deformations, an objective strain rate tensor in the intermediate configuration is needed. By the use of the lower Oldroyd rate $\overset{\triangle}{\boldsymbol{\Gamma}}_\mathrm{v} = \dot{\boldsymbol{\Gamma}}_\mathrm{v} + \boldsymbol{l}^T_\mathrm{v}\boldsymbol{\Gamma}_\mathrm{v} + \boldsymbol{\Gamma}_\mathrm{v}\boldsymbol{l}_\mathrm{v}$ with the viscous deformation rate $\boldsymbol{l}_\mathrm{v} = \dot{\boldsymbol{F}}_\mathrm{v}\boldsymbol{F}^{-1}_\mathrm{v}$, the viscous

stress tensor is assumed to be

$$\boldsymbol{\Sigma}^{D}_{\mathrm{v,SVK}} = 2\eta \overset{\triangle}{\boldsymbol{\Gamma}}{}^{D}_{\mathrm{v}}. \tag{2.107}$$

for the Saint Venant-Kirchhoff material, while for the neo-Hookean material the viscous stress tensor is given by

$$\boldsymbol{\Sigma}^{D}_{\mathrm{v,NH}} = \eta \overset{\triangle}{\boldsymbol{\Gamma}}{}^{D}_{\mathrm{v}}. \tag{2.108}$$

This distinction is explainable by the different deviatoric stress coefficients of the material formulations and will be discussed in more detail in Section 7.5. Based on the additive decomposition of the total strain, also the additive decomposition of the strain rate tensor is valid with the elastic strain rate $\overset{\triangle}{\boldsymbol{\Gamma}}_{\mathrm{e}} = \dot{\boldsymbol{\Gamma}}_{\mathrm{e}} + \boldsymbol{l}_{\mathrm{v}}^{T}\boldsymbol{\Gamma}_{\mathrm{e}} + \boldsymbol{\Gamma}_{\mathrm{e}}\boldsymbol{l}_{\mathrm{v}}$ and the viscous one $\overset{\triangle}{\boldsymbol{\Gamma}}_{\mathrm{v}} = \dot{\boldsymbol{\Gamma}}_{\mathrm{v}} + \boldsymbol{l}_{\mathrm{v}}^{T}\boldsymbol{\Gamma}_{\mathrm{v}} + \boldsymbol{\Gamma}_{\mathrm{v}}\boldsymbol{l}_{\mathrm{v}}$. As mentioned earlier, the choice of the objective rate is not unique. However, Haupt (2000) showed the applicability of the Oldroyd rate to a finite viscoelastic Maxwell model. In order to derive the constitutive equation of the internal variable, the generalization of eq. (2.77) to finite deformations is needed. Therefore, only the isochoric part of the elastic stress tensor is equated with the isochoric part of the viscous stress tensor. This approach is chosen analogously to the small deformation case as the volumetric stresses are assumed to induce purely elastic deformations. The simplest formulation for the Saint Venant-Kirchhoff material is

$$2\eta \overset{\triangle}{\boldsymbol{\Gamma}}_{\mathrm{v}} = 2\mu \left[\boldsymbol{\Gamma}_{\mathrm{e}} - \frac{1}{3}\mathrm{tr}\left(\boldsymbol{\Gamma}_{\mathrm{e}}\right)\mathbf{1} \right] \tag{2.109}$$

as $\mathrm{tr}\left(\overset{\triangle}{\boldsymbol{\Gamma}}_{\mathrm{v}}\right) = 0$ due to the incompressible viscous deformation. The equation for the internal variable results in

$$2\eta \overset{\triangle}{\boldsymbol{\Gamma}}_{\mathrm{v}} = 2\mu \left[\boldsymbol{\Gamma} - \boldsymbol{\Gamma}_{\mathrm{v}} - \frac{1}{3}\mathrm{tr}\left(\boldsymbol{\Gamma} - \boldsymbol{\Gamma}_{\mathrm{v}}\right)\mathbf{1} \right] \tag{2.110}$$

using only viscous quantities.
The balance equations are set up either in the reference or the current configuration. Hence, the constitutive equations and the evolution equation for the internal variable have to be transformed to the reference or current configuration. The pull-back operation $\boldsymbol{F}_{\mathrm{v}}^{-1}(\cdot)\boldsymbol{F}_{\mathrm{v}}^{-T}$ to the reference configuration yields the second Piola-Kirchhoff stress tensor $\boldsymbol{S} = \boldsymbol{F}_{\mathrm{v}}^{-1}\boldsymbol{\Sigma}\boldsymbol{F}_{\mathrm{v}}^{-T}$. The first Piola-Kirchhoff stress tensor, which is needed to solve the quasi-static momentum balance in the reference configuration, is computed by $\boldsymbol{P} = \boldsymbol{F}\boldsymbol{S}$. Thus, the last remaining step to obtain a complete system of equations for the Saint Venant-Kirchhoff material in the reference configuration is to pull-back eqs. (2.105) and (2.110). After basic modifications, the transformation

	$\boldsymbol{\Sigma}_{\mathrm{e}_1} = \boldsymbol{\Sigma}_{\mathrm{SVK}} = \boldsymbol{\Sigma}^{\mathrm{vol}}_{\mathrm{SVK}} + \boldsymbol{\Sigma}^{D}_{\mathrm{SVK}}$ $= K\mathrm{tr}(\boldsymbol{\Gamma})\mathbf{1} + 2\mu\left[\boldsymbol{\Gamma}_{\mathrm{e}} - \frac{1}{3}\mathrm{tr}(\boldsymbol{\Gamma}_{\mathrm{e}})\mathbf{1}\right]$	$\boldsymbol{\Sigma}_{\mathrm{e}_2} = \boldsymbol{\Sigma}_{\mathrm{NH}} = \boldsymbol{\Sigma}^{\mathrm{vol}}_{\mathrm{NH}} + \boldsymbol{\Sigma}^{D}_{\mathrm{NH}}$ $= \frac{K}{2}\left(J^2-1\right)\boldsymbol{C}_{\mathrm{e}}^{-1} + \mu J^{-\frac{2}{3}}\left(\mathbf{1} - \frac{1}{3}\mathrm{tr}\left(\boldsymbol{C}_{\mathrm{e}}\right)\boldsymbol{C}_{\mathrm{e}}^{-1}\right)$
$\boldsymbol{\Sigma}^{D}_{\mathrm{v,SVK}} = 2\eta\overset{\triangle}{\boldsymbol{\Gamma}}_{\mathrm{v}}$ $\boldsymbol{\Sigma}^{D}_{\mathrm{v,NH}} = \eta\overset{\triangle}{\boldsymbol{\Gamma}}_{\mathrm{v}}$ $\boldsymbol{\Gamma} = \boldsymbol{F}_{\mathrm{v}}^{-T}\boldsymbol{E}\boldsymbol{F}_{\mathrm{v}}^{-1}$	$\boldsymbol{S}^{\triangle}_{\mathrm{SVK}} = \frac{K}{2}\left[\mathrm{tr}\left(\boldsymbol{C}\boldsymbol{C}_{\mathrm{v}}^{-1}\right) - 3\right]\boldsymbol{C}_{\mathrm{v}}^{-1}$ $+\mu\left[\boldsymbol{C}_{\mathrm{v}}^{-1}\boldsymbol{C}\boldsymbol{C}_{\mathrm{v}}^{-1} - \frac{1}{3}\mathrm{tr}\left(\boldsymbol{C}\boldsymbol{C}_{\mathrm{v}}^{-1}\right)\boldsymbol{C}_{\mathrm{v}}^{-1}\right]$ $\eta\dot{\boldsymbol{C}}_{\mathrm{v}} = \mu\left(\boldsymbol{C} - \frac{1}{3}\mathrm{tr}\left(\boldsymbol{C}\boldsymbol{C}_{\mathrm{v}}^{-1}\right)\boldsymbol{C}_{\mathrm{v}}\right)$	$\boldsymbol{S}^{\triangle}_{\mathrm{NH}} = \frac{K}{2}\left(J^2-1\right)\boldsymbol{C}^{-1}$ $+\mu J^{-\frac{2}{3}}\left(\boldsymbol{C}_{\mathrm{v}}^{-1} - \frac{1}{3}\mathrm{tr}\left(\boldsymbol{C}_{\mathrm{v}}\boldsymbol{C}^{-1}\right)\boldsymbol{C}^{-1}\right)$ $\eta\dot{\boldsymbol{C}}_{\mathrm{v}} = \mu J^{-\frac{2}{3}}\left(\boldsymbol{C}_{\mathrm{v}} - \frac{1}{3}\mathrm{tr}\left(\boldsymbol{C}_{\mathrm{v}}\boldsymbol{C}^{-1}\right)\boldsymbol{C}_{\mathrm{v}}\boldsymbol{C}^{-1}\boldsymbol{C}_{\mathrm{v}}\right)$
$\boldsymbol{\Sigma}^{D}_{\mathrm{v,SVK}} = 2\eta\overset{\triangledown}{\boldsymbol{\Gamma}}_{\mathrm{v}}$ $\boldsymbol{\Sigma}^{D}_{\mathrm{v,NH}} = \eta\overset{\triangledown}{\boldsymbol{\Gamma}}_{\mathrm{v}}$ $\boldsymbol{\Gamma} = \boldsymbol{F}_{\mathrm{v}}\boldsymbol{A}\boldsymbol{F}_{\mathrm{v}}^{T}$	$\boldsymbol{S}^{\triangledown}_{\mathrm{SVK}} = \frac{K}{2}\left[\mathrm{tr}\left(\boldsymbol{C}^{-1}\boldsymbol{C}_{\mathrm{v}}\right) - 3\right]\boldsymbol{C}_{\mathrm{v}}^{-1}$ $+\mu\left[\boldsymbol{C}^{-1} - \frac{1}{3}\mathrm{tr}\left(\boldsymbol{C}^{-1}\boldsymbol{C}_{\mathrm{v}}\right)\boldsymbol{C}_{\mathrm{v}}^{-1}\right]$ $\eta\dot{\boldsymbol{C}}_{\mathrm{v}}^{-1} = \mu\left(\boldsymbol{C}^{-1} - \frac{1}{3}\mathrm{tr}\left(\boldsymbol{C}^{-1}\boldsymbol{C}_{\mathrm{v}}\right)\boldsymbol{C}_{\mathrm{v}}^{-1}\right)$	$\boldsymbol{S}^{\triangledown}_{\mathrm{NH}} = \frac{K}{2}\left(J^2-1\right)\boldsymbol{C}^{-1}$ $+\mu J^{-\frac{2}{3}}\left(\boldsymbol{C}_{\mathrm{v}}^{-1} - \frac{1}{3}\mathrm{tr}\left(\boldsymbol{C}_{\mathrm{v}}\boldsymbol{C}^{-1}\right)\boldsymbol{C}^{-1}\right)$ $\eta\dot{\boldsymbol{C}}_{\mathrm{v}}^{-1} = \mu J^{-\frac{2}{3}}\left(\boldsymbol{C}_{\mathrm{v}}^{-1} - \frac{1}{3}\mathrm{tr}\left(\boldsymbol{C}_{\mathrm{v}}\boldsymbol{C}^{-1}\right)\boldsymbol{C}^{-1}\right)$

Table 2.1: Summary of two elastic stress relations formulated in the intermediate configuration, namely the Saint Venant-Kirchhoff material $\boldsymbol{\Sigma}_{\mathrm{SVK}}$ and the neo-Hookean material $\boldsymbol{\Sigma}_{\mathrm{NH}}$. Consequent elasticity relations $\boldsymbol{S}$ and evolution equations of the internal variable $\boldsymbol{C}_{\mathrm{v}}$ formulated in the reference configuration using the lower ($\triangle$) or upper ($\triangledown$) Oldroyd rate in the intermediate configuration. Equations formulated in the intermediate configuration are black and their corresponding equations in the reference configuration are colored blue.

of eq. (2.105) leads to

$$\boldsymbol{S}^{\triangle}_{\mathrm{SVK}} = \boldsymbol{F}_{\mathrm{v}}^{-1}\boldsymbol{\Sigma}_{\mathrm{SVK}}\boldsymbol{F}_{\mathrm{v}}^{-T} \tag{2.111}$$

$$= \frac{\lambda + \frac{2}{3}\mu}{2}\left[\mathrm{tr}\left(\boldsymbol{C}\boldsymbol{C}_{\mathrm{v}}^{-1}\right) - 3\right]\boldsymbol{C}_{\mathrm{v}}^{-1} + \mu\left[\boldsymbol{C}_{\mathrm{v}}^{-1}\boldsymbol{C}\boldsymbol{C}_{\mathrm{v}}^{-1} - \frac{1}{3}\mathrm{tr}\left(\boldsymbol{C}\boldsymbol{C}_{\mathrm{v}}^{-1}\right)\boldsymbol{C}_{\mathrm{v}}^{-1}\right], \tag{2.112}$$

where $(\cdot)^{\triangle}$ denotes that the corresponding viscous relation is derived by the objective lower Oldroyd rate. Equation (2.112) is the elasticity relation in the reference configuration with the viscous right Cauchy-Green tensor $\boldsymbol{C}_{\mathrm{v}} = \boldsymbol{F}_{\mathrm{v}}^{T}\boldsymbol{F}_{\mathrm{v}}$. This quantity is still unknown as the multiplicative decomposition of the deformation gradient does not directly result in the viscous deformation gradient $\boldsymbol{F}_{\mathrm{v}}$. The viscous right Cauchy-Green tensor captures the history of the deformation hence, this quantity is applied as an internal variable. The pull-back operation of eq. (2.110) with $\boldsymbol{F}_{\mathrm{v}}^{T}(\cdot)\boldsymbol{F}_{\mathrm{v}}$ gives the evolution equation for the internal variable $\boldsymbol{C}_{\mathrm{v}}$

$$\eta\dot{\boldsymbol{C}}_{\mathrm{v}} = \mu\left(\boldsymbol{C} - \frac{1}{3}\mathrm{tr}\left(\boldsymbol{C}\boldsymbol{C}_{\mathrm{v}}^{-1}\right)\boldsymbol{C}_{\mathrm{v}}\right). \tag{2.113}$$

Hence, the first system of equations is formulated in the reference configuration and summarized in Table 2.1. These equations are used to model the Saint Venant-Kirchhoff material by applying the lower Oldroyd rate as the objective rate.

Another possibility for the viscous material equation is to take the upper Oldroyd rate. In this case, the strain tensor $\boldsymbol{\Upsilon} = \boldsymbol{F}_\mathrm{v}\boldsymbol{A}\boldsymbol{F}_\mathrm{v}^T$ derived from the contravariant Piola strain tensor $\boldsymbol{A}$ is required. Analogously to eq. (2.99), the elastic part of this strain tensor results in $\boldsymbol{\Upsilon}_\mathrm{e} = 1/2(\boldsymbol{F}_\mathrm{e}^{-1}\boldsymbol{F}_\mathrm{e}^{-T} - \mathbf{1})$ and the viscous part in $\boldsymbol{\Upsilon}_\mathrm{v} = 1/2(\mathbf{1} - \boldsymbol{F}_\mathrm{v}\boldsymbol{F}_\mathrm{v}^T)$. The equations of the Saint Venant-Kirchhoff material with the upper Oldroyd rate $(\cdot)^\triangledown$ in eqs. (2.105) and (2.110) transform to the stress relation and reads

$$\boldsymbol{S}_\mathrm{SVK}^\triangledown = \frac{\lambda + \frac{2}{3}\mu}{2}\left[\mathrm{tr}\left(\boldsymbol{C}^{-1}\boldsymbol{C}_\mathrm{v}\right) - 3\right]\boldsymbol{C}_\mathrm{v}^{-1} + \mu\left[\boldsymbol{C}^{-1} - \frac{1}{3}\mathrm{tr}\left(\boldsymbol{C}^{-1}\boldsymbol{C}_\mathrm{v}\right)\boldsymbol{C}_\mathrm{v}^{-1}\right] \tag{2.114}$$

with

$$\eta\dot{\boldsymbol{C}}_\mathrm{v}^{-1} = \mu\left(\boldsymbol{C}^{-1} - \frac{1}{3}\mathrm{tr}\left(\boldsymbol{C}^{-1}\boldsymbol{C}_\mathrm{v}\right)\boldsymbol{C}_\mathrm{v}^{-1}\right) \tag{2.115}$$

in the reference configuration. The modification in the evolution equation of the internal variable (2.115) results from the change in the pull-back operation $\boldsymbol{F}_\mathrm{v}^{-1}(\cdot)\boldsymbol{F}_\mathrm{v}^{-T}$ for the Piola strain tensor. Based on the latter equation, it is more useful to choose the internal variable $\boldsymbol{C}_\mathrm{v}^{-1}$, if the upper Oldroyd rate is used.
Finally, the system of equations of the neo-Hookean material in the intermediate configuration

$$\boldsymbol{\Sigma}_\mathrm{NH}^\triangle = \frac{\left(\lambda + \frac{2}{3}\mu\right)}{2}\left(J^2 - 1\right)\boldsymbol{C}_\mathrm{e}^{-1} + \mu J^{-\frac{2}{3}}\left(\mathbf{1} - \frac{1}{3}\mathrm{tr}\left(\boldsymbol{C}_\mathrm{e}\right)\boldsymbol{C}_\mathrm{e}^{-1}\right) \tag{2.116}$$

$$\eta\overset{\triangle}{\boldsymbol{\Gamma}}_\mathrm{v} = \mu J^{-\frac{2}{3}}\left(\mathbf{1} - \frac{1}{3}\mathrm{tr}\left(\boldsymbol{C}_\mathrm{e}\right)\boldsymbol{C}_\mathrm{e}^{-1}\right) \tag{2.117}$$

is transformed into the reference configuration and reads as follows

$$\boldsymbol{S}_\mathrm{NH}^\triangle = \boldsymbol{F}_\mathrm{v}^{-1}\boldsymbol{\Sigma}_\mathrm{NH}\boldsymbol{F}_\mathrm{v}^{-T} \tag{2.118}$$

$$= \frac{\left(\lambda + \frac{2}{3}\mu\right)}{2}\left(J^2 - 1\right)\boldsymbol{C}^{-1} + \mu J^{-\frac{2}{3}}\left(\boldsymbol{C}_\mathrm{v}^{-1} - \frac{1}{3}\mathrm{tr}\left(\boldsymbol{C}_\mathrm{v}\boldsymbol{C}^{-1}\right)\boldsymbol{C}^{-1}\right) \tag{2.119}$$

$$\eta\dot{\boldsymbol{C}}_\mathrm{v} = \mu J^{-\frac{2}{3}}\left(\boldsymbol{C}_\mathrm{v} - \frac{1}{3}\mathrm{tr}\left(\boldsymbol{C}_\mathrm{v}\boldsymbol{C}^{-1}\right)\boldsymbol{C}_\mathrm{v}\boldsymbol{C}^{-1}\boldsymbol{C}_\mathrm{v}\right). \tag{2.120}$$

The stress-strain relation of the neo-Hookean material is not dependent on the selected strain tensor, see eq. (2.116). Hence, if the upper instead of the lower Oldroyd rate is applied, only the evolution equation for the internal variable will change and we have $\boldsymbol{S}_\mathrm{NH}^\triangle = \boldsymbol{S}_\mathrm{NH}^\triangledown$. An analogous procedure yields the last missing equation in the reference configuration

$$\eta\dot{\boldsymbol{C}}_\mathrm{v}^{-1} = \mu J^{-\frac{2}{3}}\left(\boldsymbol{C}_\mathrm{v}^{-1} - \frac{1}{3}\mathrm{tr}\left(\boldsymbol{C}_\mathrm{v}\boldsymbol{C}^{-1}\right)\boldsymbol{C}^{-1}\right) \tag{2.121}$$

using the upper Oldroyd rate as the objective rate. In summary, all conjugate model equations are presented in Table 2.1.

3 Modeling Concept

Beside basal melting and changes in surface mass balance, ice shelves primarily lose mass in consequence of iceberg calving. However, this process is still not well understood. The determination of physical-based calving rates as well as calving criteria belong to ongoing topics of research. In current ice sheet models, more phenomenological approaches prevail so far (Alley et al., 2008; Albrecht et al., 2011) to specify the mechanisms of calving, see Section 1.1. In order to get a better description of the mass loss based on a physical-motivated model, a continuum mechanical approach to analyze causes of calving is presented in this work. For different material models stress states as well as strain or strain rate distributions are analyzed more precisely with respect to time. These internal state quantities have crucial effects on the calving behavior of ice shelves and thus their influencing factors are studied in detail.

The calving fronts of ice shelves amount a length of 60 % of the total Antarctic coastline (Wesche et al., 2013). Along these fronts, the extent between 77 % and 89 % of the ice thickness is located below the water surface and consequently 23 % to 11 % above. The exact proportion depends on the buoyancy equilibrium and thus on the present ice density. This value ranges between $\rho_{\text{ice}} = 790\,\text{kg/m}^3$ and $\rho_{\text{ice}} = 910\,\text{kg/m}^3$ for Antarctic ice. The prevailing ice-shelf geometry looks like a ramp with a decreasing thickness towards the calving front mainly caused by basal melting and freezing. However, the slight thickness change consists of only a few hundreds of meters over several hundreds of kilometers of horizontal extent. The area of investigation for this work is far enough away from the grounding line, the region where the ice becomes afloat. The results will show that influences of this transitional zone are insignificant. At the ice front boundary, the ocean exerts a normal stress onto the face below the water surface due to the sea water pressure, while the ice part above experiences only a negligible atmospheric pressure, see Fig. 3.1. In this work, the inequality of ice or water and atmospheric pressure is called *boundary disturbance* or *boundary perturbation* at the ice front. This disturbance leads to a bending moment and thus to tensile stresses in flow direction for the upper and compressive stresses of the lower ice shelf part, cf. Section 4.1. In addition this section reveals that especially the highest tensile stress is located at the upper surface of the ice shelf. The sea water pressure is insufficient to buttress the ice shelf entirely. Hence, the ice shelf experiences a horizontal stretching and a vertical compression of the thickness. Based on this viscous ice flow and the absence of the buttressing force at the upper part of the ice front, the maximum horizontal strain also occurs at the upper surface of the ice shelf, see Chapter 5.

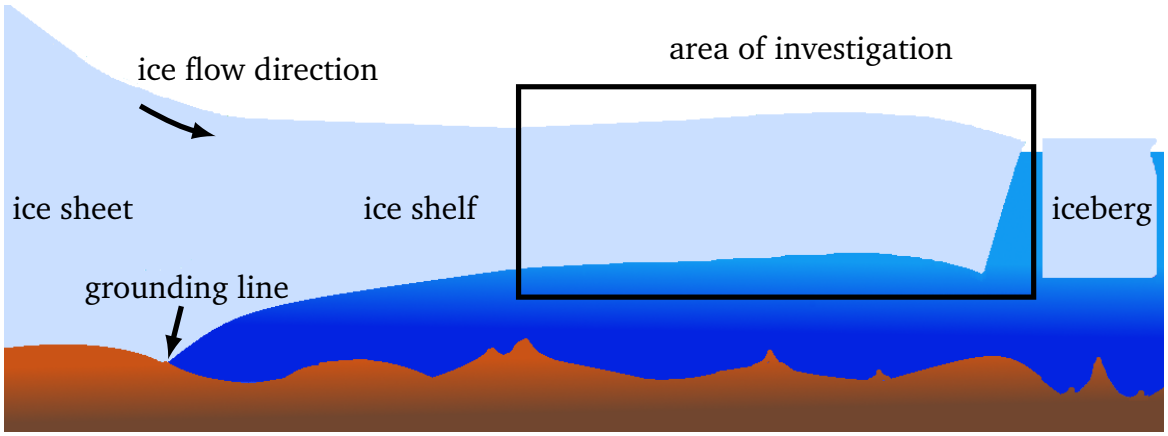

Figure 3.1: Schematic cross section of an ice sheet – ice shelf model showing the deformation based on the boundary disturbance at the ice front. This deformation is exaggerated.

The behavior outlined above is reproduced as accurately as possible by a mathematical model at the end of this chapter. In Section 4.1 the lateral effects on stress and strain states in an ice shelf are investigated by the comparison of 2d and 3d model results. The tides engender an overall lifting and lowering of the ice shelf that solely influence the load situation at the grounding line. As already mentioned above the processes in this area are insignificant for the kind of calving considered in this work and not studied furthermore. Beyond the ice shelf front, no more ice, for example sea ice, is considered that prevents the extension in the horizontal direction. Another simplification in the model is the disregard of the accumulation.
In order to understand the special kind of calving examined in this study, different possible calving processes are discussed in the next section. Subsequently, various geometries, boundary conditions, and numerics to model the ice shelf behavior within the finite element framework are given in this chapter.

3.1 Different Types of Calving at Ice Shelves

Along the fronts of ice shelves, different mechanisms of iceberg calving occur. For the first type not further investigated in this work, ice shelves expand over several years to decades until they eventually calve off. In this case large icebergs in the order of $10\,\mathrm{km}^2$ to $1\,000\,\mathrm{km}^2$ or even gigantic icebergs with areas above $1\,000\,\mathrm{km}^2$ are formed. These events are singular in time and for this kind of calving cracks propagate, turn into rifts and finally penetrate the ice shelf. Hence, the occurrence and the distribution of rifts in ice shelves control the calving of large tabular icebergs. The formation of cracks happens at grounding lines, at shear margins or downstream of ice rises or rumples, the grounded pinning points of ice shelves. Crack initiations as well as propagations are considered in many works and only a selection of them is listed below as a short summary. For instance, crevasses arise at the upper surface as consequences of stresses at the grounding line or at shear margins, see Van der

Veen (1998a). These surface structures are observable by satellite images. To model crack expansions, a distinction between horizontal and vertical crevasse propagation is sensible, see Plate (2015). Reasons for vertical crack propagation are investigated by Nye (1955) and Weertman (1973). The extension to the commonly used stress intensity factors for fracture mechanical problems were discussed by Smith (1976), Van der Veen (1998a,b) and Rist et al. (2002). For the horizontal rift propagation, two different methods are pursued. On the one hand, fractured areas are modeled as weak zones by Rist et al. (1999), Sandhäger et al. (2005), and Weis et al. (1999). Applications of ice shelves studied by this method were shown by Humbert et al. (2009) for the Brunt Ice Shelf and by Jansen et al. (2010) for the Larsen C Ice Shelf. A combination of crack initiation, transporting and healing was discussed in Albrecht and Levermann (2012). On the other hand, rifts were considered as geometric features by Larour et al. (2004a, b) and Hulbe et al. (2010). The latter also concluded that a crack tip arrest in suture zones is possible. Beside this, rift propagation is tolerant against external short-term forces like winds and tides, see Bassis et al. (2008). In addition, the existence of basal channels and crevasse-like features was first pointed out by Weertman (1973). Based on ice-penetrating radar measurements, Bentley et al. (1987) indicated that bottom crevasses only occurred downstream the grounding line. For their formation, the basal water pressure studied in a linear elastic fracture model by Van der Veen (1998b) must almost reach the ice overburden pressure fulfilled only for a floating glacier. In satellite images, strip-like structures at the upper surface are found at several ice shelves. The location of the basal characteristics coincides with surface troughs shown by Luckman et al. (2012) for the Larsen C Ice Shelf and by Humbert et al. (2015) for the Jelbart Ice Shelf. Exemplary situations were discussed for a lot of prominent ice shelves in Antarctica. For instance, Luckman et al. (2012) investigated basal crevasses at the Larsen C Ice Shelf as the result of stresses well downstream the grounding line. The crack formation due to shear margins was studied in Glasser and Scambos (2008) for the Larsen B Ice Shelf, in Fricker et al. (2002), Walker et al. (2015) for the Amery Ice Shelf and in Humbert and Steinhage (2011) for the Fimbul Ice Shelf. The latter also showed rifts due to ice rises or rumples and Jezek and Bentley (1983) discussed this rift formation for the example of the Ross Ice Shelf. However, this special kind of huge iceberg calving is influenced by rift propagation and is not part of the subsequent study.

In contrast, the second type of calving happens for instance at ice shelves, where no surface or basal crevasse exists. Wesche et al. (2013) classified the surface types of calving fronts in Antarctica. Overall 7.4 % of the ice shelves have no structures on the upper surface near the termination. In particular, these ice shelves exhibit a homogeneous, crevasse-free surface in the vicinity of the calving front. Even so, calving events still occur at these ice shelves (no calving of the first type) to contribute to their mass balance. More precisely, small icebergs in the order of $100\,\mathrm{m}^2$ to several km^2 detach after several months to few years. Until now physics-based descriptions of this rather continuous calving process are missing in current ice sheet

models but are necessary to describe accurately the mass balance of Antarctica. During this work the frequent calving processes are called *small-scale calving* and are investigated in the following. Previous studies often disregarded small-scale calving as they assumed that the mass loss due to calving is dominated by the detachment of rather sporadic tabular icebergs. However, Liu et al. (2015) stated that 95 % of all calving events in Antarctica consist of small or medium sized icebergs of 1 km^2 to 100 km^2. These termination events generated 38 % of the total mass loss caused by calving during a study time of 7 years. In order to describe such calving behaviors, other causes than preexisting rifts have to induce these events. Alley et al. (2008) derived a phenomenological calving criterion, which included the spreading rate, the width and the thickness of the ice shelf. Alternatively, the movement of the calving front was approximated with a finite difference grid by Albrecht et al. (2011). Every grid cell at the ice front was eliminated when the thickness drops below a certain bound. A similar approach was given by Amundson and Truffer (2010), where calving was initiated if the terminus thins to a certain value. In another approach Bassis (2011) treated iceberg calving as a stochastic process and the probability of calving was evaluated with a normal distribution function.
Presumably, a crucial point for the modeling of small-scale calving is to consider the influence of the stress balance due to the boundary condition at the ice front. In this context, several more theoretical models tried to explain small iceberg calving, see Reeh (1968), Holdsworth (1978), Fastook and Schmidt (1982), and Hughes (1992). However, no physics-based description was developed until now to explain the observations of calving at crevasse-free ice tongues. The mathematical model for this purpose has to compensate the weight by the water pressure at the bottom and hence the ice shelf is, in general, in buoyancy equilibrium. The shear stress of the grounded ice disappears once the ice becomes afloat and plug flow occurs in the ice shelf, see Greve and Blatter (2009). More critical is the point to reflect the traction-free part and the water pressure at the ice front as precisely as possible in the model. Consequently a bending moment appears and the buoyancy equilibrium is not fulfilled in the vicinity of the ice front due to the current deflection. This boundary disturbance results in a bell-shaped stress curve including the maximum tensile stress at the upper surface, which may cause calving events. The stress and additionally the strain states are examined to understand the essential factors that trigger small-scale calving. This process is not only predominant at crevasse-free surfaces, in fact maximum tensile stresses and strains due to the boundary perturbation occur in all ice shelves. For instance, large tabular icebergs as well as small-scale calving occur at the floating parts of Pine Island and Thwaites Glaciers, see Liu et al. (2015). To understand its reciprocal correlation to preexisting rifts is also of importance in a next step when the complete investigation of unaffected processes is done.
Large calving events are more often monitored as the resolution of satellite data was for a long time to low to study small-scale calving. Its observation is still limited, however, the increasing temporal coverage by satellite missions and the resolution

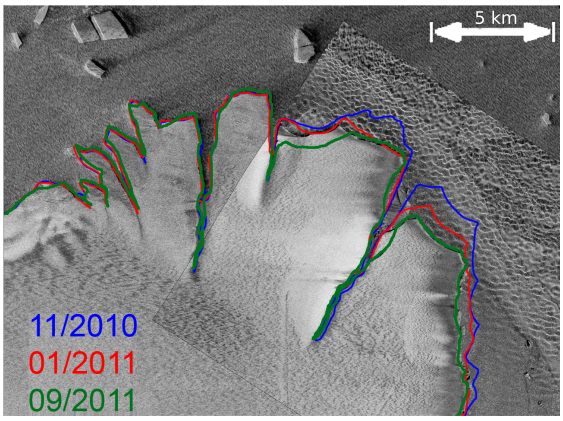

Figure 3.2: Ekström Ice Shelf, East Antarctica: Comparison of calving front positions of TerraSAR-X imagery.
© DLR, 10 February 2011

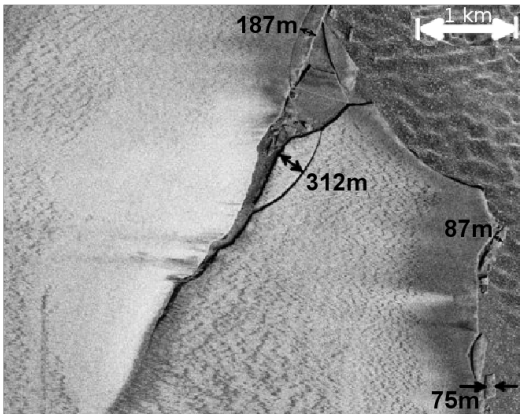

Figure 3.3: Exemplary iceberg lengths of small-scale calving at the ice front of Ekström Ice Shelf.
© DLR, 10 February 2011

of the imagery allow to more and more determine the frequency of such calving events and their corresponding iceberg sizes. As an example, the TerraSAR-X satellite, which started 2007, raised the accuracy to a resolution of 3 m. Thus, also small icebergs with extensions of several meters are perfectly recognizable. Nevertheless, time series of small-scale calving are not available until now. In this work, exemplary TerraSAR-X imageries show the ice front position over nearly one year of the Ekström Ice Shelf, East Antarctica. In order to compare modeling results to some measurements, this position is extracted and analyzed. The crevasse-free smooth surface is a basic requirement to investigate the process of small-scale calving at this ice shelf as no correlation to preexisting rifts arises. The formation of different ice tongues in the vicinity of the ice front is characteristic for this ice shelf. The imagery, which shows icebergs formed in the late summer (10 February 2011, Fig. 3.2 background), acts as a reference scene for the position of the ice front. A magnification of the most significant part is illustrated in Fig. 3.3 and illustrates small isolated icebergs at the calving front. The length of the recently detached icebergs ranges from 75 m to 312 m. These values give a hint on the iceberg dimensions of calving at crevasse-free ice shelves. In Fig. 3.2 three additional ice-front positions are included. The first one, just eleven days before the reference scene (30 January 2011, Fig. 3.2 red line), depicts the calving front previously to the iceberg formation shown in Fig. 3.3. Additionally, the position prior to these two situations is provided by a picked ice front position in early summer of the southern hemisphere (3 November 2010, Fig. 3.2 blue line). In consequence, the calving events occur during the summer between November 2010 until February 2011 and certainly also beyond this date. At the end of the austral summer the reference imagery is obviously not affected of the backpressure of the sea ice. Also other quantities that lead to changes of the calving front position like the viscous flow velocity or basal melting rates are assumed to be insignificant during this short time period. Hence, the retreat of the ice shelf is assumed to be mainly caused by the calving events and

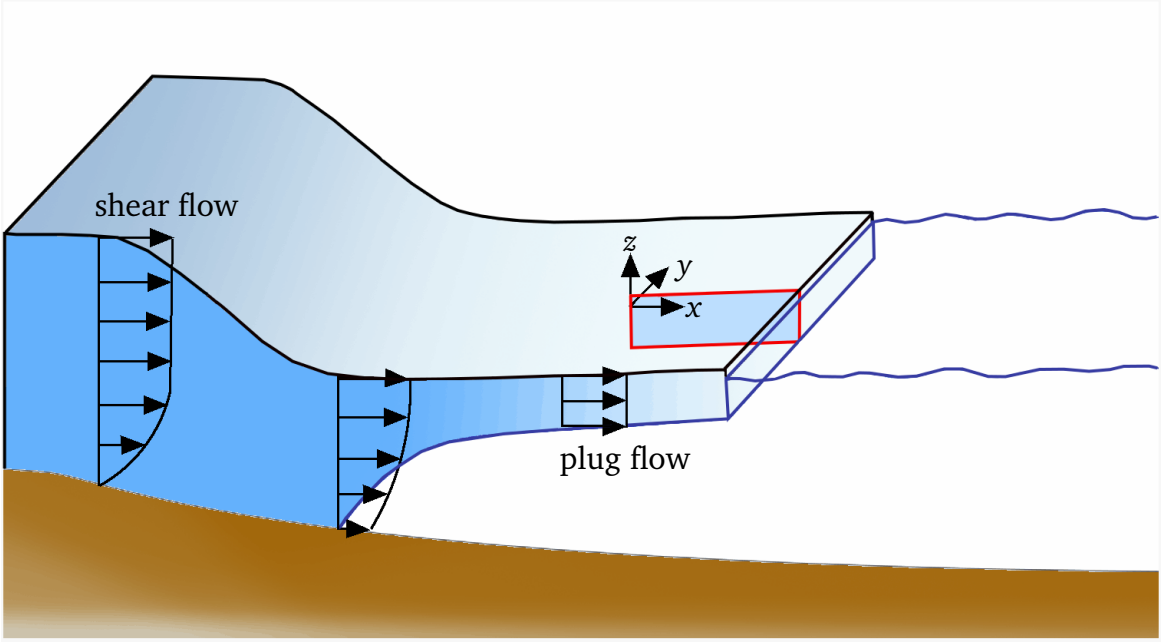

Figure 3.4: The area of investigation is highlighted in red and schematic flow systems are given including plug flow in the floating ice shelf. Horizontal lengths of ice shelves exceed several kilometers versus few hundreds of meters of thickness.

is clearly visible by the comparison of the blue curve with the reference scene. In order to determine the effect of small-scale calving after one year, the green line depicts the calving front position in spring 2011 (11 September 2011, Fig. 3.2 green line). The green curve is similar to the reference scene in the background and hence the spreading in the austral winter has to compensate the calving events during this period. It is obvious that the ice front position is not spread to reach the reference one again. In this case, the position of the ice front is influenced more than one year by the calving of small icebergs. A more frequent cover by satellite images is preferable to exactly detect the time span and the effects of consecutive calving events.

3.2 Modeling Domain

The floating ice shelves in Antarctica usually reach a length of several kilometers, while the thickness is limited to few hundreds of meters. Taking also into account huge ice shelves like Ross Ice Shelf, Filchner-Rønne Ice Shelf and Amery Ice Shelf, Greve and Blatter (2009) specified commonly used values for ice shelves with a horizontal length of $L = 500\,\text{km}$ and a vertical thickness of $H = 500\,\text{m}$. Hence, the dimensions differ by three orders of magnitude. Correspondingly, the ice shelf geometry is generally idealized by the assumption of a constant thickness. However, resultant differences to measured geometries for instance to the one of the Ekström Ice Shelf, East Antarctica are established in Section 4.2.2.

In this work it is sufficient to consider only the part near the ice front of ice shelves for the examination of small-scale calving as this part includes the maximum internal stress and strain value. This is caused by the influence of the bending moment induced by the water pressure at the ice front, which decreases by increasing the distance to the ice front. In Section 4.2, this behavior and the size of the affected part are studied in more detail. The area of investigation in this work is hence far away from the region affected by the grounding line. As a consequence, the shear stresses at the ice base vanish for the floating ice tongue and plug flow that is constant over the thickness is dominant, see Fig. 3.4. The velocity v_x (velocity vector $\boldsymbol{v} = (v_x, v_y, v_z)^T$) and the displacement u in flow direction are assumed to be constant over the thickness of the ice shelf. In all subsequent studies, the displacement vector $\boldsymbol{u} = (u, v, w)^T$ contains the unknowns of the system. In Antarctica, basal melting and freezing occur at the ice base and front due to the ocean forcing. The consequent variation of the loading situation is partly analyzed later in Section 4.2.3. For simplification, the accumulation and ablation at the upper atmospheric surface are disregarded during the entire work. A further assumption in order to reduce the computational complexity is the use of a plane geometry instead of the 3d ice shelf. Different possibilities to model the loading situation in plane cross sections of ice shelves are discussed subsequently.

3.2.1 Plane Strain Model

Many technical issues correspond to 2d problems based on the geometry, the loading, and the boundary conditions. Two general types of plane settings are commonly used and outlined below. Detailed information is given in Becker and Gross (2002) or any other textbook on continuum mechanics.
In the first 2d simplification, thin plates loaded by forces in the plane only are approximated with plane stress assumptions. In the case of plane stress, the normal stress σ_{zz} as well as the shear stresses σ_{xz} and σ_{yz} are assumed to be zero. This approach provides good results but does not fulfill all given requirements exactly. The horizontal crack propagation in ice shelves is investigated in Plate (2015) by the use of plane stress conditions to reduce the number of unknowns and equations. However, this technique is not appropriate to model the impact of the bending moment at the ice front. Furthermore, the stresses in thickness direction do not vanish based on gravitational forces acting in this direction.
The more important 2d simplification is the plane strain setting to describe small-scale calving. In an infinitely wide ice shelf it is sufficient to consider events in the xz-plane, while the shape and the loading do not vary in y-direction, cf. Fig. 3.4. In Section 4.1, the stress state is shown to be independent of the third dimension, if the width of the 2d ice shelf is sufficiently large. For the plane strain state, the displacement v in y-direction is zero and hence all strain components in the direction of the width vanish, i.e. $\varepsilon_{yy} = \varepsilon_{xy} = \varepsilon_{yz} = 0$. The non-trivial equations of the static,

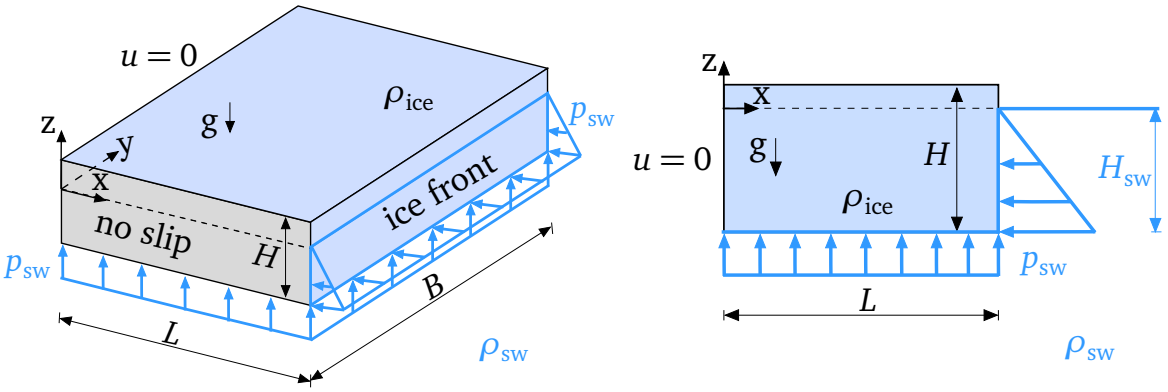

Figure 3.5: Boundary conditions for the 3d (left) and 2d (right) ice shelf model.

local momentum balance eq. (2.53) reduce to

$$\frac{\partial \sigma_{xx}}{\partial x} + \frac{\partial \sigma_{xz}}{\partial z} = 0, \tag{3.1}$$

$$\frac{\partial \sigma_{xz}}{\partial x} + \frac{\partial \sigma_{zz}}{\partial z} - \rho_{\text{ice}}\, g = 0 \tag{3.2}$$

with the volume force of the ice weight $f_z = -\rho_{\text{ice}}\, g$, the ice density ρ_{ice} and the acceleration g due to gravity.

3.3 Boundary Conditions

This section points out the importance of reasonable boundary conditions for ice shelves to solve the balance equations, the kinematic relations and the material equations uniquely. In summary, the ice shelf is affected by the sea water pressure as a function of depth at the ice front and buoyancy forces at the bottom. Plug flow, see Fig. 3.4, is assumed at the inflow because the area of investigation is far away from the grounding line. The implementation of these conditions is initially presented for the 2d problem and afterwards further conditions for the 3d case are suggested. Finally, the changes of boundary conditions when regarding finite deformations are also considered.

Figure 3.5 illustrates the boundary conditions for the 3d (left) and the 2d (right) ice shelf model. For all configurations considered during this work, ice flows from left to right and is terminated by the calving front on the right-hand side. As mentioned above the investigated domain is far away from the grounding line to ensure that a constant inflow over the whole ice thickness is present. The inflow of ice is hence only influenced by the displacement in the flow direction and independent of the other two displacements v and w. The movement at this upstream side is described by a *Dirichlet boundary condition*. However, prescribed displacements lead to rigid body motions, while stress and strain states are unchanged. These later discussed state quantities do not depend on the absolute value but rather on the

spatial variation of the displacements. As a consequence, the constant displacement in the flow direction is set to zero ($u = 0$) at the inflow boundary. At the bottom and the ice front, the pressure of sea water needs to be described by suitable boundary conditions. The condition at the bottom balances the weight of the ice shelf to adjust buoyancy equilibrium, while the condition at the ice front leads to a bending moment. To describe the impact of the sea water pressure acting in the normal direction on these two boundary faces ($p_{\mathrm{sw}}\boldsymbol{n}$) at first a *Neumann boundary condition* is applied. The pressure condition is specified by the traction σ_n as follows

$$p_{\mathrm{sw}} = \sigma_n = \begin{cases} 0 & \text{for } z \geq 0 \quad (3.3) \\ \rho_{\mathrm{sw}} g(-z) & \text{for } z < 0 \quad (3.4) \end{cases}$$

with the sea water density ρ_{sw}. Equation (3.3) ensures a traction-free part above sea level, the so-called *freeboard*. This part of the ice front is only influenced by the atmospheric pressure that prevails there. An identical condition is also established at the last undefined boundary, namely the upper surface of the ice shelf. Equation (3.4) involves the water pressure increased by the depth that induces the bending moment at the calving front.

Preliminary results are presented to highlight the effect of the Neumann boundary conditions to model the pressure of the sea water. This is exemplarily done for a rate-independent linear elastic material model using $E = 9\,\mathrm{GPa}$ and $\nu = 0.325$ as suitable material values for consolidated ice. The thickness of $H = 100\,\mathrm{m}$ is chosen accordingly to the measured geometry of the Ekström Ice Shelf studied in Section 4.2.2. Figure 3.6 presents the vertical displacement w by different colors as well as by a deformation. The results are shown for different ice shelf lengths with $L = 1\,\mathrm{km}$ (top) and $L = 10\,\mathrm{km}$ (bottom). Its thickness variation is depicted and it is obvious that the vertical displacement is almost constant over the thickness. For the Neumann boundary conditions applied for the left column of Fig. 3.6 a clear length dependency of the displacement w is identifiable. More precisely this correlation is proportional and an unrealistic displacement of $w(x = L) = -38\,\mathrm{m}$ occurs at the ice front for a length of $L = 10\,\mathrm{km}$, cf. left image at the bottom of Fig. 3.6. Hence, the defined pressure at the lower boundary does not compensate the weight of the ice shelf and buoyancy equilibrium is not fulfilled. A reason for this is that the traction condition ignores the vertical displacement and only depends on the initial geometry. In order to involve the missing deformation w, a weighted combination of Neumann and Dirichlet boundary conditions, the so-called *Robin boundary condition*, is required. Thus, the traction of eq. (3.4) is replaced by

$$p_{\mathrm{sw}} = \sigma_n = \rho_{\mathrm{sw}} g(-z - w) \quad \text{for } z + w < 0, \qquad (3.5)$$

while eq. (3.3) still holds. The consequent displacement w is illustrated in the right column of Fig. 3.6 for $L = 1\,\mathrm{km}$ (top) and $L = 10\,\mathrm{km}$ (bottom). The results with the length $L = 1\,\mathrm{km}$ are similar for the Neumann and Robin boundary condition. However, the results for $L = 10\,\mathrm{km}$ differ considerably. Applying Robin boundary

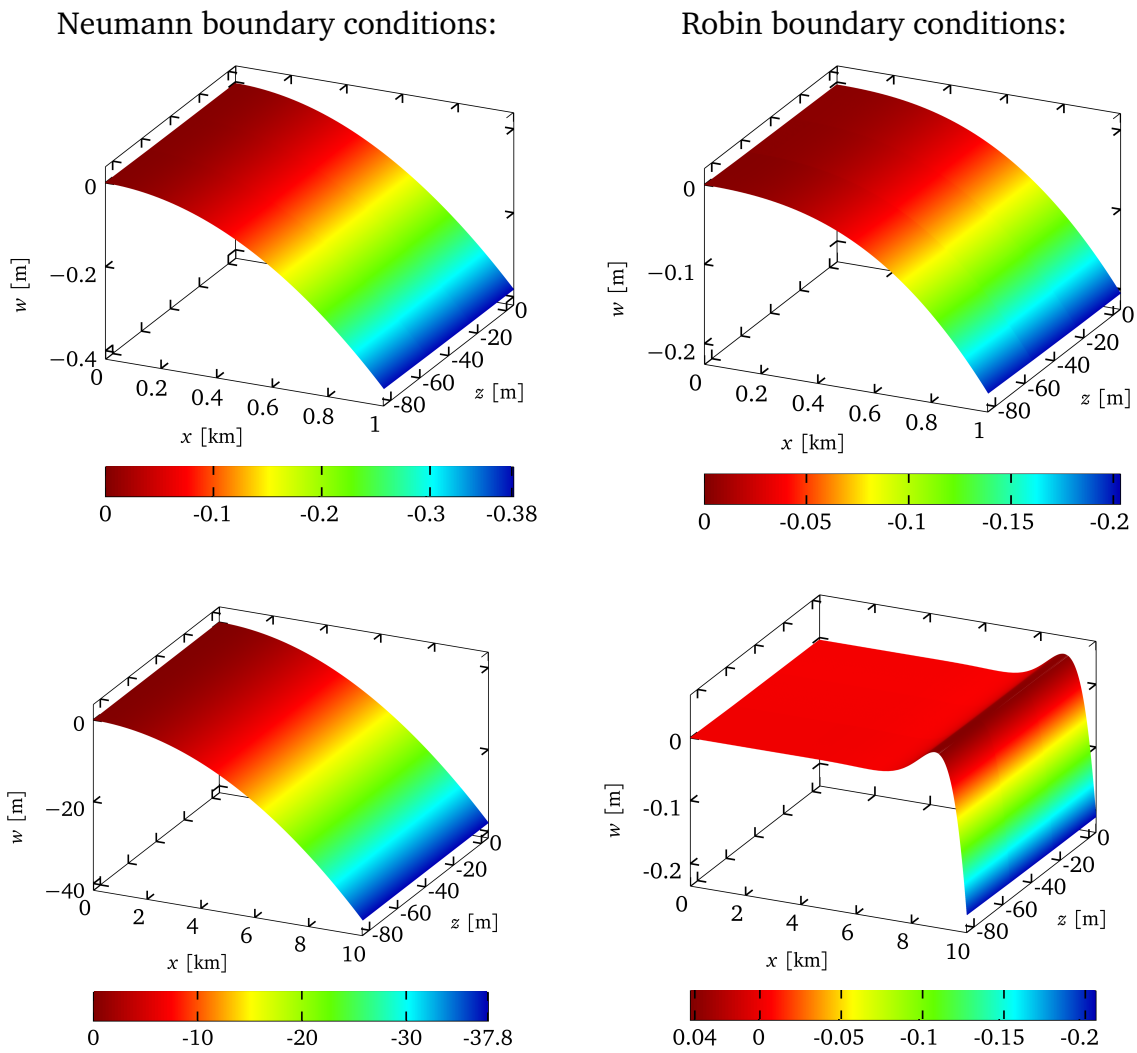

Figure 3.6: Neumann (left) and Robin (right) boundary conditions for an ice shelf length $L = 1\,\text{km}$ (top) and $L = 10\,\text{km}$ (bottom). The vertical displacement w is illustrated by different colors as well as by the deformation.

conditions, the maximum deflection at the ice front of $w(x = L) = -0.2\,\text{m}$ is preserved for both lengths. Reasonable vertical displacements result independent of the ice shelf length and a bell-shaped deformation (with positive vertical displacements up to 0.04 m) terminates the buoyancy equilibrium. In the vicinity of the ice front this special deformation arises due to the frontal sea water pressure. For a length of 1 km, the deflection is not completely developed and thus the outcome depends on the inflow boundary. To avoid this problem, a study that ensures length independence of all required quantities is presented in Section 4.2. Therein, further results also show other parameter relations.

The only difference of the 3d and the 2d model is the existence of two more boundaries on the sides in the lateral direction. In the left image of Fig. 3.5, the no-slip conditions mean that the ice is frozen at the lateral boundaries to for example valley walls. Dirichlet boundary conditions are applied and $u = v = 0$ holds for the system

to be statically determined. Still, the ice shelf has the possibility to react on geometry changes by the balance of buoyancy equilibrium as the displacement w in the thickness direction is unconstrained.
For a comparison of 2d with 3d results, it is useful to model corresponding boundary conditions for both cases. This is achieved by a 2d cross section in the middle of a sufficient wide 3d ice shelf. Additionally, the movement in flow direction has to be unconfined at the side boundaries. In this special case, only the condition $v = 0$ remains on the side boundaries in order to describe the same loading situation in the 3d model as for the 2d plane strain case.

Boundary Conditions for Finite Deformations

For finite deformations, all equations and boundary conditions have to be formulated either in the reference or current configuration. In this work the former configuration is selected based on the unchanged mesh and the known normal vectors as already mentioned in Section 2.7.3. The difficulty for the formulation in the current configuration is that a degeneracy of the mesh may be possible due to the viscous ice flow. In addition, the normal vector in the current configuration must not be computed in each time step to formulate the boundary condition $p_{\mathrm{sw}}\boldsymbol{n}$ in a rate-dependent material model. Based on Nanson's formula eq. (2.8) the pressure condition in the reference and current configuration are related by

$$p_{\mathrm{sw}} J \boldsymbol{F}^{-T} \boldsymbol{N} = p_{\mathrm{sw}} \boldsymbol{n}. \tag{3.6}$$

The pressure conditions eq. (3.3) and eq. (3.5) are valid in this context and hence assumed for p_{sw}. In consequence of the involved deformation gradient, the boundary conditions are formulated dependent on the actual geometry. In addition to that the weight is consequently updated by

$$f_z = -\rho_0 \, g = -J \rho_{\mathrm{ice}} \, g. \tag{3.7}$$

The effect on the vertical displacement w is discussed in Section 7.2. There the comparison of the upper and lower surface position after 30 years provides crucial differences when using a viscoelastic model for finite or small deformations.

3.4 Initial Conditions for Finite Deformations

In addition to the boundary conditions, the material assumptions valid for the model expecting small deformations have already been transferred to the concept of finite deformations, cf. Section 2.7.3. However, one basic requirement is not regarded until now and discussed in the following. In the approach for small deformations the volume change is assumed to occur only due to elasticity, while a viscous volume change is excluded. Hence, the viscous deformation is considered incompressible. With the application of suitable initial conditions the incompressibility con-

dition $\operatorname{tr}\left(\dot{\boldsymbol{\varepsilon}}_{\mathrm{v}}\right)=0$ leads to the disappearance of the trace of the viscous strain tensor $\operatorname{tr}\left(\boldsymbol{\varepsilon}_{\mathrm{v}}\right)=0$. This requirement is automatically achieved by initial values of zero for the internal variable $\boldsymbol{\varepsilon}_{\mathrm{v}}$. In fact, this requirement is physical-based due to the vanished viscous deformation at the beginning of the simulation. Furthermore, the second introduced possibility to derive the stress-strain relation for a Maxwell material in Section 2.5.3 guarantees that the incompressible viscous behavior is directly included in the material assumptions.
In order to also ensure the incompressibility of the internal variable $\boldsymbol{C}_{\mathrm{v}}$ for finite deformations, one of the following equivalent conditions has to be fulfilled

$$\det \boldsymbol{C}_{\mathrm{v}}=1 \qquad \Leftrightarrow \qquad \left(\det \boldsymbol{C}_{\mathrm{v}}\right)^{\cdot}=0. \tag{3.8}$$

At the start of the simulation, this is realized by the application of the second order unit tensor as an initial condition for the internal variable $\boldsymbol{C}_{\mathrm{v}}(t=0)=\mathbf{1}$. In addition, the incompressibility of the viscous strain tensor for finite deformations is immediately complied by the established equations of the material model as shown in the following. The evolution eq. (2.113) of the internal variable for the Saint Venant-Kirchhoff material using the lower Oldroyd rate ensures that

$$\dot{\boldsymbol{C}}_{\mathrm{v}}\boldsymbol{C}_{\mathrm{v}}^{-1}=\frac{\mu}{\eta}\left(\boldsymbol{C}\boldsymbol{C}_{\mathrm{v}}^{-1}-\frac{1}{3}\operatorname{tr}\left(\boldsymbol{C}\boldsymbol{C}_{\mathrm{v}}^{-1}\right)\mathbf{1}\right). \tag{3.9}$$

To derive the incompressible viscous behavior of ice with respect to eq. (3.8), the trace of eq. (3.9) is of interest

$$\operatorname{tr}\left(\dot{\boldsymbol{C}}_{\mathrm{v}}\boldsymbol{C}_{\mathrm{v}}^{-1}\right)=\frac{\mu}{\eta}\left(\operatorname{tr}\left(\boldsymbol{C}\boldsymbol{C}_{\mathrm{v}}^{-1}\right)-\frac{1}{3}\operatorname{tr}\left(\boldsymbol{C}\boldsymbol{C}_{\mathrm{v}}^{-1}\right)\operatorname{tr}(\mathbf{1})\right)=0. \tag{3.10}$$

Hence, it is obtainable

$$\begin{aligned}\operatorname{tr}\left(\dot{\boldsymbol{C}}_{\mathrm{v}}\boldsymbol{C}_{\mathrm{v}}^{-1}\right)&=\operatorname{tr}\left((\dot{\boldsymbol{F}}_{\mathrm{v}}^{\mathrm{T}}\boldsymbol{F}_{\mathrm{v}}+\boldsymbol{F}_{\mathrm{v}}^{\mathrm{T}}\dot{\boldsymbol{F}}_{\mathrm{v}})\boldsymbol{F}_{\mathrm{v}}^{-1}\boldsymbol{F}_{\mathrm{v}}^{-\mathrm{T}}\right)=\operatorname{tr}\left(\boldsymbol{F}_{\mathrm{v}}^{-1}\dot{\boldsymbol{F}}_{\mathrm{v}}\right)^{T}+\operatorname{tr}\left(\dot{\boldsymbol{F}}_{\mathrm{v}}\boldsymbol{F}_{\mathrm{v}}^{-1}\right) &(3.11)\\ &=2\operatorname{tr}\left(\dot{\boldsymbol{F}}_{\mathrm{v}}\boldsymbol{F}_{\mathrm{v}}^{-1}\right)=0 &(3.12)\end{aligned}$$

with the well-known properties: $\operatorname{tr}(\boldsymbol{A})=\operatorname{tr}\left(\boldsymbol{A}^{\mathrm{T}}\right)$ and $\operatorname{tr}(\boldsymbol{A}\boldsymbol{B})=\operatorname{tr}(\boldsymbol{B}\boldsymbol{A})$ for arbitrary second order tensors $\boldsymbol{A}$ and $\boldsymbol{B}$. An important alternative expression for the rate of the viscous deformation is thus established by $\operatorname{tr}\left(\dot{\boldsymbol{F}}_{\mathrm{v}}\boldsymbol{F}_{\mathrm{v}}^{-1}\right)=\operatorname{tr}\left(\boldsymbol{l}_{\mathrm{v}}\right)=0$.
This results in the following condition for an incompressible viscous strain rate tensor $\overset{\triangle}{\boldsymbol{\Gamma}}_{\mathrm{v}}$:

$$\operatorname{tr}\left(\overset{\triangle}{\boldsymbol{\Gamma}}_{\mathrm{v}}\right)=\frac{1}{2}\left(\operatorname{tr}\left(\boldsymbol{l}_{\mathrm{v}}\right)+\operatorname{tr}\left(\boldsymbol{l}_{\mathrm{v}}^{\mathrm{T}}\right)\right)=\operatorname{tr}\left(\boldsymbol{l}_{\mathrm{v}}\right)=0. \tag{3.13}$$

As already discussed above suitable initial conditions lead to an incompressible viscous strain tensor $\boldsymbol{\Gamma}_{\mathrm{v}}$. Furthermore, it is possible to show that

$$\left(\det \boldsymbol{C}_{\mathrm{v}}\right)^{\cdot}=2\det \boldsymbol{F}_{\mathrm{v}}\left(\det \boldsymbol{F}_{\mathrm{v}}\right)^{\cdot}=2\det \boldsymbol{F}_{\mathrm{v}}\det \boldsymbol{F}_{\mathrm{v}}\operatorname{tr}\left(\boldsymbol{l}_{\mathrm{v}}\right)=0 \tag{3.14}$$

with the help of

$$\det \boldsymbol{C}_{\mathrm{v}} = \det\left(\boldsymbol{F}_{\mathrm{v}}^{T}\boldsymbol{F}_{\mathrm{v}}\right) = \det \boldsymbol{F}_{\mathrm{v}}^{T} \det \boldsymbol{F}_{\mathrm{v}} = \det \boldsymbol{F}_{\mathrm{v}} \det \boldsymbol{F}_{\mathrm{v}}. \tag{3.15}$$

Additionally, an analog derivation of the known relation $\dot{J} = J\mathrm{tr}(\boldsymbol{l}) = \det \boldsymbol{F}\mathrm{tr}(\boldsymbol{l})$, cf. textbooks on nonlinear continuum mechanics such as Holzapfel (2001), results in the analog relation

$$\left(\det \boldsymbol{F}_{\mathrm{v}}\right)^{\cdot} = \det \boldsymbol{F}_{\mathrm{v}}\mathrm{tr}\left(\boldsymbol{l}_{\mathrm{v}}\right). \tag{3.16}$$

For all other material models of finite viscoelasticity introduced in this work the above derivation is realizable in a similar way. In summary, the Maxwell material model for small as well as finite deformation contains the incompressible viscous behavior of ice without the consideration of further equations.

3.5 Finite Element Implementation

Numerical solutions of differential equations in two and three dimensions are developed in this work using finite element methods (FEM). Implementation ideas and applications are described in detail in many books such as Hughes (2000), Wriggers (2008), Zienkiewicz et al. (2013) or Zienkiewicz et al. (2014a,b). The basic idea is to formulate the boundary value problem in a variational or weak form to reduce continuity requirements. Afterwards, finite elements are introduced to divide the continuous domain, for instance of an ice shelf, into a finite number of subdomains. In this spatial discretization, the differential equations are rewritten into a finite dimensional set of equations for the discrete nodal unknowns. These equations are then solved using the commercial finite element software COMSOL[1]. The nodal unknowns are the displacement vector $\boldsymbol{u}$ as well as the internal variables $\boldsymbol{\varepsilon}_{\mathrm{v}}$ or $\boldsymbol{C}_{\mathrm{v}}$ if necessary. To get their global distribution, the unknown field is interpolated by admissible shape functions between the respective nodal values of each finite element. Thus, approximations of the desired quantities are obtained in the whole domain. The accuracy of these results is affected by the element size and the shape functions. In this work, only fundamental principles of the finite element methods are applied without problem-related extensions. Because of the wide use of finite element methods, a more precise derivation of this approach is omitted. The reader is referred to get detailed descriptions in one of the various textbooks on this subject. Nevertheless, the features specifically applied to model ice shelf dynamics in the context with finite elements are mentioned below. The system of coupled differential equations consists of the balance of linear momentum eq. (2.57) or eq. (2.52), the kinematic relation eq. (2.55) or eq. (2.10), and the material equations Section 2.5 or Section 2.7.3 for small or finite deformations respectively. The variational form of these equations can be looked up for instance in the books of Zienkiewicz et al. (2013, 2014). The 2d ice shelf geometry is discretized using triangular elements, while tri-

[1] www.comsol.com

angular prism elements are applied for the 3d domain. The mesh is adapted to the particular application and depends on material models and geometric challenges. Hence, the mesh used is described at the beginning of each chapter presenting results. If a mesh convergence study leads to considerable characteristics, these effects are shown there. Four noded quadrilateral elements are also tried out. However, this spatial discretization reacts stiffer and relatively small elements are required to get the same result quality as for the triangular mesh. Consequently, the mapped mesh is not part of this work.
In general, the Lamé constant λ is infinite for a purely incompressible problem with $\nu = 0.5$ and locking of elements can occur for linear shape functions. If fewer integration points of the shape functions are used, this artifact will disappear. In this case, hour-glassing can happen as bending deformations are possible without additional forces and a stabilization of this issue is necessary. To overcome these problems, a mixed formulation with the pressure as an additional unknown is commonly applied in laminar flow models of ice sheets. In this work, Lagrange shape functions of quadratic polynomial order are used to approximate the displacements $\boldsymbol{u}$. The internal variables $\boldsymbol{\varepsilon}_{\mathrm{v}}$ or $\boldsymbol{C}_{\mathrm{v}}$ are related to spatial derivatives of the displacements and their suitable shape functions need to be one polynomial order less. In consequence, all internal quantities are approximated by linear Lagrangian shape functions. The convergence of ν close to 0.5 leads to sufficient results as locking is prevented by the use of quadratic shape functions for the displacements. Additionally, a comparison of the results obtained in this work to the one of the laminar flow results is done in Section 5.2.
In order to solve the large sparse system of equations that arises from the finite element method, the direct solver MUMPS (MUltifrontal Massively Parallel sparse direct Solver), which includes row reduction, is used to solve the problem. This solver was developed by the French group of Amestoy in the year 1998. For more details see Amestoy et al. (2000). Later on, several parameter studies are performed by the help of the computation tool MATLAB[2], which has an application interface to COMSOL. The rate-dependent viscous and viscoelastic flow of ice requires a time integration in addition to the spatial discretization. The backward differential formula, an implicit integration scheme, is utilized to solve the initial value problem by a Newton-Raphson method. This method evaluates the algebraic equation caused by the implicit approach. The most commonly used backward differential formula of first order conforms to the backward Euler method. Finally, time stepping is auto-controlled by the time-dependent solver of COMSOL.

[2] www.mathworks.com

4 Linear Elasticity

The field distributions that result from the elastic or viscous material model are discussed separately before the impact of viscoelasticity is analyzed. Thus, the sole effect of each material approach on crucial quantities inside the ice shelf is demonstrated and subsequently the combined viscoelastic behavior is comprehensible. To understand the process of small-scale calving, stress and strain states are relevant. Once a critical bound is exceeded, these values will lead to calving events without preexisting cracks. Until now only a few studies dealt with explicit values for crack initiation and propagation, because of the lack of in situ measurements. Furthermore, the load situation is hard to recover in laboratory tests. For instance, Pralong (2005) on the basis of Hayhurst (1972) suggested a critical stress value of $\sigma_{\text{crit}} = 330\,\text{kPa}$ for consolidated ice. Surface crevasses likely occur between $90 - 320\,\text{kPa}$ which is stated by Vaughan (1993). As an upper stress bound, "instantaneous failure of full-density ice is expected at stresses of around 1 MPa" (Vaughan et al., 2012). Hence, the initiation of surface and bottom crevasses and especially iceberg calving will occur somewhere in between these values. In the following, absolute values and their dependencies on geometric and material parameters lead to estimations of possible reasons for calving. In these studies, the values given above are available benchmarks to assess the risk originating from the examined quantities.
Stress fields of a linear elastic material at a certain time t depend only on the deformation state at this time and not on the history of the deformation. The stress state is constant (rate-independent) for a fixed system and changes only based on geometry or parameter variations. In consequence, elastic stress and strain responses are considered independent of time. In the load situation of an ice shelf, the purely elastic strain distribution is too small to reach a crucial situation. In addition, the strain state develops similarly to the stress distribution based on the linear deviatoric stress-strain relation. Hence, only stress states are considered in this chapter. The influence of the strain state becomes more important in the next chapters in which the viscosity lead to an increase of the longitudinal spreading. The consequent growth of the horizontal strain suggests specifying critical strain values, too.

4.1 Three-Dimensional Model

The 3d ice shelf is introduced in Fig. 3.5 (left) and the stress state in flow direction σ_{xx} is shown in Fig. 4.1 for five cross sections over the whole width. The ice shelf has a constant thickness of $H = 100\,\text{m}$, a length of $L = 5\,\text{km}$ and a width

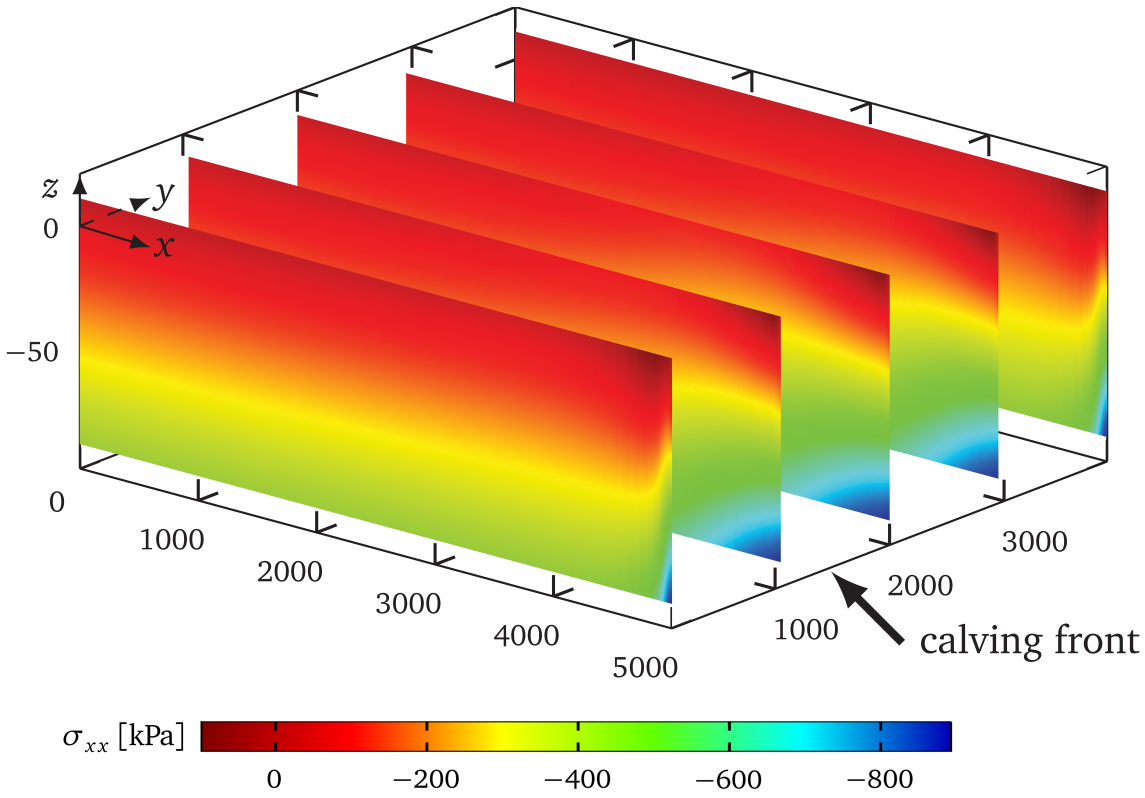

Figure 4.1: 2d cross sections of the stress state in flow direction σ_{xx} influenced by the bending moment of the water pressure at the ice front.

of $B = 4\,\text{km}$. The domain is discretized with triangular prism elements, refined in the vicinity of the calving front (arrow in Fig. 4.1) and a fixed number of 5 elements in the thickness direction. This spatial discretization induces over one million degrees of freedom. The mesh was illustrated in Trost (2013) and convergence studies as well as consequences of different mesh types for instance quadrilateral elements with four nodes were investigated. In general, the mesh resolution for this linear elastic problem is rather trivial as the material description, the external load, and the geometry are simple. In Fig. 4.3 an exemplary grid is depicted of the more precisely studied 2d case. To compute the stress distribution in Fig. 4.1 material values for consolidated ice are assumed, i.e. Young's modulus $E = 9\,\text{GPa}$, Poisson's ratio $\nu = 0.325$, a density of ice $\rho_{\text{ice}} = 910\,\text{kg/m}^3$ and sea water $\rho_{\text{sw}} = 1028\,\text{kg/m}^3$. Effects of divergences of these so-called reference parameters and their possible ranges for ice are discussed in the next section. The stress situation near the ice front in Fig. 4.1 reflects the impact of the bending moment caused by the boundary perturbation at the ice margin. Tensile stresses occur in the frontal part near the upper surface (darkly red) and compression mainly in the part below the water level. The highest tensile stress is directly located at the upper surface within a certain distance to the calving front. The influence of the disturbance at the ice front declines with the enlargement of the distance to this boundary. Hence, the stress state is only affected by the bending moment in the vicinity of the calving front and it is sufficient to consider the processes in this region.

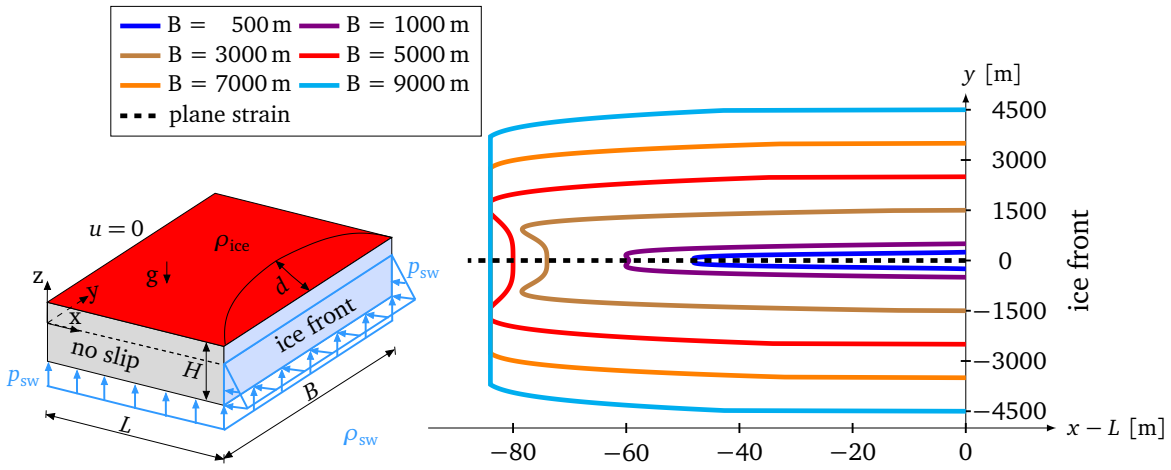

Figure 4.2: Bird's-eye view of the distance from the maximum tensile stress $\sigma_{xx}^{\max}$ to the calving front at the upper surface for different widths B.

In width direction, the stress distributions in the middle of the ice shelf are quite similar. Differences obviously occur near the lateral margins, where the ice is constrained by the boundary conditions on the side. In order to determine their reach, the FEM calculations are performed for different widths B. Of utmost interest is the behavior of quantities that have an influence on small-scale calving. The stress in thickness direction σ_{zz} mirrors the hydrostatic ice pressure and is almost unaffected by the bending moment at the ice front. In addition, the normal stress σ_{yy} and all shear stresses of the grounding line or lateral boundaries vanish for the area of investigation located in the center of an ice shelf. For calving caused by the boundary perturbation at the ice front, these stresses are hence insignificant. More critical is the maximum value of the stress in flow direction $\max(\sigma_{xx})$ denoted with $\sigma_{xx}^{\max}$ and its position. Both highly depend on the boundary disturbance and the position of the highest tensile stress is equivalent to the most probable location of the next calving event. As already mentioned before, the maximum stress occurs at the upper surface marked in red for the model setup at the lower left in Fig. 4.2. The parameter d corresponding to the distance between the maximum tensile stress and the ice front is schematically illustrated. The evaluation of this distance at the upper surface is shown on the right of Fig. 4.2 for different widths B. Obviously, the position of the maximum stress is influenced by the lateral expansion until a certain width is reached. In the regarded case this width is $B = 7$ km. For wider ice shelves the processes in the middle do not notice prescribed constraints at the sides and hence the state of plane strain is attained, see the black dashed line. This width independence is mainly affected by the thickness of the ice shelf due to larger induced stresses that occur in a greater distance to the ice front, see Section 4.2. If the width is too small ($B < 7$ km for $H = 100$ m), the results will be constrained by side effects and the distance d is not completely developed. Consequently, the position of the maximum tensile stress moves more and more to the ice front. In this situation, the plane strain model fails to describe the states inside the ice shelf. On the one hand, no-slip

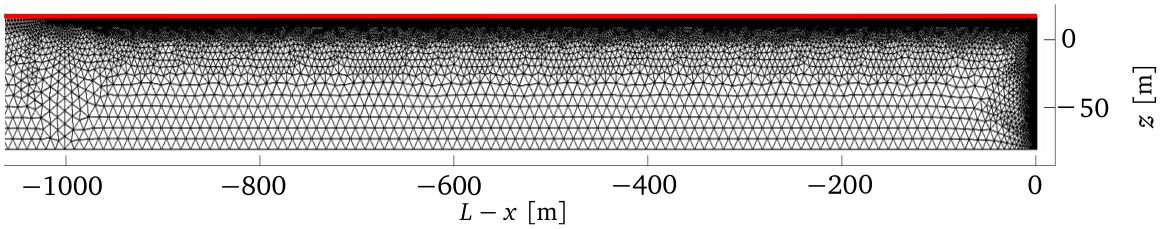

Figure 4.3: The spatial discretization of the 2d model refined at ice front as well as at the frontal part of the upper surface where the maximum tensile stress occurs.

boundaries at the side are an extreme case of ice frozen to walls. On the other hand free slip boundaries for instance with a small water film between ice and rock lead to a constant distance d over the entire width. Often conditions in between these extreme situations appear in the case that the ice shelf is bounded by valley walls. In contrast when the ice shelf is surrounded by the ocean, the water pressure leads to additional boundary disturbances from the side similar to the ice front. The latter case is discussed in Section 4.2.2 for the example of the Ekström Ice Shelf. Anyway, in Antarctica most ice shelves exceed horizontal extensions of several kilometers and therefore a 2d plane strain model is sufficient to compute the effect of critical state quantities on calving. In the following, the 2d model introduced in Fig. 3.5 (right) is supposed to highlight significant parameters by the consideration of its stress state and small-scale calving position. A statement about the time between two calving events is not possible based on the rate-independent elasticity. This is an issue treated in the viscous and viscoelastic material models later on.

4.2 Two-Dimensional Model

For the 2d model, the plane strain state is substantiated. Consequently, the spatial discretization in width direction drops out and computational costs are reduced. The mesh of the remaining 2d domain is illustrated in Fig. 4.3. This grid consisting of triangles has the maximum edge length of 10 m for all elements. Additionally, the mesh is refined to a maximum element size of 1 m at the ice front and at the upper surface within the first kilometer from the front. In this refined part, the most interesting quantities for small-scale calving reach their maximum values. As an outcome, this mesh results in 215 942 degrees of freedom for the thickness $H = 100\,\mathrm{m}$ and the length $L = 5\,\mathrm{km}$. Mesh convergence studies indicate that a coarsening of the mesh for a purely elastic problem is possible without the loss of result quality. However, this kind of spatial discretization is also used for the viscous and the viscoelastic model in which this fine resolution is needed. The additional computation time of the nonessential elements is quite small for the rate-independent elastic model. In particular, identical meshes are applied for all models that assume small deformations to get valid comparisons of the results from different material models. In this section, parameter studies are shown to illustrate the dependence of the stress states on geometry and material assumptions. By means of these investiga-

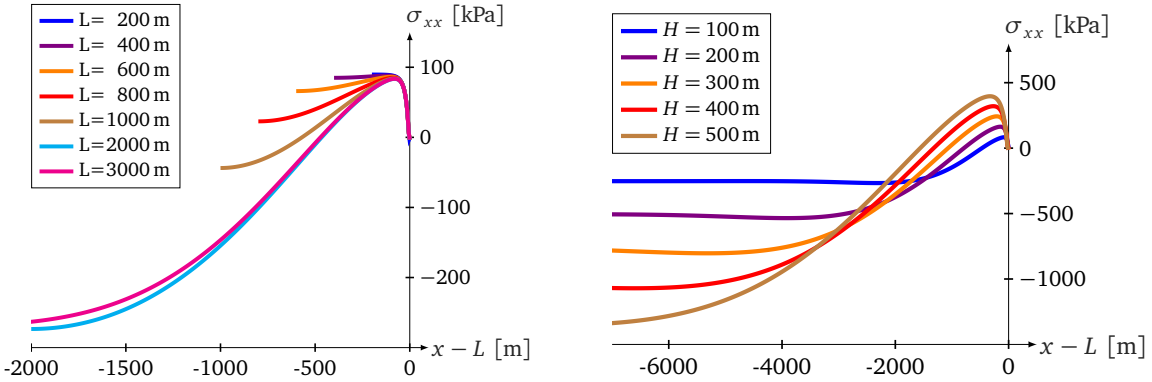

Figure 4.4: Stress states in flow direction at the upper surface over the negative distance to the calving front dependent on length L (left) and thickness H (right).

tions the importance of different variables to increase stresses to critical points are demonstrated. Afterwards the results are challenged and verified by the use of well-known outcomes for 1d beams. To discuss the difference to measured geometries, two cross sections of the Ekström Ice shelf, East Antarctica, are also examined and their stress states are compared to those with a constant thickness. At the end, the influence of frontal melting and preexisting bottom crevasses is also considered.

Influence of Geometric Parameters

All outcomes of the rate-independent linear elastic material in this chapter are computed by a stationary solver. In the previous section, the results depend on the width until a certain spreading is reached. This effect also occurs for different lengths L as depicted in Fig. 4.4 (left). The plot contains the stress distribution in flow direction at the upper surface (marked red in Fig. 4.3) in the vicinity of the ice shelf front. Similarly to the already shown 3d state, the maximum tensile stress is as well reached at the surface for the plane strain setting. At this specific boundary, the most critical parameters for calving are developed and hence only results on the upper boundary are subsequently examined.
Based on the vanishing traction prescribed at the freeboard and the absence of loads in z-direction at the entire ice front, the shear stress σ_{xz} and the stress in flow direction σ_{xx} are zero. The consequent boundary condition at the upper right corner causes bell-shaped curves of the stress component σ_{xx} at the surface, which achieve the value zero at the ice front while the maximum stress is located at a certain distance. The length of the computational domain varies from 200 m to 3 000 m in Fig. 4.4 (left) and all other parameters are constrained to their reference values given in Section 4.1. Obviously, the bell-shaped stress states in Fig. 4.4 (left) differ for different lengths L until the ice shelf exceeds a sufficient extent for a constant thickness H. The following analysis shows that the freeboard thickness, the size of the traction-free part above sea level, mainly influences the stress maximum. Hence, the magnitude and the location remain almost constant for different lengths as the

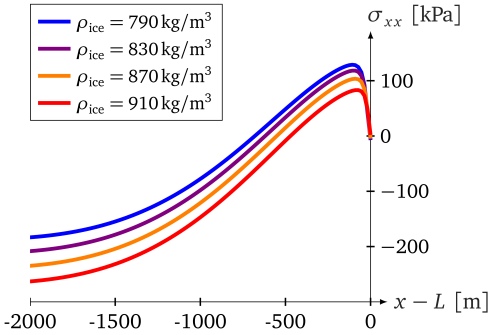

Figure 4.5: Stress in flow direction at the upper surface dependent on the mean ice density ρ_{ice}.

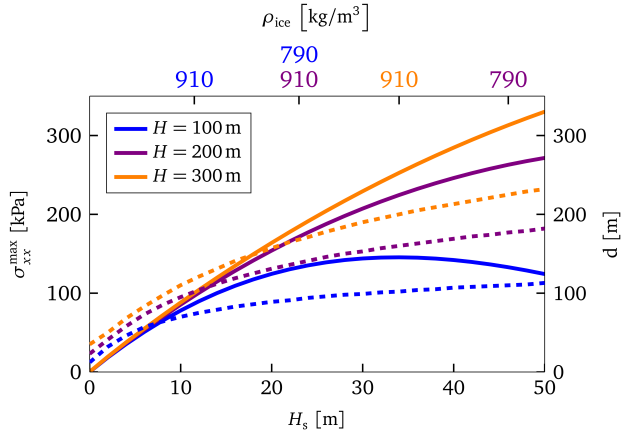

Figure 4.6: Maximum tensile stresses σ_{xx}^{max} (solid lines) and consequent distances d (dashed lines) over freeboard thicknesses H_s.

freeboard is unchanged. Nevertheless, the slope of the stress will only be length independent, if the extension in flow direction exceeds $20H$ verified by several simulation results. Minor differences also arise for $L = 2\,km$ compared to $L = 3\,km$, see Fig. 4.4 (left), however the stress states for $L > 3\,km$ coincide. To sum up, all impacts from further upstream will be insignificant, if the distance in the flow direction to the ice front is large enough. Vice versa the disturbance caused by the boundary conditions at the ice front only influences stresses in the vicinity of this boundary. For small-scale calving due to bending it is sufficient to compute the impact of the ice front perturbation near this boundary to obtain calving criteria and positions. To save computation time the length for the subsequent simulations is set to $L = 5\,km$ if not mentioned otherwise.

The next parameter study depicts different ice thicknesses and their significance on frontal stress states of ice shelves. Similar to the length dependence the results in Fig. 4.4 (right) describe the stress distribution in the vicinity of the calving front with respect to thicknesses ranging from 100 m to 500 m. The required ice shelf lengths are expanded to $30H$ to ensure results independent of the inflow. All other parameters are identical to Section 4.1. The maximum stress value and the area influenced by the calving front condition increase with the thickness. More precisely the maximum stress reaches 83 kPa for $H = 100\,m$ at a distance of $d = 0.78H$ away from the ice front to 396 kPa for $H = 500\,m$ with $d = 0.68H$. Hence, the position of the maximum differs about 14 %, while the absolute value of the maximum increases linearly with the thickness. However, it is not obvious whether the increase of the freeboard or the larger water pressure at the ice front or a combination of both leads to the rise in stress.

To clarify this the ratio of the freeboard to the ice draft, the ice expansion below the water surface, is modified. Based on different ice densities the buoyancy equilibrium and consequently the freeboard extent for a constant ice thickness change. Possible mean ice densities in Antarctic ice shelves ranges from $\rho_{ice} = 790\,kg/m^3$

to $\rho_{\text{ice}} = 910\,\text{kg/m}^3$. The influence of this density interval on the stress states is depicted in Fig. 4.5. The effect of this parameter is inversely proportional. Hence, a decrease of the ice density engenders a stress increase. More precisely a decreasing ice density entails a reduction of the ice draft $H_{\text{sw}} = H\rho_{\text{ice}}/\rho_{\text{sw}}$ and a rise of the freeboard thickness $H_{\text{s}} = H - H_{\text{sw}}$ at the same time. This results in an increase of the stress in flow direction at the upper surface despite the reduced resultant of the sea water pressure at the calving front. The obvious guess is that the maximum tension is rather related to the size of the freeboard and less to the magnitude of the water pressure. In fact, the maximum tensile stress in flow direction and its distance to the ice front enlarge almost linearly with the freeboard thickness in between the possible mean ice density interval $\rho_{\text{ice}} = 910\,\text{kg/m}^3$ to $\rho_{\text{ice}} = 790\,\text{kg/m}^3$, see Fig. 4.6. The solid lines in this figure depict the maximum tensile stress $\sigma_{xx}^{\max} = \max\left(\sigma_{xx}\right)$ over the freeboard extent for three different thicknesses, while the dashed lines correspond to the vertical axis on the right and denote the distance d between $\sigma_{xx}^{\max}$ and the ice front. Related to a decrease in ice density, the slope for the linear increase of the maximum stress is almost 4 kPa/m and for the distance the consequent slope is 1.6, both independent of different ice shelf thicknesses. In addition, Fig. 4.6 illustrates that the maximum stress and its position depend on the freeboard as well as the ice thickness. For instance, the freeboard $H_{\text{s}} = 23\,\text{m}$ for $H = 100\,\text{m}$ and an assumed ice density of $\rho_{\text{ice}} = 790\,\text{kg/m}^3$ leads to $\sigma_{xx}^{\max} = 133\,\text{kPa}$ and $d = 93\,\text{m}$. In contrast the thickness $H = 200\,\text{m}$ and $\rho_{\text{ice}} = 910\,\text{kg/m}^3$ result in $\sigma_{xx}^{\max} = 172\,\text{kPa}$ and $d = 139\,\text{m}$ for the same freeboard H_{s}. If the responses only depend on H_{s}, their values will not be different for the same freeboard dimensions but unequal thicknesses. In greater detail the maximum tensile stress is considered in Section 4.2.1 by the comparison to well-known results of the 1d beam.
The sea water density does also affect the stress distribution. By a decrease in density the ice draft H_{sw} increases due to buoyancy equilibrium. As a consequence, the freeboard thickness as well as the maximum tensile stress value decreases. The density $\rho_{\text{sw}} = 1028\,\text{kg/m}^3$ does not change significantly at the coastline of Antarctica and is not further considered here.

Influence of Material Parameters

For an isotropic elastic material only two independent material parameters exist, namely Young's modulus E and Poisson's ratio ν. In literature, Rist et al. (2002) and Schulson and Duval (2009) stated that Young's moduli depend on ice densities and hence vary from 5 GPa for snow/firn layers to almost 10 GPa for consolidated ice. From early on Young's moduli were determined in laboratory tests at relatively small specimens and Gammon et al. (1983) measured values around 9 GPa. This amount coincides with most citations and is used as reference value during this work. However, from field observations of for instance ice shelf responses to tidal flexure effective Young's moduli close to 0.9 GPa were concluded by Vaughan (1995). The difference of one order of magnitude raises the question which effective Young's modulus is reasonable for large bodies of deformed ice and is hence applica-

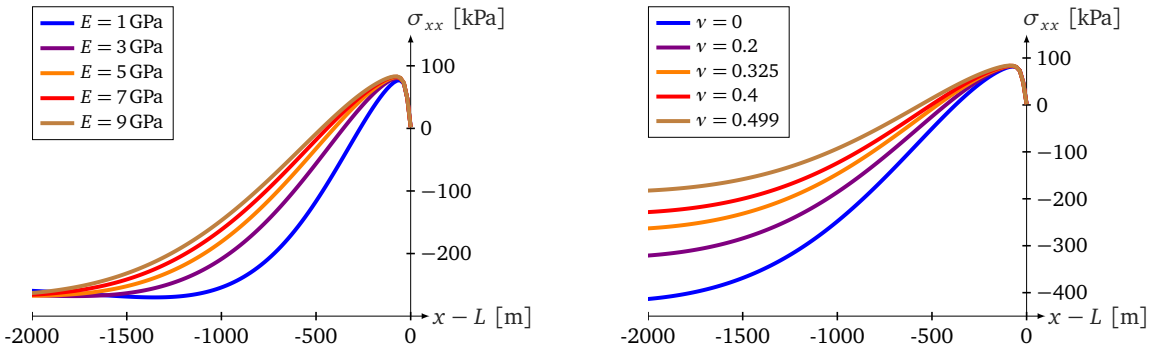

Figure 4.7: Stress in flow direction at the upper surface over the negative distance to the ice front dependent on the elastic material parameters Young's modulus E (left) and Poisson's ratio ν (right) for isotropic ice.

ble in models. Figure 4.7 (left) exhibits the stress state at the upper surface for different Young's moduli covering the mentioned range. To increase Young's modulus leads to a 1% variation in $\sigma_{xx}^{\max}$ and about 2% in the distance of this value to the ice front for the linear elastic material. Obviously, the influence on the most interesting quantities examined in this work is insignificant and thus a depth-dependent profile of Young's modulus as in Rist et al. (2002) is not further studied. Nevertheless, the area affected by the boundary condition at the calving front decreases considerably by a reduction of Young's modulus, see Fig. 4.7 (left). The stress response sufficiently far away from the ice front is again independent of different Young's moduli. A reasonable range for the second elastic constant ν specified in Schulson and Duval (2009) ranges from $\nu = 0.224$ to $\nu = 0.415$ for ice at a temperature of $-16°C$. This quantity only determines the rate-independent material answer based on pure elasticity and has no effect on the incompressible viscous creep investigated in the next section. In addition the extreme cases of $\nu = 0.499$ and $\nu = 0$ are also considered. The value $\nu = 0.499$ approximates an incompressible elastic material by defining ν close to 0.5, while the latter value is needed for comparison to the 1d beam in which no lateral contraction is allowed. The most commonly used value in literature is $\nu = 0.325$, which is the reference value for all previous and most of the subsequent studies. The results of different Poisson's ratios are depicted in Fig. 4.7 (right). Similar to variations of Young's modulus the stress maximum and its position remain unchanged by a variation of Poisson's ratio. In contrast to the results for different Young's moduli the stress values beyond the domain affected by the ice front condition vary. This behavior can be explained by the slight horizontal compression due to the calving front conditions, which lead to different vertical displacements for ν from 0.5 to 0. In particular, if no lateral contraction is assumed ($\nu = 0$), a compression in flow direction has no impact on the thickness direction.
In summary, the maximum tensile stress and its position fit to observations and existing literature for all investigated parameter studies. Reeh (1968) stated "that the stresses are greatest at a cross-section situated at a distance of about the thickness of the glacier from the front, and that the stresses are of a magnitude which very likely will lead to fracture, resulting in the formation of an iceberg".

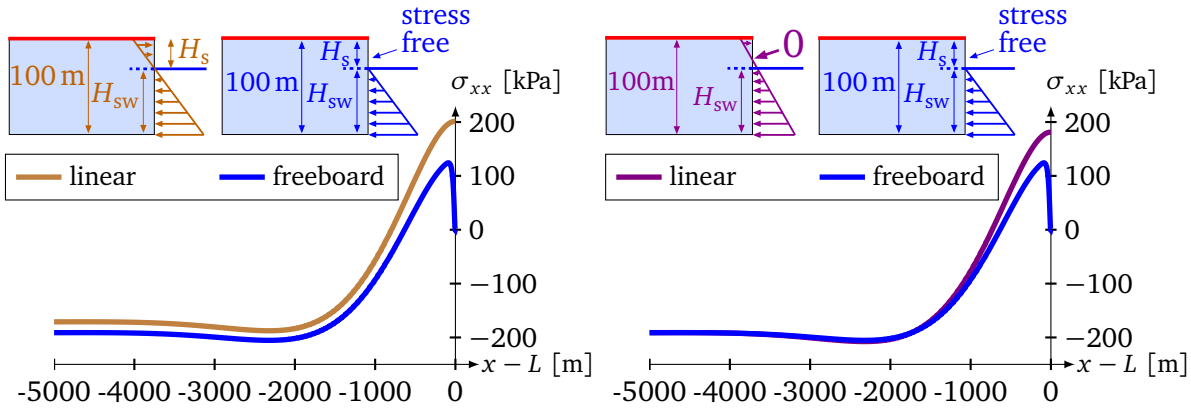

Figure 4.8: Computed stress states at the upper surface using a freeboard condition in comparison to linear traction requirements over the whole thickness with the same zero crossing at the water surface (left) or the same normal forces acting on the ice front (right) for an mean ice density $\rho_{ice} = 822\,kg/m^3$.

4.2.1 Confirmation of Stress States

In order to investigate the causes of the depicted stress states, first of all the effect of the freeboard is discussed. Therefore results of ice shelves with a freeboard condition are compared to those loaded by linear traction over the entire ice front. The latter is a fictional case for ice shelves but the consequent differences show the impact of the stress-free boundary above the water surface. Possible conditions are depicted by the brown and purple load situation distributed over the complete calving front for the schematic ice shelves shown in the upper part of Fig. 4.8. Slightly different is their traction-free point, which is at the water surface for the orange condition and at a certain distance above for the purple one. The motivation to choose these specific positions is discussed later on. In contrast, the blue condition in this figure models the part of the ice shelf that is lifted out of sea water by the freeboard condition.
In all three cases the maximum tensile stress occurs at the upper surface, marked in red in Fig. 4.8. Hence, the stress states in flow direction are again investigated at this boundary only. The colors of the plots match the ones of the boundary conditions. For both conditions applying load over the whole ice front the maximum stress is directly reached at the ice front. The ice density used in this case is reduced from the value of pure ice to a mean ice density of $\rho_{ice} = 822\,kg/m^3$. This lower value is determined by Lohse (2012) from field studies for the Ekström Ice Shelf considered in the next section. In addition this mean ice density better clarifies the stress differences from the brown to the blue curve. As a result the brown stress response is always larger than the blue one, while the purple one coincides with the blue curve beyond the area affected by the boundary disturbance, cf. Fig. 4.8. Explanations for these results are given by the well-known conclusions of beams in

the following.
Indeed the current problem has several similarities to a 1d beam loaded by boundary conditions and external forces perpendicular to its extent. For a model of ice shelves the sole external force is assumed to be gravity and the consequent ice weight is equated for a beam model by a Winkler foundation to ensure buoyancy equilibrium. This foundation is often symbolized in the literature by linear springs at the bottom and opposes the weight of the ice shelf. However, it is not possible to model the freeboard as a boundary condition of the beam. This difficulty was already elaborated in Christmann et al. (2016a) for a viscous beam. In Fig. 4.8 the importance to include the freeboard condition is also visible clearly for the linear elastic material. The maximum tensile stress is almost twice as high for the brown and purple stress curves in comparison to the blue one. Nevertheless, the knowledge of well-understood processes in beams is used to explain and verify the results in this work as often as possible.
First of all, the stress result in the domain unaffected by the boundary disturbance is similar to the response of a beam loaded by a centered normal force at the ice front. In a beam model the stress distribution attains the value $N/(H\tilde{b})$ with $\tilde{b}$ the width perpendicular to the x-, z-plane. In order to confirm this result for the 2d continuum model, the normal forces at the ice front are subsequently evaluated by

$$N = -\tilde{b} \int_{-H_{\mathrm{sw}}}^{H_{\mathrm{s}}} p(z)\,\mathrm{d}z. \tag{4.1}$$

These forces correspond to the negative resultant of the traction condition at the calving front and can be derived from fundamental principles for triangular loads. Starting with the left image of Fig. 4.8, the normal force N_{b} for the brown and N_{f} for the freeboard (blue) boundary condition are determined to

$$N_{\mathrm{b}} = -\frac{1}{2}\rho_{\mathrm{sw}} g\,\tilde{b}(H_{\mathrm{sw}}^2 - H_{\mathrm{s}}^2), \tag{4.2}$$

$$N_{\mathrm{f}} = -\frac{1}{2}\rho_{\mathrm{sw}} g\,\tilde{b} H_{\mathrm{sw}}^2. \tag{4.3}$$

The magnitude of the normal force N_{b} is obviously smaller than the one of N_{f} based on the second term in eq. (4.2). For a constant thickness of $H = 100\,\mathrm{m}$, the negative stress $N/(H\tilde{b})$ of the beam is larger for N_{b} than for N_{f}, cf. stress curves in Fig. 4.8 (left). To ensure an agreement of the stress curves for both conditions, the same normal forces have to act on the ice front, see Christmann et al. (2016a). For that purpose the absolute value of the normal force for the traction extended over the whole thickness needs to be enlarged. This is achieved by a shift of the traction-free position from the water level closer to the upper surface. The conse-

quent distance $z = \Delta H$ is established by the equalization of the normal forces

$$N_\mathrm{p} = -\frac{1}{2}\rho_\mathrm{sw} g \tilde{b} \left((H_\mathrm{sw} + \Delta H)^2 - (H_\mathrm{s} - \Delta H)^2 \right) \stackrel{!}{=} N_\mathrm{f} \tag{4.4}$$

$$\Rightarrow \Delta H = \frac{H_\mathrm{s}^2}{2H} = \frac{H}{2}\left(1 - \frac{\rho_\mathrm{ice}}{\rho_\mathrm{sw}}\right). \tag{4.5}$$

The slope of the purple traction is steeper than the blue one and the traction-free point is located 2 m above the water surface. For an ice density of $\rho_\mathrm{ice} = 910\,\mathrm{kg/m^3}$, the distance ΔH is reduced to 0.66 m and hence the difference for the brown and blue stress state is hardly visual. In Fig. 4.8(right) the normal forces are equal and as a consequence the magnitude of the stress in the domain unaffected by the boundary disturbance coincides. Validated for different thicknesses and densities, the analytical value $N/(H\tilde{b})$ differs around 0.5 % from the simulated stress of the 2d continuum for the special case $\nu = 0$. This value is in accordance with the assumptions for beams.

Beside the stress value located in the area unaffected by the boundary disturbance, the maximum tensile stress is also comprehensible based on beam responses. The load caused by the water pressure at the calving front is equivalent to an off-centered normal force acting at this boundary. Hence a bending moment M is induced additionally to the normal force N. In this case the stress is given by the superposition of both parts

$$\sigma_{xx} = \frac{N}{H\tilde{b}} + \frac{M}{I}\bar{z}, \tag{4.6}$$

see Gross et al. (2011). The coordinate $\bar{z} = z + H_\mathrm{s} - H/2$ originates in the middle of the ice thickness and points downwards. For the ice shelf the moment of inertia is denoted by $I = H^3\tilde{b}/12$. Furthermore the bending moment at the calving front correspond to

$$M = -\tilde{b} \int_{-\frac{H}{2}+H_\mathrm{s}}^{\frac{H}{2}} \bar{z}\, p(\bar{z})\, \mathrm{d}\bar{z}, \tag{4.7}$$

with the water pressure p acting in normal direction over the ice draft H_sw. To get the maximum stress at the upper surface, eq. (4.6) is evaluated at $\bar{z} = -H/2$. The relative difference of the stress response from the beam and the 2d model is on average 10 % for different geometric and material parameters. The maximum tensile stress of the beam is always lager than the one of the bell-shaped curve at the surface although equal normal forces and bending moments of the ice front condition are used.

In order to verify that this difference only occurs based on the lacking freeboard condition for the beam, the comparison of the two different methods is developed more precisely. The brown ice front condition of Fig. 4.8 (left) is accurately definable by the beam as well as the 2d continuum. So far, the bending moment of the calving front is assumed to be constant over the whole ice shelf. However, the buoyancy

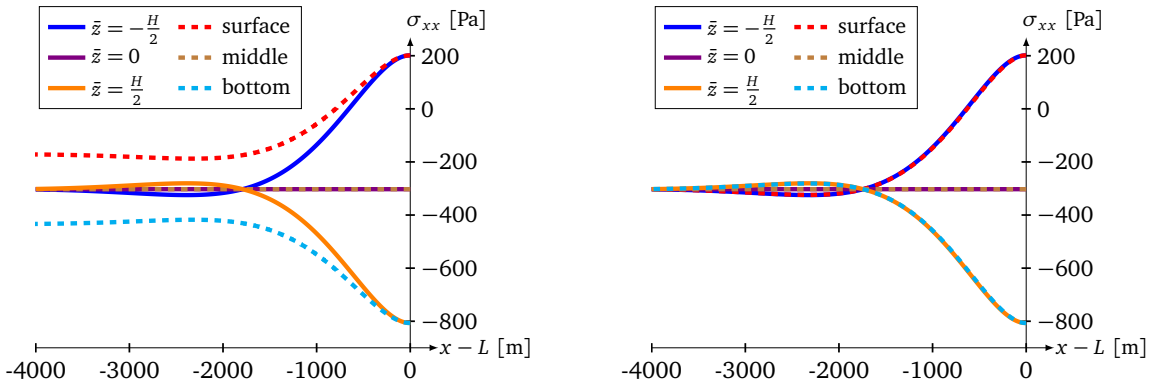

Figure 4.9: Stress state at the surface, in the middle and at the bottom of the ice shelf computed by beam model (solid lines) in comparison to the 2D model (dashed lines) for $\nu = 0.325$ (left) and $\nu = 0$ (right).

equilibrium lead to a compensation of this boundary disturbance within a certain distance to the front. The following beam equation

$$EIw^{IV}(x) - Nw^{II}(x) + \rho_{sw} g w(x) = 0 \tag{4.8}$$

with $(\cdot)^{II}$ or $(\cdot)^{IV}$ as the second or fourth derivatives with respect to space. In this equation the second summand denotes the normal force, while the third term describes the elastic foundation that contains the spring constant. The normal force can also be included in the boundary conditions, see Section 5.1.1. The consequent deflection and the bending moment $M = -EIw^{II}$ computable from eq. (4.8) depend on the horizontal coordinate x, for more details on beams and their analytical solution see Gasch et al. (2012). To insert the result in eq. (4.6) leads to the stress states depicted in Fig. 4.9 for the surface (blue solid line), the middle (purple solid line) and the bottom (orange solid line) of the ice shelf. In addition, the responses of the 2d model for the corresponding positions are also included in this figure by the dashed lines. On the left image, the stress state of both methods diverges at the surface as well as the bottom in the domain unaffected by the boundary condition. This is caused by the Poisson's ratio of $\nu = 0.325$ as already discussed above. The stress states coincide for $\nu = 0$, see Fig. 4.6 (right). In conclusion the linear elastic 2d model yield the same results as the beam model for conditions, which satisfy the assumptions of the beam theory. However, the accurate modeling of the freeboard condition as well as different Poisson's ratios is not possible with the beam model.
A remark on the frequently used first principal stress to establish a critical stress criterion is given here. This stress is computed by

$$\sigma_1 = \frac{\sigma_{xx} + \sigma_{zz}}{2} + \sqrt{\left(\frac{\sigma_{xx} - \sigma_{zz}}{2}\right)^2 + \sigma_{xz}^2}. \tag{4.9}$$

At the position of the maximum tensile stress at the upper surface, the normal stress σ_{zz} in thickness direction and the shear stress σ_{xz} are negligibly small com-

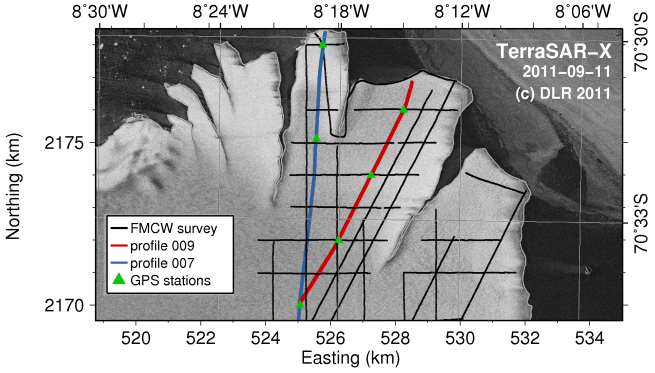

Figure 4.10: TerraSAR-X image of ice thickness measurements near the calving front of the Ekström Ice Shelf, see Lohse (2012).

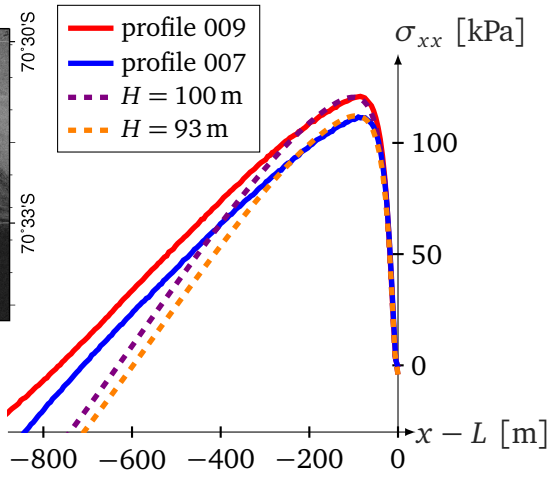

Figure 4.11: Stress state at the upper surface for the measured profiles.

pared to the stress σ_{xx} in flow direction. Hence, it holds

$$\Rightarrow \sigma_1 = \begin{cases} \sigma_{xx} & \text{if } \sigma_{xx} \geq 0 \\ 0 & \text{else} \end{cases} \tag{4.10}$$

and the maximum stress value as well as the position of this value coincides for the stresses σ_1 and σ_{xx}. A study of both quantities is thus unnecessary.

4.2.2 Ekström Ice Shelf

In Section 3.1 the calving of small icebergs is already illustrated using the example of the Ekström Ice Shelf for February 2011. In the following, the stress states at two cross sections of this ice shelf are compared to the previous results with constant thicknesses. During the Antarctic summer 2011/2012 ground-penetrating radar measurements were carried out of the area near the calving front up to the German research station Neumayer Station III. In Fig. 4.10 a TerraSAR-X scene depicts a part of this region where small-scale calving occurs. Thickness data acquired by measurements are available at all black lines. The reader is referred to Lohse (2012) for more detailed information. The red and blue line indicate two streamlines where measured geometries exist that are investigated subsequently. These profiles are located in the middle of different ice tongues with widths of almost 2 km and 4 km. In Section 4.1 the stress responses are only independent of the width if the ice shelf is wider than $B = 7\,\mathrm{km}$. However, the comparison of simulated stress states for measured and constant thicknesses is first of all relevant and thus plane strain conditions have to be expected. In contrast to the previous results shown for the 3d case the ice is not conditioned by rocks but by the ocean at the lateral boundaries. The bending moment caused by the ice front affects the stress states up to 1500 m from the ice front for $H = 100\,\mathrm{m}$, a thickness similar to the measured ice front thicknesses of both

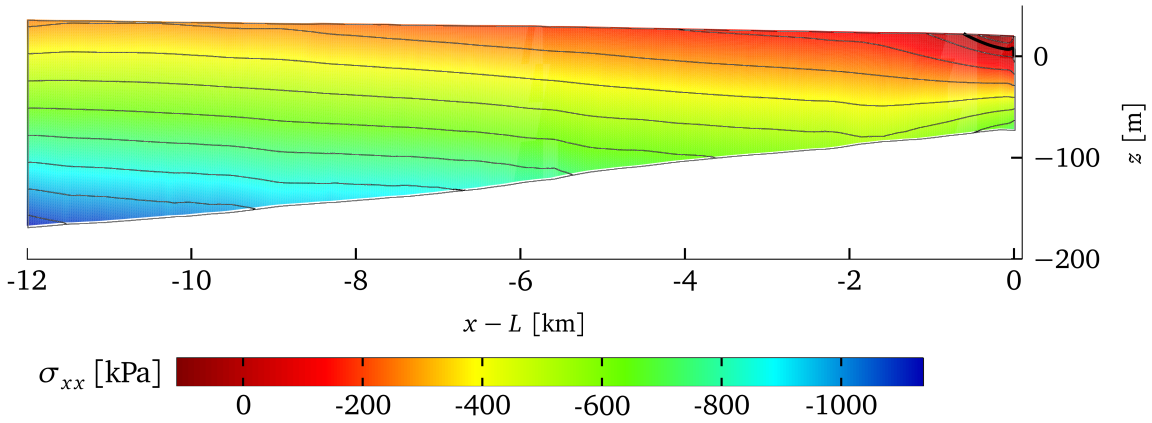

Figure 4.12: Stress in flow direction for a measured 2d geometry of the Ekström Ice Shelf (profile 009) with the transition from tension to compression denoted by the black line and additional contour lines of constant stress in gray.

profiles. In consequence, plane strain conditions are at least assumable for the wider ice tongue as for this case the effect of the lateral boundaries is insignificant in the middle of the tongue. In addition the calving events of Fig. 3.3 appeared just in this part of the ice shelf. For the smaller ice tongue superpositions of stresses based on the surrounding ocean on three sides of the most interesting area for calving should be investigated with the 3d geometry in future work.
Both measured geometries look like a ramp with a slight thickness increase of few hundreds of meters over several kilometers, see for instance Fig. 4.12. Figure 4.11 shows the bell-shaped stress distribution at the upper surface of profile 009 in red and of profile 007 in blue. The results for the measured geometries are computed with the reference values except for the inclusion of estimated ice densities. These are mean values over the thickness and vary from 798 kg/m^3 to 851 kg/m^3 to ensure buoyancy equilibrium. In addition, the stress states for $H = 93$ m and $H = 100$ m are included in Fig. 4.11. These constant values do not correspond to the ice thickness of the two profiles at the calving front but to an averaged value. This averaged thickness is obtained starting from the ice front up to 1500 m away from it. This distance is chosen based on the size of the domain affected by the bending moment of the boundary disturbance. It is obvious that these values mirror the maximum tensile stress and its position better than the result using the thickness at the ice front. This termination thickness is $H = 93$ m for the red profile 009. Hence the stress response of the frontal thickness can serve as a lower bound. Remarkably, the influence of the boundary perturbation decreases faster for the constant thickness than for the real geometry. However, this is explicable by the slight increase of thickness for the measured geometries as this fact induces larger stresses. More precisely the nearly linear slope of profile 009 is 9.3 m/km due to a thickness growth of 111 m over 12 km. For profile 007 the slope result in 10.3 m/km based on an increase of 155 m over 15 km. The geometry variation of the measured geometries is quite similar and thus the distance between their stress curves stays constant in the part that

is considered by Fig. 4.10. At a distance of 7 km from the front, the blue thickness extent and hence its stress response are smaller than the red ones based on the fact that the termination thickness of the blue profile is 7 m less.
Next Fig. 4.12 shows the stress distribution in flow direction within the red profile. In addition ten contour lines of constant stress (gray) as well as the specific line for $\sigma_{xx} = 0$ (black) are added in this plot. The stress in flow direction is larger than zero in the upper part near the ice front and decreases almost linearly to the bottom of the ice shelf. Most important the largest tensile stress is also located on the upper surface for the measured geometries.
The above discussion indicates that the results of a real ice shelf geometry differ only slightly from those with a constant thickness. Hence the conclusions of the parameter study also hold for the ice shelves in Antarctica. The computation using a constant thickness saves computation time and leads to sufficient results to estimate calving rates and positions. More precisely the distance of the maximum tensile stress from the ice front is $d = 89$ m for the red profile and $d = 85$ m for the blue one. In Fig. 3.3 the dimensions of small-scale calving are illustrated and the values for the smaller icebergs fit closely to the above-computed values. However, little larger icebergs occur in this image and a possible explanation for those is given in the next section.

4.2.3 Modified Geometry

Observations at some ice shelves show for instance cracks arising from the bottom, see Humbert and Steinhage (2011). In this case, an iceberg calves off as soon as the crack reaches the upper surface. Subsequently, reasons for this procedure are investigated. For a vertical calving front the water pressure at the termination boundary will rather lead to a closure than an opening of the bottom crevasse based on the load increased with depth. In order to model calving from bottom to top geometry variations are discussed, which force the formation and propagation of bottom cracks in the vicinity of the calving front. At the end of this section, effects of preexisting bottom cracks on the stress states are also discussed.
Directly after a calving event the ice front is vertical and the previous results consider this kind of boundary appearance only. In the following, the geometry of an advanced ice front is modeled by a modification of the calving front. Suitable to observations Orheim (1987) described ice fronts shaped like an under-water "belly" in consequence of melting processes, see Fig. 4.13. Its origin has this variation in the third mode of ice shelf melting identified by Jacobs et al. (1992). Seasonally warmer upper ocean water melts horizontal caves directly at the water surface and the surrounding ice is weakened. The maximum stress at the surface occurs above the end of the cave. As a result, small pieces of ice crumble away and underwater ”bellies“ will arise after some time, if the lower frontal edge of the ice shelf is slightly rounded due to melting. The impact of this additional change is investigated on its own afterwards. For now, the belly at the ice shelf front is modeled by half of an ellipse

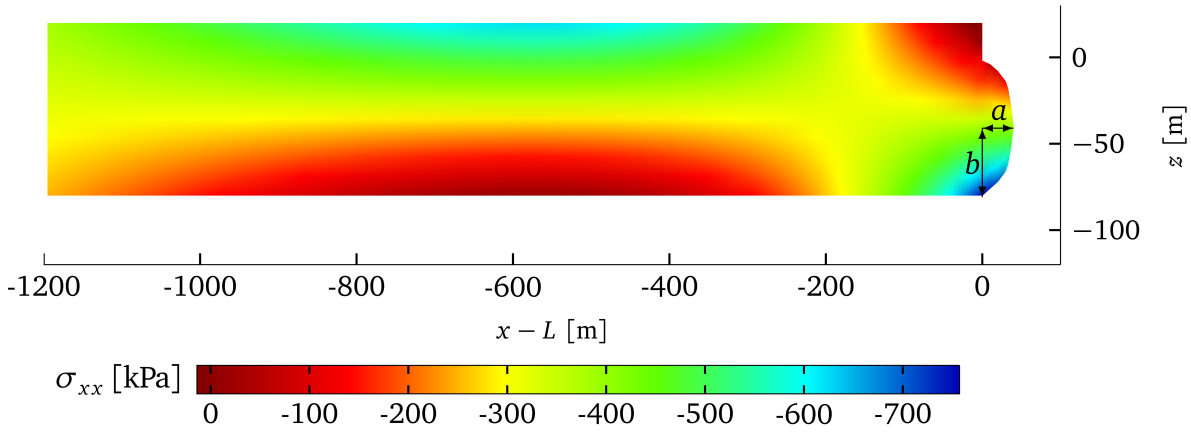

Figure 4.13: Stress distribution in flow direction of a modified geometry with an underwater "belly".

and the water pressure affects this modified boundary. The ice draft $H_{sw} = 2\ b$ is constant during all computations with the height of the ellipse b, $H = 100\,\text{m}$ and the mean ice density $\rho_{ice} = 822\,\text{kg/m}^3$ of the Ekström Ice Shelf. Figure 4.13 depicts the ellipse width a, which is the only variable quantity for this geometry modification. In this figure the stress σ_{xx} is plotted for an example of the consequent 2d geometry with $a = b$. This aspect ratio of $a/b = 1$ describes a semicircle. The deformed ice shelf of Fig. 4.13 is slightly bent upwards and the maximum tensile stress is no longer located in the upper part of the domain but at the bottom. It is no longer sufficient to consider only the stresses at the upper surface. The spatial discretization for the FE simulation is refined additionally at the bottom within the first 1000 m from the ice front. This refinement is similar to the one at the upper surface. While the maximum tensile stress σ_{xx}^{max} for a 100 m thick ice shelf with a vertical ice front occurs at $d = 0.78H$ at the upper surface, this maximum shifts to the bottom for a geometry with a sufficient large "belly". Its position moves further away from the ice front to $d_b = 6.7H$, cf. Fig. 4.13. An increase of the "belly" width a causes the stress at the bottom to rise from compressive to tensile stress for $a/b \geq 0.87$, while the tensile stresses at the upper surface decrease. Hence, this geometry modification involves the stabilization of the load condition at the surface based on the upward pressure of the "belly". If a critical stress bound for instance 330 kPa as suggested by Hayhurst (1972) is believed to cause a calving event, the width of the "belly" has to exceed half of the ice thickness H with an aspect ratio of $a/b = 1.26$. Also Wagner et al. (2014) stated "that once the foot reaches a critical length, the induced stresses are sufficient to cause calving". For smaller Young's moduli the width needs to be still larger to initiate and propagate cracks from the bottom. The lack of the rounded lower frontal edge leads to a faster increase of the stress at the bottom as the ice shelf bends further upwards to achieve buoyancy equilibrium. However, the slight melting at the lower edge is assumable as the viscous ice shelf flows several months to few years between different calving events.
Now impacts of melting at the lower frontal edge are solely analyzed. Two different

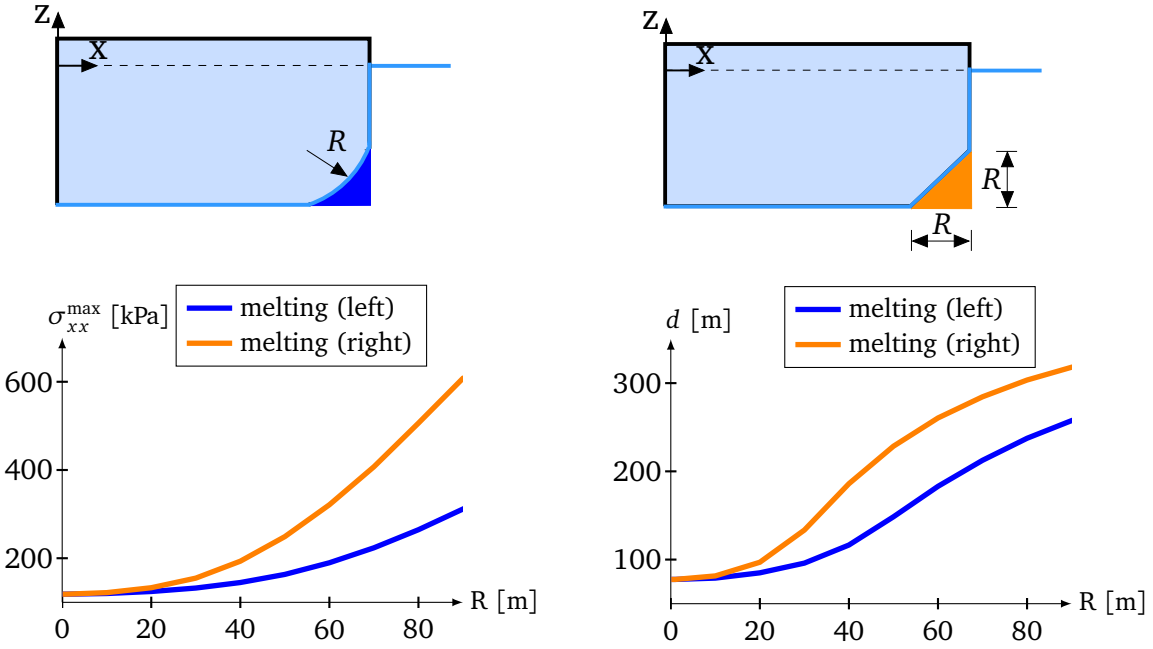

Figure 4.14: Two different kinds of melting at the calving front and their influence on the maximal tensile stress σ_{xx}^{max} (left) and its distance d to the ice front (right).

melting problems are investigated and depicted at the schematic ice shelves in the upper part of Fig. 4.14. The melted volume is half as large for the left case than for the right one. Both geometric modifications rise the maximum stress value at the surface and the proportion almost fit to the melted ice volume, see Fig. 4.14 (left). In order to determine small-scale calving events, the accurate knowledge of the ice shelf geometry at least for the part in the vicinity of the ice front is necessary. The stresses at the bottom do not increase for both geometric modifications as the buoyancy equilibrium leads to a downward bending of the anterior calving front area, which induces the stress increase at the upper surface. In both cases, a sufficient large melting at the frontal lower edge hence causes critical stress states for calving at the upper surface. Together with the stress increase the position of this stress maximum shifts further away from the ice front for both melting situations shown in Fig. 4.14 (right). In contrast to the ice loss at the surface, the position is still closer to the front for the melting at the bottom and thus for cracks starting from the top to the bottom.
This position of crack initiation at the surface varies with preexisting bottom structures. Their formation is for instance quite possible at the grounding line. A consequent drop of the upper surface in flow direction with some distance to the grounding line implies that the bottom structure moves downstream with the viscous ice flow, see for an example Humbert et al. (2015). The maximum tensile stress occurs directly above the crack tip at the upper surface as soon as the depth of the bottom structure is large enough. Obviously, the influence of this geometry modification gets larger by deeper gaps. The location of the maximum tensile stress is above the position of the bottom structure if this is sufficiently close to the ice shelf front. A

benchmark for this affected area is given by the distance $H(H_c - 1) - d$ with H_c as the depth of the crevasse and d as the distance between the maximum tensile stress of the intact ice shelf and the ice front. In fact, this is another sign that shows how important the precise geometry model is to obtain calving laws.
In conclusion, only in the case of an underwater "belly" wider than a semicircle ($a > b$) the position of the maximum tensile stress occurs at the bottom and increases to critical stresses for a constant ice thickness. This results from an upward bending caused by the ice loss in the upper part of the ice shelf. Its position is several ice thicknesses away from the ice front, which is a possible explanation for larger iceberg sizes of small-scale calving than for a vertical calving front. In this case the stress states at the upper surface are decreased even for relatively small geometry variations. In contrast, the pure melting at the bottom leads to crucial stresses for calving from the top to the bottom. The consequent increase of the iceberg size matches quite accurate with the slightly increased dimension of measured icebergs (Fig. 3.3). Iceberg calving is hence possible for homogeneous and crevasse-free surface structures in the vicinity of the calving front.

5 Linear Viscosity

The knowledge of the temporal evolution of stress and strain states in ice shelves is essential to assess the time between two calving events. The maximum stress and its position are determined for different geometries and material parameters in the linear elastic model. However, this material approach is rate- and thus time-independent and another material model is needed to obtain temporal evolutions of state quantities. For its long-term mode, ice is commonly assumed to behave like a purely incompressible viscous material. In literature this statement is based on a considerable number of investigations on long timescales, which include laboratory tests as well as field studies of ice shelves, ice sheets and glaciers. In order to evaluate the stress and strain states for a viscous ice flow, the viscous material equations (Section 2.5.2) instead of the elastic ones (Section 2.5.1) are implemented in a 2d finite element model in COMSOL.
In the following, a relevant selection of available incompressible viscous ice models is presented. On the one hand, a remarkable study was done by Reeh (1968). He transferred common methods of elastic beam theory to a linear viscous material. This material model was utilized to determine the time evolution of stress states and vertical deformations at the surface of ice shelves. On the other hand, current ice-sheet approaches solve for the velocities in incompressible laminar flow models with the pressure as an additional unknown. To prove the applicability of the viscous model presented in this work the obtained results based on the unknown deformations are compared to those given in the literature.

5.1 Viscous Beam Model

Reeh (1968) suggested a viscous material law based on the assumption that stress variations appear very slowly in the analyzed case. Hence, elastic responses of the ice are negligibly small and the well-known elastic beam model is adapted to the viscous case. Hooke's law implies the stress-strain relationship for the 1d linear elastic case and reads $\sigma = E\varepsilon$. The corresponding viscous equation $\sigma = 4\eta\dot{\varepsilon}$ leads to the stress-strain rate relation for a 1d linear viscous material. The viscous coefficient 4η is derived by the following consideration: The beam is studied under two-axial loading, namely gravity and tension, but no shear. The material law reads $\boldsymbol{\sigma}^D = 2\eta\dot{\boldsymbol{\varepsilon}}^D$, cf. eq. (2.66), with $\mathrm{tr}(\dot{\boldsymbol{\varepsilon}}) = 0$ for a 3d incompressible viscous fluid. A general hypothesis in beam theory assumes that there are no changes in the thickness and thus $\varepsilon_{zz} = \dot{\varepsilon}_{zz} = 0$. Hence, a combination of the traceless strain rate tensor and the

constant thickness results in

$$\dot{\boldsymbol{\varepsilon}} = \dot{\boldsymbol{\varepsilon}}^D = \begin{pmatrix} \dot{\varepsilon}_{xx} & 0 & 0 \\ 0 & -\dot{\varepsilon}_{xx} & 0 \\ 0 & 0 & 0 \end{pmatrix}, \tag{5.1}$$

which only takes the strain rate in flow direction into account. However, the stress tensor

$$\boldsymbol{\sigma} = \begin{pmatrix} \sigma_{xx} & 0 & 0 \\ 0 & 0 & 0 \\ 0 & 0 & \sigma_{zz} \end{pmatrix} \tag{5.2}$$

has to include a stress in thickness direction σ_{zz} to involve the ice pressure that increases with depth due to the weight of the ice. In consequence, the stress deviator is given by

$$\boldsymbol{\sigma}^D = \begin{pmatrix} \frac{2}{3}\sigma_{xx} - \frac{1}{3}\sigma_{zz} & 0 & 0 \\ 0 & -\frac{1}{3}\sigma_{xx} - \frac{1}{3}\sigma_{zz} & 0 \\ 0 & 0 & -\frac{1}{3}\sigma_{xx} + \frac{2}{3}\sigma_{zz} \end{pmatrix} \tag{5.3}$$

by the use of eq. (2.64). The insertion of this equation in the material law leads to

$$\frac{2}{3}\sigma_{xx} - \frac{1}{3}\sigma_{zz} = 2\eta\dot{\varepsilon}_{xx} \tag{5.4}$$

$$-\frac{1}{3}\sigma_{xx} - \frac{1}{3}\sigma_{zz} = -2\eta\dot{\varepsilon}_{xx} \tag{5.5}$$

$$-\frac{1}{3}\sigma_{xx} + \frac{2}{3}\sigma_{zz} = 0 \qquad \Rightarrow \sigma_{zz} = \frac{1}{2}\sigma_{xx} \tag{5.6}$$

and the equation $\sigma = 4\eta\dot{\varepsilon}$ is obtained by including eq. (5.6) in eq. (5.4). To compute the deflection w, the differential equation of an infinitely wide viscous beam on an elastic foundation is given by

$$4\eta I\dot{w}^{IV} + \rho_{sw} g w = 0 \tag{5.7}$$

similar to the elastic case, cf. Section 4.2.1.
Suitable boundary conditions, see eqs. (18), (19), (21), and (22) of Reeh (1968), are necessary to include the off-centered normal force of the calving front and presented in Section 5.1.1. In order to transfer the results to different glaciers, all variables are considered independent of dimensions. The dimensionless differential equation for a viscous beam was first given by eq. (17) in Reeh (1968). This viscous beam equation is solved for the vertical deflection w of an ice shelf with constant thickness H, see Fig. 5.1 (left). The stress resultants, namely normal force N, shear force V, and bending moment M (see Fig. 5.1, right), are computed in a post-

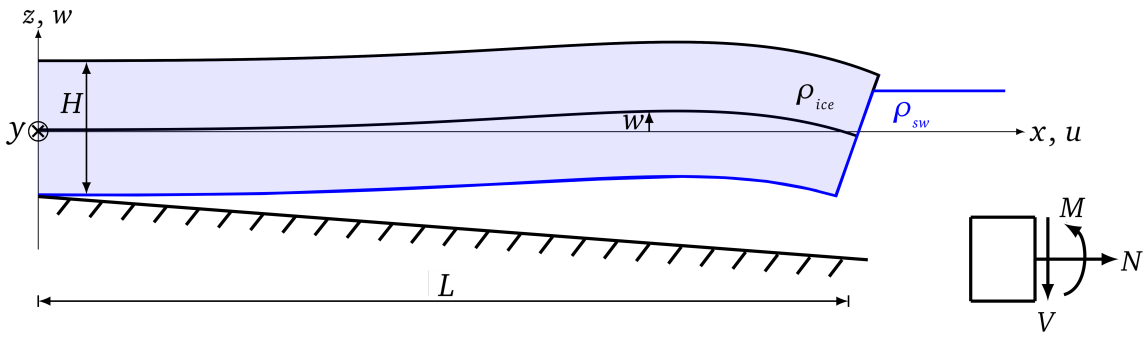

Figure 5.1: Vertical cross section of the ice shelf geometry (left) according to Reeh (1968) and corresponding stress resultants (right).

processing step. The direction of the stress resultants match to the coordinate system commonly used for beams, where the shear force V points in the direction of the positive z axis. Nevertheless, the dissimilar coordinate system of Fig. 5.1 according to Reeh (1968) is applied without inaccurate statements for the following computation of stresses in ice shelves. The normal stress σ_{xx} and the shear stress σ_{xz} (Reeh, eqs. 26 and 28) directly result from well-known formulas for beams. The normal stress σ_{zz} (Reeh, eq. 27) has to be approximated by an additional assumption of a linear decreasing stress from zero at the top to the negative water pressure at the bottom. Further details on the implementation of the viscous beam and the resulting deflections and stresses can be found in Reeh's original work.
In contrast, the displacements and hence the stress and strain states for the 2d finite element model are computed by solving the quasi-static momentum balance for a linear viscous material and small deformations. To establish a direct comparison, the same geometrical configuration of the ice shelf presented in Reeh (1968) with a length of $L = 5\,\text{km}$ and a thickness of $H = 100\,\text{m}$ is analyzed, see Fig. 5.1 (left). The spatial discretization is identical to the linear elastic model, see Fig. 4.3. In this case, a coarsening of 5 m instead of 1 m of the refined frontal part leads to a maximum stress difference of 0.9 % during the whole simulation time. Mesh convergence studies have shown that the mesh is sufficiently fine to prevent mesh dependencies of the results. In addition, time integration is implemented as described in Section 3.5.

5.1.1 Influence of Boundary Conditions at the Ice Front

The stress and strain distributions in the vicinity of the ice front are of main interest. In the front part, the ice shelf is predominantly influenced by the boundary conditions at the ice front as already investigated for the linear elastic case. However, it is impossible to model the stress-free part of the freeboard by the restrictions of a beam. To detect differences, the results of the viscous beam approach are compared to those using the 2d finite element model.
For the 1d beam in Reeh (1968) the boundary condition at the ice front is illustrated

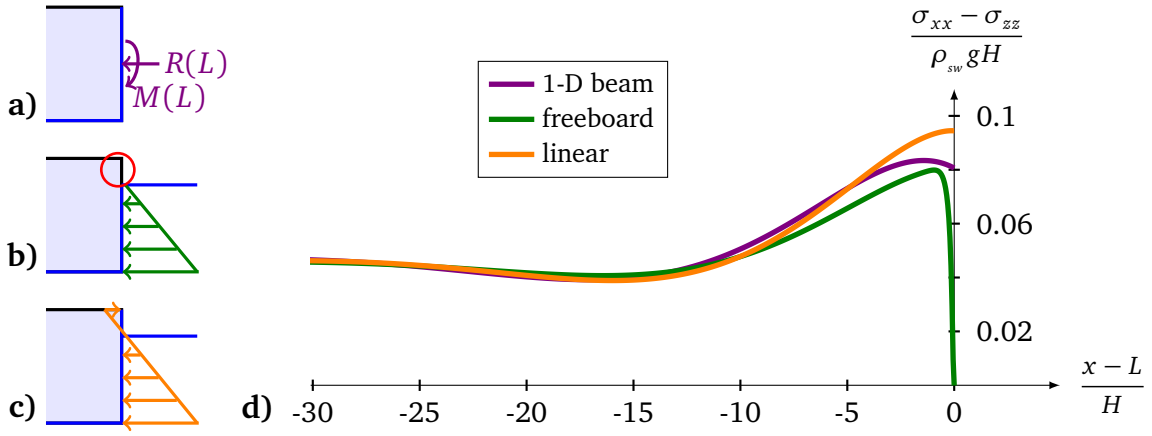

Figure 5.2: **a)-c)** Illustration of different boundary conditions at the ice front for **a)** the 1d model of Reeh (1968) and **b)-c)** the 2d finite element simulation. **d)** Stress differences at the upper surface for the different boundary conditions after a simulation time of one day.

in Fig. 5.2 a). This condition consists of a bending moment $M(L)$ originating from the off-center resultant force $R(L)$ determined by the integral of the depth dependent water pressure, cf. Section 4.2. As a consequence, the corresponding normal stress σ_{xx} varies linearly along the vertical ice front. The shear force $V(L)$ vanishes at this boundary and thus the shear stress σ_{xz} is zero. Figures 5.2 b) and c) illustrate the two different boundary conditions at the ice front for the 2d finite element simulations. The freeboard boundary condition (green) describes the present situation at an ice shelf, while the linear condition (orange) is chosen to model the 1d beam approach in a 2d setting. The remaining boundaries are not schematically illustrated as they correspond to those of the elastic case, discussed in the previous chapter and shown in Fig. 3.5 (right). To recap the situation for the 1d beam, the deflection w as well as the slope of the deflection $\partial w/\partial x$ are set to zero at the inflow boundary, see Fig. 5.1 (left). In addition, the elastic Winkler foundation has to balance the weight of the ice shelf at the bottom.

The material values are selected suitable to the parameters used by Reeh (1968) for consolidated ice. More precisely, the density ratio is $d_i = \rho_{\text{ice}}/\rho_{\text{sw}} = 0.9$, the viscosity is set to $\eta = 10^{14}$ Pa s and Young's modulus is assumed to be $E = 1$ GPa. Furthermore, Poisson's ratio ν converges against 0.5 to model incompressible ice as summarized in the first part of Section 3.4. These material parameters result in stress states at the upper surface and away from the area influenced by the freeboard condition that are identical for the beam and the finite element model at the beginning of the simulation for $t = 0$.

The resultant tensile stresses at the surface due to the three different boundary conditions are shown in Fig. 5.2 d) with consistent colors to the requirements given in Figs. 5.2 a)-c). The axes are chosen according to Reeh (1968): the horizontal axis depicts the dimensionless distance to the ice front, while the vertical axis illustrates the dimensionless stress difference at $t = 1$ d. The time of one day is arbitrarily cho-

sen, but identical for all methods and boundary conditions. Later on the absence of an applicable equilibrium state and the monotonic decrease of the stress states are discussed. At the upper surface the stress component σ_{zz} is negligibly small based on the vanished traction tensor at this boundary. Reeh (1968) included this quantity since the stress difference at the bottom of the ice shelf was also considered and there the component σ_{zz} corresponds to the water pressure.
All three boundary conditions in Figs. 5.2 a)-c) have the same stress resultant $R(L)$ to imitate the water pressure at the ice front. As already considered for linear elasticity, this resultant directly influences the stress states as long as the viscous flow is minor. All stress curves in Fig. 5.2 d) for $t = 1\,\mathrm{d}$ converge apart from the area disturbed by the ice front conditions and the 2d finite element model produces reasonable results at the beginning of the simulation. At the end of this chapter the quality of the results is also proven for later points in time.
The stress differences near the ice front occur due to the different considered boundary conditions. The ice front conditions of the 1d beam model and the linear conditions of Fig. 5.2 c) for the 2d continuum are quite similar. For the latter (orange curve) the maximum stress is directly reached at the ice front. The viscous beam accounts for the influence of freeboard through the magnitude of the applied bending moment. Thus, the stress value at the upper right corner is smaller than for the 2d case, see the purple curve. However, the beam condition cannot reproduce the stress-free boundary condition, particularly in the upper right corner of the ice front.
The freeboard condition in Fig. 5.2 b) models the stress state at the ice front of an ice shelf best. At this boundary, the water pressure increases with depth and the upper vertical face (highlighted by the red circle) is traction-free. This freeboard forces the stress to be zero for $x = L$ at the surface (cf. green curve in Fig. 5.2 d). The distinctive formation of the maximum tensile stress within a certain distance to the ice front solely appears in the case of this traction-free upper part analogous to the linear elastic model. Hence, the extension of the 1d beam model to a 2d finite element model is required to overcome the restriction of a linearly distributed boundary condition at the ice front in order to model the significant freeboard precisely. For more detailed derivations of the ice front conditions, see Christmann et al. (2016a). The freeboard boundary condition in Fig. 5.2 b) is applied in the following analysis to describe the situation at the calving front as accurately as possible.

5.1.2 Beam Theory versus Plane Strain Model

Independent of the applied modeling approach, the tensile stresses are located in the upper part of the ice shelf and in particular, the largest tensile stress occurs at the upper surface. This is caused due to the bending moment of the boundary disturbance at the ice front similar to linear elasticity. Figure 5.3 depicts the stress evolution at the upper surface for different simulation times t. Those points in time are identical to the ones analyzed in Reeh (1968). The time factor $f = \eta/(\rho_{sw} g H)$

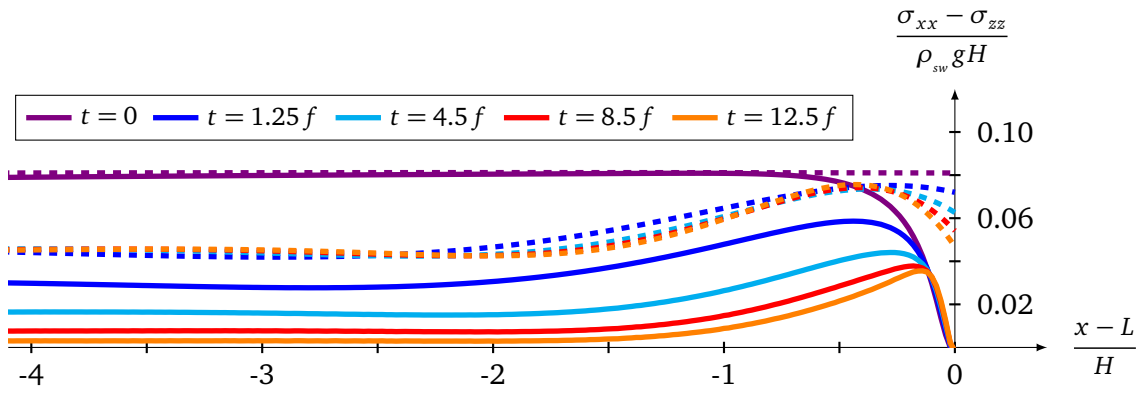

Figure 5.3: Stress differences at the upper surface; solid lines indicate the results of the 2d model and dashed lines those of the 1d beam.

is used to obtain results independent of the viscosity η. For the parameter values given in the previous section, the final time step $t = 12.5\,f$ corresponds to approximately 39 a. The solid lines in Fig. 5.3 show the dimensionless stresses for the 2d finite element model, while the dashed lines depict those of the 1d viscous beam according to the results of Fig. 9 in Reeh (1968). The stresses, which result from the beam approach, only show small changes with respect to time and the maximum stress values differ at most 9 % from the initial maximum. In contrast to these results, the solid curves of the finite element model continuously decrease with time and the location of the maximum tensile stress shifts towards the ice front. More precisely, the stress states monotonically decrease with time by more than 56% for the incompressible viscous continuum approach during the same time period. Close to the front, considerable differences of both methods based on the freeboard can be seen for all time steps. Stresses similar to the results of the beam only appear for the first time step (t=0) with a certain distance away from the front.
The stress relaxation for longer time periods was not noticed in the first 2d finite element analysis of ice shelves by Fastook and Schmidt (1982). Their computational restrictions only allowed for limited time spans (26 days at most), simple shape functions ($Q1P0$ elements), and a relatively coarse grid. For this short time interval, the results presented in Fig. 5.4 confirm the misleading observation of small changes in the stress distribution. The solid lines in this figure depict the stress states for early points in time ($t \leq 0.31\,f \hat{=} 1$ a) for the 2d model, while the orange dashed line repeats the result of the beam for the final time ($t = 12.5\,f$), cf. Fig. 5.3. It is obvious that the stress evolution of the 2d model for early points in time is well described by the almost time-independent beam results: 10 days correspond to $t = 8.5 \cdot 10^{-3}\,f$ (brown line), 30 days to $t = 2.5 \cdot 10^{-2}\,f$ (gray line), and one year to $t = 0.31\,f$ (black line). Hence, the beam model is able to sufficiently represent the stresses at early points in time. Fastook and Schmidt (1982) even assumed that it is not necessary to consider the time evolution of the stress states to study crack formation and propagation. However, this study verifies that the long-term viscous behavior is essential for the current stress shape. A stress criterion for crack formation will

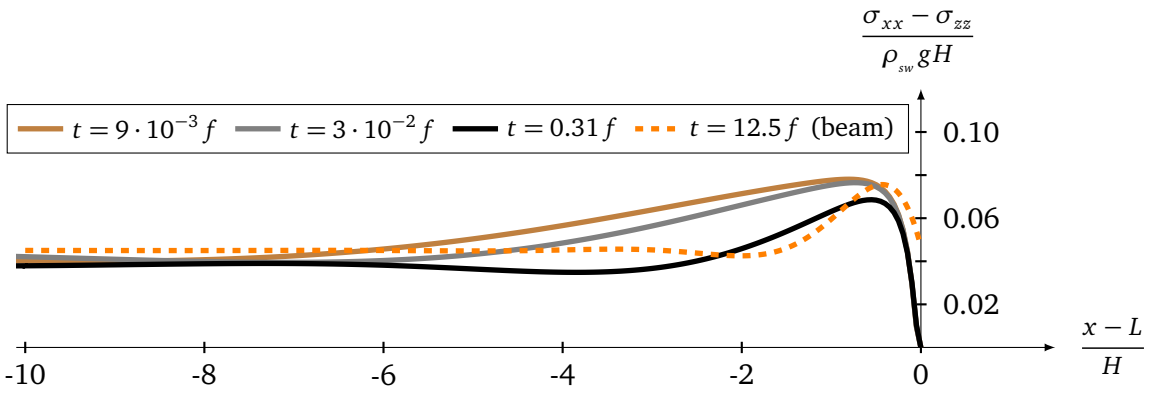

Figure 5.4: Stress differences at the upper surface; solid lines depict the solution of the 2d model and the orange dashed line the solution of the beam for $t = 12.5\,f$.

only be reasonable, if mechanisms are included, which lead to an increase of tensile stresses. Examples of such mechanisms are for instance changes in the geometry at the ice front as examined for the linear elastic model as well as suggested by O'Leary and Christoffersen (2013) for tidewater glaciers.
Figure 5.5 provides a possible explanation for the stress decrease using a 2d simulation. The horizontal strain component in the flow direction ε_{xx} monotonically increases with time. A maximum strain value is developed in the vicinity of the ice front quite similar to the maximum stress position. The strain component ε_{xx} is related to the elongation of the ice shelf in the flow direction and leads to a decrease of the ice shelf thickness and hence to a decrease of the tensile stress. This behavior is not considered in the beam model as a major simplification states a constant length of the beam. Only the vertical deflection w is established. As a consequence, the longitudinal flow is completely neglected in the beam approach. However, if the horizontal strain component reaches more than 1%, the stress response of the 2d continuum model increasingly differs from the one computed with the beam concept. The curves of the stain component converges within some distance to the ice front (Fig. 5.5). As a consequence, the strain rates as well as the stresses in the flow

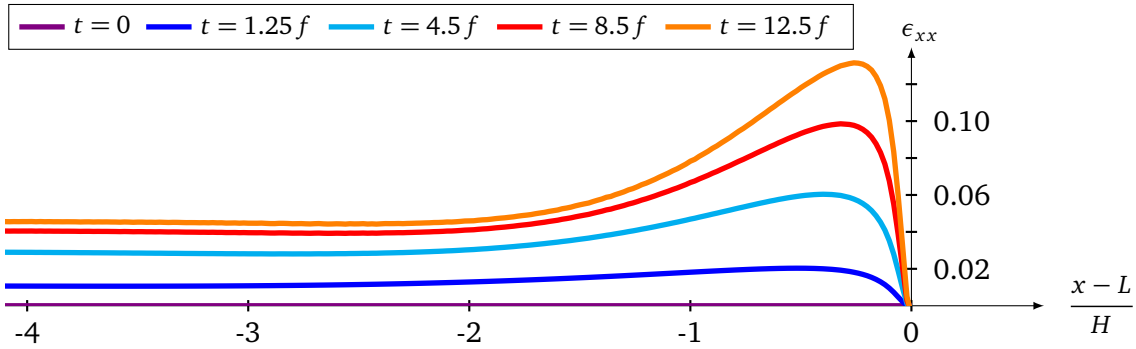

Figure 5.5: Time evolution of the horizontal strain component ϵ_{xx} at the upper surface of the 2d model.

direction decrease based on the viscous material law. This means that statements about stresses at later points in time require an approach in which the horizontal spreading of an ice shelf is included. In case of longer time periods, the total strain may exceed 10 % and thus violates the assumption of small deformations. In order to model the stress and strain states for this case, a material model that involves large deformations is needed. The effect to apply the large deformation model to the same setup is considered in Chapter 7.

In summary, the 1d beam can neither accurately model the freeboard at the ice front nor consider the extension in the flow direction. Hence, the improvement of the ice shelf model using a 2d continuum approach is necessary to describe the consequent stress decrease. This is in accordance with the decreasing thickness of the ice front with time. The influence of different boundary conditions indicates that the formation of the maximum tensile stress coincides with an accurately modeled freeboard. The boundary disturbance at the ice front hence dominates the interesting tensile stress state at the upper surface in the vicinity of the ice front also for an incompressible viscous material. Theses outcomes are in greater detail discussed in Christmann et al. (2016a).

5.2 Laminar Flow

In many ice sheet models, the incompressible ($\nu = 0.5$) viscous spreading of ice is modeled by a laminar flow approach. This ansatz contains the velocities $\boldsymbol{v}$ and in addition the pressure p as unknowns. However, this mixed formulation is not straightforward expandable to viscoelasticity in which the compressible elastic behavior of ice is included to accurately model the process of calving. In contrast, the viscous material model, introduced in Section 2.5.2, only solves for the displacements $\boldsymbol{u}$. The material is described by the deviatoric stress and a viscoelastic response is obtainable through a modification of the deviatoric part, see Section 2.5.3. In this model, the thermodynamic pressure is approximated by a constitutive assumption of an elastic isometric stress $K\mathrm{tr}(\boldsymbol{\varepsilon})$ in eq. (2.69). The advantage of such a material formulation is that the isometric stress can describe a compressible ($\nu = 0.325$) as well as a nearly incompressible ($\nu \to 0.5$) elastic ice behavior. Hence, the stress state includes the compressible/incompressible elastic response to a sudden change of the volume as well as the incompressible viscous long-term behavior. In order to also verify this approach for the purely viscous flow of ice shelves, the results of the two different approaches are compared subsequently.
An essential point is that the viscous flow of ice is in general assumed to be incompressible. However, if the elastic isometric stress is considered to describe an incompressible behavior, the bulk modulus K goes to infinity for $\nu \to 0.5$ such that a singular stiffness matrix results. Numerical artifacts like locking or hour-glassing will occur. To avoid these artifacts, the mixed formulation that uses the pressure $-p\mathbf{1}$ instead of $K\mathrm{tr}(\boldsymbol{\varepsilon})\mathbf{1}$ for the volumetric part of the stress tensor was established to de-

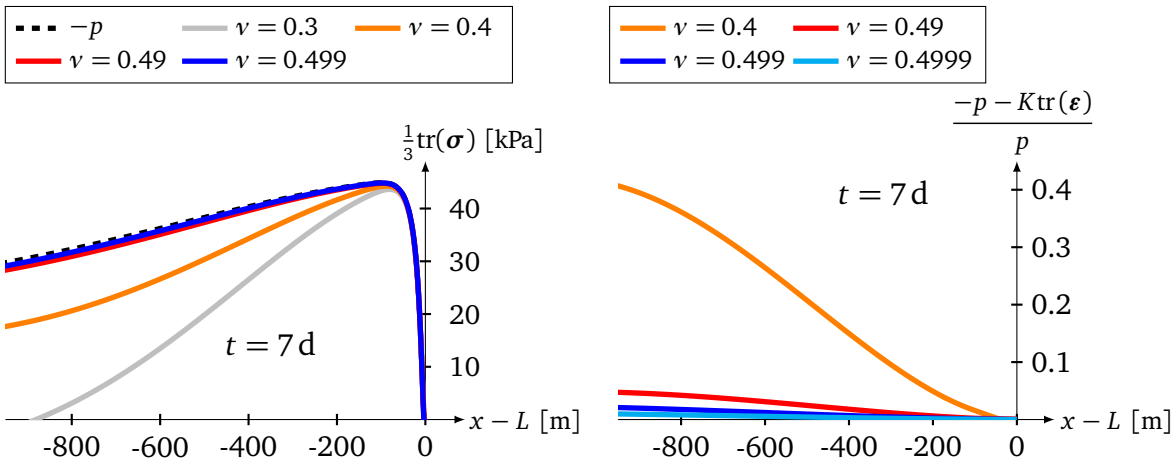

Figure 5.6: Elastic isometric stress distribution $K\mathrm{tr}(\boldsymbol{\varepsilon})$ (left) for different values of Poisson's ratio ν and relative differences of this isometric stress to the thermodynamic pressure p (right) at the upper surface.

fine an incompressible material. The finite element software COMSOL provides such a model formulation in the laminar flow module. The expression $1/3\mathrm{tr}(\boldsymbol{\sigma})$ is the volumetric part of the stress tensor in eq. (2.69) for the proposed models in this work. The following analysis of this expression confirms the satisfactory approximation of the thermodynamic pressure by the elastic isometric stress for a nearly incompressible material ($\nu \to 0.5$). In the laminar flow module, the velocities are computed with Lagrange shape functions of quadratic polynomial order, while the pressure is element-wise linear approximated with so-called $Q2P1$ elements. Additionally, the computational domain is adapted in every time step due to the velocities by a moving mesh. Figure 5.6 (left) shows the thermodynamic pressure $-p$ after a time of 7 d as a function of the distance to the ice front by the black dashed line at the upper surface. For this computation, the required material values for ice shelves are the constant thickness of $H = 100\,\mathrm{m}$, the ice density $\rho_{\mathrm{ice}} = 910\,\mathrm{kg/m^3}$, the sea water density $\rho_{\mathrm{sw}} = 1028\,\mathrm{kg/m^3}$, and the viscosity $\eta = 10^{14}\,\mathrm{Pa\,s}$. The effect of different viscosities is analyzed later in Section 6.3. For the elastic isometric stress, the material values $E = 9\,\mathrm{GPa}$ and $\nu \approx 0.5$ are additionally used. The elastic isometric stress states, see solid lines in Figure 5.6 (left), converge to the thermodynamic pressure for $\nu \to 0.5$. A Poisson's ratio of a compressible material (gray curve with $\nu = 0.3$) gives similar results starting from the ice front to the point where the maximum of the volumetric stress is reached. The stress distribution further away from the ice front has a steeper slope and differs considerably from the incompressible case. In addition, the relative difference of the thermodynamic pressure and the elastic isometric stress is depicted in Fig. 5.6 (right). This value for $\nu = 0.49$ is always smaller than 5 % (cf. red curve). To investigate small-scale calving, the maximum tensile stress is critical. The relative difference of the maximum isometric stress and the thermodynamic pressure reaches 1.9 % for $\nu = 0.4$, 0.2 % for $\nu = 0.49$ and for $\nu = 0.499$ this is already reduced to 0.05 %. The dissimilarity of $\nu = 0.499$

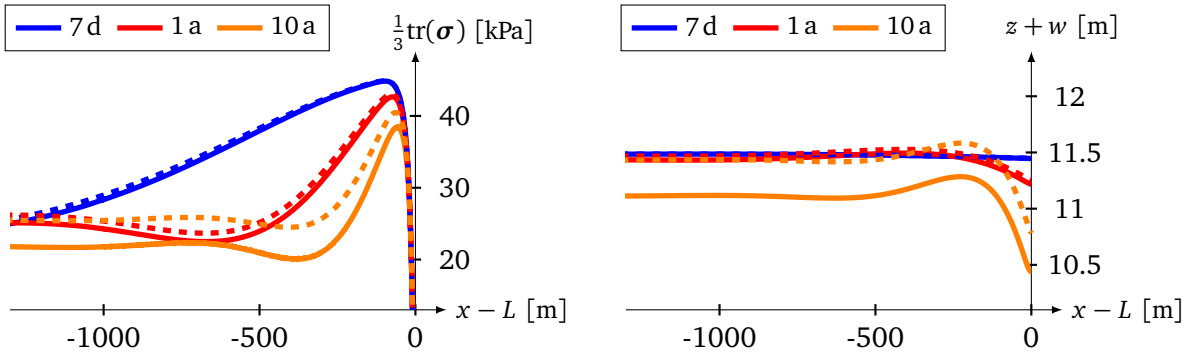

Figure 5.7: Stress distribution (left) and deflection w (right) of the upper surface for the volumetric stress described by $K\mathrm{tr}(\boldsymbol{\varepsilon})$ and $\nu = 0.499$ (solid lines) instead of $-p$ (dashed lines).

and $\nu = 0.4999$ is visually non-existent in the left plot of Fig. 5.6 however slightly identifiable in the right image of this figure. Furthermore, the approximation quality slightly depends on Young's modulus E as this value influences the bulk modulus K. The decrease of E requires Poisson's ratios closer to 0.5 to get sufficient approximations of the incompressible volumetric stress states. The absolute difference of the pressure and the elastic isometric stress with $\nu = 0.499$ is illustrated in Christmann et al. (2016b) for the entire 2d ice shelf geometry.
Subsequently, the value $\nu = 0.499$ for the elastic isometric stress is used to approximate the incompressible case. In Fig. 5.7, the stress states (left) and the deflections w (right) at the upper surface are shown. The solid lines depict these quantities computed by the elastic isometric stress approach and the dashed lines display the results of the laminar flow model. The stress distributions, already discussed above, as well as the deflections w after 7 d are similar for the two approaches, cf. the blue curves. The red curves, obtained as results after one year, are also close together. As a conclusion, it is sufficient to take the elastic isometric stress as a good approximation of the thermodynamic pressure on short time spans. However, the difference gets larger with an increase of the simulation time. After 10 years, the stress deviation of the orange curves is already significant with a maximum shift of 4.7 kPa, while the maximum stress differs by 1.9 kPa. In the right image of Fig. 5.7, the reason for this is illustrated. The position of the upper surface for the viscous model with the elastic isometric stress is beneath the one of the laminar flow model. This constant offset, in the part that is unaffected from the boundary disturbance, leads to the consistent distance in the stress states as thinner ice shelves induce smaller tensile stresses. Furthermore, the difference in the freeboard thicknesses results in the variation of the stress maximum of these two methods. In order to investigate the origin of this divergence, the two models are studied more precisely.
In the laminar flow module, the geometry is updated in every time step due to the above mentioned moving mesh influenced by the velocities. Hence, the external and internal forces are applied to the actual geometry of the current configuration. In contrast, the viscous model computes the actual displacements, while the applied

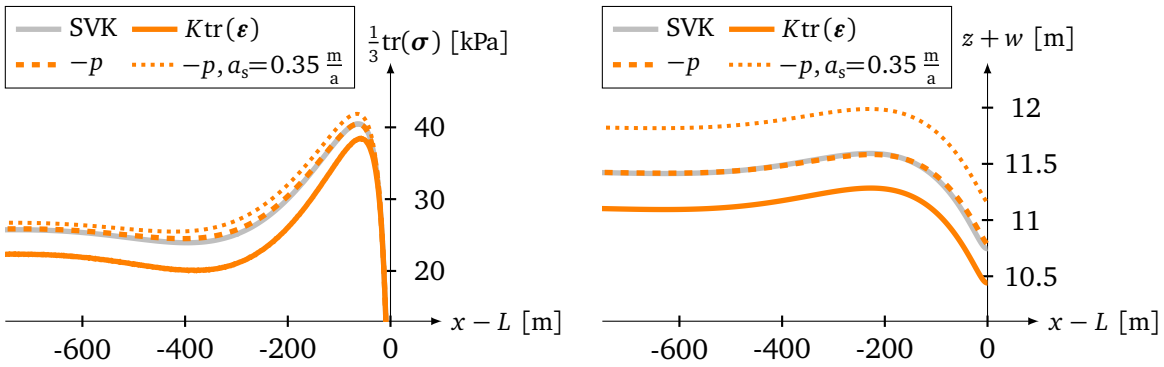

Figure 5.8: Stress distribution (left) and deflection w (right) at $t = 10\,\mathrm{a}$ of the finite deformation model (SVK, cf. Chapter 7), the elastic isometric stress $K\mathrm{tr}(\boldsymbol{\varepsilon})$ with $\nu = 0.499$, the thermodynamic pressure $-p$ (dashed lines) and the thermodynamic pressure $-p$ with an additional accumulation rate of 0.35 m/a (dotted lines).

forces act on the reference configuration since the mesh is not updated. The weight of the ice shelf is thus constant in time and not adapted to geometry modifications due to the vertical deflection of the upper surface. As a result, the bottom surface remains at the same position and does not recognize a variation of the upper surface. During the simulation, the upper surface lowers more and more based on the viscous ice spreading in horizontal direction caused by the applied weight. As a significant consequence, the buoyancy equilibrium will not be fulfilled, if the fundamental assumption of small deformations is disregarded with a horizontal strain of more than 0.05. This is precisely studied in Section 7.2.
However, the laminar flow model is also valid for large deformations due to the moving mesh. Figure 5.8 shows in addition the stress (left) and deflection (right) curve in gray for the finite viscoelastic Saint Venant-Kirchhoff (SVK) model. This material approach is suitable to consider large deformation. The viscoelastic formulation is introduced in Section 2.7 and involves a viscous long-term behavior. The stress state as well as the deflection coincides with the results of the laminar flow model at $t = 10\,\mathrm{a}$. The maximum variations of the volumetric stress and the deflection are 170 Pa and 0.01 m corresponding to a relative difference of 0.9 % and 0.1 %, respectively. Hence, the differences in the thermodynamic pressure and the viscous model assuming small deformations increased by time only occur based on the computation with respect to different configurations. In the end, the stress and strain states of the laminar flow model are sufficiently approximated by a nearly incompressible viscous material that uses the elastic isometric stress to describe volumetric changes. Further results for finite deformations are discussed in Chapter 7.
Moreover the effect of a constant accumulation rate of $a_s = 0.35\,\mathrm{m/a}$ is depicted in Fig. 5.8 for $t = 10\,\mathrm{a}$ by the dotted curve. This rate is added to the upper surface in the laminar flow model by an additional velocity. Consequently, the surface raises by 0.4 m. This corresponds exactly to the freeboard growth for a total accumulation of 3.5 m. The difference of 3.1 m is transformed to an increase of the ice draft. This accumulation rate leads to a slight increase of the stress response at the

upper surface. Conceivably, the fault of the small deformation model can be compensated by a convenient accumulation rate. However, parameter studies for the viscoelastic models are established in the next chapters without the involvement of accumulation rates to show the sole consequences of the applied material model.

6 Linear Viscoelasticity

So far purely elastic and purely viscous material models are considered separately. A large number of laboratory tests and field studies shows that the behavior of ice can be described by viscous material laws for sufficiently long timescales. Nevertheless, recent observations indicate an elastic response of ice on short timescales. For instance, the phase shift between the load and the reaction of ice streams due to tidal forces are not describable by a purely viscous material, see Gudmundsson (2011). In consequence, a more complex viscoelastic material model is needed to portray the short-term elastic as well as the long-term viscous ice behavior.
Boltzmann (1874, 1876) apparently first introduced the superposition principle for the linear theory of viscoelasticity. A short summary of essential conclusions and their extension to nonlinear continuum mechanics was reexamined by Coleman and Noll (1961). Ever since lots of works were undertaken on linear and finite viscoelasticity and Haupt (2000) termed "this conception ... to be most rewarding since its contribution to the development of an all-embracing theory of material properties is considerable".
The two fundamental models introduced in this work, see Section 2.5.3, characterize the viscoelastic behavior of solids (Kelvin-Voigt model) as well as fluids (Maxwell model). The former method reacts in the beginning viscously and ceases in the linear elastic case, while the latter one responses instantaneously elastic followed by a viscous behavior. Hence, the Maxwell material model is more appropriate to mirror the above mentioned manner of ice. However, fractures suddenly occur at local parts of the ice shelf and calving is rather a process fitting to solids. In order to understand the differences of both material models, the state variables are first assessed for the viscoelastic solid before the effects of the viscoelastic fluid are investigated. In each of these two methods different calving criteria are conceivable and their impacts on the ice shelf dynamic are analyzed in the following. Afterwards these criteria are examined for the two basic models to describe the viscoelastic behavior of an ice shelf. For a better comparison the boundary conditions and the load are equal to the purely elastic and the purely viscous case. Furthermore, the spatial discretization of the ice shelf is unchanged to the previous studies, see Fig. 4.3.

6.1 Calving Criteria

In order to figure out causes that lead to small-scale calving different possibilities for termination criteria are conceivable, while in numerous continuum mechanical models critical stress values often force the material failure. Such criteria have to be

independent of the choice of the coordinate system. Hence invariant quantities are often analyzed to specify the rupture of the material. Examples for invariants of a second order tensor are the trace or the determinate of this tensor. It is possible to express the principal stresses by invariants. The largest principal stress is essential to resist the loads and thus suitable as a crucial stress state for a calving criterion. For an ice shelf the maximum of this stress value coincides with the maximum tensile stress in the flow direction, see eq. (4.10), and is already investigated for the elastic and viscous material. In addition critical strain limits serve as a failure criterion. For the 2d ice shelf the largest strain also occurs in flow direction based on the viscous ice flow from the ice stream into the ocean. Even phenomenological approaches include the strain value in the calving criterion. Alley et al. (2008) as well as Albrecht et al. (2011) determined calving laws due to the spreading rate, which is correlated to the strain distribution with respect to time. The third criterion considered within this work is subsequently denoted as self-similarity criterion. For this purpose a critical situation such as the achievement of a stationary case is defined and the next calving event appears once this condition is reached again.
These criteria enable the evaluation of parameters with the most relevant impact on calving. If the calving criteria are reached, an iceberg will calve off at the position of maximum stress or strain in the examined ice shelf. The precise process of crack initiation and its propagation is not studied in this work. A critical quantity directly leads to the next calving event. Indeed this method is reasonable to describe calving as the bending moment of the ice front involves more critical situations at the crack tip once a crack is initiated near the calving front. After a calving event the initial conditions of the remaining ice shelf are specified by the state quantities prior to calving. In consequence the water pressure has a sudden effect on the new ice front and the ice shelf has to adjust to the modified load until the next calving event will take place.
The position d (distance of the critical value to the ice front) and the time t_c between two consecutive calving events define the calving rate $c^\perp$ in the following way

$$c^\perp = v_{\text{flow}} - v_{\text{loss}} \qquad \text{with} \qquad v_{\text{loss}} = \frac{d}{t_c}. \tag{6.1}$$

In this equation the velocities v_{flow} and v_{loss} correspond to the measured one of the ice flow and the computed one of the ice loss. A positive calving rate $c^\perp$ conforms to the extension of the ice shelf, for a rate of zero the ice shelf is stationary and otherwise the ice shelf retreats with time. This means that the position of the calving front with respect to time is correlated to the calving rate whereas the loss velocity coincides with the velocity of iceberg calving. While the surface flow velocity of an ice shelf is determined with GPS stations or satellite remote sensing, the loss velocity has to be approximated by a suitable calving criterion. However, the calving process at ice shelves does not lead directly to variations in global sea level as the ice is already afloat. By their buttressing force the ice shelves reinforce the ice shield of Antarctica and the grounded ice in the ice sheet is stabilized by this back

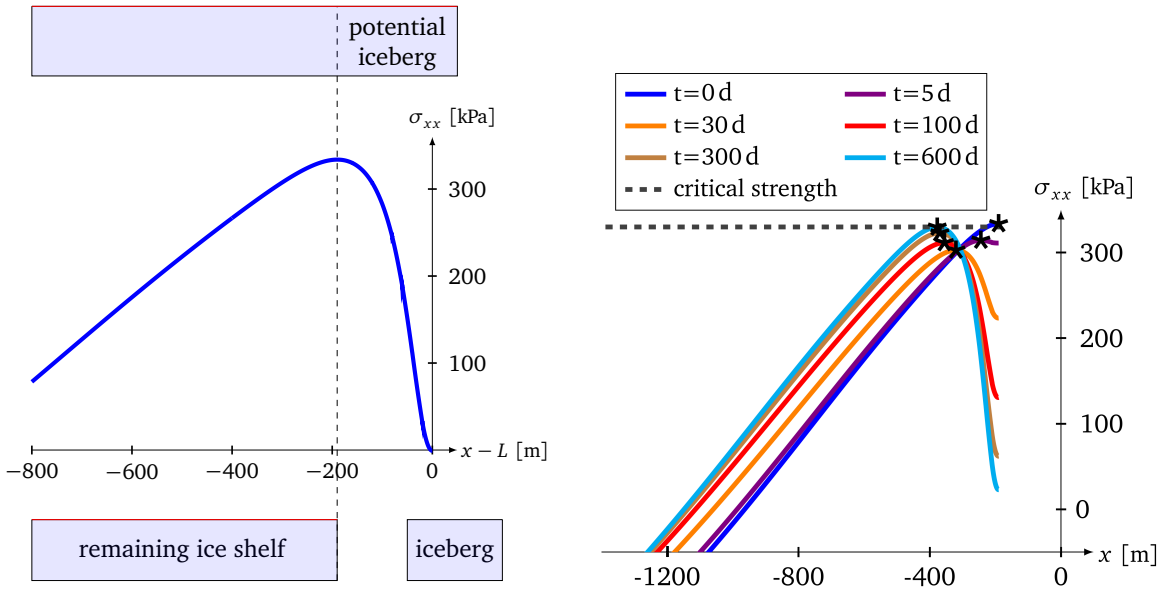

Figure 6.1: Stress states in flow direction at the upper surface directly before a calving event (left) and after this event at the remaining ice shelf with respect to time (right).

pressure, see Dupont and Alley (2005). Prognostic studies for future ice sheet evolution and the contribution of ice sheets to sea-level change thus requires an efficient implementation of calving, cf. Section 1.1.

6.2 Kelvin-Voigt Material

In the first viscoelastic model, the deviatoric stress tensor is additively decomposed into an elastic and a viscous part to describe the behavior of a viscoelastic solid. The response to unchanged load conditions converges to the linear elastic case. Consequently, a stationary state is obtained dependent on the characteristic time of the material. The analysis of a 1d Cosserat beam was done by Lang et al. (2013) for this linear viscoelastic material model.
In order to describe the fracture behavior of this kind of solid a constant maximum stress criterion is an established procedure in continuum mechanics. However, the results from the next section demonstrate the disadvantages due to this calving criterion for ice shelves regardless of the value of the critical stress.

6.2.1 Stress Criterion

In order to model small-scale calving with the use of a stress criterion, a critical bound of $\sigma_c = 330\,\text{kPa}$ derived in Hayhurst (1972) is assumed for consolidated ice. The stress maximum for the viscoelastic model is reached at the upper surface similar to the purely elastic and viscous case. Hence the stress evolution is only

investigated at this boundary.
In Fig. 6.1 (left) the stress component in flow direction attains the critical strength and the ice shelf achieves the crucial situation just before the next calving event occurs. For this special situation the thickness $H = 280\,\mathrm{m}$ and the mean ice density $\rho_{\mathrm{ice}} = 822\,\mathrm{kg/m^3}$ are assumed to reach the stress bound σ_{c} almost for the linear elastic case. The maximum tensile stress is located at the distance of $d = 190\,\mathrm{m}$ from the ice front and at this position an iceberg breaks off, cf. the schematic ice shelf depicted at the bottom of Fig. 6.1 (left). For the remaining ice shelf the first step is initialized with the results of the last time step prior to calving, see the blue curve in Fig. 6.1 (right). The forces at the new ice front suddenly change and the consequent stress evolution with time is additionally depicted in this plot. The initial stress decrease coincides with the reduction of the viscous stress for the Kelvin-Voigt model. After the minimal stress state is attained at $t = 30\,\mathrm{d}$ the subsequent stress increase is correlated to the growth of the elastic stress. Finally the curve almost converges towards the purely elastic result, while the critical stress value is reached again. After the termination time $t_{\mathrm{c}} = 600\,\mathrm{d}$ the next calving event occurs at -380 m. Independent of the number of previous calving events, the iceberg width (190 m) as well as the time span between different calving events (600 d) is always identical for the stress criterion supposing unchanged load conditions and material parameters.
In this simulation the characteristic time τ of the Kelvin-Voigt material is 306 days based on the viscosity $\eta = 10^{16}\,\mathrm{Pa\,s}$, Poisson's ratio $\nu = 0.325$, and Young's modulus $E = 1\,\mathrm{GPa}$. The results show if more than once the characteristic time τ is passed, the iceberg width is uniquely defined by the position of the maximum tensile stress for the elastic case. The time between different calving events is almost 2τ and hence proportional to η and inversely proportional to E for the commonly used Poisson's ratio of 0.325. A reduction of η by for instance two orders of magnitude to the lower bound of possible ice viscosities leads to a time interval of 6 days between two adjacent calving events. An additional increase of Young's modulus for example to 10 GPa, which is the largest reasonable value for pure ice results in the termination time of roughly 60 days. Different choices of Poisson's ratio are more precisely discussed later on in Section 6.3.1.
The marks in Fig. 6.1 (right) highlight the maximum of each stress curve. The time evolution of these maxima is additionally illustrated in Fig. 6.2 for a better visualization. This plot depicts the characteristic behavior of the Kelvin-Voigt material where the stress increase proceeds exponentially until the creep function converges against the maximum tensile stress of the linear elastic material. Caused by external forces a calving event may occur at an early point in time, for example at $t_{\mathrm{c}} = 1/10\tau$ when the lowest stress maximum in time is obtained. In this case the variance of the iceberg width is 15 % and the stress value is around 8 % smaller than the critical strength.
The issue for this type of calving criterion has already been focused on in the chapter of linear elasticity: the stress states are thickness dependent. Increasing the thickness causes higher tensile stresses based on the increased water pressure and

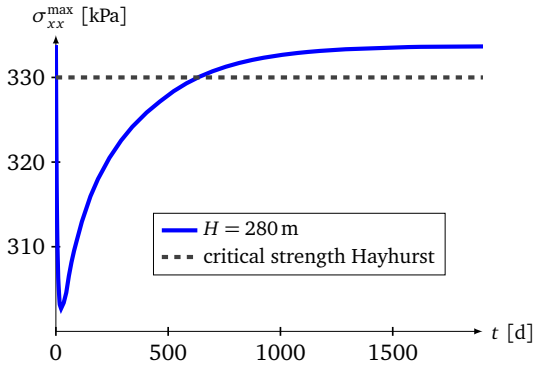

Figure 6.2: Viscoelastic time evolution of the maximum tensile stress after a calving event.

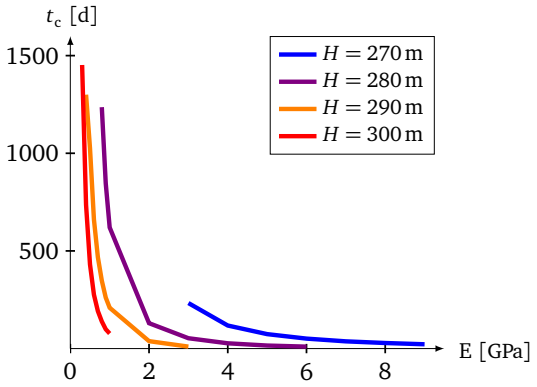

Figure 6.3: Termination time to reach the critical strength of Hayhurst for different Young's moduli and thicknesses.

freeboard thickness at the ice front. In consequence the stress criterion of Hayhurst is only attainable within the ice thickness range from $H = 270\,\text{m}$ to $H = 300\,\text{m}$. The termination time t_c between two calving events changes rapidly for this small thickness interval as visible in Fig. 6.3. While this time is 600 days for $H = 280\,\text{m}$, the critical strength is reached at about 200 days for $H = 290\,\text{m}$ and 74 days for $H = 300\,\text{m}$ for the same material parameters. The stress difference between the lowest maximum stress and the stress bound σ_c gets smaller and is correlated to smaller time lags between the calving events. In consequence these differences are insufficient to determine a clear statement about the termination time based on a stress criterion as the lowest maximum stress is almost as critical as the stress value of Hayhurst.
Furthermore, Young's modulus of $E = 9\,\text{GPa}$ often given in literature is only applicable for $H = 270\,\text{m}$ with a termination time of 99 d. This parameter set results in an ice loss velocity of $v_{\text{loss}} = 675\,\text{m/a}$, which is a too high value for Antarctic ice shelves. For smaller Young's moduli the termination time increases and conforms better to values obtained for small-scale calving. As mentioned in Section 4.2 the effective Young's modulus is close to 0.9 GPa for field observations. Consequently, most investigations in this chapter assume the lower bound of Young's modulus $E = 1\,\text{GPa}$. The impact of different termination criteria on the calving of ice shelves using the same material parameters is discussed. However, the outcome of Young's modulus $E = 9\,\text{GPa}$ is analyzed additionally, if crucial information emerges out of this parameter modification. In most situations the effect of different Young's moduli is similar to a modification of the viscosity, which is also vague restricted in between two orders of magnitude.
In the end a stress criterion to describe calving with the use of a viscoelastic Kelvin-Voigt model will only be convincing if it is assumed to depend on parameters influencing the stress values in a linear elastic material. A higher critical strength than the elastic stress maximum is not possible as a calving criterion, while a too small stress criterion is equivalent to the disintegration of the ice shelf. In Fig. 6.4 the possible critical strength interval for the constant thicknesses of $H = 100\,\text{m}$ (left)

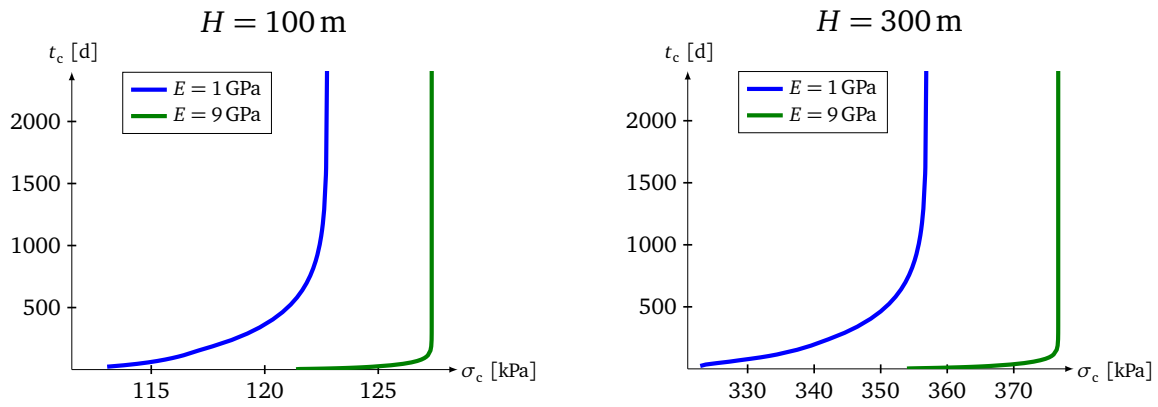

Figure 6.4: Possible critical strength intervals and consequent termination times t_c for $H = 100\,\mathrm{m}$ (left) and $H = 300\,\mathrm{m}$ (right).

and $H = 300\,\mathrm{m}$ (right) with Young's modulus values of $E = 1\,\mathrm{GPa}$ and $E = 9\,\mathrm{GPa}$ are determined. The steep slope in the termination time coincides with the achievement of the linear elastic case, where the stress state from the Kelvin-Voigt material converges to the one of the rate-independent elastic case. It is obvious that the nearly stationary situation is reached earlier for a stiffer material. The difference of the stress maxima between $E = 1\,\mathrm{GPa}$ and $E = 9\,\mathrm{GPa}$ is given by 1 % for $H = 100\,\mathrm{m}$ and pure ice with the density $\rho_{\mathrm{ice}} = 910\,\mathrm{kg/m^3}$, see Section 4.2. For a mean density of $\rho_{\mathrm{ice}} = 822\,\mathrm{kg/m^3}$ as considered in this case, this difference slightly increases to 4 % for a thickness of $H = 100\,\mathrm{m}$ and to 5 % for $H = 300\,\mathrm{m}$.
In summary, the main problem of a critical strength criterion is that the termination time rises rapidly for restrictive values near the linear elastic case. A small change of the stress bound or the thickness leads to a huge variation in the termination time and thus in the loss velocity of the ice shelf. Based on inaccuracies of measurements and parameter variations in between large intervals, the results for calving have to be stable for small changes of critical values or loads. In addition the small thickness interval for a constant critical stress bound is undesirable. The subsequent approach using self-similar stress states to describe calving events is suggested to avoid the instability of the results and is appropriate for all thicknesses.

6.2.2 Self-Similarity Criterion

The general aim of a self-similarity criterion is to define a critical situation when fracture is likely to occur. In the context of small-scale calving of ice shelves the next iceberg breaks off the ice shelf at any time the circumstances of the criterion is reached again. Conditioned by the choice of the Kelvin-Voigt model the convergence of the stress states to the rate-independent linear elastic response is predetermined. The decreasing difference of maximum stress values with time is used to define a calving criterion by a convergence bound. As soon as the variation of the maximum tensile stress of two consecutive time steps is smaller than this bound the next calving event occurs. In addition, the most crucial state for calving is obtained

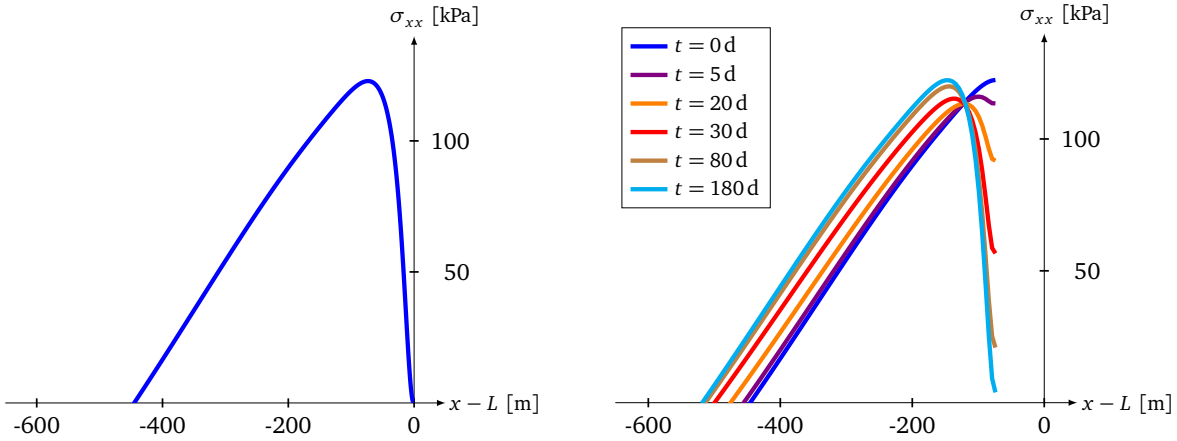

Figure 6.5: Stationary stress state before calving (left) at the upper surface and its time evolution (right) after the iceberg breaks off at the position of the maximum tensile stress.

for the largest stress value corresponding to the maximum stress of a linear elastic material. The asymptotic approximation to the termination bound is independent of any geometric or material parameter. For unchanged load conditions only the time to reach a certain percentage of the elastic response depends on the characteristic time τ. This calving criterion is thus valid for the whole thickness range of Antarctic ice shelves. The time-dependent solver using the automatic time stepping control of COMSOL is changed to the time discrete solver. At prescribed points in time the results are computed and especially the time step is definable by a constant value. Consequently, the self-similarity criterion is established for certain convergence bounds that constrain the difference of two maximum stress values for the same time intervals.
In the previous section the long-term behavior for the maximum tensile stress of the Kelvin-Voigt model is already investigated for the thickness $H = 280\,\mathrm{m}$. The general procedure of the critical stress criterion permits to study the calving behavior from ice shelves with smaller thicknesses, for instance the Ekström Ice Shelf. For the self-similarity criterion a comparison to results from the measured thickness in contrast to the constant one is straight forward possible and is shown at the end of this section. First, the stationary stress state of the linear elastic case is depicted for the upper surface of the ice shelf in Fig. 6.5 (left). In order to develop the improvement due to the self-similarity criterion, the geometric and material values are chosen identically to the previous section with the exception of the smaller ice thickness $H = 100\,\mathrm{m}$. If this current situation in Fig. 6.5 (left) is assumed to induce small-scale calving, an iceberg calves at the position of the maximum tensile stress. This happens upstream the ice shelf at a distance of $d = 74\,\mathrm{m}$ to the ice front. In the right plot of Fig. 6.5 the time evolution of the stress states of the remaining ice shelf is depicted at the upper surface. The small difference between the curves at $t = 80\,\mathrm{d}$ and at $t = 180\,\mathrm{d}$ indicates the convergence of the stress response to the upper bound

constant thickness $H = 100$m:

b^{st}	d [m]	t_{c} [d]	v_{loss} [m/a]
$2.5 \cdot 10^{-5}$	74	117	230
$1.5 \cdot 10^{-5}$	74	180	150
$1 \cdot 10^{-5}$	74	287	94

Ekström Ice Shelf:

b^{st}	d [m]	t_{c} [d]	v_{loss} [m/a]
$2.5 \cdot 10^{-5}$	69	121	208
$1.5 \cdot 10^{-5}$	69	182	138
$1 \cdot 10^{-5}$	69	290	87

Table 6.1: Termination time and loss velocity for different self-similarity bounds. The results are computed for a constant thickness (left) and the geometry measured at the Ekström Ice Shelf (right).

(linear elastic). To define a termination value b^{st}, the maximum tensile stress values of two adjacent time steps t_{n-1} and t_n are compared by the following condition

$$\left| \frac{\max\left(\sigma_{xx}\left(t_n\right)\right) - \max\left(\sigma_{xx}\left(t_{n-1}\right)\right)}{\max\left(\sigma_{xx}\left(t_0\right)\right)} \right| < b^{\mathrm{st}}. \tag{6.2}$$

In the case b^{st} is achieved the computation is interrupted and the next iceberg is cut off the ice shelf. In order to compare the results of the model to measured small-scale calving some day, the time between two calving events is required on scales of days not hours. Hence, the time discrete solver computes the results during this analysis once a day. The independence of the results on the time steps of the discrete solver has been verified but not shown in this work. As already mentioned above the evaluation of the termination bound b^{st} is enabled without any dependencies on time steps.
The convergence bound is stated as a relative difference of maximum stress values. It is specified with respect to the maximum stress value of a linear elastic material reached at $t_0 = 0$ when an iceberg breaks off. In Table 6.1 different convergence bounds are given to define the achievement of the linear elastic case using a constant thickness (left) and the measured one of the Ekström Ice Shelf (right). While this additional unknown parameter b^{st} does not influence the position d of the stress maximum, the termination time t_{c} clearly depends on this value. Hence, the loss velocity v_{loss} and the consequent calving rate $c^{\perp}$ of eq. (6.1) are affected by the choice of the limit b^{st}. The results using the constant thickness slightly overestimate those velocities obtained for the ramp-like geometry with nearly the same ice front thicknesses, see Section 4.2.2. For both geometries, the statement of the calving rate is quite similar with respect to the measured flow velocity $v_{\mathrm{flow}} = 162\,\mathrm{m/a}$ of the surface determined with GPS-stations in Lohse (2012). For the smallest convergence bound the ice shelf retreats, for the middle one the ice shelf is nearly in a stationary state and for the largest one the ice shelf expands. It is obvious that the magnitude of the convergence bound is not physically explicable. An additional, arbitrary parameter is included in the material model and has to be determined in some way by the use of measurements. Fur this purpose an approximation of the convergence bound is necessary. The termination time has to coincide with measured time intervals between two adjacent calving events at a specific ice shelf. Finally this value is

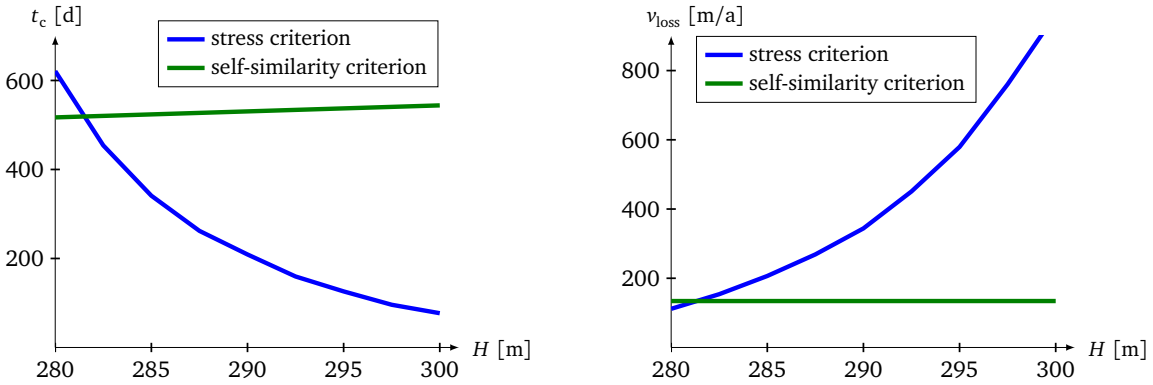

Figure 6.6: Termination time t_c (left) and loss velocity v_{loss} (right) for both introduced calving criteria of the Kelvin-Voigt material.

checked for other ice shelves.
With the use of the self-similarity criterion a rather stable solution (small changes in the thickness or the termination value leads to small changes in the results) is achieved. This is an improvement to the stress criterion discussed in the previous section. In Fig. 6.6 the termination time (left) and the consequent loss velocity (right) are illustrated for both approaches. For the critical stress criterion the steep decrease of the termination time t_c and the resultant increase in the loss velocity v_{loss} near the linear elastic case is not reasonable. In contrast, the steady distribution of the self-similarity criterion leads for similar thicknesses to almost the same loss velocities for calving. The latter criterion enables more realistic results of small-scale calving and is furthermore not restricted to a small thickness extent.
In summary the self-similarity criterion with an initial adjustment to measurements yields a possibility to determine calving rates for all ice shelves. For the measured calving rate it has to be guaranteed that the calving behavior at this special ice shelf is only caused by the bending moment at the ice front. Other factors like existing rifts have to be excluded. Nevertheless, the long-term behavior of the Kelvin-Voigt model does not coincide with the viscous material behavior of ice. A termination time of half a year to a year is not part of the linear elastic short-term response of at least several days to a few months. In addition only a small increase in the maximum stress leads to a calving event although the stress earlier is almost as critical (asymptotic calving criterion).
To overcome these problems the Maxwell material is considered in the following section to model the behavior of ice more appropriate. For this type of viscoelastic fluid calving criteria are investigated by the means of elastic compressibility or increasing strain values.

6.3 Maxwell Material

In consequence of a constant load, for example the water pressure at the ice front, the long-term behavior of ice is viscous, while for sudden load changes the response is instantaneously elastic. These material reactions fit best to the characteristics of a Maxwell material. Until now purely elastic or purely viscous constitutive equations are often applied in literature to describe the processes at ice shelves, while viscoelastic models in particular using Glen's flow law or finite deformations are seldom used. For instance linear viscoelasticity was utilized to tidal dependent aspects such as the tidal bending of glaciers investigated by Reeh et al. (2003), the flexure and migration of the grounding line considered by Tsai and Gudmundsson (2015) or the variations of ice velocities at the grounding line, see Rosier et al. (2014). Furthermore, MacAyeal et al. (2015) discussed the drainage of meltwater for a Maxwell material with the use of Glen's flow law. However, physical-based stress and strain studies at ice shelves including a viscoelastic material behavior to get suitable calving laws are missed. At Antarctic ice shelves the viscous expansion not completely retarded by the sea water pressure happens usually slow and the calving event with the sudden sea water load at the new ice front occurs usually rapid. The timescales correlated with these mechanisms justify a viscoelastic Maxwell model to investigate small-scale calving.
Ice shelf calving based on a stress criterion seems unlikely during decreasing maximum tensile stress values. As already seen in Chapter 5 the stress states in an ice shelf relax with time for a purely incompressible viscous material. The maximum stress is reached immediately at the beginning of the simulation and a stress criterion is not reasonable as it leads to continuous calving. However, if compressible elasticity is combined with incompressible viscosity, the possibilities to get a calving criterion are first of all discussed. Afterwards, in a second approach a critical strain criterion is investigated. Indeed the viscous flow elongates the ice shelf, the strain increases in time and when a critical spreading is reached the next iceberg calves off the ice shelf. In the end, the effects of the self-similarity criterion applied to strain states as well as using the Glen-type viscosity are discussed.

6.3.1 Elastic Compressibility

A Poisson's ratio of $\nu = 0.5$ describes the pure incompressibility of the viscoelastic material. In the work at hand, this is called elastic incompressibility to express that not only the viscous behavior of the material is incompressible but also the elastic one. If this elastic constant is approximately assumed in the Maxwell model, the stress states relax monotonically with time similar to the viscous case. Hence a stress criterion yields no useful statements for calving at ice shelves for the viscoelastic model. This fact is illustrated in detail in Christmann et al. (2016a).
In the past different values for Poisson's ratio were cited in the literature for consolidated ice. For instance Hutter (1978) and Mellor (1975) stated $\nu = 0.31$, while

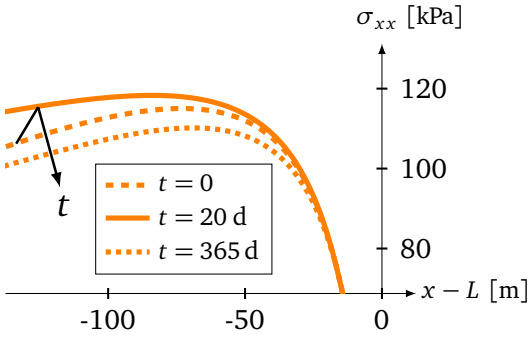

Figure 6.7: Viscoelastic stress states at the surface for $\nu = 0.325$ for different times. The direction of the arrow indicates an initial stress increase in time.

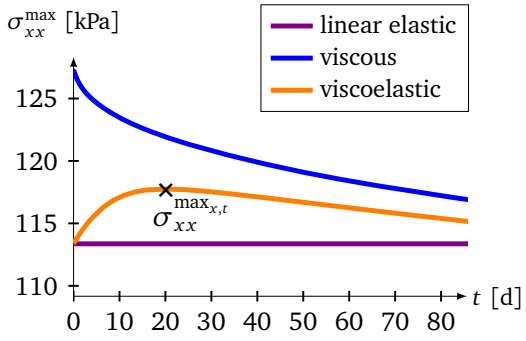

Figure 6.8: Maximum tensile stress for elastic and viscoelastic materials with $\nu = 0.325$ in comparison to the result for incompressible viscous materials.

Petrenko and Whitworth (1999) specified $\nu = 0.325$ for isotropic polycrystalline ice at a temperature of $T = -16°C$. Even intervals of Poisson's ratio were given with $0.22 \leq \nu \leq 0.42$ by Gammon et al. (1983). In the general theory investigations of time- or frequency-dependent approaches were developed for arbitrary viscoelastic materials. A comprehensive overview of Poisson's ratios in linear viscoelasticity was published by Tschoegl et al (2002). Time effects on Poisson's ratios caused by temperature variations were often discussed for viscoelastic materials, see Pritz (1998), Lakes and Wineman (2006), and Pandini and Pegoretti (2011). However, Hutter (1975) argued on the basis of Röthlisberger (1972) that a nearly constant "relationship was sufficient to account for the temperature dependence of the elastic constants" for polycrystalline ice. Hence a Poisson's ratio of $\nu = 0.325$ is used to model the compressible elastic behavior of ice in the work at hand. This indicates a value in the middle of the interval presented above and is close to the established constant values.

Also for the Maxwell model the maximum tensile stress caused by the boundary perturbation at the ice front is located at the upper surface. This is in agreement with the results of the purely elastic and purely viscous material models, which provide the basis of the viscoelastic Maxwell model. The stress states at the surface are depicted in the vicinity of the ice front for three different times in Fig. 6.7. The material constants are chosen identical to the previous simulations and are given in the first line of Table 6.2 as standard values. The dimensionless density ratio ρ_{ice}/ρ_{sw} was already considered in previous works, for instance in the viscous beam approach of Reeh (1968). A relative density of $\rho_{ice}/\rho_{sw} = 0.8$ represents an Antarctic ice shelf fitting to the values of the Ekström Ice Shelf with $\rho_{ice} = 822\,kg/m^3$ and $\rho_{sw} = 1028\,kg/m^3$. The time-dependent stress states are computed as before by the use of the freeboard boundary combined with Robin-type conditions to model the pressure of the sea water, see Section 3.3.

The direction of the arrow in Fig. 6.7 indicates in the case of elastic compressibility ($\nu = 0.325$) an initial stress increase from the dashed orange line ($t = 0$)

to the solid one ($t = 20\,\mathrm{d}$) with a subsequent monotonic decrease to the dotted curve ($t = 1\,\mathrm{a}$). In order to get the maximum tensile stress value inside the whole domain of the ice shelf with time, the temporal evolution of the spatial maximum stress $\sigma_{xx}^{\max} = \max(\sigma_{xx})$ in the ice shelf is considered in Fig. 6.8. For the viscoelastic Maxwell model the largest tensile stress results from the maximum of the orange evolution curve (highlighted by the cross in Fig. 6.8). It is denoted by $\sigma_{xx}^{\max_{x,t}}$ to clarify this stress as the spatial and the temporal extreme value of all stress states and it is reached at $t = 20\,\mathrm{d}$. In addition, the spatial stress maximum of the time-independent elastic and the viscous material model are included by the purple and blue curve in this figure. On the basis of their development the response of the Maxwell material is reasonable. At first the instantaneous stress value coincides with the one of the elastic model. Afterwards the long-term behavior converges to the one of the viscous material and the crucial initial stress increase is comprehensible. All material models are defined through the deviatoric stress, while the volumetric stress is assumed to behave elastically. Hence the elastic constants affect the viscous stress response as well. To obtain the blue curve of Fig. 6.8 the incompressible Poisson's ratio ($\nu = 0.5$) is applied. Another possibility is to choose $\nu = 0.325$ to compute the elastic volumetric stress for the viscous material. In consequence the initial stress growth occurs for the viscous material similar to the viscoelastic response and the stress states of both model converge faster (Christmann et al., 2016a). The relative difference at $t = 20\,\mathrm{d}$ is 0.2 % in contrast to 3 % (Fig. 6.8) using the incompressible elasticity of the viscous material.

Many ice shelf quantities are poorly determined by laboratory experiments or on-site measurements. The sensitivity of the stress results to variations in their amount is investigated in the following for the viscoelastic Maxwell material. First, the influence of geometric and material parameters on the stress maximum $\sigma_{xx}^{\max_{x,t}}$ is considered. Its value, its distance to the ice front and the time when this value is obtained is summarized in Table 6.2 for plausible parameter limits occurring at Antarctic ice shelves. The range of the computed maximum stress values matches to suggested stresses for crack nucleation ($90 - 320\,\mathrm{kPa}$), see Vaughan (1993). As mentioned above calving at ice shelves based on a critical stress criterion seems unlikely when the maximum tensile stress decreases in time. Consequently, the parameters are of most interest for small-scale calving that lead to a stress increase after an iceberg detaches. The time between two calving events is assumed to be not longer than the time to reach the maximum tensile stress.

The stress maximum $\sigma_{xx}^{\max_{x,t}}$ gets larger by an increase of the elastic material properties, Young's modulus E and Poisson's ratio ν, cf. Table 6.2. However the time until the maximum tensile stress is reached decreases for this parameter variations. In the extreme case of incompressible elasticity assumed for the viscoelastic material with $\nu = 0.5$, the maximum stress value is obtained directly at the beginning of the simulation for $t = 0$. For this case the maximum of the orange curve in Fig. 6.8 shifts to higher stress values but the curve monotonically decreases with time comparable to the blue one. Once the critical stress value is obtained and the crucial geometric

H[m]	E[GPa]	η[Pa s]	$\rho_{\text{ice}}/\rho_{\text{sw}}$	ν	$\sigma_{xx}^{\max_{x,t}}$[kPa]	d[m]	t[d]
100	1	10^{14}	0.8	0.325	118	84	20
100	**0.1**	10^{14}	0.8	0.325	103	61	177
100	**10**	10^{14}	0.8	0.325	124	104	2
100	1	$\mathbf{5 \cdot 10^{14}}$	0.8	0.325	118	84	100
100	1	$\mathbf{10^{15}}$	0.8	0.325	118	84	213
100	1	10^{14}	0.8	**0.1**	114	78	40
100	1	10^{14}	0.8	**0.2**	116	80	30
100	1	10^{14}	0.8	**0.4**	120	89	12
200	1	10^{14}	0.8	0.325	229	155	20
300	1	10^{14}	0.8	0.325	337	222	20
100	1	10^{14}	**0.85**	0.325	99	77	20
100	1	10^{14}	**0.9**	0.325	73	67	20

Table 6.2: Magnitude, distance to the ice front, and evaluation time of the maximal stress in flow direction dependent on relevant parameters for a Maxwell material. Bold numbers mark deviations in the material parameters from the reference values used in this study.

conditions are identical before and after the calving event, the next termination directly occurs subsequent to the previous one. This results in the doubtful collapse of the ice shelf. If the geometric variation is essential to achieve the stress criterion due to melting or freezing, the vertical face after the calving event will no longer lead to a critical situation. Hence, incompressible elasticity can result in meaningful calving laws. This calving ansatz caused by geometry variation is investigated for the instantaneous elastic material model in Chapter 4. In addition it should be examined for the Maxwell material in future works and especially compared to high-resolution measurements of geometries from Antarctic ice shelves just before a calving event. In the following a stress criterion for the discrete calving based on the boundary perturbation is investigated for a compressible elastic ice behavior. For Young's modulus $E = 10\,\text{GPa}$, a possible upper bound for ice of the second elastic constant, the evolution time of the stress maximum is close to zero (Table 6.2). Small-scale calving in Antarctica happens on timescales of several months to few years. For the stiffer material the additional increase of the viscosity leads to larger and hence more sensible times between two calving events. The computational results in Table 6.2 show that the time interval is almost proportional to the viscosity and inversely proportional to Young's modulus and Poisson's ratio. In conclusion, the evaluation time of the maximum stress behaves similarly to the characteristic time for the Maxwell material model and impacts of geometric quantities are missing.

The stress state with its maximum and its position is completely independent of the variation in viscosity, see Table 6.2. This single quantity of the viscous flow only leads to the linear contraction or enlargement of the maximum stress response in

Fig. 6.8. The parameters with crucial influence on the magnitude of the stress maximum are the density ratio and the thickness. Similar to the elastic and viscous analysis the freeboard at the ice front enables the formation of the stress maximum at the upper surface for the viscoelastic model. This maximum is located within half the thickness to the whole thickness upstream the ice front, suitable to intervals commonly given in the literature. As shown in Table 6.2, not only the formation of the stress maximum but also its magnitude depends on the freeboard thickness. Particularly an increase of the density ratio engenders a decrease of the freeboard and consequently the stress maximum decreases. The corresponding results for the relative density $\rho_{\text{ice}}/\rho_{\text{sw}} = 0.9$ suitable to a higher ice density of pure ice are precisely discussed in Christmann et al. (2016a). Furthermore, twice the thickness leads to a doubling of the freeboard and roughly doubles the maximum stress value. In other words thicker ice shelves are more prone to the type of calving examined in this work compared to thinner ice shelves. However, this leads to a problem of the stress criterion. For instance the huge ice shelves in Antarctica like the Ross and Filchner-Ronne Ice Shelf have ice front thicknesses of more than 400 m. With these thicknesses the critical stress of Hayhurst has surpassed already for the linear elastic case and these ice shelves would totally collapse due to the stress criterion. In the model the only way to stabilize the ice shelves is to include ice rises or lateral effects to decrease the stress states at the ice front, which is no adequate description of the present situation. On the other side, an ice shelf like the Ekström Ice Shelf with 100 m thickness at the ice front will only obtain the critical stress at some point if melting or freezing changes the ice front appearance to such a high extent that the Hayhurst criterion is achieved. In spite of these problems the size of icebergs and the time, until the maximum tensile stress is reached and calving occurs, fit well to the few available measurements of small-scale calving, cf. Section 3.1.
The advantages of the self-similarity criterion will remove these problems if it succeeds to define the critical situation for calving based on the ice front bending (boundary perturbation) once. It is also conceivable to induce the crack initiation but not the crack propagation and thus no direct calving with the help of the stress criterion. Investigations of certain conditions of stable or unstable cracks are given in Plate (2015) and are not part of this study. After a few more comments with respect to the stress criterion, another calving principle by the use of strain values is discussed in the next section.
The distance d of the maximum tensile stress to the ice front is influenced by the same parameters like its amount, namely the elastic material values and the geometry. With the assumption of calving occurring at the position of the stress maximum, these parameters affect the size of the iceberg. The most significant quantity to modify the iceberg size with almost 30 % variance is Young's modulus controlling the stiffness of the material. The correlation between the thickness and the density ratio is inversely proportional and shifts the position of the maximum stress towards the ice front for an increase of these parameters, see Table 6.2.
In order to show the influence of uncertainties related to material parameters on

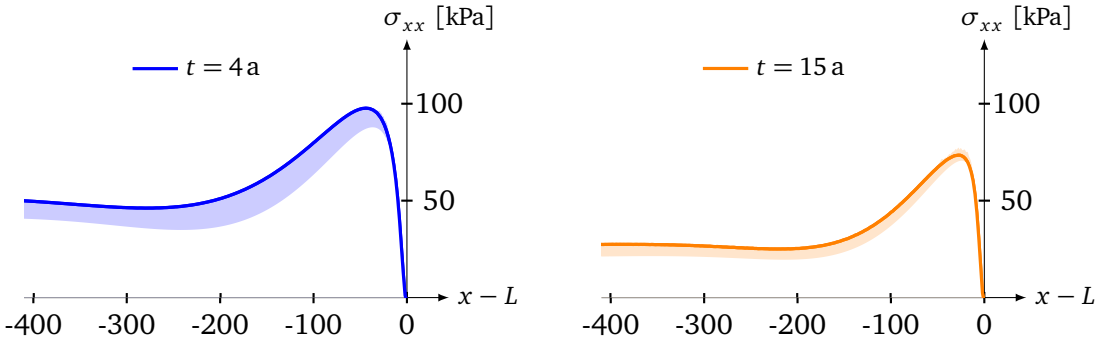

Figure 6.9: The shading indicates the stress variation due to elastic material parameter variations within the limits for Antarctic ice shelves given in Table 6.2 for $t = 4\,\mathrm{a}$ (left) and $t = 15\,\mathrm{a}$ (right). Solid lines correspond to the standard parameters (first line Table 6.2).

the stress states, Fig. 6.9 illustrates the changes due to the variation of reasonable elastic quantities for ice after 4 a (left) and 15 a (right). For a better comparison, the geometric parameters are identical to the standard parameters ($H = 100\,\mathrm{m}$, $d_i = 0.8$) used before. For a stiff material with $E = 10\,\mathrm{GPa}$ the stress curves differ only slightly for different Poisson's ratios. In the computation with smaller Young's moduli, the influence of Poisson's ratio is considerably larger. The shaded domains in Fig. 6.9 are limited by the upper bound achieved with $E = 10\,\mathrm{GPa}$ and $\nu = 0.4$ and the lower bound obtained by $E = 0.1\,\mathrm{GPa}$ and $\nu = 0.1$. All other stress distributions within these parameter ranges are located inside the shaded area. The decrease of the stresses for longer time periods is thus not influenced by those uncertainties since the decrease appears for all applied material parameters. Especially noticeable is that the shaded area is smaller for $t = 15\,\mathrm{a}$ compared to $t = 4\,\mathrm{a}$. In consequence the uncertainties in the elastic material values have fewer effects for later points in time. Based on Fig. 6.9 (left) the importance to include the elasticity in the viscous model is obvious. The elastic material constants have a conspicuous influence also at points of several hundred times the characteristic time of the Maxwell model.

6.3.2 Strain Criterion

In literature, only a few works deal with the specification of a critical strain value for polycrystalline ice. The seminal work is from Glen (1955) with an approximation of $\varepsilon_c = 0.025$ at the temperature $T = -12.8^\circ\,\mathrm{C}$. This value emerges from an extrapolation of measurements done for few hours from specimen loaded by a constant stress and is used subsequently. However, the results of the linear viscoelastic material model are easily transferable to other critical values. It is not part of this study to confirm any termination strain but rather to show its impact on calving and especially on the time between two subsequent calving events.
In order to establish a strain criterion for small-scale calving, the general procedure is similar to the case using the stress criterion. Once the critical value is reached, the

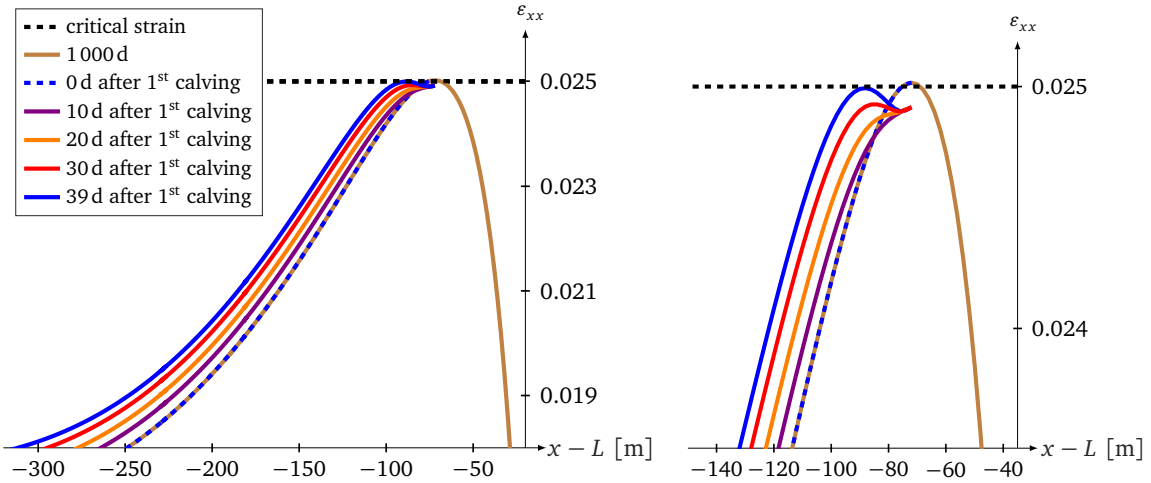

Figure 6.10: Strain ε_{xx} in flow direction between the first and second calving event caused by the achievement of a critical strain ε_c. The right plot is the magnification of the most interesting part showing the time evolution of the strain maximum.

ice shelf calves at the position of the maximum strain. Based on the viscous spreading the largest strain value occurs in the flow direction. Additionally, this value is located at the upper surface of the ice shelf caused by the freeboard condition and the depth-dependent water pressure at the ice front. Hence also these results are discussed at the upper boundary only.
In Fig. 6.10 different strain curves between the first and second calving event are shown. At the beginning of the simulation the ice shelf has no existing elongation, it is undeformed. The strain curve develops comparable to the stress evolution with a bell-shaped slope and the maximum strain at the surface in some distance d upstream the ice front. Until the critical strain ε_c (black dashed line) is reached for the first time nearly three years are passed based on a linear increase of the strain state with time. The Maxwell model using the reference parameters, see the first line in Table 6.2, results in small-scale calving at a distance of $d = 72\,\mathrm{m}$, thus 12 m less in comparison to the stress criterion. The consequent iceberg is separated from the remaining ice shelf at which the computation is carried on with the states directly before the calving event. Consequently, the ice shelf has now a viscous history, it is already deformed and the next calving situation happens just 39 d after the first one. The blue dashed line in Fig. 6.10 is the initial condition directly after the first termination event. This condition is the starting point and results in the second calving occurrence and thus both curves are illustrated by the same color. Based on the preexisting strain distribution, the achievement of the critical strain is a lot faster in contrast to the undeformed ice shelf. The depicted curves in between these two events give an explanation of the shift of the strain maximum. It starts directly at the ice front and develops to a new critical strain maximum in a distance $d = 17\,\mathrm{m}$ upstream the calving front. In the magnification on the right side of Fig. 6.10 the strain evolution in time slightly drops after calving as the bending and hence the

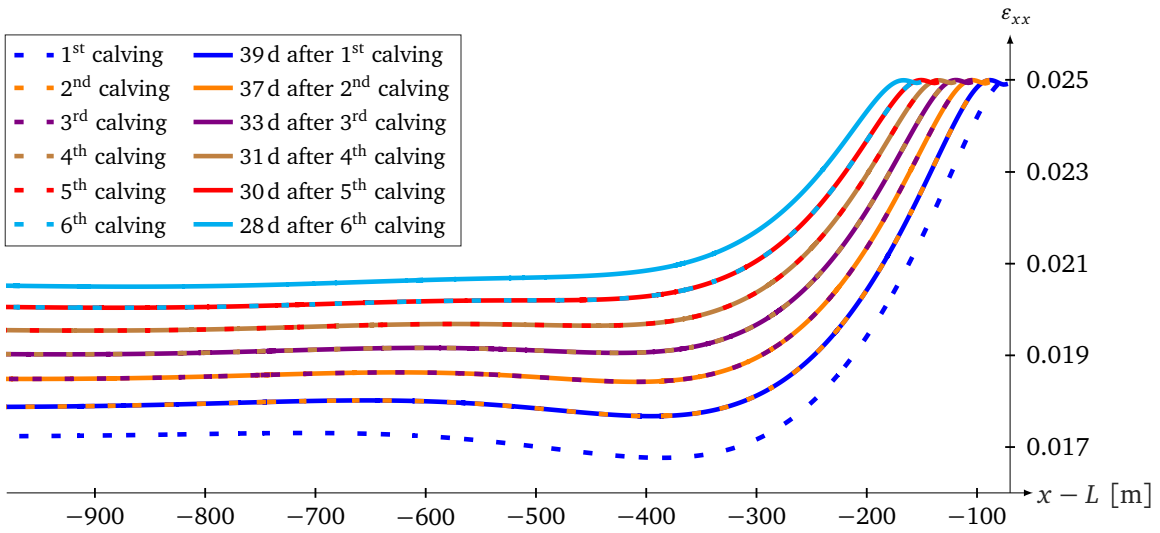

Figure 6.11: Sequence of successive calving events with the initial strain condition depicted by the dashed lines and its resultant strain state shown by the solid lines before the next calving event takes place.

deformation of the new ice front is smaller than before. The strain maximum has to evolve from this strain state at the truncated ice shelf and starts to increase again. Certainly it obtains the critical value faster in comparison to the case of no elongation with an almost linear strain increase caused by the Maxwell model. Even if the deformation at the new ice front is forced to be zero after a calving event, the elongation in the remaining ice shelf and especially the larger values in the vicinity of the ice front will lead to nearly the same termination time like without this assumption. In nature the initial case of no elongation does not occur. The ice shelf extends over the whole length of the grounded ice to the ice front and the calving events after this first initial one are of more interest in the following.
Figure 6.11 shows the sequence of several successive calving events applying the critical strain criterion with $\varepsilon_c = 0.025$. The initial curve directly after a calving event is highlighted by the dashed line in the same color as the solid curve of the subsequent calving event. Termination times to reach the critical strain once more after an iceberg breaks off are additionally given in this figure. The general rise of the strain values in time and thus from one calving situation to the next one is obvious. The strain history in the part not affected by the ice front condition increases linearly to the point where the critical strain value is also obtained there. This results in the total collapse of the modeled ice shelf domain. In addition, the increased elongation of the ice shelf supports the above mentioned process to reach the strain criterion. As a consequence the termination time between two adjacent calving events decreases more and more. For this type of calving criterion the deformation history, the memory of strains from the past leads to an escalation of the calving events with time. In contrast to this the stress states considered for the stress criterion or the self-similarity criterion are unattached by the past experiences of the

ice shelf.
The more detailed image of the strain states near the calving front is given in Fig. 6.12. The distance between two neighboring strain peaks and hence the width of the iceberg is almost constant with respect to time and between 15 m to 17 m for the standard parameters. These dimensions considerably differ from the iceberg width often given in literature of half the thickness to the whole thickness of the ice shelf. The distance $d = 72\,\mathrm{m}$ for the first calving event fits better to this stated interval. To regain this situation the deformation history has to be reset after each calving event. In consequence the time interval between two adjacent calving events and the iceberg widths are constant in time. This seems to be a useful way to define a strain criterion for small-scale calving. However, it is not possible to physically motivate the vanishing deformation history of an ice shelf subsequent to a calving event.
The reliance on the past of the strain criterion arises independently of the critical strain amount. Further computations show that for larger critical values the time needed to obtain the first calving event is higher. On the other side the decrease in the termination time of consecutive calving events is faster for smaller critical strain values. In general the impact of the material parameters on the strain states are instructive because the Maxwell model is the most basic material model to describe the viscoelastic behavior of ice shelves. The variation of crucial quantities in between the possible ranges for ice gives information which of these parameters alter the strain distribution. In particular the viscosity has a nearly linear influence on the time between two calving events and no influence on the iceberg width. Thus its effect is comparable to the statements given for the stress criterion. Indeed this is the only parameter where an increase of the viscosity leads to a larger termination time, while the enlargement of the thickness, the ice density or the elastic parameters result in decreased times between two calving events. Certainly a thicker ice shelf yields larger iceberg widths based on an increased distance of the maximum strain to the ice front. Contrarily a stiffer material or a higher ice density engenders smaller iceberg widths.
The analysis so far shows that the maximum strain value increases almost linearly in time for the viscous as well as the viscoelastic Maxwell material model. Hence a self-similarity criterion based on the strain response is unreasonable as on the one hand no stationary state is reached (convergence criterion). On the other hand, this type of calving criterion leads for certain critical values to the same results than the approach discussed before (critical strain criterion). In the next section the strain response obtained by a nonlinear viscosity with the use of Glen's flow law is investigated to point out differences to the until now assumed constant viscosity.

6.3.3 Glen-type Viscosity

In this section the viscosity is computed in each time step by the use of Glen's flow law, see eq. (2.83). Consequently the viscous material parameter is dependent on

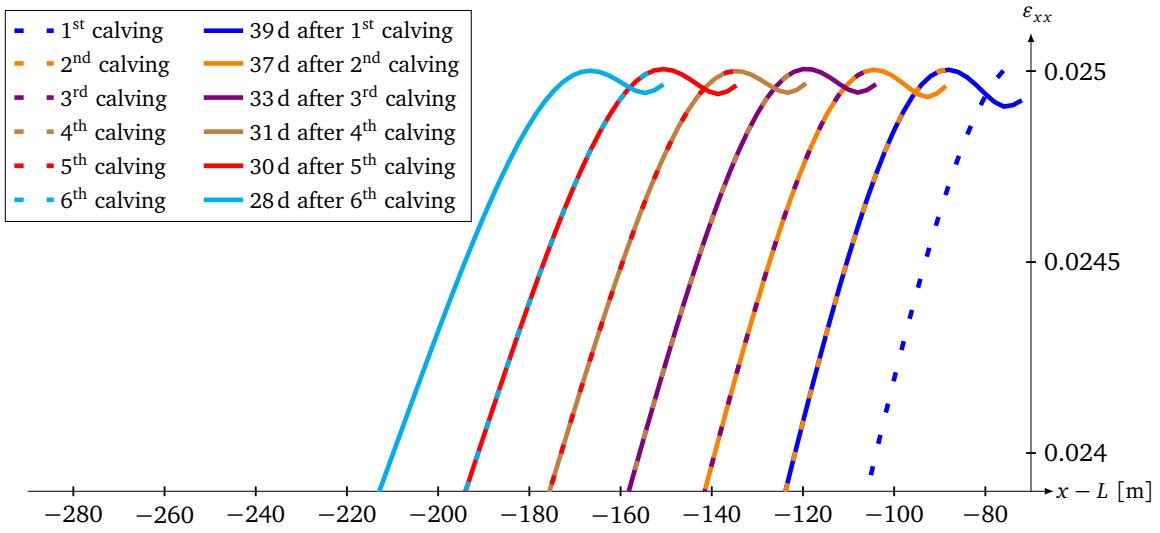

Figure 6.12: Magnification of the successive calving events depicted in Fig. 6.11 near the calving front (dashed lines: initial strain state after calving, solid lines: consequent strain state before calving).

the effective strain rate and hence on the current deformation. The stress exponent $n = 1$ result in a constant viscosity similar to the one considered until now, while Glen's flow law with $n > 1$ is equivalent to a nonlinear viscosity description. For small strain rates an infinite viscosity and thus a singularity may appear in the computation. To overcome this computational problem the initial state for the nonlinear viscosity is computed by a constant value $\eta = 10^{14}\,\mathrm{Pa\,s}$. Furthermore an artificial value near the computational accuracy is added to the effective strain rate to avoid singularities due to numerical issues. In order to obtain a sufficient accuracy of the nonlinear viscosity distribution, the mesh has to be refined. In addition to the mesh improvement at the ice front and the surface within the first 1 000 m using a maximum element length of 1 m, this domain is everywhere improved by a maximum element length of 2 m. Hence, the spatial discretization consists of 1 714 108 elements.

One additional parameter occurs for the viscosity evaluation in Glen's flow law. According to the Arrhenius law this constant is given by $A = 4.9 \cdot 10^{-25}\,1/(\mathrm{s\,Pa^3})$ in Greve and Blatter (2009) for the stress exponent $n = 3$. For the beginning of the simulation the largest variation of the viscosity is located at upper part near the ice front. This is caused by the traction-free stress condition of the freeboard as the effective strain rate is greatest in this area. The remaining viscosity has only small variations around $\eta = 3 \cdot 10^{14}\,\mathrm{Pa\,s}$. In Fig. 6.13 the viscosity near the ice front is depicted for the deformed ice shelf after one year. The highest viscosity is still near the freeboard condition and additionally in the front part close to the bottom boundary. The back pushing pressure from the sea water is clearly identifiable due to the deformation illustrated in this figure. In the rest of the ice shelf domain a nearly constant value $\eta = 6.4 \cdot 10^{12}\,\mathrm{Pa\,s}$ is computed, which is more than one order

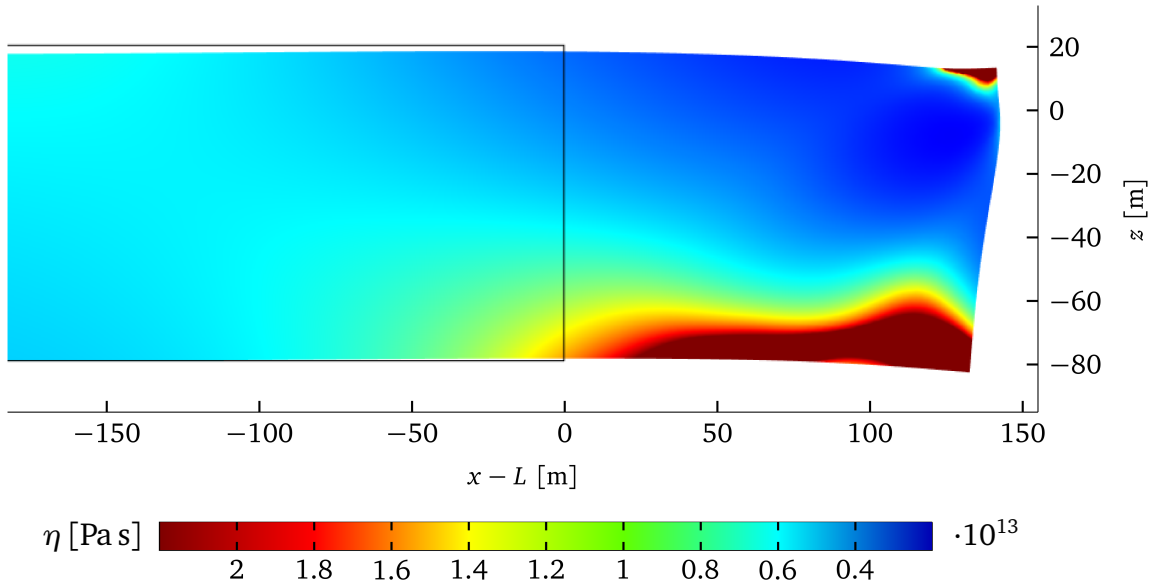

Figure 6.13: Nonlinear viscosity distribution using Glen's flow law after $t = 1\,\mathrm{a}$ at the deformed ice shelf in the vicinity of the ice front. The gray box depicts the undeformed ice shelf geometry.

of magnitude smaller than the constant viscosity assumed so far.
With this rate-dependent viscosity that decreases in time, the faster increase of the maximum strain value shown in Fig. 6.14 is comprehensible. Using the viscosity based on Glen's flow law (blue curve in Fig. 6.14) causes an almost linear increase of the strain maximum with a steeper slope compared to the constant viscosity $\eta = 10^{14}\,\mathrm{Pa\,s}$ (green curve in Fig. 6.14). An extreme in time of this crucial quantity is reached when the freeboard is nearly zero meaning that the ice surface near the front is close to the water surface. This is only possible due to the contravention of the buoyancy equilibrium in the small deformation model to guess out of Fig. 6.13. After the achievement of the maximum strain value the blue curve shows a strain decrease followed by a nearly constant value. However, this model of viscoelasticity is only valid for small strains specified by the linearized strain-stress relation. The results for an elongation larger than $0.1 \mathrel{\widehat{=}} 10\,\%$ should be mistrusted. In the end, the nonlinear viscosity in a small deformation model can also be described with a constant viscosity as the response of the maximum strain in the ice shelf domain increases almost linearly restricted to small strains. Additionally, the position at $d = 76\,\mathrm{m}$ of the strain maximum after $t = 1\,\mathrm{a}$ is close to the result if a constant viscosity is applied. An increase of the parameter A described by the Arrhenius law leads to an increase of the viscosity and hence a smaller slope for the strain maximum is achieved.

All results in this chapter are obtained without the consideration of the ice shelf velocity from which the stress and strain states are independent of. The outcomes induce additional quantities to be combined with the flow velocity to get calving

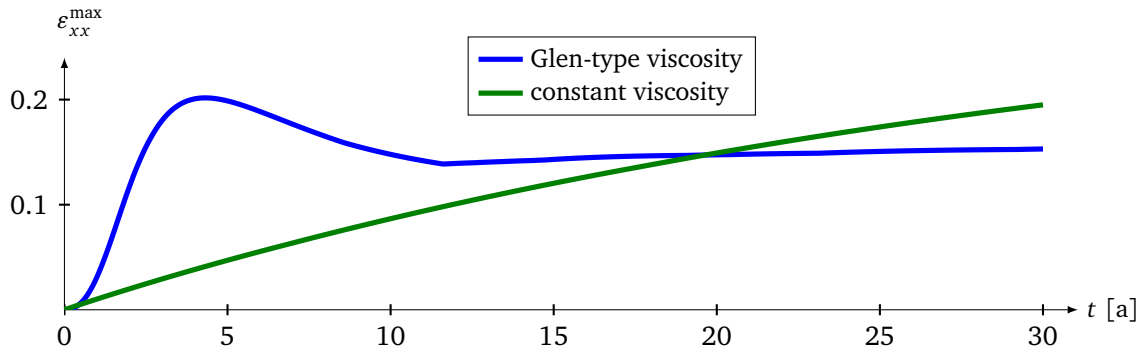

Figure 6.14: Maximum strain distribution in time using either the nonlinear Glen-type viscosity or the constant viscosity $\eta = 10^{14}$ Pa s of the previous section.

rates. In order to obtain these rates the simulation has to run for a convincing number of successive calving events. However, the deformation of the ice shelf after several years lead to senseless results where the surface of the ice shelf lowers more and more, while the bottom boundary remains unchanged in a model assuming the simplification of small deformations. Even in Fig. 6.13 this problem slightly appears, although the maximum strain value is only 3 %. The larger the strain values get (> 10 %) the more problematic is the disregard of the buoyancy equilibrium as the linearized kinematic relation assumed for the Maxwell model is violated. Hence, the finite deformation model of a Maxwell material and its consequent effect on the stress and strain states are the topic of the next Chapter 7. This more complex model approach reveals first of all results where buoyancy equilibrium is satisfied all the time.

7 Viscoelasticity for Finite Deformation

In the following the theory of finite viscoelasticity, described in Section 2.7, is implemented by 3d finite element models in COMSOL. The aim to implement these more sophisticated model formulations is to analyze the time period in which the simplified small deformation model is inappropriate. For comparison of stress or strain behaviors, the state of plane strain is also assumed for the finite viscoelastic models by a suitable choice of boundary conditions, see Section 3.3.
In the case of finite deformations, the implemented model has to solve the quasi-static momentum balance and the corresponding evolution equations either in the reference or the current configuration. The choice of the formulation is not unique as stress or strain quantities for example in the reference configuration are convertible to the current configuration. However, it is important to formulate all equations required for the calculation of the unknown displacements in the same configuration. In this work, the model equations are specified in the reference configuration, see Section 2.7. The Cauchy stress tensor and all other quantities needed in the current configuration are computed in a post-processing step. The slight gain of the formulation in the reference configuration is that the traction boundary conditions are stated with respect to the initial geometry $\boldsymbol{T} = \boldsymbol{P}\boldsymbol{N} = pJ\boldsymbol{F}^{-T}\boldsymbol{N}$ with p the water pressure in the actual configuration but $\boldsymbol{N}$ the normal vector in the reference configuration. Hence, the computation of the normal vector $\boldsymbol{n}$ of the current configuration is not necessary for each time step.
First, the Saint Venant-Kirchhoff formulation is applied to describe the elastic response in the finite viscoelastic material. In addition, the lower Oldroyd rate is used as an objective time derivative for the viscous flow relation. Later on, the influence of the neo-Hookean material description and the upper Oldroyd rate are examined to compare the results for different constitutive equations of finite viscoelastic models.

7.1 Mesh

In this section the influence of the mesh is examined. It is very important to model the boundary conditions sufficiently exact by the applied mesh to obtain reasonable stress and strain results during the simulation.
Figure 7.1 shows a mesh, which has a maximum element length on all boundaries of $l_{\max} = 3\,\mathrm{m}$ and thus 752 238 degrees of freedom. In the same figure, the corre-

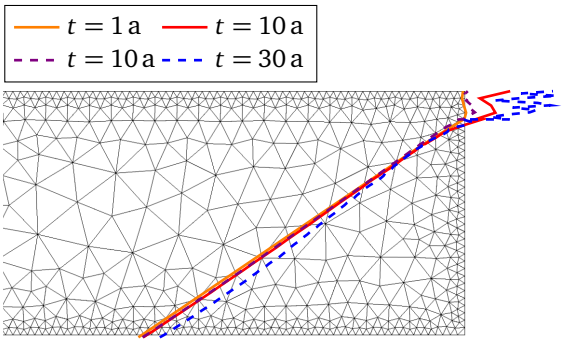

Figure 7.1: Initial mesh including the x-component of the traction $(\boldsymbol{\sigma n})_x$ at the ice front boundary for different points in time: solid lines for a maximum element length of $l_{\max} = 3\,\mathrm{m}$ at the boundaries, dashed lines for $l_{\max} = 1\,\mathrm{m}$.

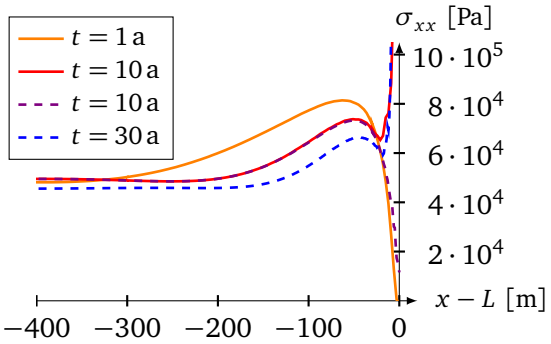

Figure 7.2: Stress σ_{xx} in flow direction at the upper surface, colors are chosen consistent to the traction component in Fig. 7.1: solid lines for a maximum element length of $l_{\max} = 3\,\mathrm{m}$ at the boundaries, dashed lines for $l_{\max} = 1\,\mathrm{m}$.

sponding x-component of the traction $\boldsymbol{t}_x = (\boldsymbol{\sigma n})_x$ in the actual configuration depicts the nature of the current stress state in normal direction at the ice front boundary. For these investigations, only the shape of these stress states is important and not the exact values. The selected traction component has to model the water pressure p, which is specified through the applied boundary conditions, as accurately as possible. Hence, the traction component in flow direction has to be zero at the freeboard and the compressive stress has to linearly increase with depth. The solid orange curve in Fig. 7.1 nearly illustrates this behavior for $t = 1\,\mathrm{a}$ and $l_{\max} = 3\,\mathrm{m}$. At a later point in time, the quality of the mesh is not sufficient to model the applied ice front condition shown by the solid red curve for $t = 10\,\mathrm{a}$. Especially at the freeboard, the traction component is not zero anymore and shows fictitious oscillations. The consequent effect on the stress in flow direction at the upper surface is illustrated in Fig. 7.2 by the solid red curve at $t = 10\,\mathrm{a}$. Based on the non-zero traction value of the upper right corner at the ice front, the stress value has a misleading maximum directly at the ice front. Indeed, the solid orange curve for $t = 1\,\mathrm{a}$ describes the bell shaped stress curve based on the bending moment at the ice front and the stress value of zero at the upper right corner much better. In order to show that the problem for $t = 10\,\mathrm{a}$ is explainable by the quality of the mesh and more precisely by the element length of the mesh on the boundaries, the dashed lines depict the results for $l_{\max} = 1\,\mathrm{m}$. In this case, the model has 1 851 030 degrees of freedom. The dashed purple line in Fig. 7.1 is closer to the actual applied ice front condition than the solid red curve at $t = 10\,\mathrm{a}$. In addition, the value of the dashed purple line at the upper right corner is nearly zero. Hence, the corresponding stress component in flow direction in Fig. 7.2 depicts a more sensible result for the refined mesh near the ice front. Nevertheless, the maximum stress value, which is located at some distance to the ice front, is similar for the two different meshes and differs only about 0.7 %. Main differences of these two meshes occur in the area, where the

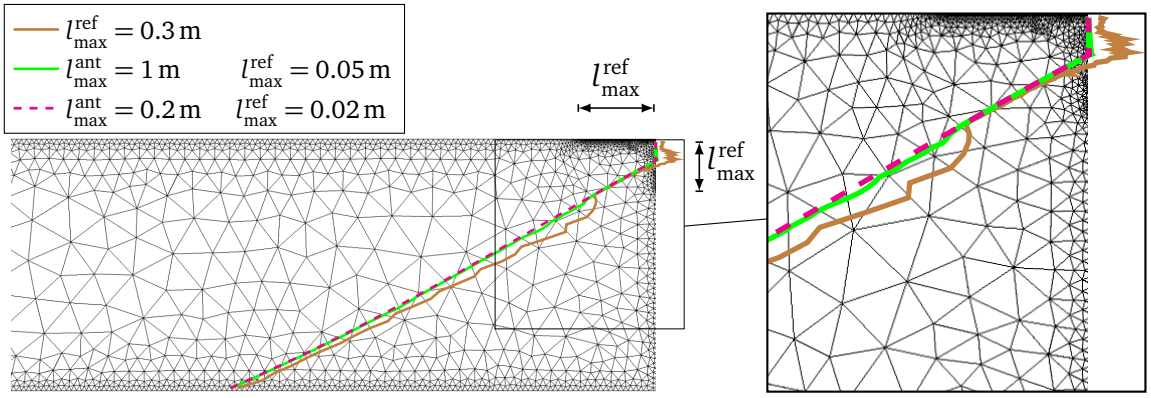

Figure 7.3: Initial mesh that includes the x-component of the traction $(\boldsymbol{\sigma n})_x$ at the ice front boundary for different meshes at $t = 30\,\text{a}$: maximum element length of $l_{\max} = 3\,\text{m}$ at all boundaries, refinement $l_{\max}^{\text{ant}}$ at all adjacent boundaries up to 300 m from the ice front and additional refinement $l_{\max}^{\text{ref}}$ in the area near the freeboard.

stress values for the coarser mesh begin to rise, which happens at a distance of 21 m away from the ice front. By an expansion of time to $t = 30\,\text{a}$ the oscillations in the area of the freeboard also increase for the refined mesh. Hence, the finer mesh leads to a delayed occurrence of mesh artifacts verifiable by the non-zero stress state at the upper right corner.

The analysis above shows that an overall decrease in the element size at the boundaries will lead to better results, but for later points in time (in this case $t = 30\,\text{a}$) further refinements are necessary. However, these mesh improvements are not needed in areas further away from the ice front as no doubtful features occur there. Hence, the mesh is refined in certain areas, where the results show a mesh sensitivity and a refinement is required. Figure 7.3 displays a mesh with the maximum element length $l_{\max} = 3\,\text{m}$ on all boundaries. In addition, the mesh is refined with a maximum element length $l_{\max}^{\text{ref}} = 0.3\,\text{m}$ at the upper surface up to 30 m from the ice front as well as in the upper part of the ice front up to 10 m below the water surface. This mesh has 816 372 degrees of freedom and the computational costs are barely higher than for the case of $l_{\max} = 3\,\text{m}$ at all boundaries, the respective mesh without selectively refined boundaries. The brown curve in Fig. 7.3 suggests that the vanishing x-component of the traction at the freeboard is better approximated by the coarser mesh with $l_{\max} = 3\,\text{m}$ and refined areas with $l_{\max}^{\text{ref}} = 0.3\,\text{m}$ than in the case of the finer mesh with $l_{\max} = 1\,\text{m}$ everywhere, cf. Fig. 7.1. The actual values are even more than 6 times smaller, namely $\max(\boldsymbol{\sigma n})_x^{1\text{m}} = 184.8\,\text{kPa}$ and $\max(\boldsymbol{\sigma n})_x^{3\text{m},0.3\text{m}} = 29.1\,\text{kPa}$. The positive impact of the partly refined mesh on the stress state is obvious, although small oscillations are still visible for the brown curve in Fig. 7.4. However, another problem appears for this mesh. In particular, larger variations arise in areas, where the finer grid changes into the coarser mesh. To avoid on the one hand these problems in the transition zone, the maximum element length $l_{\max}^{\text{ant}}$ is introduced at all adjacent boundaries up to 300 m. Thus, the mesh is refined in smaller steps. On the other hand, the oscillations are reduced by a further decrease of $l_{\max}^{\text{ref}}$ to 0.05 m,

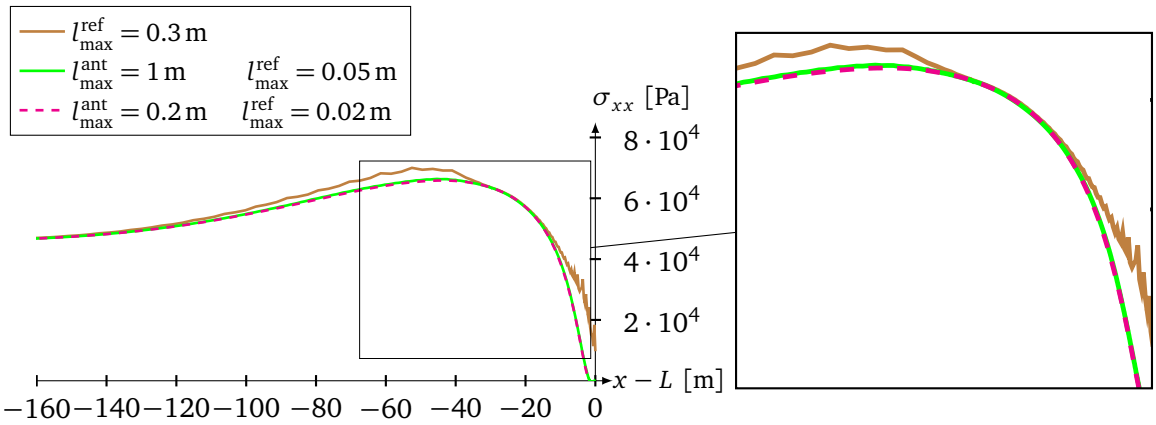

Figure 7.4: Stress σ_{xx} in flow direction at the upper surface at $t = 30\,\text{a}$, colors are chosen consistent with the traction component in Fig. 7.3 and their corresponding refined meshes are the same.

which yields 1 696 671 degrees of freedom for this mesh. As a result, the pressure of the sea is well transferred to the traction component in the flow direction, see the green curve in Fig. 7.3. Additionally, the oscillations in the stress curve, cf. Fig. 7.4, are avoided. Only slight variations are observable in the transition zone of the mesh at the ice front. To clarify the effect of this feature, an additional refinement provides the results for $l_{\max}^{\text{ant}} = 0.2\,\text{m}$ and $l_{\max}^{\text{ref}} = 0.02\,\text{m}$. This mesh creates a finite element model with 5 962 533 degrees of freedom. The improvement on the stress state at $t = 30\,\text{a}$ is not noticeable. Thus the former mesh is sufficient to compute the stress and strain states at the boundaries.
In conclusion, the optimization of the mesh is important and in particular depends on the simulation time. On the one hand, it has to be small enough to solve the current problem without unacceptable mesh sensitivity and artifacts. On the other hand, the computational costs should be minimized.

7.2 Buoyancy Equilibrium

In this part, the effect of the geometry is demonstrated using the finite deformation model instead of the one that is only valid for small deformations. The positions of the upper and bottom surfaces of the idealized ice shelf are analyzed in time using the constant thickness $H = 100\,\text{m}$. The initial position of the surfaces is based on the buoyancy equilibrium and therefore the bottom surface is located at $z = -H_{\text{sw}} = -H\rho_{\text{ice}}/\rho_{\text{sw}}$ below sea level. The sea water density $\rho_{\text{sw}} = 1028\,\text{kg/m}^3$ and the ice density $\rho_{\text{ice}} = 910\,\text{kg/m}^3$ result in the location of the bottom surface at $-H_{\text{sw}} = -88.5\,\text{m}$. Consequently, the upper surface is located $H_{\text{s}} = H - H_{\text{sw}} = 11.5\,\text{m}$ above sea level.
Figure 7.5 shows the current positions of the geometry near the ice front after a simulation time of 30 a. For this computation, common material values for ice are

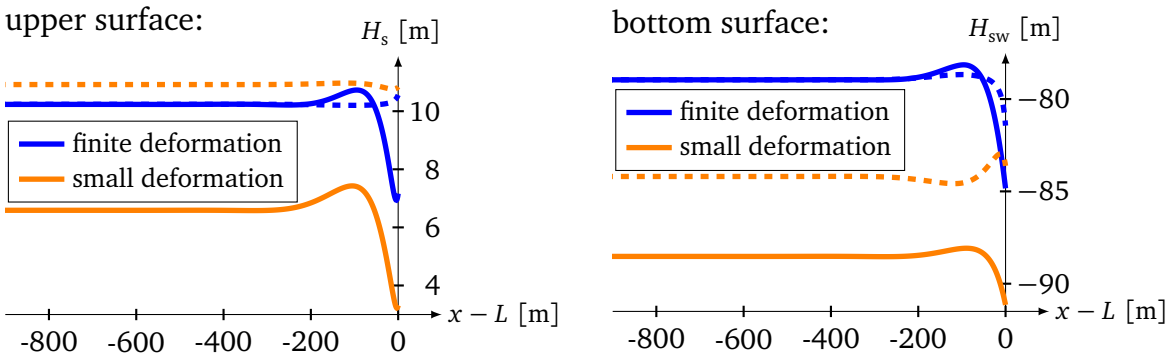

Figure 7.5: Position of upper and bottom surface after 30 a using the concept of small and finite deformation, respectively; dashed lines show the current positions of the buoyancy equilibrium.

assumed, i.e. Young's modulus $E = 9\,\text{GPa}$, Poisson's ratio $\nu = 0.325$, and the viscosity $\eta = 10^{14}\,\text{Pa s}$. The orange curves depict the results assuming the simplification of small deformations. Directly at the ice front, the location of the ice shelf is disturbed and a local variation of the buoyant equilibrium is possible. With enough spatial distance to the influenced area of this boundary perturbation, the position of the bottom surface stays constant with time at $-H_{sw} = -88.5\,\text{m}$, see the solid orange curve in Fig. 7.5 (right). However, the upper surface monotonically decreases with time and the consequent value of $H_s = 6.6\,\text{m}$ at $t = 30\,\text{a}$ is depicted by the orange line in Fig. 7.5 (left). Thus, the deformed ice shelf diminishes with time although the position of the bottom surface remains unchanged. This leads to the unphysical case that the buoyancy equilibrium is not fulfilled. In order to illustrate this problem, the actual equilibrium position is depicted by the dashed orange curves for the current ice shelf geometry assuming small deformations. The upper and bottom surface location do not coincide with the equilibrium position. However, the buoyancy force has to balance the weight of the floating ice at a certain distance to the ice front. In the small deformation model, the weight of the ice is constant in time although the thickness reduces based on the displacement w at the upper surface. A distinction between different configurations and their adapted internal and external forces is not possible. Hence, the buoyancy boundary condition at the bottom is always related to the initial configuration and thus, the weight of the ice shelf at the beginning of the simulation. This means that the boundary condition at the bottom does not account for the geometry variation due to the displacement w at the upper surface. In addition, the weight is not updated. Thus, the position of the bottom is still constant in time while the position at the upper surface decreases as the viscous ice flows under its own weight into the ocean.
In order to overcome this problem, the formulation for large deformations is used. The positions of the upper and bottom surface for this formulation are depicted by the blue curves in Fig. 7.5. A finite deformation model obviously satisfies exactly the buoyant equilibrium away from the boundary disturbed part at the ice front. The reason is that the weight of the ice and the boundary conditions depend on

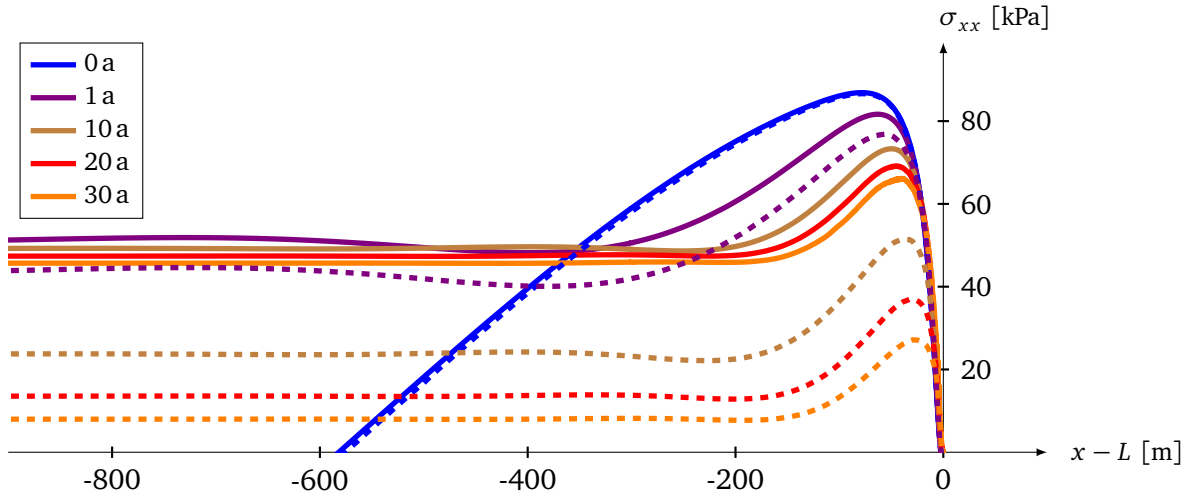

Figure 7.6: Stress component σ_{xx} at the upper surface using the concept of finite deformation (solid lines) in contrast to the assumption of small deformations (dashed lines).

the deformation gradient. Hence, the internal and external forces are adapted to the actual geometry in each time step. Furthermore, the two formulations reveal to two different geometries based on the unequal retention force of the ice front boundary condition. With the simplification of small deformations, the freeboard of the ice shelf becomes smaller although the part under water stays the same. The stress resultant in normal direction due to the water pressure is constant at the ice front boundary. The viscous flow of the ice in this case is less than the flow for the finite deformation model, where the ice shelf geometry decreases in time and the buoyant equilibrium is fulfilled. Thus, the retention force of the ice front boundary becomes smaller with time. For the finite deformation formulation, the ice shelf spreads horizontally faster than in the case assuming small deformations.

7.3 Stress State

Next, the effect of the finite deformation model on stress states is considered to demonstrate the influence of the two different formulations on calving. The discussion above illustrates that after 30 a different geometries with various freeboard thicknesses are developed by the finite and small deformation model. As the stress state is highly dependent on the geometry and especially on the freeboard, the chosen formulation will critically affect the results. The model assuming only small deformations will describe the results in the beginning sufficiently as the deformations and thus the strains are small. With an increase of the simulation time, the differences become larger based on growing deformations in flow direction. Hence, the point in time is of interest until the small deformation model provides tolerable approximations of the stress states.

For this study, common reference values for ice shelves are assumed, i.e. the ice density $\rho_{\text{ice}} = 910\,\text{kg/m}^3$, the sea water density $\rho_{\text{sw}} = 1028\,\text{kg/m}^3$ and for instance a constant thickness $H = 100\,\text{m}$. In addition, typical material values are Young's modulus $E = 9\,\text{GPa}$, Poisson's ratio $\nu = 0.325$, and a constant viscosity $\eta = 10^{14}\,\text{Pa s}$. The largest tensile stresses, caused by the boundary disturbance at the ice front, occur for the finite and the small deformation model at the upper surface in flow direction (σ_{xx}). A comparison of the stress distributions at the upper boundary is depicted in Fig. 7.6 for different points in time. The solid lines in this figure show the results for the finite deformation formulation and the dashed lines the results computed with the assumption of small deformations. At the beginning, the stress curves of the two formulations coincide. With increasing simulation time the stress states differ more and more based on grown deformations due to the viscous ice flow. The stresses for finite viscoelasticity are always larger than the ones assuming small deformations. This is due to the faster decrease of the freeboard computed with the assumption of small deformations, cf. Section 7.2, as a smaller freeboard induces smaller tensile stresses. Hence, the necessity to model the freeboard thickness as accurate as possible is observable.
Crucial differences occur at the latest when $t = 10\,\text{a}$, see the brown curves in Fig. 7.6. The maximum stress values at this point in time differ around 30 % and the linearized strain ε_{xx} in flow direction reaches a maximum of 0.07. In the part of the ice shelf that is not influenced by the ice front disturbance ($x - L \leq -700\,\text{m}$), the stress states deviate around 52 % at $t = 10\,\text{a}$. However, differences are also visible at $t = 1\,\text{a}$, where the maximum of the dashed purple curve is 6 %, namely 4.8 kPa, smaller than the maximum of the solid purple curve. The continuous small-scale calving, investigated in this work, happens on time scales of several months to few years. Thus, the selected formulation will also influence the results for this kind of calving. This influence is examined more precisely in the following.

Influence of the Material Parameters

It is sufficient to consider only the evolution of the maximum stress value. A crack will originate and hence, small-scale calving will occur only dependent on this value if a stress criterion is applied. In order to demonstrate crucial differences between the maximum stress values, parameter studies of characteristic material values of ice are carried out for the small- and finite deformation approaches. These studies include uncertainties of material parameters as they cover the range of possible variations by extremal values for polycrystalline ice.
Figure 7.7 depicts the maximal stress value of σ_{xx} in the whole ice shelf with respect to time for different Young's moduli, which range from 1 to 9 GPa. As discussed above, this maximum stress is located at the upper surface during the examined time interval. All other parameters are the same as mentioned before for Fig. 7.6. The model for finite deformations yields the stress states denoted by the solid lines in Fig. 7.7 and the dashed lines result from the model that assumes

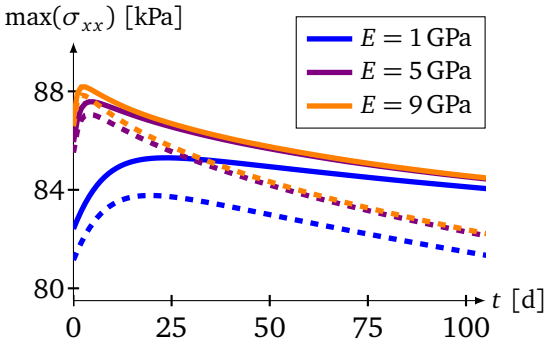

Figure 7.7: Maximum stress at the upper surface with time dependent on E using the concept of finite deformation (solid lines) and small deformation (dashed lines).

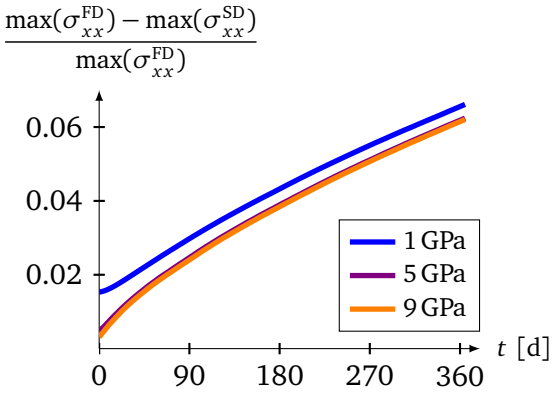

Figure 7.8: Relative difference of the maximum of $\sigma_{xx}^{\mathrm{FD}}$, the stress value computed with finite deformations, and the maximum of $\sigma_{xx}^{\mathrm{SD}}$, the stress of the small deformation model.

small deformations. The difference of the finite to the small deformation model is rather insignificant in the beginning, more precisely 0.3 % for $E = 9\,\mathrm{GPa}$ up to 1.6 % for $E = 1\,\mathrm{GPa}$. Consequently, the offset of the initial results is 20 times lesser than the one after one year due to small deformations at the beginning, see Fig. 7.8. A deviation more than 10 % occurs after almost 2 a with ε_{xx} around 0.01. In the early stages the results of finite viscoelasticity with higher computational costs are well approximated by the model only valid for small deformations. In order to model small-scale calving, the difference of stress values is of most interest until the maximum stress in time is reached. The differences at this point range between 0.5 % reached at $t = 2\,\mathrm{d}$ for $E = 9\,\mathrm{GPa}$ and 1.8 % reached at $t = 24\,\mathrm{d}$ for $E = 1\,\mathrm{GPa}$. These relative small variations will add up if the ice shelf is analyzed over a sequence of several calving events as the stress and deformation states are carried over in the remaining ice shelf. Impacts of this progression need to be analyzed in greater detail. However, the mesh of the remaining ice shelf after a calving event is not sufficient at the new ice front anymore, see Section 7.1. Additional mesh points have to be included and the values at these new points need to be interpolated. Thus, this approach is not straightforward feasible and not discussed subsequently.

The convergence of the solid as well as the dashed lines in Fig. 7.7 with time demonstrates that the influence of different Young's moduli is limited to the start of the simulation. The larger the Young's modulus, the shorter is the time interval of its influence. This fits to the characteristic of a Maxwell material, in which the elastic response is predominant immediately after a change in the stress situation and decreases dependent on the characteristic time $\bar{\tau} = \eta/\mu$. Hence, it is essential to determine the elastic parameters as exactly as possible for the situation shortly after a calving event. In this case, the boundary condition at the new ice front of the remaining ice shelf causes that the stress state there differs from the state

prior to calving. The maximum stress value from $E = 9\,\text{GPa}$ to $E = 1\,\text{GPa}$ differs more than 3 %, namely 2.9 kPa, for finite viscoelasticity. Especially, the time to reach this maximum varies around 22 d for different Young's moduli as discussed above. Considering only one calving event, the impact of a realistic Young's modulus on calving and its rate is hence more important than an extension to finite viscoelasticity.

The stress in flow direction computed with the model that assumes only small deformations is denoted by σ_{xx}^{SD}, while σ_{xx}^{FD} stands for the stress of the finite deformation model. The relative difference between the maximum of these stresses is more precisely shown in Fig. 7.8. This difference increases monotonically with time, however, the slope of the relative difference decreases. Accordingly, the results of the two different formulations differ increasingly, but the largest increase of the relative difference occurs directly at the beginning. Figure 7.8 also shows the relative difference of 6 %, which is reached after only one year. In general, the same analysis is possible for the position of the upper right corner directly at the ice front not shown in the here considered plots. This location indicates the time evolution of the freeboard thickness as the z-axis originates at the water surface. It is important to consider the freeboard thickness as this quantity mainly causes the tensile stress behavior and the development of the maximum tensile stress at the upper surface in time. The general tendency is similar to the maximum stress value with respect to time (cf. Fig. 7.7), at first the freeboard thickness slightly increases, before it monotonically decreases. The maximum value of the upper right corner in time is reached a few days earlier than the maximum stress value. The relative difference of the freeboard thickness for the different model formulations reaches 3 % (0.32 m) after one year and describes an almost linear growth. For that reason, the decrease of the stress state is not exactly proportional to the decrease of the freeboard, however both experience a comparable behavior.

Depending on the model formulation, the impact of the not yet investigated material parameters, namely Poisson's ratio ν and the viscosity η, is discussed in the following. Figure 7.9 is created with the same model parameters as Fig. 7.7, except that Young's modulus is $E = 9\,\text{GPa}$, while Poisson's ratio (left plot) and the viscosity (right plot) are varied. The influence of an incompressible elastic material is illustrated by a Poisson's ratio of $\nu \approx 0.5$ in the left plot of Fig. 7.9. In this case, the maximum stress in time is reached at $t = 0$ and decreases monotonically with respect to time. Hence, the stress trend coincides with the stress result of the small deformation model and a stress criterion for small-scale calving is not feasible. Additionally, the limited influence of different Poisson's ratios during the first days is proven through the convergence of the solid and the dashed lines, respectively. This confirms the expected behavior of the finite viscoelasticity described through a Maxwell material, as the influence of both elastic parameters E and ν is restricted to the initial period of time.

In order to show the influence of the only viscous quantity in the model, the constant viscosity η is varied within a possible viscosity interval of ice. The right plot

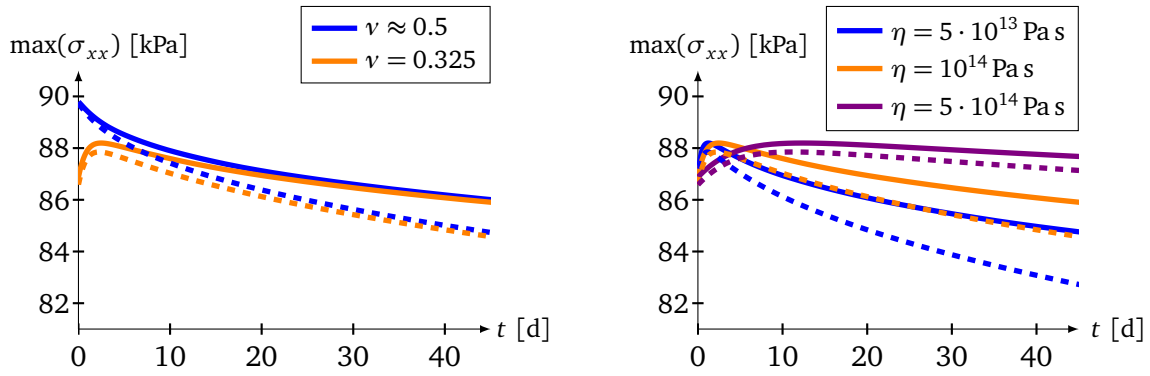

Figure 7.9: Maximum stress at the upper surface with time dependent on ν (left) and η (right) using the concept of finite deformation (solid lines) and small deformation (dashed lines).

of Fig. 7.9 illustrates the maximum stress results with time, where the viscosity η ranges from $5 \cdot 10^{13}$ Pa s to $5 \cdot 10^{14}$ Pa s. It is obvious that the higher the viscosity, the slower is the ice flow and therefore, the longer becomes the time interval, in which the assumption of small deformations yields sufficient results. However, the initial stress does not depend on the viscosity. For the beginning at $t = 0$ d, the relative difference between the maximum of the stresses $\sigma_{xx}^{\mathrm{SD}}$ and $\sigma_{xx}^{\mathrm{FD}}$ is the same for all three viscosities, namely 0.3 %. The point where this relative difference is larger than 1 % is observed at $t = 12$ d for $\eta = 5 \cdot 10^{13}$ Pa s, at $t = 23$ d for $\eta = 10^{14}$ Pa s, and at $t = 111$ d for $\eta = 5 \cdot 10^{14}$ Pa s. Thus, the viscosity and the relative difference correlate almost linear. For the model assuming small deformations, the nearly linear dependence of the viscosity and the stress result was already shown. Hence, the relation of the stress response to the viscosity is also roughly linear for finite viscoelasticity.

Influence of Geometric Parameters

The crucial influence of the freeboard on the stress behavior is already discussed above. The stress states and the evolution of the freeboard are related to each other. It is obvious that geometric parameters such as the thickness or the ice density have a crucial effect on the freeboard extension. Thicker ice shelves have larger freeboards and hence the stresses, especially the maximum of the tensile stresses, are higher. This behavior was already shown for the small deformation model, see Section 6.2.1.

To compactly depict the maximum stress values as a function of the thickness H with respect to time in only one image, the maximum $\max(\sigma_{xx})$ is multiplied by the factor H_{ref}/H. This means that the stress states for the reference quantities with $H = H_{\mathrm{ref}} = 100$ m are unchanged. However, the stress values for the thicknesses $H = 200$ m and $H = 300$ m are divided by 2 and 3, respectively. Thus, the blue and violet curves in the left plot of Fig. 7.10 do not indicate that the stress

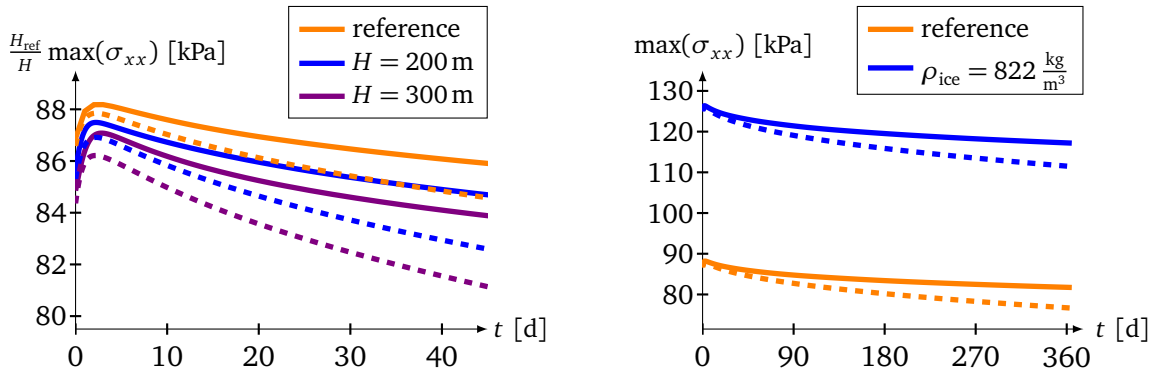

Figure 7.10: Maximum stress at the upper surface with time dependent on H (left, $H_{ref} = 100\,m$) and ρ_{ice}(right) using the concept of finite deformation (solid lines) and small deformation (dashed lines).

values decrease for thicker ice shelves. Instead, it shows that the maximum stress evolution for thicker ice shelves, for instance of $H = 200\,m$, is a bit smaller than two times the maximum stress values of $H = 100\,m$.
In Fig. 7.10 (left), the results for the finite viscoelastic material model as well as for the model that assumes only small deformations are included by solid and dashed lines. The maximum stress behavior is similar for different thicknesses, after a slight increase the maximum stress monotonically decreases in time. However, the relative difference between the maximum stress with respect to time of the finite and small viscoelasticity increases with the thickness of the ice shelves. A relative difference of 0.5 % for $H = 100\,m$ rises to 0.7 % for $H = 200\,m$ and reaches 1 % for $H = 300\,m$. In general, the deviations of the stresses for the two different model formulations increase faster for thicker ice shelves.
Finally, the influence of the ice density is discussed. The right plot of Fig. 7.10 illustrates the considerable increase of stresses due to a decrease of the ice density. For both material models, this is can be explained by the inverse relation of the ice density and the freeboard. If the ice density gets smaller, the freeboard extension will increase and hence, the tensile stresses will get larger. The curves of the reference quantities as well as the curves of the reduced ice density keep almost the same distance between the solid and dashed lines. Hence, the offset of the stresses based on the model formulation is nearly independent of the ice density.

Position of the Maximum Stress

So far, the maximum of the tensile stress in dependence on material and geometric parameters was analyzed with time. In order to compute a calving rate, the iceberg width and therefore, the position of the next calving event is additionally of importance. If a stress criterion for calving is used, the iceberg width will coincide with the distance of the maximum stress to the ice front.
Table 7.1 summarizes the maximum tensile stresses along the whole ice shelf and the simulation time for the most important material and geometric quantities. In

addition, the distance to the ice front and the evaluation time, when these stresses are achieved, are also included. The values in black are computed by the finite viscoelastic Maxwell model, while the gray values are obtained for the model that is only valid for small deformations. The position of the maximum stresses for the finite viscoelasticity varies slightly with the elastic material parameters but independent of the viscosity. This was already expected based on the results of the small deformation model. The distance $d\left(\sigma_{xx}^{\max_{x,t}}\right)$ increases almost linear with the thickness of the ice shelf and its position is shifted away from the ice front with decreasing ice density. Hence, the geometry has to be determined as accurately as possible to obtain sufficient approximations for the distance of the maximum tensile stress to the ice front. The material parameters are not that important for this analysis. In contrast, to determine the timespan to reach the maximum stress, the results of the small deformation model are transferable to finite viscoelasticity. This means that the timespan is only dependent on the material parameters and hence, the characteristic time of the Maxwell model and not on the geometry.
Furthermore, the maximum stress in the whole ice shelf after one year and its distance to the ice front are also presented in Table 7.1. The stress values and the distances are underestimated by the model that assumes small deformations. After one year, the influence of different elastic parameters is negligible as their consequent stress and distance results are alike to the reference values. In addition, the viscosity has a rather small impact on the maximum tensile stress in contrast to the effect of different geometries or ice densities.

7.4 Strain State

In the small deformation model, the Green-Lagrange strain tensor $\boldsymbol{E}$ of the reference configuration and the Euler-Almansi strain tensor $\boldsymbol{e}$ of the current configuration coincide with the linearized strain tensor $\boldsymbol{\varepsilon}$. The largest strain component is the strain in flow direction inside an ice shelf. For the case of small deformations, this component is located at the upper boundary and the critical strain value for small-scale calving is given by $\varepsilon_{\mathrm{c}} = 0.025$, see Section 6.3.2.
In order to determine a physics-based calving rate, a strain criterion can also be used in the context of finite viscoelasticity. One possible criterion is that the ice shelf will calve, if the strain component in flow direction reaches a critical value. For the finite viscoelastic model, the strain measures of the reference and the current configuration differ. In this work, the Euler-Almansi strain tensor $\boldsymbol{e}$ is examined as the strain in the current configuration is a measure of the actual elongation of the ice shelf.
In Fig. 7.11, the maximum of the strain component in flow direction e_{xx} is analyzed in time. This maximum value occurs at the upper surface due to the lack of the retention force of the sea water at the freeboard. The reference values are chosen similar to the stress investigation, with $H = 100\,\mathrm{m}$, $\rho_{\mathrm{ice}} = 910\,\mathrm{kg/m^3}$, $\rho_{\mathrm{sw}} = 1028\,\mathrm{kg/m^3}$, $E = 9\,\mathrm{GPa}$, $\nu = 0.325$, and $\eta = 10^{14}\,\mathrm{Pa\,s}$. Based on the nearly constant ice front

study	$\sigma_{xx}^{\max_{x,t}}$ [Pa]	$d\left(\sigma_{xx}^{\max_{x,t}}\right)$ [m]	t [d]	$\sigma_{xx}^{\max_{x,t=1\,\mathrm{a}}}$ [kPa]	$d\left(\sigma_{xx}^{\max_{x,t=1\,\mathrm{a}}}\right)$ [m]
reference	$8.82 \cdot 10^4$	85	2	81.7	63
	$8.78 \cdot 10^4$	85	2	76.6	58
$E = 1\,\mathrm{GPa}$	$8.53 \cdot 10^4$	72	24	81.6	63
	$8.38 \cdot 10^4$	70	20	76.5	58
$\nu = 0.5$	$8.98 \cdot 10^4$	98	0	81.7	63
	$8.97 \cdot 10^4$	98	0	76.6	58
$\eta = 5 \cdot 10^{14}$	$8.82 \cdot 10^4$	85	12	85.1	74
	$8.78 \cdot 10^4$	85	11	83.3	70
$H = 200\,\mathrm{m}$	$17.50 \cdot 10^4$	163	2	159.5	119
	$17.38 \cdot 10^4$	161	2	143.4	106
$H = 300\,\mathrm{m}$	$26.12 \cdot 10^4$	240	2	235.2	171
	$25.86 \cdot 10^4$	232	2	203.7	148
$\rho_{\mathrm{ice}} = 822\,\frac{\mathrm{kg}}{\mathrm{m}^3}$	$12.64 \cdot 10^4$	97	2	117.2	74
	$12.60 \cdot 10^4$	96	2	111.4	70

Table 7.1: Magnitude, distance to the ice front and evaluation time of the maximum tensile stress for the concept of the finite viscoelastic Maxwell model in black and the linearized Maxwell model that assumes only small deformations in gray. After one year, the maximum stress values and distances of these stresses are also included.

condition in time, the strain component for these parameter values increases linearly with time, see the orange curve in Fig. 7.11. This means that the sea water pressure is not sufficient to prevent horizontal spreading of the ice shelf. The critical strain $\varepsilon_{\mathrm{c}} = 0.025$ is reached after $t = 4\,\mathrm{a}$ to identify more exactly maximum strain differences in this parameter study.

The change of one elastic material parameter E or ν leads to very similar strain results compared to the one with the reference parameters. Indeed the dashed blue or dotted red curve lie above the orange one in Fig. 7.11. Hence, the strain component is nearly independent of a variation of elastic parameters as the influence of these parameters is limited to the initial part of the simulation. The strain and thus the differences of the strain values for different elastic parameters are still very small in the beginning. More precisely, the maximum difference between the strain from simulations with reference values and the strain, where $E = 1\,\mathrm{GPa}$ is $6.5 \cdot 10^{-5}$ reached at $t = 0\,\mathrm{d}$. For $\nu \approx 0.5$, this leads to an even smaller difference of 10^{-6} also reached directly at the beginning of the simulation.

The only material parameter that has an effect on the long-term behavior of the strain is the viscosity. The purple curve in Fig. 7.11 shows that the strain becomes smaller for an increase of the viscosity. More specifically, this behavior is inversely proportional (5 times the viscosity nearly corresponds to strain values divided by 5). The slope of the analyzed strain component is thus critically influenced by the viscosity. If a strain criterion for calving is used, the viscosity is the only material quantity,

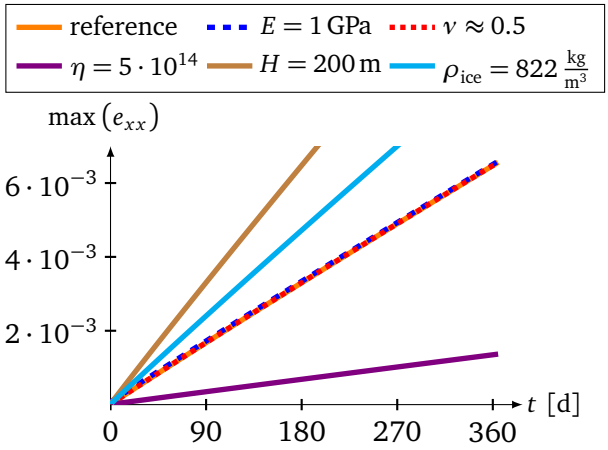

Figure 7.11: Dependence on material and geometric parameters of the maximum strain at the upper surface with time using the concept of finite deformation.

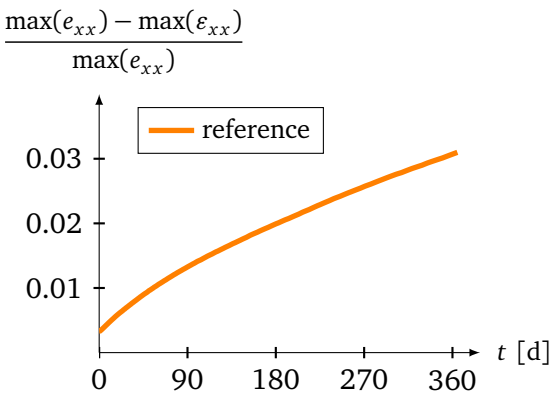

Figure 7.12: Relative difference of the maximum of the strain components e_{xx} and ε_{xx}, computed with the finite and small deformation model, respectively.

which affects the timespan between calving events. Hence, only this parameter has to be fitted to measurements.
The geometric parameters also influence the strain state. The correlation between strain and thickness is proportional (doubling the thickness results in twice the strain value). This means that for thicker ice shelves the critical strain value is reached more quickly. For instance, the critical strain $\varepsilon_{\mathrm{c}} = 0.025$ is obtained for the reference material parameters and a thickness of $H = 300\,\mathrm{m}$ after $t_{\mathrm{c}}^{\mathrm{FD}} = 492\,\mathrm{d} = 1.3\,\mathrm{a}$ for finite viscoelasticity. At this point in time, the relative difference of the maximum of $e_{xx}(t_{\mathrm{c}}^{\mathrm{FD}})$ and $\varepsilon_{xx}(t_{\mathrm{c}}^{\mathrm{FD}})$, the strain computed with the concept of small deformations, is 7.6 %. The critical strain is achieved 54 d later at $t_{\mathrm{c}}^{\mathrm{SD}} = 546\,\mathrm{d}$ for the model assuming small deformations.
The current strain component in flow direction e_{xx} for finite viscoelasticity is comparable with the horizontal flow component ε_{xx} for the model that assumes small deformations. The relative difference of the maximum of these values is depicted in Figure 7.12. The curve increases comparable to the stress situation in Fig. 7.8 and reaches a difference of 3 % after one year. The strain state is always underestimated in the model that assumes small deformations. Thus, the critical strain criterion leads to a 10 % faster calving rate for the finite deformation viscoelastic Maxwell model in comparison to the model with the assumption of small deformations. In the small deformation model, the memory effect of the remaining ice shelf leads to a shortening of the time intervals between successive calving events, see Section 6.3.2. To overcome this problem, the effect of several consecutive calving events on the strain state of a finite viscoelastic model needs to be investigated in the future.

In summary, the stress and strain states are computed by a Maxwell model, which is extended to finite viscoelasticity by the use of a constitutive law according to Saint

Venant-Kirchhoff. Additionally, the lower Oldroyd rate is assumed as an objective rate. Based on these model assumptions, the buoyancy equilibrium is fulfilled during the whole simulation period. The stress results for this type of finite viscoelasticity satisfy the fact that the initial stress state almost coincides with the state computed with the assumption of small deformations. Furthermore, the differences get larger similar to the increase of the viscous flow and thus, to the increase of the deformation. In addition, the discussion above verifies that the response of this kind of finite viscoelasticity is initially dependent on the elastic parameters. The influence of elasticity decreases after several days or months and then only the viscous material behavior is relevant. In order to determine a calving rate, the measurements of the geometry and the ice density have to be as accurately as possible based on their crucial influence on the maximum tensile stress and its distance to the ice front. The strain state linearly increases in time and is proportional to the thickness and inversely proportional to the viscosity. Given that geometry and ice density are well-known, the only parameter that influences the achievement of the critical strain is the viscosity.

7.5 Neo-Hookean Material

For small deformations the results for finite viscoelasticity need to coincide with the results of the linearized model. The previous investigations show that the Saint Venant-Kirchhoff material fulfills this requirement. However, this material is restricted to problems with large deformations but small strains as discussed in Section 2.7.3. For finite viscoelasticity, the neo-Hookean material is a common other constitutive assumption to specify a material for the case of large strains. In the following, the stress and strain results of these two formulations are compared to illustrate the differences in the simulation of calving processes with the referenced ice parameters.
In Fig. 7.13, the maximum stress (left) and strain (right) situation are depicted for the two different viscoelasticity models for finite deformation with respect to time. In addition, the results for the linearized model, which are only valid for small deformations, are also included by the blue curves. The initial maximum stress value of the neo-Hookean formulation is 1.6 % higher than the one of the Saint Venant-Kirchhoff description. In fact, a crucial difference is that the stress response of the neo-Hookean material (red curve in the left image of Fig. 7.13) decreases in the first part of the simulation up to half a day. After this time interval, the stress curves of the neo-Hookean and Saint Venant-Kirchhoff material almost coincide reaching the same maximum stress value after 3 d. The similar behavior of the two models corresponds to expectations as the strains depicted in the right plot of Fig. 7.13 are small. However, the initial decrease of the maximum stress values is unusual and is considered in more detail later on. From Fig. 7.13 (right) it is obvious, that the Saint Venant-Kirchhoff and the neo-Hookean model describe a similar strain behavior. This behavior coincides for small deformations with the correlated component

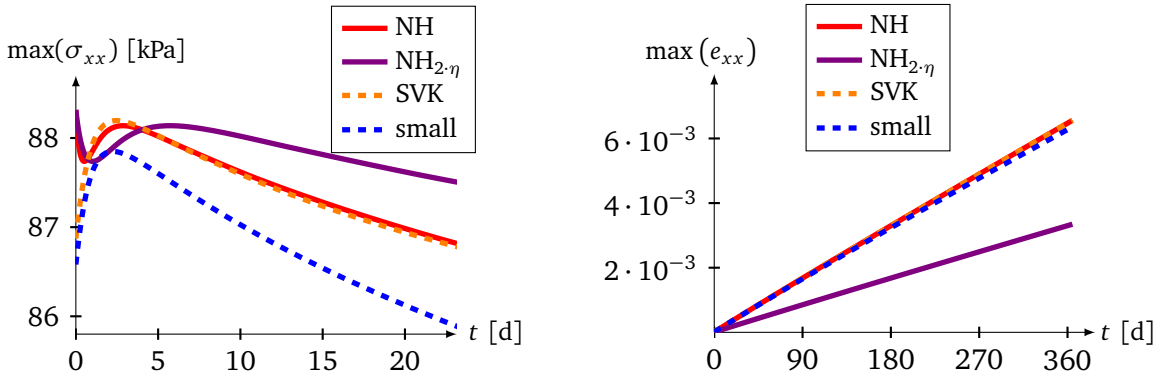

Figure 7.13: Maximum stress (left) and maximum strain (right) in flow direction with time for Saint Venant-Kirchhoff (SVK) and the neo-Hookean (NH) finite viscoelasticity. In addition, the curves of the small deformation model are added.

of the linearized strain tensor $\boldsymbol{\varepsilon}$ and slightly diverges for larger deformations.
In order to show the impact of doubling the viscosity for the neo-Hookean material, the purple curves are also included in Fig. 7.13. This corresponds to the case, in which the same viscous flow relation as for the Saint Venant-Kirchhoff material eq. (2.107) is used. For the viscosity $\eta = 2\cdot10^{14}$Pa s, the maximum stress value in time is independent of the viscosity and is reached after almost 6 d. However, the initial maximum stress decrease is visible even for the higher viscosity up to 1 d. After 5 d, the maximum stress value is always larger than the one for the smaller viscosity. The larger maximum stress is a result of the slower horizontal ice flow and consequently the slower decrease of the freeboard. This leads to the linear strain increase (purple curve in the right plot of Fig. 7.13) with values roughly half the size of the other strain responses. Furthermore, the neo-Hookean results are in the same way dependent on parameter variations as the Saint Venant-Kirchhoff material. In this work, this parameter dependency is only verified by the example of the viscosity.
The initial decrease of the stress maximum is not explainable by a change of the viscosity or any other geometric or material parameter. Hence, this crucial discrepancy between the neo-Hookean and Saint Venant-Kirchhoff model is analyzed in the following. The material equations are constitutive assumptions, which describe the characteristic features preferably realistic. Hence, it is possible to adapt the material description based on the current problem. To simulate the process of calving, the finite viscoelastic response for small deformations needs to be similar to the behavior of the model, which is only valid for small deformations. Thus far, this is not the case for the short-term behavior of the neo-Hookean material, see Fig. 7.13. The loading response of this material model is especially dependent on the volumetric part $\Sigma^{\text{vol}}_{\text{NH}}$ for the initial timespan. To change this part, the physics-based conditions that the stresses are infinite for an infinitely large volume as well as infinitesimal for an infinitesimally small volume have to be fulfilled. This is achieved by the adjustment of the coefficients in the so-called growth condition, suggested in Ciarlet

(1988). In this condition, the coefficients must be positive, but still they are not uniquely defined and can be adapted. In order to shift the stress distribution and therefore, the initial maximum stress value at the beginning of the simulation, the coefficients in the growth condition are modified. For instance, if the coefficient $\lambda/2$ is chosen instead of $K/2$ in front of the volumetric part of eq. (2.106), the maximum initial stress will be smaller. The general shape with the initial stress decrease remains unchanged, cf. the cyan curve in Fig. 7.14. However, the maximum stress value in time is in this case very close to the value for the small deformation model and is reached after 4 d.
In nonlinear continuum mechanics, another possible formulation of the neo-Hookean stress relation for compressible materials is often given by

$$\boldsymbol{\Sigma}_{\mathrm{NH_{com}}} = \frac{\lambda}{2}\left(J^2-1\right)\boldsymbol{C}_{\mathrm{e}}^{-1} + \mu\left(\mathbf{1}-\boldsymbol{C}_{\mathrm{e}}^{-1}\right). \tag{7.1}$$

in the intermediate configuration. Although the separation in a purely volumetric and purely deviatoric part is missing in this equation, the effect of such a material model on the maximum stress distribution with respect to time is considered in the following. To obtain the condition for the internal variable, the deviatoric viscous flow relation eq. (2.107) is equated with the second part of eq. (7.1) that includes the viscosity μ. This is not entirely correct as this part also contains volumetric instead of purely deviatoric deformations due to the deformation gradient $\boldsymbol{F}_{\mathrm{e}}$ in the right Cauchy-Green tensor $\boldsymbol{C}_{\mathrm{e}}$. In the case of eq. (2.106), the deformation gradient is multiplicatively decomposed and the viscous flow relation is approximated only by the deviatoric part of the material. However, the impact of this assumption is estimated through the comparison with the incompressible neo-Hookean material response.
Wriggers (2008) verified that the linearization $\boldsymbol{L}$ of eq. (7.1) with respect to the reference configuration ($\boldsymbol{\varphi} = \boldsymbol{X}$) leads to Hooke's relation for isotropic materials

$$\boldsymbol{L}\left[\boldsymbol{\Sigma}_{\mathrm{NH_{com}}}\right]_{\boldsymbol{\varphi}=\boldsymbol{X}} = \lambda \mathrm{tr}(\boldsymbol{\varepsilon})\mathbf{1} + 2\mu\boldsymbol{\varepsilon}. \tag{7.2}$$

Hence, the stress distribution for small deformations of this kind of a neo-Hookean material is similar to the response of the model with the assumption of small deformations. The pull-back operation transforms eq. (7.1) into the reference configuration and the purple curve of Fig. 7.14 shows the maximum stress for the compressible neo-Hookean material model. It is obvious, that the initial maximum stress is the same as for the Saint Venant-Kirchhoff material. The shape of the initial period considering the maximum stress evolution of the compressible neo-Hookean material is similar to the shape of the model that assumes only small deformations. Hence, the initial stress decrease in the incompressible neo-Hookean model originates of the splitting into volumetric and deviatoric part of the material equation based on the decomposition of the deformation gradient. The error to take the flow dependent part of the material equation instead of the purely deviatoric part

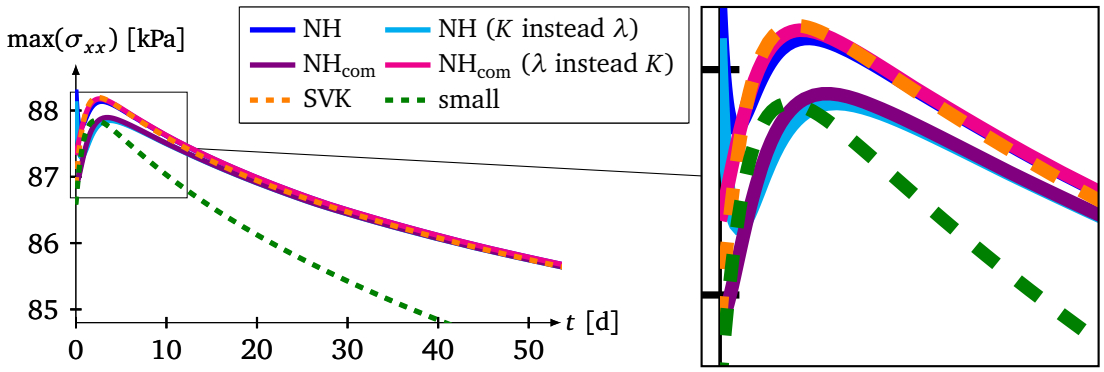

Figure 7.14: Comparison of maximum stress states for different possibilities of the neo-Hookean material description.

is small. This is visible due to the stress states that almost coincide for the compressible and incompressible neo-Hooke material in Fig. 7.14. If the coefficient in front of the first part of eq. (7.1) is changed to $K/2$ instead of $\lambda/2$, the compressible neo-Hookean model starts at a slightly higher maximum stress value, see the magenta curve of Fig. 7.14. However, the stress distributions of the Saint Venant-Kirchhoff and the compressible neo-Hookean material are the same except of this initial value. In the end, the stress states of all considered finite viscoelastic models converge to each other after the first 13 d and the applicability of these different models is demonstrated to compute stress and strain states inside an ice shelf. In the next section, the effect using the upper instead of the lower Oldroyd rate is investigated to detect differences of varied objective time derivatives.

7.6 Upper Oldroyd Rate

The upper Oldroyd rate serves as an additional option of an objective time derivative. The contravariant Piola strain tensor $\boldsymbol{A}$ is a convenient strain measure in the reference configuration. Hence, the inverse of the viscous right Cauchy-Green tensor $\boldsymbol{C}_{\mathrm{v}}^{-1}$ is used as an internal variable, while so far $\boldsymbol{C}_{\mathrm{v}}$ base on $\boldsymbol{E}$ is used, see Section 2.7.3. The compressible neo-Hookean material approximates the small deformation stress results best for the initial elastic part of the simulation shortly after a stress modification, cf. the previous section. Hence, the upper Oldroyd rate is only considered for the stress distributions of this material, see Table 2.1. The simpler choice of the Jaumann-Zaremba rate as an alternative objective time derivative results in stress and strain oscillations, which are not physically explainable or induced by the mesh accuracy. For the special case of simple shear, this behavior was already pointed out by Haupt (2000).
The stress states of the compressible neo-Hookean material with the upper (NH_{uO}) or lower (NH_{com}) Oldroyd rate are very similar, cf. the cyan and purple curves in Fig. 7.15 (left). In Fig. 7.15 (right), the purple curve shows the absolute difference of the maximum flow stress computed by these different objective rates. This curve

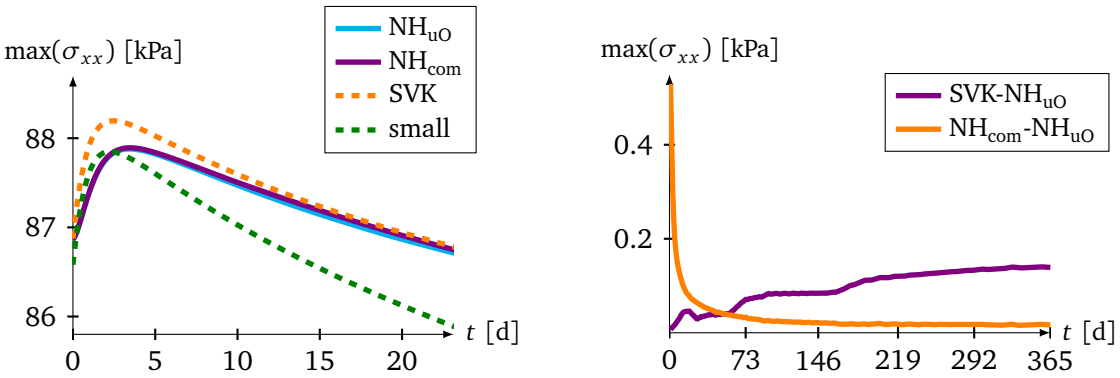

Figure 7.15: Maximum stress (left) in flow direction of the compressible neo-Hookean material computed with the objective upper Oldroyd time derivative (NH$_{uO}$). Absolute maximum stress difference (right) of this material model and the Saint Venant-Kirchhoff (SVK) or the compressible neo-Hookean material (NH$_{com}$) computed with the lower Oldroyd rate.

increases slightly with time until the difference of 139 Pa is achieved after 1 a. In order to compare the compressible neo-Hookean material with the upper Oldroyd rate and the Saint Venant-Kirchhoff material with the lower Oldroyd rate (SVK), the orange curve is also included in Fig. 7.15 (right). Remarkably this difference decreases in time. The highest absolute difference of 530 Pa occurs directly at the beginning. This can be explained based on the different coefficients in front of the elastic parts in the material equation (K for SVK and λ for NH$_{uO}$) as discussed above. After 54 d, this difference is smaller than the one of NH$_{com}$ and NH$_{uO}$, while after 160 d a value smaller than 20 Pa is reached. Hence, the Saint Venant-Kirchhoff material with the lower Oldroyd rate leads to the same viscous stress and strain results as the neo-Hookean material with the upper Oldroyd rate. All in all, each investigated finite viscoelastic material model results in similar stress and strain states, at least for the viscous flow after several days. Furthermore, these results differ more and more for increased deformations from the stress states of the model that assumes only small deformations as it was expected.

8 Conclusions and Outlook

This work has addressed calving of small-sized icebergs from Antarctic ice shelves. The aim of the study was to find and evaluate a criterion that defines situations at which a fracture of the material separates an iceberg from the floating ice shelf. A calving law is therefore a failure criterion in the continuum mechanical context. Possible calving criteria have been discussed for ice shelves modeled through viscoelastic material properties. In the first part of the study, a separate analysis of the linear elastic and the linear viscous material models – the two basic elements in viscoelasticity – explained the fundamentals to get a deeper insight in the impact of each material law.
Independent of time, the elastic response yields a stress maximum at the upper surface caused by the boundary disturbance at the ice front. This maximum is located at a distance between half the thickness to the whole thickness inward from the ice front. The variation in the horizontal position of the stress maximum can be attributed to reflect the uncertainties in the material properties of ice. In order to develop the time evolution of the mechanical quantities the viscous model is used. A strain maximum has been shown to form at the surface nearly at the same position as the stress maximum. Its value increases almost linearly in time. Different viscoelastic material models were examined in this work: the Kelvin-Voigt solid (short-term viscous and long-term elastic response) and the Maxwell fluid (short-term elastic and long-term viscous response). Small-scale calving was analyzed based on three failure criteria: stress, self-similarity, and strain criterion.

1. Stress criterion: Calving is assumed to occur if a critical stress is reached. During this work the critical stress from Hayhurst (1972) with a constant stress value of $\sigma_{\text{crit}} = 330\,\text{kPa}$ was applied. It turned out that independent of the material the maximum tensile stress changes proportional to the ice thickness and depends as well on the height of the freeboard that is determined by the mean density. For the Kelvin-Voigt material the stress criterion can be applied for a small thickness interval close to 300 m at the ice front. However, this material approach describes a viscoelastic solid and its stress state converges to the rate-independent elastic response so that the long-term viscous behavior of ice is inaccessible.
In previous studies the deformation of ice was often specified by an incompressible viscous material only. Concerning the stress criterion this principle does not work with a purely viscous approach for small-scale calving as the magnitude of the stress maximum decreases with time. The largest stress state occurs at the beginning of the simulation and thus the ice shelf either collapses completely by immediate iceberg detachments or becomes less and less critical in time. The process of calving is also

affected by the short-term elastic behavior of ice. Combining a compressible elastic component with the incompressible viscous one in the Maxwell model leads to the initial stress increase reversed into a monotonic decrease. In general, the evolution of stresses is determined by the characteristic time of the material. Therefore, the material parameters determine the time between calving events, while the impact of the geometric quantities vanishes. Similar to the Kelvin-Voigt solid the critical stress is attained solely for a small thickness range.
In order to study the effect of the shape of the ice shelf for the stress criterion the geometry has been modified. On the one hand, if the stresses are too small to reach the critical value, appropriate melting processes at the ice front may enforce a stress increase, for example the melting at the ice front leading to an underwater "belly". On the other hand, if the maximum stress value surpasses the critical strength the ice shelf has to be stabilized by geometry variations or the coastline to prevent calving. While such a physics-based stress criterion is conceivable, the relevant parameters have to be verified at real ice shelf situations.

2. Self-similarity criterion: For the second calving criterion, the requirement to reach a constant stress value valid for all ice shelves is no longer necessary. In the self-similarity approach a critical state of an arbitrary physical quantity is defined and each time this condition is achieved the next calving event occurs. Consequently the geometry variations to fulfill the stress criterion are no prerequisite, however, a critical situation valid for the majority of ice shelves has to be determined. In case of the Kelvin-Voigt model the convergence to the stationary state offers a possible termination bound. Once the maximum stress difference of two adjacent time steps is below a certain value, which was adapted to observations, an iceberg calves off. This criterion leads to robust and stable calving rates for small-scale calving of ice shelves independent of the thickness. For an arbitrary geometry with a constant thickness as well as for the measured geometry of the Ekström Ice Shelf a similar calving behavior is obtained. The inclusion of available measurements of the flow velocity at this specific ice shelf has resulted in time-independent calving rates. With invariant geometries and traction conditions, constant iceberg lengths and times between consecutive calving events are obtained. For the Maxwell material the identification of a critical situation is less straightforward. The point in time when the maximum tensile stress is reached yields one conceivable possibility to initiate a timing event, but this is not physically motivated and merely an assumption.

3. Strain criterion: As a last calving criterion the temporal evolution of the strain state in the flow direction was investigated. In the purely viscous and the viscoelastic Maxwell model this quantity increases almost linearly in time due to the divergent flow of ice that results in the thinning of the ice shelf. The position of calving is closer to the ice front and consequently the icebergs are smaller than for the stress criterion. For a sequence of calving events based on a critical strain, the time between two successive events decreases more and more. This is caused by the strain states of the whole ice shelf which are history-dependent and continue growing with

time by the viscous elongation. The strain which builds up outside the area influenced by the boundary perturbation of the sea-water pressure leads in the extreme model case to the total collapse of the ice shelf. A calving law with a constant iceberg length and break-off time is only obtained if the strain history is lost after each calving event. A non-linear viscosity based on the effective strain rate in Glen's flow law and thus on the current deformation causes an even faster strain increase and therefore larger calving rates. Similar to results using a constant viscosity, the extension of the ice shelf ends only when the freeboard height approaches zero while the draft remains unchanged. In this situation the assumption of small deformations is violated and the Maxwell model was extended to finite deformations.

To investigate the impact on calving for simulations exceeding several times the characteristic time $\tau = \eta/\mu$ with the viscosity η and Lamé constant μ, the results from the nonlinear material model also valid for large strains are considered. With increasing time, the computed stresses for the small and large deformation models diverge. Only for strains below 5 % both models agree well. The Maxwell approach for finite deformation yields more critical stress situations as the stresses are larger compared to the one of the linear Maxwell model. The same trend has been found for the strains but the deviations are half as large as for the stresses. However, the numerics require a very fine discretization at the ice front in this case and the simulations become costly. Unfortunately, the allocation of added nodes for an essential mesh refinement at the new ice front after a calving event is not straightforward.

In summary, the equation-based implementation of the viscoelastic Maxwell material in COMSOL offers a flexible tool to depict the material behavior of ice. It is very important to include beside the viscous flow also the elastic short-term response as small-scale calving happens for a time span in which the elastic response is still relevant. The extension of the linear viscoelastic models with one viscous and one elastic element into those involving more viscous and elastic components is straightforward but additional material parameters are needed. These quantities have to be determined out of a limited number of measurements to achieve viscoelastic parameters additionally to the viscosity and Young's modulus. Ongoing simulation results with the 3-parameter fluid just show a slight variation to the ones of the viscoelastic models investigated in this work.
In order to substantiate any criterion for iceberg calving, a continuous sequence of successive calving events obtained from dense time series of satellite images is absolutely essential to prove the plausibility of the obtained results. In the future, several consecutive calving events with the use of the third criterion regarding critical strains will be considered also for the nonlinear Maxwell material legitimate for large deformations. Moreover other calving situations can be investigated with the approach developed in this thesis. For example, the crucial quantities for calving of grounded tidewater glaciers can be determined by exchanging the buoyancy force at the bottom of the ice body with a sliding law. Also the effect of tides on grounding line dynamics requires a viscoelastic approach.

In this thesis the viscoelastic analysis of different calving criteria has shown that the geometry mainly influences the position of calving while the material parameters mainly determine the time between two calving events. A physics-based description of calving in ice sheet models requires the knowledge about the ice shelf characteristics to be more accurate and detailed than it is currently available for the investigation of entire Antarctica. Stresses depend very strongly on the geometry of the ice shelf in the vicinity of the ice front, while strains are affected by the ice deformation history. In any real situation, calving will always be a combination of effects, a superposition of the individual criteria developed and evaluated for idealized situations here. For all viscoelastic models, especially the nonlinear Maxwell model that mimics the dynamics of the ice shelf best, a resolution of several hundreds of meters across the ice flow and only a few meters along the ice front is required to allow for the model to converge. Only at such a fine discretization it is possible to specify the boundary condition at the ice front and particularly involve the crucial freeboard height.
A cheap and easy solution to the problem of iceberg calving is therefore not available still and may well be impossible to find. However, ice sheet modelers have learned to accept the fact that an adequate representation of grounding line dynamics requires at least a horizontal resolution of half the ice thickness or less. It may be time to abandon the efficiency target also for the ice front and aim for a concept of ice sheet models that keeps track of information about the material parameters of ice, the accurate geometry, and its strain and fracture history. Using this additional knowledge in combination with a high-resolution mesh the realistic representation of iceberg calving can eventually close one of the missing links between ice sheet and ocean models.

Bibliography

Albrecht, T., Martin, M., Haseloff, M., Winkelmann, R. and Levermann, A.: Parameterization for Subgrid-Scale Motion of Ice-Shelf Calving-Fronts. The Cryosphere, Vol. 5, 35–44, 2011.

Albrecht, T. and Levermann, A.: Fracture field for large-scale ice dynamics. Journal of Glaciology, Vol. 58, No. 207, 165–176, 2012.

Alley, R. B., Horgan, H. J., Joughin, I., Cuffey, K. M., Dupont, T.K., Parizek, B. R., Anandakrishnan, S. and Bassis, J.: A Simple Law for Ice-Shelf Calving. Science 28, Vol. 322, No. 5906, 1344, 2008.

Amestoy, P. R., Duff, I. S., and L'Excellent, J.-Y.: Multifrontal parallel distributed symmetric and unsymmetric solvers. Comput. Methods Appl. Mech. Engrg., Vol. 184, 501–520, 2000.

Amundson, J. M. and Truffer, M.: A unifying framework for iceberg-calving models. Journal of Glaciology, Vol. 56, No. 199, 822–830, 2010.

Altenbach, H.: Kontinuumsmechanik: Einführung in die materialunabhängigen und materialabhängigen Gleichungen. Springer-Verlag, Berlin Heidelberg, 2012.

Bamber, J. L., Griggs, J. A., Hurkmans, R. T. W. L., Dowdeswell, J. A., Gogineni, S. P., Howat, I., Mouginot, J., Paden, J., Palmer, S., Rignot, E., and Steinhage, D.: A new bed elevation dataset for Greenland. The Cryosphere, Vol. 7, 499–510, 2013.

Bassis, J. N., Fricker, H. A., Coleman, R., and Minster, J.: An investigation into the forces that drive ice-shelf rift propagation on the Amery Ice Shelf, East Antarctica. Journal of Glaciology, Vol. 54, No. 184, 17–27, 2008.

Bassis, J. N.: The statistical physics of iceberg calving and the emergence of universal calving laws. Journal of Glaciology, Vol. 57, No. 201, 3–16, 2011.

Becker, W. and Gross, D.: Mechanik elastischer Körper und Strukturen. Springer-Verlag, Berlin Heidelberg, 2002.

Benn, D. I., Warren, C. R., and Mottram, R. H.: Calving processes and the dynamics of calving glaciers. Earth Science Reviews, Vol. 82, 143–179, 2007.

Bentley, C. R., Shabtaie, S., Blankenship, D. D., Rooney, S. T., Schultz, D. G., Anandakrishnan, S., and Alley, R. B.: Remote sensing of the Ross ice streams and adjacent Ross Ice Shelf, Antarctica. Annals of Glaciology, Vol. 9, 20–29, 1987.

Bindschadler, R. A., Nowicki, S., Abe-Ouchi, A., Aschwanden, A., Choi, H., Fastook, J., Granzow, G., Greve, R., Gutowski, G., Herzfeld, U., Jackson, C., Johnson, J., Khroulev, C., Levermann, A., Lipscomb, W. H., Martin, M. A., Morlighem, M., Parizek, B. R., Pollard, D., Price, S. F., Ren, D., Saito, F., Sato, T., Seddik, H., Seroussi, H., Takahashi, K., Walker, R., and Wang, W. L.: Ice-sheet model sensitivities to environmental forcing and their use in projecting future sea level (the SeaRISE project). Journal of Glaciology, Vol. 59, No. 214, 195–224, 2013.

Boltzmann, L.: Zur Theorie der elastischen Nachwirkungen. Wiener Berichte, Vol. 70, 275–306, 1874.

Boltzmann, L.: Zur Theorie der elastischen Nachwirkungen, Ergänzungsband. Analen der Physik und Chemie, Vol. 7, 624, 1876.

Bueler, E., Lingle, C. S., and Kallen-Brown, J. A.: Fast computation of a viscoelastic deformable Earth model for ice sheet simulation. Annals of Glaciology, Vol. 46, 97–105, 2007.

Christmann, J., Plate, C., Müller, R., and Humbert, A.: Viscous and viscoelastic stress states at the calving front of Antarctic ice shelves. Annals of Glaciology, Vol. 57, 10–18, 2016a.

Christmann, J., Rückamp, M., Müller, R., and Humbert, A.: Discussion of Different Model Approaches for the Flow Behavior of Ice. Proc. Appl. Math. Mech., Vol. 16, 313–314, 2016b.

Ciarlet, P. G.: Mathematical Elasticity Volume I: Three-Dimensional Elasticity. Elsevier Science Publishers B.V., 1988.

Coleman, B. D., Noll, W.: Foundations of Linear Viscoelasticity. Reviews of Modern Physics, Vol. 33, No. 2, 239–249, 1961.

Cornford, S. L., Martin, D. F., Payne, A. J., Ng, E. G., Le Brocq, A. M., Gladstone, R. M., Edwards, T. L., Shannon, S. R., Agosta, C., van den Broeke, M. R., Hellmer, H. H., Krinner, G., Ligtenberg, S. R. M., Timmermann, R., and Vaughan, D. G.: Century-scale simulations of the response of the West Antarctic Ice Sheet to a warming climate. The Cryosphere, Vol. 9, 1579–1600, 2015.

Cuffey, K. M. and Paterson, W. S. B.: The physics of glaciers. Academic Press, 2010.

Darby, R.: Viscoelastic fluids: an introduction to their properties and behavior. M. Dekker, New York, 1976.

De Angelis, H. and Skvarca, P.: Glacier Surge After Ice Shelf Collapse. Science, Vol. 299, No. 5612, 1560–1562, 2003.

Depoorter, M. A., Bamber, J. L., Griggs, J. A., Lenaerts, J. T. M., Ligtenberg, S. R. M., van den Broeke, M. R. , and Moholdt, G.: Calving fluxes and basal melt rates of Antarctic ice shelves. Nature, Vol. 502, 89–92, 2013.

Dupont, T. K. and Alley, R. B.: Assessment of the importance of ice-shelf buttressing to ice-sheet flow. Geophysical Research Letters, Vol. 32, L04503, 2005.

Fastook, J. L. and Schmidt, W. F.: Finite element analysis of calving from ice fronts. Annals of Glaciology, Vol. 3, 103–106, 1982.

Flügge, W.: Viscoelasticity. Springer, Berlin Heidelberg, 1975.

Fretwell, P., Pritchard, H. D., Vaughan, D. G., Bamber, J. L., Barrand, N. E., Bell, R., Bianchi, C., Bingham, R. G., Blankenship, D. D., Casassa, G., Catania, G., Callens, D., Conway, H., Cook, A. J., Corr, H. F. J., Damaske, D., Damm, V., Ferraccioli, F., Forsberg, R., Fujita, S., Gim, Y., Gogineni, P., Griggs, J. A., Hindmarsh, R. C. A., Holmlund, P., Holt, J. W., Jacobel, R. W., Jenkins, A., Jokat, W., Jordan, T., King, E. C., Kohler, J., Krabill, W., Riger-Kusk, M., Langley, K. A., Leitchenkov, G., Leuschen, C., Luyendyk, B. P., Matsuoka, K., Mouginot, J., Nitsche, F. O., Nogi, Y., Nost, O. A., Popov, S. V., Rignot, E., Rippin, D. M., Rivera, A., Roberts, J., Ross, N., Siegert, M. J., Smith, A. M., Steinhage, D., Studinger, M., Sun, B., Tinto, B. K., Welch, B. C., Wilson, D., Young, D. A., Xiangbin, C., and Zirizzotti, A.: Bedmap2: improved ice bed, surface and thickness datasets for Antarctica. The Cryosphere, Vol. 7, 375–393, 2013.

Fricker, H. A. , Young, N. W., Allison, I., and Coleman, R.: Iceberg calving from the Amery Ice Shelf, East Antarctica. Annals of Glaciology, Vol. 34, 241–246, 2002.

Gammon, P. H., Kiefte, H., Clouter, M., and Denner, W. W.: Elastic Constants of Artifical and Natural Ice Samples by Brillouin Spectroscopy. Journal of Glaciology, Vol. 29, No. 103, 433–460, 1983.

Gasch, R., Knothe K., and Liebich, R.: Strukturdynamik Diskrete Systeme und Kontinua, Springer, Berlin Heidelberg, 2012.

Giggs, J. A. and Bamber, J. L.: Antarctic ice-shelf thickness from satellite radar altimetry. Journal of Glaciology, Vol. 57, No. 203, 485–498, 2011.

Glasser, N. F. and Scambos, T. A.: A structural glaciological analysis of the 2002 Larsen B ice shelf collapse. Journal of Glaciology, Vol. 54, No. 184, 3–16, 2008.

Glen, J. W.: The creep of polycrystalline ice. Proceedings of the Royal Society of London, Series A, Mathematical and Physical Sciences, Vol. 228, No. 1175, 519–538, 1955.

Greve, R. and Blatter, H.: Dynamics of Ice Sheets and Glaciers. Springer-Verlag, Berlin Heidelberg, 2009.

Greve, R., Saito, F., and Abe-Ouchi, A.: Initial results of the SeaRISE numerical experiments with the models SICOPOLIS and IcIES for the Greenland ice sheet. Annals of Glaciology, Vol. 52, 23–30, 2011.

Gross, D., Hauger W., Schröder J.,Wall W.A. and Bonet, J.: Engineering Mechanics 2, Mechanics of Materials, Springer, Berlin Heidelberg, 2011.

Gudmundsson, G. H.: Ice-stream response to ocean tides and the form of the basal sliding law. The Cryosphere, Vol. 5, 259–270, 2011.

Habbal, F., Larour, E., Morlighem, M., Seroussi, H., Borstad, C. P., and Rignot, E.: Optimal numerical solvers for transient simulations of ice flow using the Ice Sheet System Model (ISSM versions 4.2.5 and 4.11). Geoscientific Model Development, Vol. 10, 155–168, 2017.

Haupt, P.: Continuum Mechanics and Theory of Materials. Springer-Verlag, Berlin Heidelberg, 2000.

Hayhurst, D. R.: Creep-rupture under multi-axial states of stress, Journal of the Mechanics and Physics of Solids, Vol. 20, No. 6, 381–382, 1972.

Holdsworth, G.: Some mechanisms for the calving of icebergs. Iceberg Utilization, Proceeding, First International Conference and Workshops on Iceberg Utilization for Fresh Water Production, Weather Modification and Other Applications, Pergamon Press New York, 160–175, 1978.

Holzapfel, G. A.: Nonlinear Solid Mechanics: A Continuum Approach for Engineering. Wiley, 2001.

Hughes, T. J. R.: Theoretical Calving Rates from Glaciers Along Ice Walls Grounded in Water of Variable Depths. Journal of Glaciology, Vol. 38, No. 129, 282–294, 1992.

Hughes, T. J. R.: The Finite Element Method: Linear Static and Dynamic Finite Element Analysis. Dover Publications, Inc., Mineola, New York, 2000.

Hulbe, C. L., LeDoux, C., and Cruikshank, K.: Propagation of long fractures in the Ronne Ice Shelf, Antarctica, investigated using a numerical model of fracture propagation. Journal of Glaciology, Vol. 56, No. 197, 459–472, 2010.

Humbert, A., Kleiner, T., Mohrholz, C., Oelke, C., Greve, R., and Lange, M.: A comparative modeling study of the Brunt Ice Shelf/Stancomb-Wills Ice Tongue system, East Antarctica. Journal of Glaciology, Vol. 55, No 189, 53–65, 2009.

Humbert, A., Steinhage, D.: The evolution of the western rift area of the Fimbul Ice Shelf. The Cryosphere, Vol. 5, 931–944, 2011.

Humbert, A., Steinhage, D., Helm, V., Hoerz, S., Berendt, J., Leipprand, E., Christmann, J., Plate C., and Müller, R.: On the link between surface and basal structures of the Jelbart Ice Shelf, Antarctica. Journal of Glaciology, Vol. 61, No 229, 975–986, 2015.

Hutter, K.: A general theory for floating ice plates. Archives of Mechanics, No.27, 617–638, 1975.

Hutter, K.: On the mechanics of floating ice sheets. Mitteilungen der Versuchsanstalt für Wasserbau, Hydrologie und Glaziologie an der ETH Zürich, No.28, 1978.

Iken, A.: Movement of a large ice mass before breaking off. Journal of Glaciology, Vol. 19, No. 81, 595–605, 1977.

Jacobs, S. S., Helmer, H. H., Doake, C. S. M., Jenkins, A., and Frolich, R. M.: Melting of ice shelves and the mass balance of Antarctica. Journal of Glaciology, Vol. 38, No. 130, 375–387, 1992.

Jansen, D., Kulessa, B., Sammonds, P. R., Luckman, A. J., King, E., and Glasser, N. F.: Present stability of the Larsen C Ice Shelf, Antarctic Peninsula. Journal of Glaciology, Vol. 56, No. 198, 593–600, 2010.

Jezek, K. C. and Bentley, C. R.: Field studies of bottom crevasses in the Ross Ice Shelf, Antarctica. Journal of Glaciology, Vol. 29, No. 101, 118–126, 1983.

Korobeynikov, S. N.: Objective Tensor Rates and Applications in Formulation of Hyperelastic Relations. Journal of Elasticity, Vol. 93, 105–140, 2008.

Lakes, R. S. and Wineman, A.: On Poisson's Ratio in Linearly Viscoelastic Solids. Journal of Elasticity, Vol. 85, 45–63, 2006.

Lang, H., Leyendecker, S., and Linn, J.: Numerical experiments for viscoelastic Cosserat rods with Kelvin-Voigt damping. ECCOMAS Multibody Dynamics 2013, 453–462, 2013.

Larour, E., Rignot, E., and Aubry, D.: Processes involved in the propagation of rifts near Hemmen ice rise, Ronne Ice Shelf, Antarctica. Journal of Glaciology, Vol. 50, No. 170, 329–341, 2004a.

Larour, E., Rignot, E., and Aubry, D.: Modelling of rift propagation on Ronne Ice Shelf, Antarctica, and sensitivity to climate change. Geophysical Research Letters, Vol. 31, No. 16, 1–4, 2004b.

Larour, E., Seroussi, H., Morlighem, M., and Rignot, E.: Continental scale, high order, high spatial resolution, ice sheet modeling using the Ice Sheet System Model (ISSM). Journal of Geophysical Research: Earth Surface, Vol. 117, F01022, 2012.

Levermann, A., Albrecht, T., Winkelmann, R., Martin, M. A., Haseloff, M., and Joughin, I.: Kinematic first-order calving law implies potential for abrupt ice-shelf retreat. The Cryosphere, Vol. 6, 273–286, 2012.

Liu, Y., Moore, J. C., Cheng, X., Gladstone, R. M., Bassis, J. N., Liu, H., Wen, J., and Hui, F.: Ocean-driven thinning enhances iceberg calving and retreat of Antarctic ice shelves. PNAS, Vol. 112, No. 11, 3263–3268, 2015.

Lohse, J.: Tidally induced ice dynamics at the calving front of Ekstroemisen, Antarctica, in the context of flow and fracture mechanics. Master Thesis, University of Hamburg, Institute of Geophysics, 2012.

Luckman, A., Jansen, D., Kulessa, B., King, E. C., Sammonds, P., and Benn, D. I.: Basal crevasses in Larsen C Ice Shelf and implications for their global abundance. The Cryosphere, Vol. 6, 113–123, 2012.

MacAyeal, D. R., Sergienko, O. V., and Banwell, A. F.: A model of viscoelastic ice-shelf flexure. Journal of Glaciology, Vol. 61, No. 228, 635–645, 2015.

Marsden, J. E. and Hughes, T. J. R.: Mathematical Foundations of Elasticity. Dover, New York, 1994.

Mellor, M.: A review of basic snow mechanics. Proceedings of the International Symposium on Snow Mechanics, IAHS Publication 114, 251–291, 1975.

Nowicki, S., Bindschadler, R. A., Abe-Ouchi, A., Aschwanden, A., Bueler, E., Choi, H., Fastook, J., Granzow, G., Greve, R., Gutowski, G., Herzfeld, U., Jackson, C., Johnson, J., Khroulev, C., Larour, E., Levermann, A., Lipscomb, W. H., Martin, M. A., Morlighem, M., Parizek, B. R., Pollard, D., Price, S. F., Ren, D., Rignot, E., Saito, F., Sato, T., Seddik, H., Seroussi, H., Takahashi, K., Walker, R., and Wang, W. L.: Insights into spatial sensitivities of ice mass response to environmental change from the SeaRISE ice sheet modeling project I. Antarctica. Journal of Geophysical Research: Earth Surface, Vol. 118, No. 2, 1002–1024, 2013.

Nowicki, S., Bindschadler, R. A., Abe-Ouchi, A., Aschwanden, A., Bueler, E., Choi, H., Fastook, J., Granzow, G., Greve, R., Gutowski, G., Herzfeld, U., Jackson, C., Johnson, J., Khroulev, C., Larour, E., Levermann, A., Lipscomb, W. H., Martin, M. A., Morlighem, M., Parizek, B. R., Pollard, D., Price, S. F., Ren, D., Rignot, E., Saito, F., Sato, T., Seddik, H., Seroussi, H., Takahashi, K., Walker, R., and Wang, W. L.: Insights into spatial sensitivities of ice mass response to environmental change from the SeaRISE ice sheet modeling project II. Greenland. Journal of Geophysical Research: Earth Surface, Vol. 118, No. 2, 1025–1044, 2013.

Nye, J. F.: Comments on Dr. Loewe's letter and notes on crevasses. Journal of Glaciology, Vol. 2, No. 17, 512–514, 1955.

Ogden, R. W.: Non-Linear Elastic Deformations. Dover Civil and Mechanical Engineering, New York, 1997.

Oldroyd, J. G.: On the formulation of rheological equations of state. Proceedings of the Royal Society of London, Series A, Mathematical and Physical Sciences, Vol. 200, No. 1063, 523–541, 1950.

O'Leary, M. and Christoffersen, P.: Calving on tidewater glaciers amplified by submarine frontal melting. The Cryosphere, Vol. 7, 119–128, 2013.

Orheim, O.: Evolution of under-water sides of ice shelves and icebergs, Annals of Glaciology, Vol. 9, 176–182, 1987.

Pandini, S. and Pegoretti, A.: Time and temperature effects on Poisson's ratio of poly(butylene terephthalate), eXPRESS Polymer Letters, Vol. 5, No. 8, 685–697, 2011.

Petrenko, V. F. and Whitworth, R. W.: Physics of Ice, Oxford University Press, 1999.

Plate, C.: Fracture Mechanical Analysis of Failure Processes in Antarctic Ice Shelves. PhD thesis, Technische Universität Kaiserslautern, Lehrstuhl für Technische Mechanik, 2015.

Pralong, A.: On the instability of hanging glaciers, Dissertation, ETH Zürich, No. 16046, 2005.

Pritchard, H. D., Ligtenberg, S. R. M., Fricker, H. A., Vaughan, D. G., van den Broeke, M. R., and Padman, L.: Antarctic ice-sheet loss driven by basal melting of ice shelves. Nature, Vol. 484, 502–505, 2012.

Pritz, T.: Frequency dependences of complex moduli and complex Poisson's ratio of real solid materials. Journal of Sound and Vibration, Vol. 214, No. 1, 83–104, 1998.

Rackow, T., Wesche, C., Timmermann, R., Hellmer, H., Juricke, S., and Jung, T.: A simulation of small to giant Antarctic iceberg evolution: differential impact on climatology estimates. Journal of Geophysical Research: Oceans, accepted, 2017.

Reeh, N.: On the calving of ice from floating glaciers and ice shelves. Journal of Glaciology, Vol. 7, No. 50, 215–232, 1968.

Reeh, N., Christendes, E. L., Mayer, C, and Olesen, O. B.: Tidal bending of glaciers: a linear viscoelastic approach. Annals of Glaciology, Vol. 37, 83–89, 2003.

Rignot, E., Velicogna, I., van den Broeke, M. R., Monaghan, A., and Lenaerts, J. T. M.: Acceleration of the contribution of the Greenland and Antarctic ice sheets to sea level rise. Geophysical Research Letters, Vol. 38, L05503, 2011.

Rist, M. A., Sammonds, P. R., Murrell, S. A. F., Meredith, P. G., Doake, C. S. M., Oerter, H., and Matsuki, K.: Experimental and theoretical fracture mechanics applied to Antarctic ice fracture and surface crevassing. Journal of Geophysical Research, Vol. 104, No. B2, 2973–2987, 1999.

Rist, M. A., Sammonds, P. R., Oerter, H., and Doake, C. S. M.: Fracture of Antarctic shelf ice. Journal of Geophysical Research, Vol. 107, No. B1, ECV 2-1–ECV 2-13, 2002.

Rosier, S. H. R., Gudmundsson, G. H., and Green, J. A. M.: Insights into ice stream dynamics through modelling their response to tidal forcing. The Cryosphere, Vol. 8, 1763–1775, 2014.

Röthlisberger, H.: Seismic exploration in cold regions. USA CRREL Monograph II–A2a, 1972.

Sandhäger, H., Rack, W., and Jansen, D.: Model investigations of Larsen B Ice Shelf dynamics prior to the breackup. FRISP Report, 1–8, 2005.

Schaffer, J., Timmermann, R., Arndt, J. E., Kristensen, S. S., Mayer, C., Morlighem, M., and Steinhage, D.: A global, high-resolution data set of ice sheet topography, cavity geometry, and ocean bathymetry. Earth System Science Data, Vol. 8, 543–557, 2016.

Schulson, E. M. and Duval, P.: Creep and fracture of ice, Cambridge University Press, 2009.

Seddik, H., Greve, R., Zwinger, T., Gillet-Chaulet, F., and Gagliardini, O.: Simulations of the Greenland ice sheet 100 years into the future with the full Stokes model Elmer/Ice. Journal of Glaciology, Vol. 58, No. 209, 427–440, 2012.

Simo, J. C.: On a Fully Three-Dimensional Finite-Strain Viscoelastic Damage Model: Formulation and Computational Aspects, Computer Methods in Applied Mechanics and Engineering, Vol. 60, 153-173, 1987.

Simo, J. C. and Hughes, T. J. R.: Computational Inelasticity, Springer-Verlag, New York, 1998.

Smith, R. A.: The Application of Fracture Mechanics to the Problem of Crevasse Penetration. Journal of Glaciology, Vol. 17, No. 76, 223–228, 1976.

Trost, D.: Untersuchung des Randeffekts an antarktischen Schelfeisen mittels FEM. Master Thesis, University of Kaiserslautern, Institute of Applied Mechanics, 2013.

Tsai, V. C. and Gudmundsson, G. H.: An improved model for tidally modulated grounding-line migration. Journal of Glaciology, Vol. 61, No. 226, 216–222, 2015.

Tschoegl, N. W., Knauss, W. G., and Emri I.: Poisson's ratio in Linear Viscoelasticity - A Critical Review. Mechanics of Time-Dependent Materials, Vol. 6, 3–51, 2002.

Van Der Veen, C. J.: Fracture mechanics approach to penetration of surface crevasses on glaciers. Cold Regions Science and Technology, Vol. 27, No.1, 31–47, 1998.

Van Der Veen, C. J.: Fracture mechanics approach to penetration of bottom crevasses on glaciers. Cold Regions Science and Technology, Vol. 27, No. 3, 213–223, 1998.

Vaughan, D. G.: Relating the occurrence of crevasse to surface strain rates. Journal of Glaciology, Vol. 39, No. 132, 255–266, 1993.

Vaughan, D. G.: Tidal flexure at ice shelf margins. Journal of Geophysical Research Atmospheres, Vol. 100, No. B4, 6213–6224, 1995.

Vaughan, D. G., Corr, H. F. J., Bindschadler, R. A., Dutrieux P., Gudmundsson, G. H., Jenkins, A., Newmann, T., Vornberger, P., and Wingham, D. J.: Subglacial melt channels and fracture in the floating part of Pine Island Glacier, Antarctica. Journal of Geophysical Research, Vol. 117, F03012, 2012.

Wagner, T. J. W., Wadhams, P., Bates, R., Elosegui, P., Stern, A., Vella, D., Abrahamsen, E. P., Crawford, A., and Nicholls, K. W.: The "footloose" mechanism: Iceberg decay from hydrostatic stresses. Geophysical Research Letters, Vol. 41, No. 15, 5522–5529, 2014.

Walker, C. C., Bassis, J. N., Fricker, H. A., and Czerwinski, R. J.: Observations of interannual and spatial variability in rift propagation in the Amery Ice Shelf, Antarctica, 2002-14. Journal of Glaciology, Vol. 61, No. 226, 243–252, 2015.

Weis, M., Greve, R., and Hutter, K.: Theory of shallow ice shelves. Continuum Mechanics and Thermodynamics, Vol. 11, 15–50, 1999.

Weertman, J.: Can a water-filled crevasse reach the bottom surface of a glacier? International Association of Scientific Hydrology Publication, Vol. 95, 139–145, 1973.

Wesche, C., Jansen, D. and Dierking, W.: Calving Fronts of Antarctica: Mapping and Classification. Remote Sensing, Vol. 5, No. 12, 6305–6322, 2013.

Wriggers, P.: Nonlinear Finite Element Methods. Springer-Verlag, Berlin, Heidelberg, 2008.

Xiao, H., Bruhns, O. T., and Meyers, A.: Objective stress rates, path-dependence properties and non-integrability problems. Acta Mechanica, Vol. 176, 135–151, 2005.

Zienkiewicz, O. C., Taylor, R. L., and Zhu J. Z.: Finite Element Method: Its Basis and Fundamentals. Butterworth-Heinemann, Elsevier Ltd, Oxford, 7th edition, 2013.

Zienkiewicz, O. C., Taylor, R. L., and Fox D. D.: Finite Element Method for Solid and Structural Mechanics. Butterworth-Heinemann, Elsevier Ltd, Oxford, 7th edition, 2014.

Zienkiewicz, O. C., Taylor, R. L., and Nithiarasu, P.: Finite Element Method for Fluid Dynamics. Butterworth-Heinemann, Elsevier Ltd, Oxford, 7th edition, 2014.

Curriculum Vitae

Name:	Julia Christmann
Geburtsort:	Neustadt an der Weinstraße

09.1992 – 07.1996	Johannes-Leonhardt-Schule, Grundschule Maikammer
09.1996 – 05.2005	Maria Ward Schule, Gymnasium Landau Abschluss: Allgemeine Hochschulreife
10.2005 – 10.2010	Studium der Technomathematik mit Schwerpunkt Modellierung und Wissenschaftliches Rechnen an der Technischen Universität Kaiserslautern Diplomarbeit: *Zustandsschätzung und Fehlererkennung mittels nichtlinearer Filter bei Dynamischen Systemen* Abschluss: Diplom Technomathematikerin
01.2011 – 10.2011	Promotionsstudentin am Lehrstuhl für Technische Mechanik, Fachbereich Maschinenbau und Verfahrenstechnik der Technischen Universität Kaiserslautern
seit 10.2011	Wissenschaftliche Mitarbeiterin am Lehrstuhl für Technische Mechanik, Fachbereich Maschinenbau und Verfahrenstechnik der Technischen Universität Kaiserslautern